TECHNISCHE UNIVERSITÄT MÜNCHEN

Ingenieurfakultät Bau Geo Umwelt
Lehrstuhl für Verkehrswegebau

The Functional Performance of Engineered Cementitious Composites Material for Electrified Roadway Application in Singapore

Ali Aryo Bawono

Vollständiger Abdruck der von der Fakultät für Ingenieurfakultät Bau Geo Umwelt der Technischen Universität München zur Erlangung des akademischen Grades eines

Doktor-Ingenieurs

genehmigten Dissertation.

Vorsitzende(r): Prof. Dr.-ing. Constantinos Antoniou

Prüfer der Dissertation:

1. Prof. Dr.-Ing. Stephan Freudenstein
2. Associate Prof. En-Hua Yang, Ph.D., LEED AP
   Nanyang Technological University, Singapore
3. Associate Prof. Yiik Diew Wong, Ph.D.
   Nanyang Technological University, Singapore

Die Dissertation wurde am 15.04.2020 bei der Technischen Universität München eingereicht und durch die Ingenieurfakultät Bau Geo Umwelt am 11.09.2020 angenommen.

Acknowledgement

I would like to thank Prof. Stephan Freudenstein at the Technical University of Munich (TUM) in Germany for his expert advice and guidance throughout this challenging research. His extensive experience and knowledge in infrastructure engineering were really helpful in getting me the right direction for my research. Prof. Freudenstein has been very supportive since day one to the final stage of my research.

I would like to express gratitude to Prof. En-Hua Yang at the Nanyang Technological University (NTU) in Singapore for his continuous guidance. Prof Yang has been a constant and great source of knowledge and playing a big role in my research from the material science perspective. I am grateful to be able to learn how to balance between doing a good research and to be able to present the research in the journal-form to benefitting greater communities.

I would like to acknowledge, with special gratitude, to Dr. Bernhard Lechner for all of the advice, energy, enthusiasm, and encouragement. I might not have started the doctoral study, and finally to be in this stage without his important roles. Through extensive mentoring, I have learned to understand the essence of the research and embrace it.

I am thankful to PPI Prof. Fritz Busch and PI Dr. Andreas Rau who always supporting and giving me the responsibility and freedom to carry out the research. And to create a very positive environment in TUMCREATE.

I am also thankful to all of my friends, colleagues, and students in the RRT Department (Nen, Teron, Zain, Xiaodong, Freddy, Mike, Meng, Emmeline, Christian v.S), the BGU TUM (David, Sophie, Matthias, Kangle, Martina, Norbert, Yang, Christian, Dr. Simon, Dr. Geisler, Alhaz, Emre, Janaki) and the Living Stone Research Group (Jishen, Zhitao, HeShan, Krishnan, Junxia, Murugan, Cem, Jiawei, XiaoXi, Johnson). Countless guidance, help, support, and motivation I got from all you always made me feel blessed to be as a member of this big family.

The research project done in collaboration between two universities TUM and NTU was really an amazing experience for me. I was never really felt unnecessary pressure, but instead, I found two amazing, humble, and warm families who might have different principles, but both have the similar spirits for the greater purpose in science and education.

I am grateful to my beloved Mom and my Dad (may you have peace in heaven) for raising and educating me. I would like to say thank you for the endless support, love, and understanding from my lovely Desi Adiyati and Alia Alessandra Bawono.

My humble gratitude is due to Subagyo and Hedy Rahadian for their continuous supports.

This work was financially supported by the Singapore National Research Foundation under its Campus for Research Excellence and Technological Enterprise (CREATE) programme.

“Praise be to Allah S.W.T, the almighty God,
the source of life and strength of knowledge and wisdom.”

Table of Contents

List of Symbols

Vf	volume fraction of fiber	
lf	length of fiber	
df	diameter of fiber	
Ef	elastic modulus of fiber	
σfu	tensile strength of fiber	
Km	fracture toughness of ECC matrix	
Em	elastic modulus of ECC matrix	
a_0	initial flaw size distribution of ECC matrix	
τo	interfacial frictional stress of interface	
GD	chemical bond of interface	
f	snubbing coefficient of interface	
f'	strength reduction factor of interface	
β	slip-hardening behavior of interface	
SN	skid number	
F	tractive force	N
W	dynamic vertical load on a test wheel	N
MuN	Mu Number	
BPN	British Pendulum Number	
Sp	speed number	
a,b	calibration constants	
TX	macrotexture (MPD or MTD) measurement	mm
$F(60)$	friction number	
$FR(60)$	adjusted value of friction measurement at selected slip speed S to a slip speed of 60 kilometers per hour	
λ	wavelength	
A	amplitude	
μ	friction level	
MTD	mean texture depth of pavement macrotexture	mm
V	sample volume	mm^3
D	average diameter of the area covered by the material	mm
Sx	cross slope	m/m
S	longitudinal gradient	m/m
Sr	slope of resultant flow path	m/m
Lf	length of flow path	M
L	pavement width	m
WD	water depth above the top of the surface asperities	mm
WFT	water film thickness	mm
TF	length of flow path	m

TXD	texture depth	mm
I	average rainfall intensity	mm/hr
Sr	slope of resultant flow path	m/m
Qr	peak runoff at the point of design	m^3/s
C	runoff coefficient	
I	average rainfall intensity	mm/hr
A	catchment area	hectares
w	relative weight of importance	
x	performance value	
n	decision criteria	

List of Abbreviations

AAC	Autoclaved aerated concrete
APTM	Accelerated Pavement Tracking Machine
BPT	British Pendulum Tester
BPN	British Pendulum Number
COP	Code of Practice
CPB	Controlled pass-by (noise test)
CPX	Close Proximity (noise test)
CTIM	Continuous flow traffic time-integrated model (noise test)
DART	Dynamic Autonomous Rapid Transit
DFT	Dynamic Friction Tester
DOT	Department of Transportation
DPT	Dynamic Power Transfer
DPUR	Dirt Pick-Up Resistance
DWPT	Dynamic Wireless Power Transfer
ECC	Engineered Cementitious Composite
ECC-Cor	Engineered Cementitious Composite mixed with corundum
ECC-SS	Engineered Cementitious Composite mixed with silica sand
EPA	Environmental Protection Agency (of United States)
FEM	Finite Element Method
FHWA	Federal Highway Administration, agency of USA
HPFRCC	High Performance Fiber Reinforced Cementitious Composites
IPT	Inductive Power Transfer
IRI	International Roughness Index
JRCP	Jointed Reinforced Concrete Pavement
JTC	Jurong Town Corporation (Singapore State Owned Company)
KAIST	Korea Advanced Institute of Science and Technology
LCCA	Life Cycle Cost Analysis
LTA	Land Transport Authority (of Singapore)
LWAC	Light weight aggregate concrete
MPD	Mean Profile Depth
MTD	Mean Texture Depth
NEA	National Environment Agency (of Singapore)
NTU	Nanyang Technological University (of Singapore)
NWC	Normal Weight Concrete
OBSI	On board sound intensity
OFT	Outflow Meter Test
OLEV	On-Line Electric Vehicle

PAC	Portland Asphalt Concrete
PCC	Portland Concrete Cement
PDDA	Performance-Driven Design Approach
PFA	Pulverized fuel ash
PrI	Profile Index
PSR	Present Serviceability Index
PUB	The Public Utilities Board (of Singapore)
PUTW	Precast Ultra-Thin Whitetopping
PV	Photovoltaics
PVC	Polymerizing Vinyl Chloride
PZT	Piezoelectric transducer
RhB	Rhodamine B
ROW	Right of Way
SCRIM	Sideway-force Coefficient Routine Investigation Machine
SDRE	Standard Details of Road Elements
SHCC	Strain Hardening Cementitious Composites
SP	Superplasticizer
SPB	Statistical Pass-by (noise test)
SPERoN	Statistical Physical Explanation of Rolling Noise
SPM	Sand Patch Method (test)
SRT	Semi Rapid Transit
TRL	Transport Research Laboratory
TUM	Technical University Munich (of Germany)
TUMCREATE	Technical University Munich and Nanyang Technological University join forces as part of the Campus for Research Excellence And Technological Enterprise (CREATE).
TWT	Thin Whitetopping
UHI	Urban Heat Island
URA	Urban Redevelopment Authority (of Singapore)
UTW	Ultra-Thin Whitetopping
UV	Ultraviolet (Light)
VL	Visible Light
VMA	Viscosity Modifying Agent
XPS	X-ray photoelectron spectroscopy

Abstract

The concept of electrified roadway for wireless inductive charging of electric vehicles (EVs) was proposed as a solution for electromobility to achieve an ultimate public transport system. In megacities such as Singapore, in order to reduce construction time and to minimize road closure duration, a new pavement system named Precast Ultra-thin Whitetopping (PUTW) was developed for rapid retrofitting and conversion of existing road infrastructure into electrified roadways.

Engineered Cementitious Composite (ECC) is a high-performance fiber-reinforced cementitious composite exhibiting extreme tensile strain capacity several hundred and flexural strength 2-3 times that of normal concrete. These enable the design of PUTW for electrified roadway as the thickness of whitetopping can be greatly reduced without the need for steel reinforcement as reinforcement can cause interference of electromagnetic field of inductive charging and lead to reduction of charging efficiency. However, due to the omission of coarse aggregates in ECC mix design, pavement made of ECC generally shows low skid resistance which might cause skid-accidents in highway traffic. On top of that, high intensity of rainfall might increase the risk of hydroplaning which also leads to wet-skid accident.

It is challenging to study the functional performance of a surface pavement with new material without learning the existing solutions. Therefore, a method to study the functional performance from existing surface treatments has been developed. The optimum solution is then defined based on Multi-Criteria Design Analysis (MCDA) including, microtexture, macrotexture, pavement drainage (splash and spray), pavement unevenness, noise, cost, and durability. The understanding acquired is then used as a foundation for the study.

The scope of the study is focused on the functional performance of pavement made of the modified ECC material, especially on the safety aspect. The ECC is modified with fine aggregates, corundum (ECC-Cor) and silica sand (ECC-SS), to improve the surface texture. As for the safety-related functions, the skid resistance and surface water drainage are deeply studied with the laboratory experiments and numerical tools validated with field tests. Additionally, the tyre-road noise for ECC-Cor has been measured and analyzed with numerical tools. The ECC is then further improved for future-green-infrastructure for better liveability in megacities. The ECC is modified with bright color fine aggregates silica sand, called ECC-SS, and carbon modified T_iO_2 to engage self-cleaning functions.

The resulting ECC-Cor possesses satisfactory mechanical performance (i.e., compressive strength > 50 MPa, tensile strength > 4.5 MPa, and tensile strain capacity > 4%) and high skid resistance (BPN > 70). ECC-Cor also shows good durability. Further surface treatment with grooves capable in minimizing the risk of hydroplaning (water outflow time < 4 s) but also by improving the skid resistance (BPN > 90). The sound level of ECC-Cor is higher than ECC (69.2 dB > 64.6 dB). However, with modification by introducing grooves, the sound level can be reduced to less than 65 dB. ECC-SS produces high surface reflectivity with a brightness value of 90. Furthermore, it shows strong visible-light activated photocatalysis property with 90% reflectance recovery after 4 h visible light irradiation and only 8% surface brightness reduction after the accelerated dirt pick-up resistance test.

In summary, this study is highly important as it can be used as the foundation for other studies in relation to the modification of fiber based cementitious material for pavement application, both for electrified and normal roadways. In particular in tropical megacities.

Keywords: ECC, functional performance, skid resistance, surface water drainage, texture, noise, MCDA, electrified roadway, Singapore.

1. Introduction

Chapter one explains the background, the objective, and the outline of the research. Nowadays, safety is becoming as one of the essential factors, which cannot be neglected. Road designers (and roadway authorities) are raising the bar in designing the roadways. The roadways should be operationally efficient and comfort, structurally stable, and importantly provide safety for the driving experience.

1.1. Research background

The concept of electrified roadway with wireless inductive charging for electric vehicles (EVs) was proposed as a solution for electromobility to achieve an ultimate public transport system. In megacities such as Singapore, in order to reduce the construction time and to minimize the road closure duration, a new pavement system named Precast Ultra-thin Whitetopping (PUTW) was developed for rapid retrofitting and conversion of existing road infrastructure into electrified roadways and or conventional roadways.

Engineered Cementitious Composite (ECC) is a high-performance fiber-reinforced cementitious composite exhibiting extreme tensile strain capacity several hundred and flexural strength 2-3 times that of normal concrete. These enable the design of PUTW for electrified roadway as the thickness of whitetopping can be greatly reduced and without the need for steel reinforcement as reinforcement can cause interference of electromagnetic field of inductive charging and lead to the reduction of charging efficiency. However, due to the omission of coarse aggregates in ECC mix design, pavement made of ECC generally shows low skid resistance which might cause skid-accidents in highway traffic. On top of that, Singapore experiences high intensity of rainfall with almost half of the year are rainy days with the hourly average precipitation of 120 mm, which might increase the risk of hydroplaning that also lead to wet-skid accident.

The functional performance of the pavement is based on its ability to serve the user, which is based on significant indicators such as roughness, skid resistance, risk of hydroplaning, appearance (texture), and other safety considerations. These indicators are related to surface properties of the pavement, which is identified as texture [1].

Related laboratory and field measurements were conducted to get a better perspective of safe pavement. Simulation using numerical tools is also performed. Simulation is used to broaden the understanding by extending the scale of pavement system used in the laboratory. Other valuable data are obtained by field measurements, which also used to validate the numerical calculation.

Yet, designing surface properties should not have considered the safety parameter only, but also other parameters. Geometrical aspect, durability, workability, noise, and (life cycle) cost are recently, brightness and self-cleaning properties, are mainly taken into account by many agencies when designing surface properties of the pavement.

Even though a perfect solution, which maximizes all these parameters might be challenging to be achieved. An optimum solution to make safe pavement can be identified with the help of Multi-Criteria Decision Analysis (MCDA) tool. MCDA is used to identify criteria including safety parameter and another parameter. Those criteria then are being scored and weighted. Finally, the results are visually presented with the spider chart.

1.2. Research objectives and its scopes

The main research objective is to improve the performance of electrified roadways through enhancing the safety and imparting additional functions into the ECC-PUTW. Ultimately, the electrified roadway proposed, can provide a robust system that not only reliable on the structural but also functional performance. Scopes of research include:

- To study the state of the art of electrified roadways, from the functional performance (surface pavement properties) perspective.
- To identify the optimum solution of the functional performance for surface pavement by developing Multi-Criteria Decision Analysis.
- To develop material for an electrified roadway which fulfils the functional performance of safety requirement. The requirements include the studies of skid resistance and surface water drainage performance. The scope of the study covers laboratory test, field investigation, and simulation using numerical tools.
- To further develop green material for an electrified roadway, which has the function of low noise, high solar reflectance to reduce urban heat island, as well as self-cleaning capabilities to maintain the high reflectance.

1.3. Research outline

The research outline structured as:

- Chapter 1 : Introduction covers background, scope, and outline.
- Chapter 2 : Electromobility for Singapore
- Chapter 3 : State of the art: Precast Ultra-Thin Whitetopping (PUTW) and ECC
- Chapter 4 : State of the art: The functional performance of pavement
- Chapter 5 : Multi Criteria Analysis on functional performance for pavement
- Chapter 6 : Study of mechanical properties
- Chapter 7 : Study of skid resistance: laboratory test
- Chapter 8 : Study of skid resistance: field test
- Chapter 9 : Study of skid resistance: modelling
- Chapter 10 : Study of surface water drainage: laboratory field test
- Chapter 11 : Study of surface water drainage: field test
- Chapter 12 : Study of surface water drainage: modelling
- Chapter 13 : Correlation between skid resistance and surface water drainage
- Chapter 14 : Study of noise
- Chapter 15 : Study of self-cleaning function
- Chapter 16 : Summary and Conclusion

2. Electro-mobility solution towards the ultimate public transport system with a case study of Singapore

Chapter two describes the current condition of road transport in Singapore and how it leads to the needs of an innovative solution to achieve the ultimate public transport system in Singapore. An electric taxi concept called EVA for Singapore environment was then developed. A new system, Dynamic Autonomous Rapid Transit (DART) which will close the transport gap between Mass Rapid Transport (MRT) and Bus is also introduced. Yet, both EVA and DART are based on electrification, which will be stored on batteries. This leads to an alternative solution for future pavement design, the electrified roadway concept.

2.1. Towards the Ultimate Public Transport System for Singapore

A concept of electromobility in megacities is introduced with Singapore as a case study [2]. The assessment was done on the traffic and power infrastructure in Singapore. An electric taxi concept for Singapore, called EVA, was then developed and introduced. It is claimed that EVA can reach 200 km range with only 15 minutes of recharge based on Singaporean driving patterns. By replacing fuel-burning vehicles with electric, emissions, as well as noise, are expected to be reduced. However, it was concluded that the manufacturing EVA in Singapore was not feasible due to several reasons, including the cost.

(a) (b)

Figure 2.1 (a) The electric taxi EVA (b) Dynamic Autonomous Rapid Transit system

The concept was then leveraged to a different level to achieve the ultimate public transport system in Singapore. A new objective has been set, which is to increase comfort and efficiency for commuters. Therefore, there is a need to close the existing transport gap between current system, Mass Rapid Transport (MRT) and Bus. The new proposed system is called Dynamic Autonomous Rapid Transit (DART) which will optimize public mobility by using electrification and autonomous method for the vehicles.

DART will use modular powertrain for the energy storage solution. DART is a 30-seater unit with dimensions of 6 m x 2.7 m x 2.9 m with fully a laden weight of approximately 7000 kg. As can be seen from Figure 2.1, the operation can be running on platooning mode with up to 10 modules connected by electronic coupling. The maximum speed is 78 km/h with electronically limit of 60 km/h as per Singapore traffic regulation. When it is fully charged, the DART with 120 kWh battery will be able to provide public transport service for an estimated more than 8 hours covering 192 km. DART operation will be autonomous, mainly to reduce the accident rate. In the usual case, DART has a higher level than private vehicles so that the private vehicles need to give way to DART. The prioritization will be enabled by virtual right of way (V-ROW).

Static charging stations implementation was then analyzed to maintain the state of charge of the usage of UVs in Singapore. Placement of charging stations with fast charging performance was proposed only at locations where EVs are likely to run out. Alternatively, charging stations can be placed where ECs started or ended their trips. At the same time, TUMCREATE was also conducting research on innovative pavement system based on local conditions. The proposed system provides possibilities for implementation of electrified roadways as well as enables fast replacement for maintenance with a long life-cycle.

2.2. Road traffic in Singapore and its emissions

Singapore has a total population of 5.5 million in 2016, within an area of 700 sq. Km. Due to land scarcity, Singapore embraces public transport to achieving long term plan transport sustainability. Many challenges needs are facing increasing travel demand, limited land, declining public transport modal share, changing demographics with their expectations for better transportation. Three strategies are planned to tackle those challenges: firstly by enhancing quality of public transport, managing road usage, and meeting diverse needs [3]. Ridership of public transportation based on roadways in comparison to railway based is even normally higher, in daily basis. LTA had added more than double the number of premium or high-quality bus services annually. As 91 bus services per January 2013 compared to only about 42 bus services in 2008 [3]. Reciprocally, in 2014, the total number of average daily ridership for MRT and LRT has doubled in the last 10 years, 2900 passenger-trips only. While, during the same period, bus and taxi cover 4700 passenger-trips [4]. Singapore is maintaining the number of private vehicles in a specific range of numbers to keep the balance of the modal shares. There is no significant increase in the number of motor vehicle population from 2010 to 2015. Within 2010 to 2014, the vehicle population increased 2.8% approximately, and then the population was decline 1.2% in the following year, which was caused by the declination number of cars and motorcycles with 4.1% and 0.8%, respectively. Only buses as public transport vehicles are increased from 2014 to 2015, with 3.6% incremental. Further details about motor vehicle population can be seen in Table 2.1 [5].

Table 2.1 Motor vehicle population in Singapore

Motor vehicle population	2010	2014	2015
Cars	584,399	600,176	575,353
Rental cars	13,347	18,847	29,369
Taxi	26,073	28,736	28,259
Buses	16,309	17,554	18,183
Motorcycles	148,160	145,026	143,900
Goods & others	157,541	161,698	162,182
Total	945,829	972,037	957,246

According to the Land Transport Statistic in brief of Singapore [5], the total length of paved road in Singapore in 2012 is about 3425 km (9080 lane-kilometers) approximately which covers 161 km (1059 lane-kilometers) of expressways, 652 km (3054 lane-kilometers) of arterial roads, 561 km (1584 lane-kilometers) of collector roads, and 2051 km (3381 lane-kilometers) local access roads. Yet, this number increased to 9264 lane-kilometers in 2015 [6]. Please see Figure 2.2. This is resulting in road density in Singapore as 5 Km/sq.Km approximately.

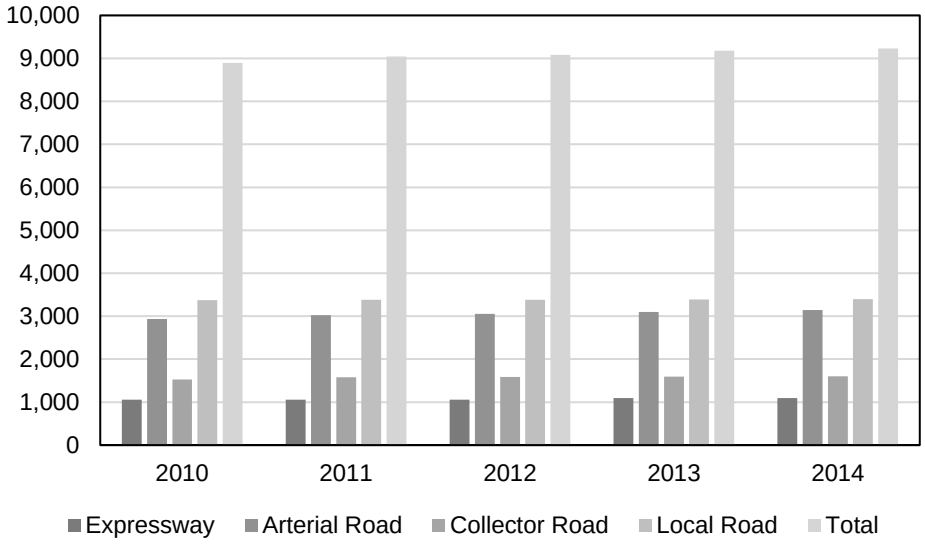

Figure 2.2 Length of roadway (Lane-Kilometers) in Singapore

Singapore contributes around 0.11% of global emissions. In 2015, Singapore ranked 123rd of 142 countries in terms of CO_2 emissions per dollar GDP [7]. It is projected that the Business-as-usual (BAU) emissions in Singapore are expected to reach 77.2 million tons in 2020 [7]. It was then mentioned by Balakrishnan citing the Sustainable Singapore Blueprint 2015, Singapore is aiming to reduce its carbon emissions up to 11% below business-as-usual-scenario levels by 2020 [8].

2.3. Current pavement design in Singapore

Current Singapore pavement design is standardized in the Standard Details of Road Elements (SDRE) issued by LTA. Currently, three types of pavement design are applied in Singapore: asphalt pavement design, concrete pavement design, and semi-rigid pavement design. Asphalt pavement is typically used on the carriageway, while concrete pavement and semi-rigid pavement could also be applied on bus bays and intersections.

2.3.1. Asphalt (flexible) pavement

Typically, asphalt pavement in Singapore consists of four layers: sub-base, base course, base course, and asphaltic wearing course. However, an additional layer with porous asphalt is also introduced to reduce the noise. LTA introduces four different types of asphalt pavement: Type 1A, 1B, 2, and 3 [9]. Each type has different thickness and material properties, and its usage depends on the road type. The illustration is shown in Figure 2.3, and explanations are elaborated in Table 2.2.

2.3.2. Concrete (rigid) pavement design

LTA publishes rigid pavement design not only for road carriageway but also for bus bay and intersection applications. Rigid pavement used in Singapore is typically a jointed reinforced concrete pavement (JRCP) type with a thickness of 225 mm. Typically, using the base course as unbound support layer supported with a geotextile membrane to separate between each layer. Rigid pavements can be used altogether with asphalt pavements for carriageway. Indeed, three meters transition slab is needed to provide a gradual transition as without this. A bump may appear over a period of time on the AC pavement side [10]. The picture is shown in Figure 2.4.

In Singapore, rigid pavement is also used on bus bays and intersections to handle the higher stresses due to braking force and acceleration force, particularly from heavier vehicles such as buses and trucks. On bus bay, a small transition is longitudinally designed where 105 mm thickness from the bottom part concrete pavement is extruded into the asphalt pavement with a width of 150 mm. See Figure 2.5 (1) and (2) for details.

2.3.3. Semi-rigid pavement design

In Singapore, significant application of the semi-rigid pavement is for traffic light junction with a typical thickness of 50 mm as the wearing layer [11]. Semi-rigid pavement is designed as an open-graded asphalt with a void between 25 % to 30 % by volume (Marshall) filled with high strength cementitious mortar [12]. It is basically the combination of Porous Asphalt Concrete (PAC) and Portland cement concrete (PCC) pavements. The semi-rigid pavement has to achieve a compressive strength of 7-10 MN/m² at 28 days and flexural strength of approximately 3.5 MN/m². High strength cementitious mortar consists of a dense packing of cementitious inorganic material mixed with water. The mortar needs to achieve a compressive strength of 110 MN/m² at 28 days and flexural strength of approximately 15 MN/m². The mix design should use water to binder ratio within a range between 0.226 and 0.278 [12]. Some advantages of semi-rigid pavements including higher resistance to rutting compare to asphalt concrete, relatively easier to construct and to maintain, and faster in respect of open to traffic which can be done less than 24 hours. Yet, filling high strength cementitious mortar should be done carefully to avoid excessive material on the surface. The excessive material can cover the aggregates, which may cause lower skid resistance. The service life of semi rigid commonly known as higher than asphalt concrete but less than PCC. However, semi-rigid has their disadvantages include surface-initiated cracking (top-down cracking and thermal fatigue cracking), instability rutting, fatigue cracking of cement-treated materials, shrinkage cracking and reflective cracking [13].

Table 2.2 Type of asphalt (flexible) pavement

Type of flexible pavement	Road type	Thickness				
		a	b	c	d	e
Type 1A (with porous asphalt)	Expressway Semi-Expressway Arterial Road Road in Industrial Area	40	30	120	250	300
Type 1B (without porous asphalt)		0	50	120	250	300
Type 2	Primary Access	0	40	90	200	300
Type 3	Local Access	0	25	75	200	200

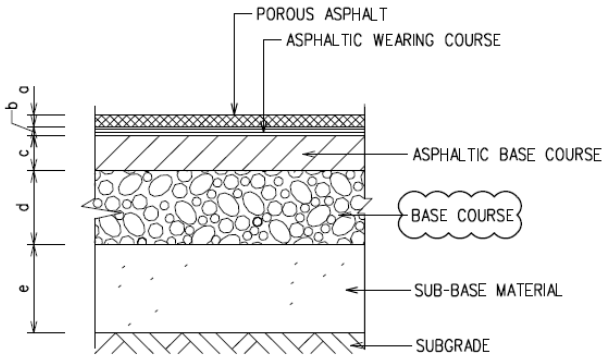

Figure 2.3 Asphalt (flexible) pavement structure design

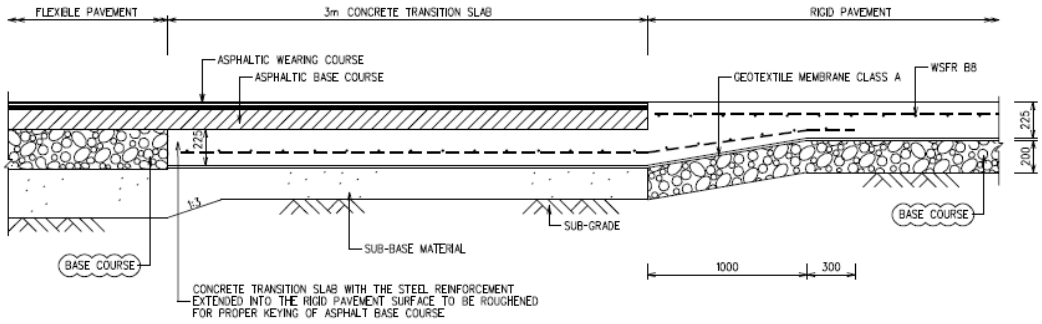

Figure 2.4 Rigid pavement and its connection with flexible pavement

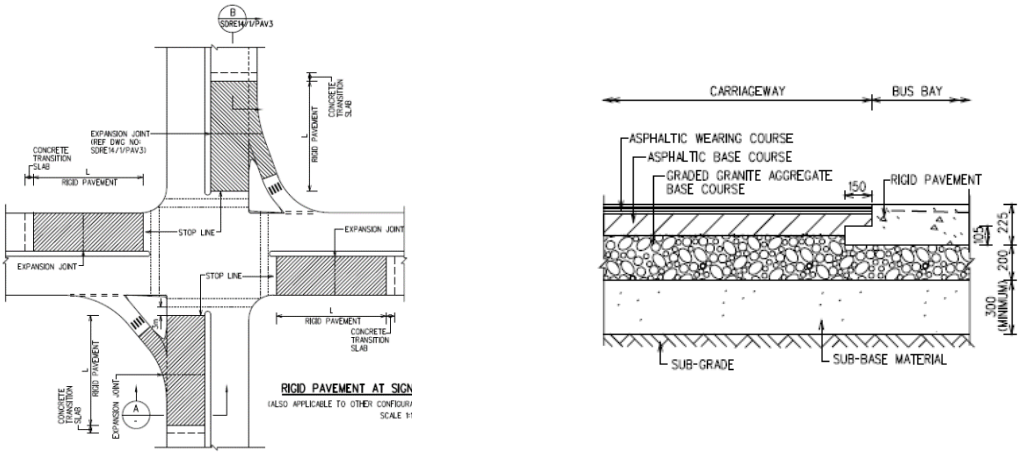

(a) (b)

Figure 2.5 (a) Top view of pavement design at intersection, (b) structure for bus bay

2.4. Future pavement design: electrified roadways

On one side, vehicle technologies are significantly advancing to fight against the emission. As technology develops, ultra-low emission vehicles (ULEVs) include pure electric vehicles, plug-in hybrid and fuel cell electric vehicles are trending nowadays. Those vehicles are available on the market and will be a common sight in Singapore in the coming years. On the other side, transport infrastructures are also developing not only to help to reduce the emissions but also to allow longer and safer journeys for those vehicles above.

Currently, two technologies are available for charging the battery of the electric vehicles: plug-in charging and inductive charging. Plug-in charging system operates at a specific supply point. It requires a cable and a socket, which is connected to the vehicle. The inductive charging operates differently. This system, which is commonly known as electrified roadways, provides a charge to electric vehicle batteries without the need for plugging the vehicle into a charging supply point. This allows charging the vehicle when the vehicle is station (static charging) or on the move (known as dynamic charging). The dynamic charging, which also called an opportunity charging, results an increased operating time by a factor of 2 to 3. This allows reducing the battery costs and weighting per vehicle as well as space for the battery, which is in an overall reducing life cycle cost [14].

2.4.1. Development of electrified roadway

The installations of plug in charging system have mainly done in urban city environments. However, there is a requirement for the dynamic charging system, which embedded in the pavement, that will enable electric vehicles to travel in greater distances on the strategic road network by using only electric power [15]. This system is often called electrified roadway. A recent article explains that the adoptions of electric vehicles are still remaining low due to the fact that the battery has many issues such as expensive price, heavy, and it offers a low range of distance [16]. Surveys show that EVs users worries about charging, whether where can they do it, and how long it will take. A similar hypothesis is given by the Guardian [17] with conclusion there is a need to have an extension of charging infrastructure.

The concept of the electrified roadway was firstly invented for railway application by Hutin and Leblanc [18] in 1894. Until then in 1970, a 6 kW proof of concept was tested at Lawrence Berkeley and Lawrence Livermore National Libraries. However, the conclusion drawn from tests shows that the system was not suitable for the operational aspect. A similar outcome was given from the Santa Barbara Electric Bus Project (1979) consists of a planning and feasibility study followed with preliminary engineering and prototype development and testing.

A project called Roadway Powered Electric Vehicle (RPEV) was done by California Partners for Advanced Transit and Highways (PATH), Institute of Transportation Studies, UC Berkeley, and the Southern California Association of Governments (SCAG) in the 1980s. It is then recognized as the first successful test in dynamic charged pavement [19,20]. Within the project, approximately 200 m road track was constructed in their facility. The track consisted of two 60 m electrified segment. An electric bus of 35 passengers with a maximum speed of 64 km/h was used. Details of RPEV components can be seen in Appendix A.

Korea Advanced Institute of Science and Technology (KAIST) developed a shaped magnetic field in resonance (SMFIR) in 2009 to enable wireless electric power transmission for moving vehicles. The electrified roadway was built in Seoul Grand Park with the total length of the powered track is 372.5 m. The system is operating in 2013 on a 25 km line in Gumi. It is reported that the advantage of KAIST system is that the battery the rechargeable bus is only 1/5 the size of a normal electric bus battery. Recharging pads cover only up to 15% of the bus.

In 2009, Bombardier introduced PRIMOVE offering a wireless power supply for all vehicles. A testbed of 600 m was built at Augsburg. It is using a power supply of 750 DC. In 2010, Bombardier continues their research by demonstrating another testbed in Lommel for a bus. The testbed has 125 m length built on concrete roads. Then recently, in 2015, PRIMOVE Mannheim project has been developed for bus line 63 along nine kilometers. The system consists of four charging stations with approximate charging time for two minutes.

In 2015, an executive agency of Highways England published a feasibility study with the topic of powering electric vehicles on England’s major roads [21]. It is reported that the electrified roadway testbed consists of a track length of approximately one km with at least two lanes, each of 3.5 m. Based on their investigation on road construction methods, the in-situ full-width lane was the preferred option for the off-road trial, and suitable on highways later on.

The first charging rail-based electric roadway installed in Sweden by 2017 through the eRoadArlanda project with two kilometers constructed between Arlanda and the Roserberg logistic area. The electrified roadway is intended to be used by logistic trucks mainly. However, this is not the first time Sweden has a pilot project for such a system. Back to in 2012, they had a testbed with a total length of 200 meters. An additional 150 meters of electric rails were then installed in 2014. It is then followed with another 50 meters of rail installed with the new generation of rail tracks [22].

2.4.2. Dynamic Power Transfer (DPT)

Currently, research institutes and industries developing the new technology which allows power transfer to the electrified vehicle powertrain options, including hybrid powertrains. A vehicle can make use of a power transfer system to charge the on-board Rechargeable Energy Storage System (RESS – the battery) or to provide power to the electric motor.

Typically, such power transfer systems are plug-in electric chargers that charge the vehicle batteries at varying levels of power while the vehicle is stationary and switched off. However, it is also possible to use Wireless Power Transfer (WPT) to charge the batteries while stationary, using charging “pads”. Both solutions are adequate for charging at home or in car parks but still require the vehicle to stop in an appropriate location to charge the battery. Inductive Power System (IPT) or Dynamic Power Transfer (DPT) is another option for supplying power to electric vehicles and, as it can be used while the vehicle is moving, it can help to reduce or eliminate issues with restricted range. DPT can be either conductive or wireless. According to the Transport Research Laboratory, the required power transfer level from a Dynamic Wireless Power Transfer (DWPT) system on a motorway is around 20 kW to 40 kW per vehicle for cars and light vans, and between 100 kW and 180 kW for trucks and coaches, based on the power required to maintain constant motorway speed [21,23]

Standard and regulations for inductive charging for EVs were set. One of the first is ICNIRP 1998/2010L Guidelines for limiting exposure to time-varying EM fields [24], which regulates requirement related to Living Tissue affected by Power Dissipation caused by Electromagnetic Fields, a Limitation of Human Body SAR (Specific Absorption Rate, [W/kg]) by Limiting Electric and Magnetic Fields, and the distinction between “General Public” and “Occupational Exposure”. Another standard was set in 2013. Under SAE J2954 Wireless Charging Standard, it explains the baseline for the safety consideration. It is stated that the common operating frequency is 85 kHz, the minimum charging efficiency should be at least 90%, parameters regarding interoperability, safety features, and validation methods, and as well as the charging levels are divided into three levels (1) WPT1 private low power is up to 3.7 kW, (2) WPT2 private and public space is up to 7.7 kW, and (3) WPT 3 for fast charging is up to 22 kW.

One of the first inductive charging systems was introduced in RPEV technology. It consists of the Inductive Coupling System (ICS) which transfers energy from a coil buried beneath the pavement surface to the vehicle through a magnetic field. In the RPEV system, the power conditioner used is an inverter with a three-phase 60 Hz power and then puts out a single phase at a higher frequency. As results, the system allowed peak output up to 60 kW to be transferred from the electrified roadway to the moving electric bus with an efficiency of up to 60%. As consequences, the electric bus can be operated up to 400 km, much more compared to previous performance which only up to 30 km.

Bombardier is one of the leading companies for WPT technology. They can provide a system of up to 200 kW. They have applications spreading in Europe countries. While among research groups, KAIST is showing a big interest by significantly developing the system continuously. Up to now, they successfully improved and implemented the system in Korea. According to the results reported by KAIST, the new wireless electric power transfer technology which is named as shaped magnetic field in resonance (SMFIR) shown a good performance with the efficiency of up to 85% with air gap of 20 cm between the pavement surface and the pick-up installed on the vehicle [25]. The Wireless Power Transfer (WPT) systems are summarized in Table 2.3 and it is listed from the highest to the lowest power level.

Table 2.3 Summary of WPT technology from different group

System	Air gap	Power Level	Efficiency	Application and Demos
EATON HyperCharger	30.5 cm (12 inch)	200 kW to 1 MW.	-	Electric buses US targets: Tallahassee FL, Stockton CA, and Worcester
Bombardier PRIMOVE	4 cm	200 kW high power	95%	Electric buses and LRVs Germany and Belgium, 2011-2013
OLEV SMFIR KAIST	20 cm	100 kW	Up to 85%	Electric bus and LRVs KAIST and Gumi, Korea, 2009-13
PATH	6 cm	60 kW	60%	Electric bus
Technology (former Conductix-Wampfler)	4 cm	60 kW module in roadway, 30 kW modular onboard bus	> 90%	Electric Buses. Turin and Genoa, Italy; Utrecht, Netherlands Utrecht since 2010; Lucerne, Switzerland; Lörrach, Germany; Rotorua, New Zealand.
WAVE	20 cm	50 kW for 40 ft. bus & up to 140 KHz;	90%	Electric Buses USU, Logan, Utah; Monterey-Salinas Transit (MST); 2012-2014
Stanford	-	10 kW	> 97%	Electric Vehicles
ORNL		7 kW	90 – 94%	Electric Vehicles
Siemens	15 cm	3.6 kW	> 90%	Electric Vehicles
WiTricity	15-200 cm	3.3 kW	> 90%	Small Electric Vehicles

KAIST has been developing OLEV for over than a decade by now. The first successful demonstration of SMFIR system was done in 2009, which is identified as the 1st Generation (1G). Until the 4th Generation, the rail width, which needed is relatively wide, even though they are successfully reduced from 140 cm (1G) to 80 cm (2G, 3G, and 4G). Only until the I-type is introduced, they can have rail width with only 10 cm [26]. This narrow power supply with a width of 10 cm results in the overall power efficiency of 74% (including an inverter) at an output power of 27 kW and a large air gap of 20 cm. The electromagnetic field (EMF) is reduced significantly, with only less than 10 mG. While S-type only needs 4 cm rail width yet producing 71% power efficiency at an output power of 22 kW. Details of OLEV development can be seen in Appendix A.

OLEV has developed an innovative power supply with its latest product. Not only the rail width of the new proposed S-type is smaller, but it also has another advantage which the power supply rail adopts a module concept. As shown in Figure 0.2 (in appendix A), this concept makes it easier to fold itself by virtue of flexible thin power cables. Therefore, no power cable connection is required after being deployed [26]. With only 4 cm width is needed for the S-type power modules, this leads to easier construction work, relatively lower construction cost and faster deployment time. The modules can be embedded in asphalt or concrete pavement.

The technology of the inductive charging system is designed not as a replacement of the static system. Instead, it is to enhance as an integrated system. Both systems, static and dynamic charging have their own strength and weakness. The static system is relatively cheaper than the dynamic. But it requires the vehicles to be parked. Therefore, the system is only feasible to be placed based on fixed station wise such as at home, at the office, at the shopping mall, or at a charging station. The dynamic system is more expensive than static. However, the dynamic system allows vehicles to be driven, which can save time.

Both systems can be integrated into one system and then solve the issues related to the limited capacity of rechargeable batteries. According to Bombardier [27], with a dynamic charging, an electric bus can use only 1:5 of the batteries capacity compared to a bus with a static charging system. This leads to a bigger space for the passengers, 25% more compared to the classic electric bus. The dynamic charging system also beneficial for the battery lifetime as they claimed it could be improved to 60% extension.

2.4.3. Pavement design to embed DPT system

There are few basic requirements regarding DPT/DWPT system, including the transmitter coils of the system need to be embedded close to the surface to increase the charging efficiency. Complex cables need to be enclosed inside the pavement. The wireless charging system needs to be protected with materials, preferred non-ferromagnetic as the charging performance will be reduced when it is enclosed or surrounded by ferromagnetic material (such as steel) as there will be eddy current losses. Referring to [19], the DWPT system for RPEV is covered with sand/epoxy/fiberglass filler. Concrete material is used for coverage, but then it was found out that concrete would not have provided much protection for the cores as sand/epoxy/fiberglass even though the cost will be lower. This system is laid on the concrete pavement. Then the entire roadway was covered with a slurry seal with a thickness of fewer than 5.1 mm.

One of the first developments of the DWPT system including pavement design for the electrified roadway was done in the PATH Program. The system used roadway inductor which consists of basic components: the inductor modules and the conductor (as seen in Figure 0.1). These components were designed to withstand full traffic loads and require little maintenance.

Another concept of embedded IPT components on the prefabricated slab was patented by PRIMOVE. The 25 cm thick slab lay on 8 cm bituminous base with aluminum supports. The bond between the slab and the bituminous layer is strengthened with 2 cm of grouting. Slabs were tested on the accelerated pavement testing facility of IFSTTAR in Nantes. It is an outdoor facility with circular carousel equipped with four 20 m long arms and has a mean radius of 17.5 m and a width of 6 m, thus a total length of 110 m. The system which is illustrated in Figure 2.6 is claimed to be durable, and it has the performance of hold one million of 6.5 tons (traffic) load cycles. This is equivalent to a traffic of 150 buses per day for 20 years. No particular surface treatment was reported [28].

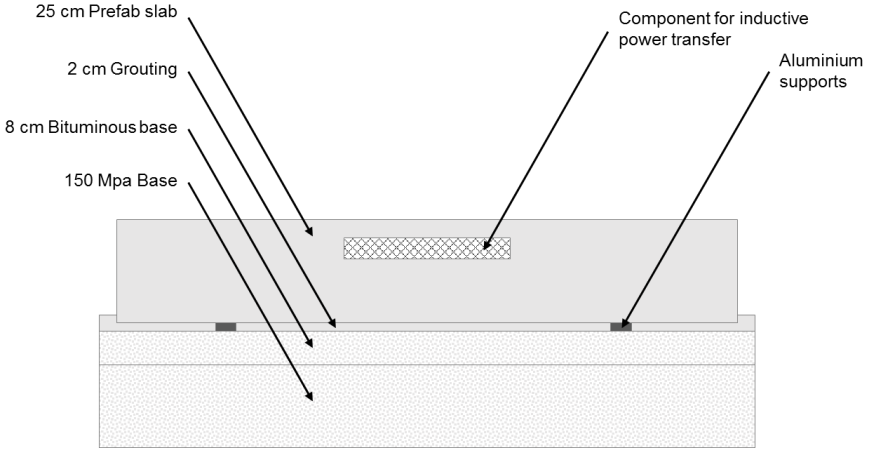

Figure 2.6 Cross section of PRIMOVE prefabricated slab [27]

Another example is given by eRoadArlanda, where they had installed the first charging rail in public road with a length of 2 kilometers in June 2013. The system introduced is railings based embedded in the pavement. They explained that it is critical to combine battery power with direct power feeds while the vehicle is driven. On the minor roads, the vehicles still can run on batteries. But on the major and frequently used roads, the batteries will be recharged continuously. Therefore, the battery-powered vehicles would only need to be designed to be driven with a section of road with an electrical feed. Vehicles can also be recharged at fixed stations. This allows optimum function for the EV since long-distance driving will be not necessary until the EV enters a major road with dynamic charging. With this system, there is only need for a grid with a size about 45 kilometers in length on approximately 20.000 kilometers of Sweden's highways. This grid will result in smaller batteries for EV, which means lower cost and a better environment [22].

2.5. Chapter discussion

In summary, this chapter explains the current emissions situation in Singapore, in particular from the road transport sector. It leads to the needs of electrification of vehicles and how the infrastructure can be modified to support on the EVs. Yet, the pavement design for electrified roadways should fulfil both requirements for the (traffic) loading and the charging system.

The emission from the road transport sector is currently increasing from year to year. Singapore contributes around 0.11% of global emissions. From 77.2 million tons in 2020, up to 14% of the emission is coming from the transport sector. Singapore is then aiming to reduce its carbon emissions up to 11% below business-as-usual-scenario levels by 2020.

Meanwhile, the electromobility concept through EV technology is then introduced in Singapore as they are aiming to have the ultimate public transport to reduce their emission. EVA and DART were some of EVs have been developed for Singapore condition. However, there are some limitations related to EVs. Three fundamental limitations for EVs are (1) battery capacity leads to limited driving range, (2) availability of charging stations, and (3) time for battery re-charging. These limitations require further innovative development as an alternative and better solution for electromobility. To enhance the static charging system, an electrified roadway with a wireless charging system using the opportunity charging method might tackle the problems as it provides higher convenience and usability for EVs.

The electrified roadway requires specific structural performance, so it will be able to bear similar traffic loading as typical roadways, a guarantee for the safe driving experience, and it needs to be embedded with a power module. At the same time, steel reinforcement inside the pavement is strictly recommended to be removed to avoid losses of eddy current rate. Meanwhile, road infrastructure in Singapore is considered as it is not fully ready for neither EVs technology nor as electrified roadways. Current pavement designs, which consist of concrete pavement, asphalt pavement, and semi-rigid, were not intended to be utilized as electrified roadways. Further, none of the studies described the functional performance of the electrified roadways.

3. State of the Art: Engineered Cementitious Composites Precast Ultra-Thin Whitetopping (ECC-PUTW)

Chapter three describes the whole picture of Precast Ultra-Thin Whitetopping (PUTW), from design, material, manufacture process, and construction. PUTW offers an option for modification so it can be utilized as electrified roadways. PUTW uses different material than rigid or flexible pavement to avoid the usage of steel reinforcement. Engineered Cementitious Composite (ECC) was then proposed for PUTW development. ECC material is also discussed in this chapter.

PUTW pavement system was developed based on Ultra-Thin Whitetopping (UTW) system with prefabricated slab method to reduce the construction time, which will cause high user delay cost. UTW or thin bonded concrete overlay over asphalt is commonly known as one good solution for preventing rutting due to heavy loads. While Precast Concrete Pavement (PCP) offers a reduction of the road closure time while providing the high performance of a conventional rigid pavement. However, joint and load transfer devices in PCP are rather complicated. In PUTW, normal joints with dowel and tie bars are not being used. The bond between slabs highly depends on the bond performance between PUTW and asphalt layer. PUTW can be installed on milled old asphalt or newly paved asphalt. However, good performance of the asphalt is required.

3.1. PUTW design

PUTW pavement system is characterized by the material properties, interface bonding in composite layer, slabs dimensions and joint performance. PUTW is designed as a high-performance pavement which is suitable for heavy traffic junctions and bus stops. To achieve the high performance, material called Engineered Cementitious Composite (ECC) is used.

ECC is a unique type of high-performance fiber-reinforced cementitious composite. The most notable characteristic of ECC, which is achieved by the formation of multiple microcracks is high tensile ductility. The compressive strength of ECC is similar to normal concrete, which usually is in the range from 30 to 90 MPa. PUTW uses very thin prefabricated slab. The slab assuredly has to be durable to withstand the traffic load and construction load (example given is slab lifting process). Due to its material properties, using reinforcement mesh is no longer needed. While, a metallic reinforcement mesh is not a good option for electrified roadways as it will interfere with the electromagnetic field. Therefore, ECC material is chosen as a potential candidate for PUTW.

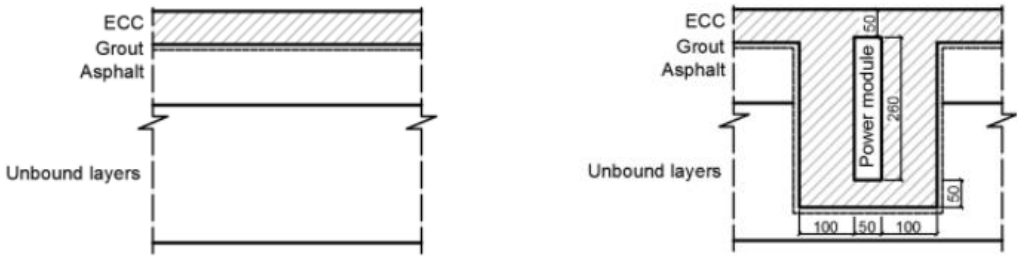

Figure 3.1 Design of (a) PUTW (b) electrified PUTW [29]

PUTW is designed so it can keep the asphaltic wearing course layer to certain thickness which will be replaced by PUTW slab. Assuming the rest of asphaltic layer still has sufficient performance, with even thin (50 mm) PUTW slab, the system is able to handle 25% more traffic load compare to conventional rigid pavement [29].

As has been mentioned, PUTW design can be modified to accommodate electrified roadways which uses power module. The structural design is similar to normal PUTW concept. However, the modified PUTW design is equipped with culvert for the power module so it can be protected. As S-Type power supply module of the latest KAIST OLEV system (5G) is proposed to be embedded in PUTW, the culvert has 50 mm thickness of top cover and bottom cover.

In PUTW, concrete and asphalt layer are bonded together by grouting to form a composite layer. The good bonding strength is the foundation for a durable and long-term performance of the system. As there is no dowel or tie bar to handle the load transfer, the bonding which ensures the positions of PUTW slabs is fulfilled by the asphalt layer. If there is no bonding, the PUTW slab will drift or even endanger road users. And moreover, similar to UTW, the bonding is particularly important for the load transfer between slabs [29–33]. The bond strength requirement is fulfilled due to the help of grout material between the slab and asphaltic layer and the convex nodes on the bottom surface [29].

PUTW slab needs to be lifted, whether during the manufacture or installation process. During the manufacture, the slab needs to be lifted from the formwork to storage place. Then the slab will be lifted from the storage place to the lorry to be transported to the site. Finally, the slab is then lifted from the lorry to be placed in the designed area. During the installation process, the slab needs to be leveled according to the standards. As the roadway geometries is ideally designed with required crossfall and slope. This can be done with the help of lifting and leveling invention device. The device is using one plate with different type of bolts. The lifting bolt is normally equipped with a hook to lift the slab, while the leveling bolt is fitted with a metal lug head, so it can be rotated to set the level.

PUTW requires higher initial construction cost compare to conventional concrete- or flexible pavements. However, with the advantage of prefabricated slab method, PUTW offers lower user delay cost due to minimum delay road closure. Additionally, with less pavement rehabilitation and less maintenance, it is resulting in a lower life cycle cost for PUTW system. Previous study compares the Life Cycle Cost Analysis (LCCA) between two pavements: cast-in-place JRCP and PUTW. The results showed that the initial cost for PUTW is relatively high. Whereas user cost is the most significant component in LCC of cast-in-place JRCP. However due to rapid installation, the user cost of PUTW construction is far less than the cast-in-place JRCP. The difference of LCC is up to 2.15 times in the case of traffic diversion ratio is 0. However, when traffic diversion ratio 30%, the LCC of the two alternatives are quite close to balance. As conclusion, PUTW has the advantage on economical LCCA, depending on construction site location and traffic volume.

3.2. Engineered Cementitious Composite (ECC)

3.2.1. The application of ECC

Engineered cementitious composites (ECC) is a unique class of the high-performance fiber-reinforced cement-based material showing extreme tensile ductility of several percent [34,35]. ECC has been used in various applications, such as to make coupling beams in high-rise buildings [36], to create a bridge deck link slab replacing expansion joints in a bridge [37], and to retrofit the surface of irrigation channel [38], dam [39], and earth retaining wall [40]. Few studies have reported potential use of ECC for rigid pavement applications. On top of that, the reflective cracking failure (which commonly occurred in overlay) can be eliminated because the high ductility of ECC overlay is able to trap the kinked-out microcracks from the interface [41]. Compared to conventional concrete and hot mix asphalt (HMA) overlay systems, ECC overlay offers lower life cycle cost over a 40 years of service life with reducing total life cycle energy by 14%, Greenhouse gas (GH) emissions by 43%, and costs by 40% [42]. It is reported that ECC can be used for repair material to provide better system performance as it is stronger, more ductile, more energy absorbing, and shows better crack control compared to concrete

[43]. Similar scenario has been reported by Qian and Li [35], that ECC pavement will be more favourable for medium to heavy traffic due to the efficiency of pavement thickness, jointless/larger joint spacing, and less maintenance required. Recently, ECC is applied on 80 m jointless test track shows that this material can be produced in large quantity and at high quality. The long-term monitoring showed that the material could handle high traffic loads and the abrasion was low [44].

3.2.2. Micromechanics-based Design of ECC

The development of ECC design is ideally based on the performance-driven design approach (PDDA) (as can be seen in Appendix C), which emphasizes micromechanics as the unifying bridge between mechanical properties and material microstructure. With PDDA, the imposed requirements of structural performance, e.g. deformation capacity, ductility, and load capacity are depicted into mechanical properties at the material level, e.g. strength, ultimate strain, toughness, and maximum crack width. Great advantage is PDDA offers systematic engineering solution rather than trial-and-error empirical experiments [45].

To achieve multiple cracking and tensile strain-hardening behavior in ECC, there are two conditions need to be fulfilled

- Crack tip toughness J_{tip} has to be less than the complementary energy J_b', which is calculated from the bridging stress σ with crack opening δ curve.

$$J_{tip} \leq \sigma_0\delta_0 - \int_0^{\delta_0} \sigma(\delta)d\delta \equiv J_b' \quad \text{(Eq. 1)}$$

  where

$$J_{tip} = \frac{K_m^2}{E_c} \quad \text{(Eq. 2)}$$

- The tensile first crack strength σ_{fc} must not exceed the maximum bridging stress σ_0.

$$\sigma_{fc} < \sigma_0 \quad \text{(Eq. 3)}$$

According to Li et al. [45], (Eq. 1 implies the stress-crack opening relationship $\sigma(\delta)$ which is regarded as a constitutive law of fiber reinforced composites, is derived from analytic analysis of fracture mechanics, micromechanics, and statistics. Where σ_0 is the maximum bridging stress corresponding to the crack opening δ_0, while E_c is the composite elastic modulus.

Due to a distribution limitation of pre-existing flaw size, a sufficient margin between complementary energy J_b' and crack tip toughness J_{tip} is desired for developing saturated multiple cracking. Examples on methods to achieve it are given:

- Reducing J_{tip}, which is correlated to matrix toughness, or
- increasing J_b'. Which is more reasonable because low matrix toughness implies low first crack strength.

In the microstructure tailoring part, three sets of parameters are considered including fiber, matrix, and interface (fiber-matrix interaction) phase. Parameters are summarized in Table 3.1.

Table 3.1 Parameters in PDDA approach for ECC design

Fiber		Matrix		Interface	
V_f	Volume fraction	K_m	Fracture toughness	τ_o	Interface frictional bond
l_f	Length	E_m	Elastic modulus	G_D	Interface chemical bond
d_f	Diameter	a_0	Initial flaw size distribution	f	Snubbing coefficient
E_f	Elastic modulus			f'	Strength reduction factor
σ_{fu}	Tensile strength			β	Slip-hardening coefficient

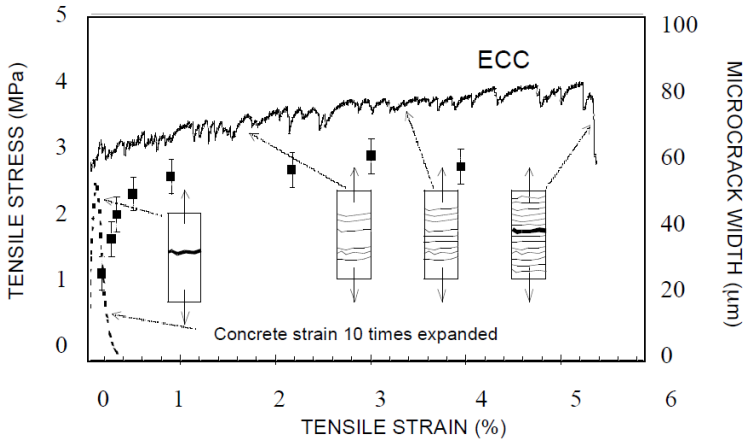

Figure 3.2 Strain-hardening behavior of ECC material [46]

3.2.3. Ingredients used in ECC

ECC consists of various ingredients with different specification. In this study, different mixture designs with different material were tested. The density of each material is summarized in Table 3.2 and Table 3.3.

Table 3.2 Density of materials for ECC

Material	Cement/ White Cement	Micro-Silica Sand	Water	Fly Ash	GGBS	Fiber PVA	Fiber PE	Super - plasticizer
Density (g/cm^3)	3.15	2.65	1.00	2.20	2.91	1.30	0.96	0.30

Table 3.3 Density of suitable aggregate for skid resistance improvement

Material	Corundum	Silica Sand	Granite	Steel Slag
Density (g/cm^3)	3.95	2.65	2.60	3.20

In this study, Type I Portland cement (CEM I 52.N) is used. Another type of cement used in ECC is Type I white cement. Type I white cement is typically used for ECC for architectural applications [47,48]. Micro-silica sand with particle size: 0.08 mm to 0.12 mm is used in ECC for this study. Normal tap water is used for ECC.

Fly ash is commonly used to reduce the chemical bonding while increasing frictional bonding of the fiber and matrix interface. Furthermore, fly ash replacement of cement means to lower the matrix toughness. Thus a matrix with higher fly ash content can be used to compensate the rate sensitivity of the material components that limits the tensile ductility at higher loading rates [49]. Fly ash improves mixture workability and material sustainability. On the other hands, high content fly ash leads to slower strength development at early stage. Similar result with Yang and Li (2002), incorporating fly ash into matrix tends to reduce both the interface bond and matrix toughness [50]. Fly ash class F with particle size: 0.01 mm to 0.15 mm is used in ECC mixture for this study.

Fibers are more expensive than the other materials used in ECC. Therefore, it is understandable to minimize the amount of fibers used while maintaining the strain hardening. Using fiber content in a low volume will lead to normal FRC tension-softening behavior. On the other hand, using fiber content greatly value leads to workability issues [51]. In this study, two different types of fibers are used. PE fiber is produced by Honeywell with type of Spectra® 1000, with a diameter of 23 μm, length of 12 mm and 19 mm. While PVA fiber is produced by Kuraray with type of REC(S) 15 with diameter of 40 μm, length of 12 mm, and 1.2 % surface oiling content.

PVA is an organic fiber offers advantages of high tenacity and modulus of elasticity when compare with other general organic fiber. PVA also provides strong bonding strength between fiber and cement matrix, and it is durable [52]. PVA fibers are hydrophilic which makes it strongly bond to the matrix. This leads to limit the multiple cracking effect and lower strain hardening behavior for the composite. Reducing the chemical de-bonding energy enhances the complementary energy by minimizing premature fiber breakage during the matrix interface de-bonding process [53]. PE fiber has an extremely high melt viscosity, toughness, cut and wear resistance, and very good chemical resistance. PE fibers enhance the toughness and flexural strength of ECC [54]. Yet, the application of PE fiber in cement composite is limited due to high cost [52]. In a single fiber pullout test, PE fiber has shown the increase of the interface friction during fiber slippage induced a slip hardening behavior which lead to the increase of strain hardening for the composite. However, the slip hardening should be limited to avoid fiber rupture. As fiber pullout results a higher ductility compare to fiber rupture [53]. Composite with PVA gives better results in compressive, split tensile and flexural strengths, followed by PE, PET and PP fiber as reinforcement [52]. PVA fiber is considered as low modulus and low strength fiber resulting low ultimate strength with high ductility of the composite. While PE fiber, has about 2-3 times higher than the PVA in terms of modulus with tensile strength is similar or to higher than the steel fiber. Therefore, a composite with PE fiber might has both high strength and high ductility [55].

As the oiling content of surface coating increases, both frictional stress and interface fracture energy will decrease significantly. As shown in Figure 3.3, complementary energy of the fiber bridging stress increases with oil content given [50]. A surface coating content between 0.8 and 1.2% by weight of fibers tends to lower then interface chemical and frictional bond properties to a level that causes the critical fiber volume fraction to drop to a minimum of about 2% [56] (see Appendix C).

Table 3.4 Fiber specification

Material	Length (mm)	Tensile strength (MPa)	Elastic modulus (GPa)	Density (g/cm^3)
PVA Fiber	12	1560	40	1.30
PE Fiber	12 / 19	3250	113	0.96

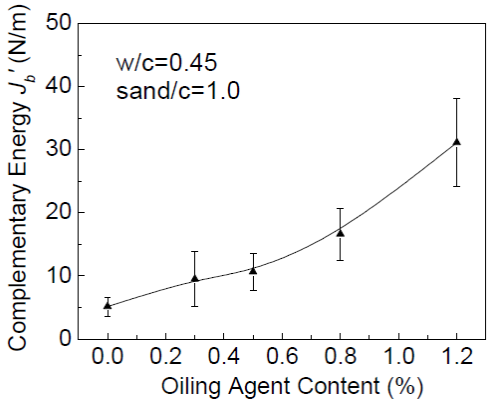

Figure 3.3 Effect of fiber surface oiling content [56]

The usage of superplasticizer is to increase workability characteristics. It allows the material to be produced with relatively low water-cement ratios without experiencing loss in strength. The usage is beneficial as ECC is relatively hard to be levelled due to fiber existence. However, the content of superplasticizer needs to be controlled as when the dosage is too much may lead to segregation. In this study, the superplasticizer is produced GCP Applied Technologies with type of ADVA® 181. It is a polycarboxylate-based superplasticizer with no added chloride in liquid form with specific gravity of 1.10 kg/liter.

Viscosity Modifying Agent (VMA) is used in the form of water-soluble polymers to increase the viscosity of concrete/ECC mix. There are at least three mechanisms of VMA action. The first one is adsorption as results of long polymer chains relate to water molecules adsorbing some part of mix water and increasing their volume. Secondly, association as in the molecules of adjacent polymer chains exhibit an attractive force by reducing the mobility of water molecules leads to gel form, thus increasing the viscosity. Third is splicing which occurs at a low shear velocity which increasing the apparent viscosity [57].

While in conventional concrete, the Portland cement paste that suffers from autogenous and drying shrinkage makes up less than 20% of the total volume [58], the Portland cement paste in ECC makes up more over 50% of the total volume [59]. It indicates that ECC would experience greater shrinkage, and when constrained, it could lead to shrinkage cracking. In a pioneer project in Michigan, U.S., shrinkage cracks were observed on the bridge link-slabs made of bendable concrete after eight days since paving, the maximum crack width can be 0.2 mm [60]. In current study, shrinkage reduction agent in powder form (Denka Power CSA Type-S) was added in the standard mix proportion design of bendable concrete. It has a specific gravity of 2.95 to 3.15 g/cm^3 with Blaine fineness more than 2000 g/cm^2.

A specific type of aggregate can be utilized to provide high skid resistance. However, there is less research working on the modification of ECC mixture design for pavement application. As can be seen below, different type of aggregate has a different performance and affecting differently to the mechanical properties of concrete/ECC.

Table 3.5 Suitable aggregates for high skid resistance

Type of Aggregate	Aggregate Size	Product
Corundum	1 – 3 mm	-
Bauxite (China-Guyana) Granite	1 – 3 mm 1 – 3 mm	Crafco HFS
Basalt and Granite Silica Sand	2 – 3 mm 2 – 3 mm	Flexogrid, Modified EP-5 Overlay
Steel slag	3 – 4 mm	Italgrip
Limestone dolomitic	1 – 3 mm	Safelane (Cargill)
Granite	1.5 – 3.2 mm	Safe-T-Grip
Calcined bauxite	1 – 3 mm	Tyregrip

Corundum is a crystalline form of aluminum oxide (Al_2O_3). Corundum is extremely hard. It is rated at nine on Mohs scale of mineral hardness (diamond rated as 10, while the most common mineral in aggregates, quartz, only rated as 7) that can scratch almost every other mineral [61]. Application of surface treatment using corundum has been reported. According to the report of Kreisverkehrsflächen in Beton: Erfahrungen in der Schweiz, Deutschland und Österreich [62], corundum material with the sizes of 1 to 3 mm has been applied to provide a high grip of the road surface by spraying an evaporative protection and followed by covering area with thermos-mats.

Table 3.6 Chemical specification of corundum

Chemical Specification (%)						
S_iO_2	Al_2O_3	Fe_2O_3	T_iO_2	CaO	MgO	FeO
14.61	61.80	12.25	8.14	N.A	N.A	N.A

Calcined bauxite is produced by heating bauxite to 1000°C to 1200°C, which increasing the alumina content. Calcination can occur either in nature during periods of metamorphism or made artificially in furnaces. The bauxite itself is a material rich in hydrated aluminum oxide [61]. Many high skid resistance surface treatments use calcined bauxite aggregate successfully. One of the examples is the Tyregrip product. Washington Department of Transport (WSDOT) applied TyreGrip on the ramp carrying southbound traffic from South East 164th Avenue to State Road 1st which has a downhill before entering the sharp horizontal curve of the ramp that merging onto State Road 14. Increasing the frictional properties of the surface pavement was proposed to eliminate the accidents occurring in this section. [63].

Granites are commonly composed of potassium feldspar, plagioclase feldspar, and quartz. This material contains a high concentrate of silica (SiO_2) and alumina (Al_2O_3) ("Granite: Igneous Rock - Pictures, Definition & More," n.d.). Due to its mineral composition and interlocking matrix, this material is hard and has an abrasive resistance. The toughness of granite is usually superior to sandstone, limestone or marble. Granites normally can provide a PSV of 62 or greater [64].

Silica material has a high abrasion resistance and high thermal stability. It can provide high skid resistance for surface treatment. Silica occurs in nature sandstone, silica sand or quartz. Silica can also exist in an amorphous form or crystalline forms [65]. The FlexoGrid system uses silica to provide surface friction. The application is designed to be installed on conventional concrete, concrete-filled steel, grid decks, steel plate decks, fiber reinforced polymer decks, and asphalt. However, based on the evaluation of the performance of the

FlexoGrid system on a highway bridge in the state of Iowa, the friction measurement only recorded 67.5 SN after the application and then decrease to 64.5 SN after four years.

Slag is produced during the separation of the molten steel from impurities in a steel-making. It must be crushed and screened to produce a suitable aggregate for surface treatments [65]. Steel slag is used in the ItalGrip system. It is an ultra-thin polymer concrete that provide the skid resistance of pavement surface. It consists of a two-part polymer resin which is sprayed on the pavement surface and covered with a steel slag with the size of 3 to 4 millimeters. The Italgrip system can be placed on either HMA or concrete pavements [66]. LTA of Singapore also used steel slags for their surface treatment aggregates. As this material can be easily found in local area and also can provide good abrasive.

Limestone is categorized as sedimentation rock that consists of more than 50% carbonate. It is made of mineral calcite comes from the beds of evaporated seas, lakes and also sea animal shells [67]. Limestone dolomitic aggregates have been used as a main material for SafeLane overlay product. With the aggregate median size of 4 mm and gradation from 3/8 inch to sieve number 30, the overlay has been done with the help of two-layer epoxy. SafeLane product can improve the skid resistance to 0.50 to 0.57 of Griptester number [65].

3.2.4. Mixture design of ECC

A typical mixture design of ECC is called ECC-M45 (see Table 3.7), has the largest experimental dataset [46]. ECC incorporates fine silica sand with sand to binder ratio of 0.36 to maintain sufficient stiffness and volume stability. The silica sand has a maximum grain size of 250 μm. ECC-M45 uses fly ash (Type F), high range water reducer (HRWR), and PVA fiber with length of 12 mm and 39 μm in diameter. The PVA fiber is surface coated by a proprietary oiling agent (1.2% by weight) to reduce the fiber/matrix interfacial bonding.

Table 3.7 Mix design of ECC (M45) [46]

OPC	Fly Ash	Sand	Water	HRWR	Fiber (vol.%)
1.0	1.2	0.8	0.56	0.012	2

For PUTW, it was proposed to use modified ECC with local materials in Singapore: ground granulated blast-furnace slag (GGBS) and river sands instead of fly ash and micro-silica sand can be used. The raw materials of this modified ECC includes Type I OPC (CEM I 42.5), GGBS provided by Engro Co. Ltd, river sands sieved to below 600 μm in particle size, and PVA fibers from Kuraray Co. Ltd. The fibers are 12 mm in length and 39 μm in diameter, the nominal fiber strength is 1600 MPa. Superplasticizer (SP) was also included to ensure the workability of ECC. Three different mix designs are shown in Table 3.8.

Table 3.8 Mix design of modified ECC-GGBS [29]

ECC-	OPC (kg/m^3)	GGBS (kg/m^3)	Sand (kg/m^3)	Water (kg/m^3)	PVA fiber (kg/m^3)	SP ($liter/m^3$)	GGBS/ binder ratio
GGBS0	1411	0	282	423	26	3.6	0%
GGBS30	976	418	279	418	26	3.0	30%
GGBS60	554	827	276	414	26	2.4	60%

3.2.5. The performance of ECC

The most notable characteristic of the ECC is the high tensile ductility which is represented by a uniaxial tensile stress-strain curve with strain capacity up to 5% due to the performance of multiple micro-cracks formation. The formation of multiple micro-cracking is the reason how ECC can behave similarly to metal. Typical mechanical properties for ECC is summarized in Table 3.9 [45]. The compressive strength of ECC ranges from 20 MPa to 95 MPa with an elastic modulus range between 18 GPa to 34 GPa. The flexural strength (modulus of rupture) of the ECC material can be achieved quite high up to 10 MPa to 30 MPa. It has also been reported that ECC has lower water permeability and lower effective chloride diffusivity in the presence of micro-cracks [37].

Table 3.9 Typical mechanical properties of ECC

Compressive strength (MPa)	First crack strength (MPa)	Ultimate tensile strength (MPa)	Ultimate tensile strain (%)	Young's modulus (GPa)	Flexural strength (MPa)
20 - 95	3 - 7	4 - 12	1 - 8	18 - 34	10 – 30

The modified ECC-GGBS have shown good performance. Test related to mechanical properties only performed on flexural strength with four point bending tensile test. It is reported that the average value or ECC-Cor is 10.50 MPa with 7.00 MPa and 15.20 MPa as maximum and minimum strength, respectively [29].

3.3. PUTW slab manufacture

The process of PUTW slab manufacture basically consists of two main steps including: (1) preparation of the formwork, and (2) manufacture process of PUTW slab. The first step, manufacturing the PUTW slab starts from the preparation of steel formwork. In this study, the steel formwork was prepared with inner dimension of 3400 mm x 2400 mm with thickness of 70 mm. The formwork is equipped with removable steel walls, so the walls can be removed after the slab is hardened. Detail dimension and location of the grouting port as well as the lifting and leveling devices can be seen in Appendix B.

A Rubber mat with convex nodes was placed inside the formwork. Six PVC pipes were prepared as grouting ports embedded to the PUTW slab. Additionally, four lifting and leveling devices were also prepared to be embedded to the PUTW slab. All of the grouting ports and leveling device need to be temporarily closed with tape so the ECC material cannot get inside during the casting process. The tape can be only opened when the ECC material is hardened.

The next step is to cast the ECC material into the formwork. Two different ECC materials are used. The first layer is made of ECC with thickness of 60 mm. Then the second layer made of modified ECC (with coarse aggregates) with thickness of 10 mm is casted on top of the first layer. To achieve homogenous material, both layers are casted fresh on fresh, which means the second layer should be casted within than one hour or less. Otherwise, the first layer of ECC is getting hardened. Yet, during the casting, it was found that leveling ECC is relatively difficult as the fibers are well embedded into the matrix.

The curing process is then started. After 18 to 36 hours the slab is then brushed with the brushing machine to expose the coarse aggregates. The brushing process cannot be directly done after the casting process as the ECC is not hardened yet. But it should be not delayed too long as when the ECC is fully hardened, and then it will very difficult to remove the cement paste resulting less coarse aggregates appear on the surface.

3.4. PUTW construction

The PUTW construction consists of different steps: lane closures, asphalt pavement preparation, slabs installation, slabs leveling, and grouting process. The construction process will take 4-8 hours [68].

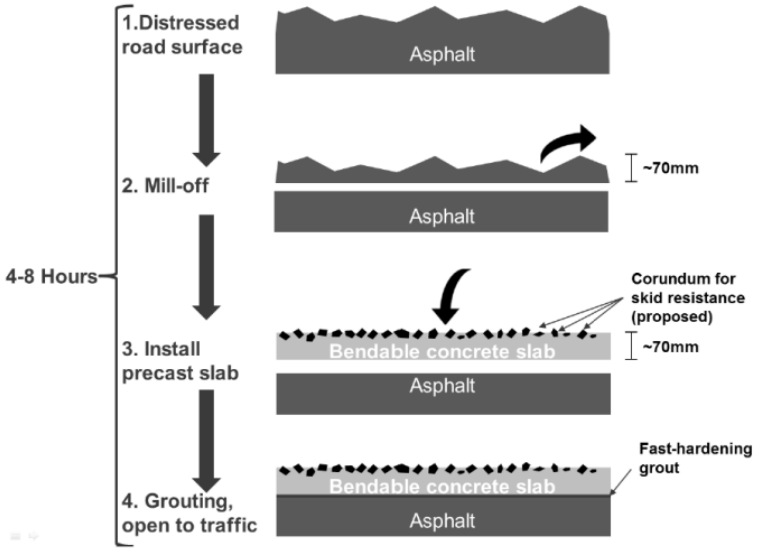

Figure 3.4 PUTW construction process

Before the construction begins, the site needs to be closed. In this study, Singapore standards are followed. The work zone requires at least 2 road lanes, the rest of the road lanes are still opened for traffic. The lane closure must comply with the agency's (LTA's) work zone traffic control guidelines [69]. Depends on the purpose, some temporary facilities (e.g. bus stop) will be provided together with guidance signs.

Since asphalt acts as the support layers for the PUTW slab, it is decisive for the overall performance of the PUTW pavement. Therefore, except for minor surface distress, the asphalt pavement structure must be in good condition. The asphalt layer needs to be milled with minimum thickness of 70 mm. Then the milled asphalt surface will be cleaned using a brush and air compressor.

By using lifting device, the PUTW slab is then lifted and installed within the designed area. The slab is then levelled with the leveling device to meet the cross fall and slope criteria. Once the slab is leveled, the fast-hardening grout is then injected through the port. It is important to reduce the amount of air bubbles trapped between the slab and asphalt layer underneath. Therefore, it is required to fill in the grout until the excess of grout is flowing out through the other ports. It is also required to check the gaps between the slabs. Ideally, all the gaps should be filled with the grout.

3.5. Chapter discussion

PUTW was designed to enhance the function of pavement system as electrified roadways. The prefabricated slab method proposed is able to reduce the construction time and leads to lower user delay cost compared to conventional cast-in situ method with either concrete or asphalt. To fulfil the requirement of PUTW, a particular material, ECC, is used as it offers many advantages such as, sufficient compressive strength, high flexural stress, and high tensile strain capacity which allow removing the needs of using steel reinforcement. As steel is considered as ferromagnetic material it causes higher eddy current loss which results in lower efficiency of wireless power transfer for the electrified roadways.

However, conventional ECC does not include coarse aggregates in its mixture design. This factor will be not become an issue when ECC is used for some applications, e.g. buildings, bridges, and dams. Yet, for (electrified) roadways, ECC may not the optimum material as it does not provide sufficient skid resistance for the surface pavement which is related to safety for driving experience. ECC mixed with coarse aggregates have been investigated, but not specifically designed for roadways. To change the mixture design of ECC, it requires deep knowledge in micromechanics approach design. The usage of large size aggregates might counter the ductility performance of ECC as it increases matrix toughness. Not to mention the risks of bleeding and segregation are increased when ECC is mixed with coarse aggregates.

The proposed method of prefabricating the slabs for PUTW and the installation process were based on conventional precast concrete slabs manufacture process combined with UTW casting process. However, those methods are specifically developed with their own characteristics which might be not feasible for PUTW. Therefore, the process of slab manufacture and construction should be improved to enhance both structural performance and functional performance of PUTW.

In summary, there are still big research questions need to be answered. Additionally, some methods are still open for improvements to achieve a comprehensive performance for both structurally and functionally. Those are including:

- Enhancement of the functional performance (e.g. skid resistance, and surface water drainage) of roadways made of ECC without sacrificing the structural performance / mechanical properties e.g. strains hardening behavior.
- Modification of the micromechanics design for ECC to find the optimum design for mechanical properties of modified ECC mixed with suitable coarse aggregates.
- Improvements of slab manufacture process to enhance the surface properties.
- Improvement of the construction process.

4. State of the Art: Functional Performance of Pavement

Chapter 4 describes the state of the art of the functional performance of the (surface) pavement. Functional performance is mainly related to a safe driving experience. On the other side, functional performance is affecting the comfort of the driver and the surrounding area. The scope includes skid resistance, surface water drainage, pavement unevenness, and noise, and driver visibility on the pavement.

4.1. Introduction: safety on pavements

The functional performance of pavement is vital as it is directly related to the safety and yet the comfort factor of driving experiences. AASHTO [1] points the functional performance of the pavement, which is based on its ability to serve the user which has major indicators of roughness, skid resistance, risk of hydroplaning, appearance, and other safety considerations. The statement is amplified by FHWA [70] stating the importance of pavement safety which is affected by pavement surfaces commonly characterized by friction, smoothness, tire-pavement noise, and texture. FHWA also indicates that durability and drainage are needed to be considered as there must be a balance between providing the required grip and providing a durable surface with the consideration of (life cycle) cost. Surface drainage is a critical factor in pavement safety. Even on the surface pavement with high skid resistance, the safety level can be significantly reduced once the water does not drain efficiently.

Few skid accidents in Singapore have been reported. Skid accidents can occur on the different type of pavements: concrete, asphalt and semi-rigid. They are taking place not only on the wet condition, but also dry condition. According to data, there are about 7000 accidents occurred in 2012, 2013, 2014, and 2015 [71]. Mainly, these accidents are related to the driving behavior of the driver. Then other factors are the vehicles and road conditions. As shown in Figure 4.1, in the early years, the number of accidents related to road conditions is similar to the number related to vehicles. But, interestingly, a few years later, Singapore was able to reduce the accidents caused by road conditions close to half than before.

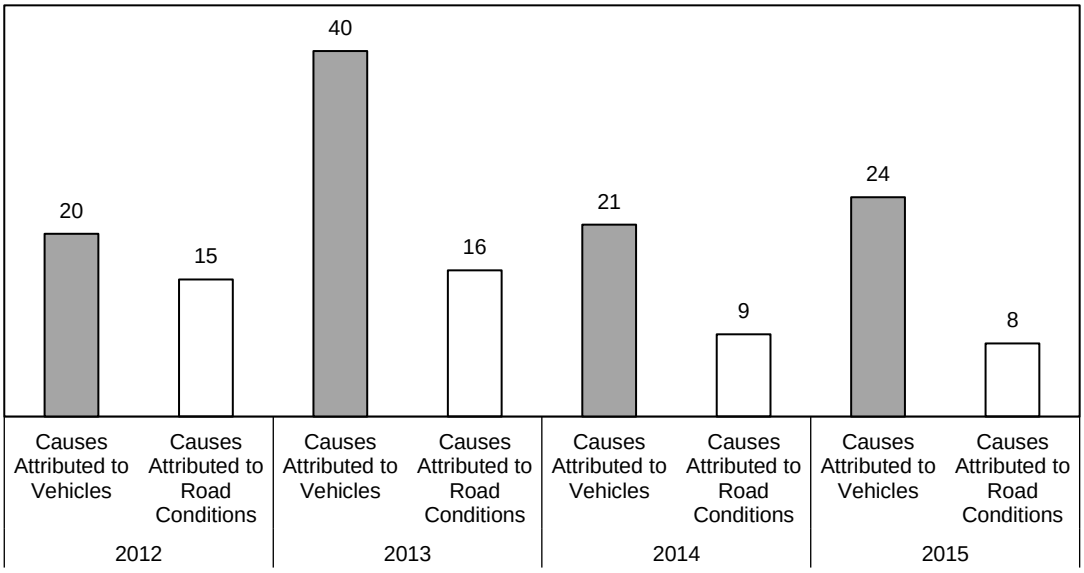

Figure 4.1 Accidents related to vehicles and road conditions in Singapore

Many essential design criteria parameters in functional performance have to be considered and carefully design in pavement engineering. However, all parameters are not linearly correlated with each other. It means, there is a possibility when one parameter is increased, the other parameter will be decreased. Henry [72] did a study by conducting surveys to agencies on the important parameters on pavement performance. As results, durability, skid resistance, and splash and spray are coming as the first three. The durability is coming as first prioritization as they are closely related to economic consideration. The performance was rated on a scale of 1 to 3, where a rating of 1 is very important, and a rating of 3 is relatively unimportant.

Table 4.1 Importance of pavement based on the functional performance [72]

Design criteria	Ranking	
	United States	Other Countries
Durability	1.1	1.3
Skid resistance	1.2	1.4
Splash and spray	2.0	1.8
Exterior noise	2.4	2.2
In-vehicle noise	2.4	2.4
Rolling resistance	2.7	2.7
Tire wear	2.7	2.9

4.2. Skid resistance

Skid resistance or friction is the counterforce developed due to the movement of the load along the pavement surface that holds the relative movement of a tire to move forward. The generated resistive force is illustrated in Figure 4.2. The skid resistance of pavement (concrete and asphalt) is essentially affected by the properties of the aggregate, the characteristics of the tire and environmental conditions. The friction coefficient is a non-dimensional coefficient, μ, which is defined as the ratio of the tangential friction force (F) between the tire and the horizontal pavement surface to the perpendicular force or vertical load (F_w).

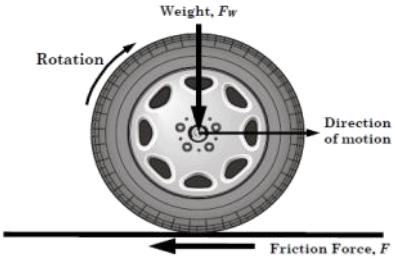

Figure 4.2 The friction force on tire-pavement

According to Corsello [73], Skid resistance can be determined in several methods: coefficient of friction (μ), Skid Number (SN), or Friction number (FN). Meanwhile, in 1992, the World Road Association, Permanent International Association of Road Congresses (PIARC), conducted the experiment to convert results generated by different methods and devices to a common scale, called the International Frictional Index (IFI).

The Friction Number (FN) or Skid Number (SN), which produced by a locked wheel testing device, represents the average coefficient of friction. According to [74], skid number or SN is the value to determine the skid resistance of the paved surface from the resulting force or torque record.

$$SN = 100(\mu) = 100(\frac{F}{W}) \quad \text{(Eq. 4)}$$

Where: F = Tractive force (horizontal force applied to the test tire at the tire-pavement contact patch, N

W = Dynamic vertical load on a test wheel, N

The reporting values range from 0 to 100, with 0 representing no friction and 100 representing complete friction.

FN values are generally designated by the speed at which the test is conducted and by the type of tire used in the test. For example, FN50S = 29 indicates a friction value of 29, as measured at a test speed of 50 miles per hour (81 kilometers per hour) and with a smooth (S) tire. The ribbed type defined as (R).

- Side Force (Mu) Number, or also known as sideways force coefficient (SFC) can be obtain by Mu-Meter which contains two freely rotating test wheels angled to the direction of motion. Based on ASTM E 670-09 – Standard Test Method for Testing Side Force Friction on Paved Surfaces Using the Mu-Meter, the relation between MuN and BPN is governed by the equation below:

$$MuN = 1.017BPN - 20.9 \quad \text{(Eq. 5)}$$

Where: MuN = Mu Number

BPN = British Pendulum Number

- International Friction Index (IFI), which was developed by PIARC which was initiated to standardize the dependency of friction on the tire sliding speed. The IFI consists of two parameters, which are the adjusted value of friction at certain slip speed (F60) and the Speed Number (Sp).

$$S_p = a + b \times TX \quad \text{(Eq. 6)}$$

Where: S_p = IFI speed number

a, b = Calibration constants dependent on the measurement method:
For MPD (ASTM E 1845), a = 14.2 and b = 89.7
For MTD (ASTM E 965), a = –11.6 and b = 113.6

TX = Macrotexture measurement, mm

$$F(60) = A + B \times FR(60) + C \times TX \quad \text{(Eq. 7)}$$

Where: $F(60)$ = IFI friction number

A, B = Adjusted value of friction measurement at selected slip speed S to a slip speed of 60 kilometers per hour

C = Calibration constants dependent on friction measuring device

$FR(60)$ = Calibration constant required for measurements using ribbed tire

Pavement surface texture influences pavement-tire interactions. Different level of texture influences different effects on pavement-tire interactions. [72], and [75] have studied the effects of various tire-pavement interactions from different ranges of texture wavelengths. Those effects are including friction, interior and exterior noise, splash and spray, rolling resistance, and tire wear. It can be seen from Figure 4.3, that the skid resistance related to friction is primarily affected by the microtexture and macrotexture.

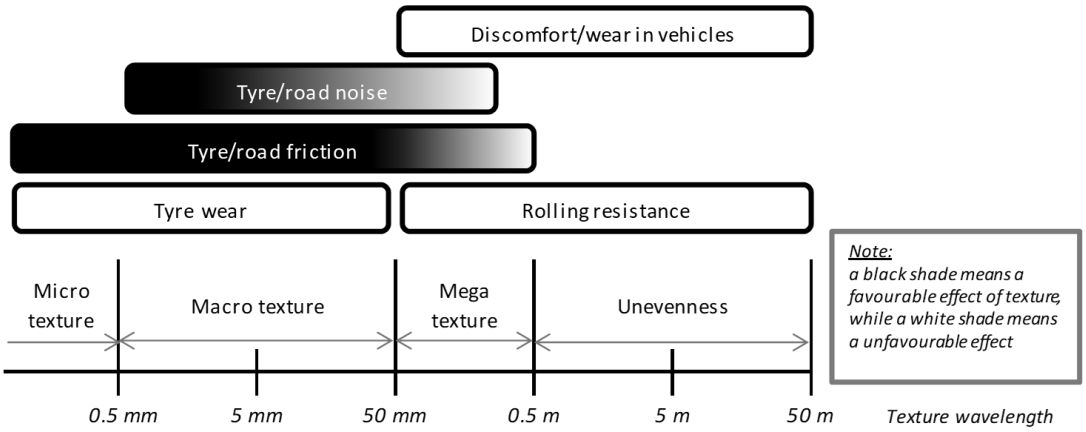

Figure 4.3 Texture wavelength influence on tire-pavement interactions [76].

In terms of the properties of the aggregate, pavement texture affects the skid resistance. Pavement surface texture is defined as the deviations of the pavement surface from a true planar surface. According to the PIARC in 1987, these deviations are divided into three levels of scale which are defined by the wavelength (λ) and peak-to-peak amplitude (A) of its components. There are three types of texture: micro texture, macrotexture and megatexture [76]. These three levels are defined as follows:

- Microtexture (λ < 0.5 mm, A = 1 to 500 μm). Surface roughness quality at the microscopic level. It is a function of the surface properties of the aggregate particles contained in the asphalt or concrete paving material.
- Macrotexture (λ = 0.5 to 50 mm, A = 0.1 to 20 mm). Surface roughness quality defined by the mixture properties (shape, size, and gradation of aggregate) of asphalt paving mixtures and the method of finishing/texturing (dragging, tining, grooving; depth, width, spacing and orientation of channels/grooves) used on concrete paved surfaces.
- Megatexture (λ = 50 to 500 mm, A = 0.1 to 50 mm). Texture with wavelengths in the same order of size as the pavement–tire interface. It is largely defined by the distress, defects, or “waviness” on the pavement surface. Wavelengths longer than the upper limit (500 mm) of megatexture are defined as roughness or unevenness (Henry, 2000). Figure 4.3 illustrates the three texture ranges, as well as a fourth level—roughness/unevenness—representing wavelengths longer than the upper limit (500 mm) of megatexture.

According to report of NCHRP number 108, there are four main factors affecting the friction between tire and pavement surface [77,78]. Those factors are pavement surface characteristics, vehicle operating parameters, tire properties and the environment. In particular, pavement surface characterized by microtexture, macrotexture, megatexture, material properties, and temperature. Skid resistance plays a significant role in wet-skid accidents [77,79–81]. Since then many countries came up with a standard related to skid resistance to increase safety. Singapore applied a high level of skid resistance to ensure the safety within their roadways.

4.2.1. Standard requirements for skid resistance

To guarantee the safety for the motorist, highway agencies are implementing standards for their new roads. The standard related to skid resistance, are mainly based on friction which is derived from skid resistance (micro- and macrotextures). Refer to the Code of Practice (COP) for Works on Public Streets [12] and Materials and Workmanship specification [82] Singapore applied a high-level standard of skid resistance for their roadways. The skid resistance for rigid pavement and asphaltic pavement the minimum limitation is 55. The intervention phase will be taken when the skid resistance value reaches 55 for expressway and 45 for both major and minor roads. All values are based on the British Pendulum Number (BPN). According to the COP, concrete surface paving on footpath shall be approved sprayed-on acrylic modified UV stable pigmented cementitious topping with a minimum thickness of 1 mm, and skid resistance not less than 50. Concrete Surface paving on carriageway shall be approved spray-on acrylic modified UV stable pigmented cementitious topping with a minimum thickness of 1mm, and skid resistance not less than 65. Yet, different countries/agencies apply different standard. Those various standards are summarized in Appendix E.

4.2.2. Test methods on skid resistance

4.2.2.1. Friction based tests

There are two types of skid measurement equipment based on their mechanism, namely high-speed friction measurement equipment and low-speed or stationary that require lane closure. High-speed friction measurement equipment is commonly categorized into four types, i.e. locked wheel testers, side force devices, fixed slip devices and variable slip devices while three alternatives can be found for the low-speed measurement methods, which are stopping distance measurement, deceleration rate measurement and portable testers. Details can be seen in Appendix D.

Locked-wheel testers can be run with a typical speed of 64 km per hour, and they measure the resistive drag force and the wheel load with the braking system is fully locked. In order to get the friction number (FN) or skid number (SN), this test can be equipped with either a ribbed tire [83], which is more sensitive to the microtexture surface or a smooth tire [84] which is better to measure the macrotexture. Even though this test is relatively simple, it can only be used on straight segments.

Side force method measures the cornering force perpendicular to the direction of travel of one or two skewed to compute the Mu Number or the sideways force coefficient (SFC). Similar to the locked-wheel tester, it can be run at the same speed. The measurement is continuous, which gives a good result. However, this test is susceptible to road irregularities that can destroy tires quickly. This method is associated with ASTM E670 [85].

The fixed-slip method measures the resistive drag force and the wheel load applied to the pavement which is used to compute the coefficient of friction, μ or FN as a result of rotational resistance of smooth tires slipping at a constant slip speed (12 to 20 percent). The advantage of this method is a continuous measurement and offer high-resolution friction data, but this method also has its disadvantage, such as it uses large amounts of water and requires skilful data reduction.

Variable-slip devices measure skid resistance as a function of slip (range between 0 to 100 percent) [86]. The result of this method can be related to longitudinal slip friction number, peak slip friction number, slip ratio, estimated friction number and Rado shape factor. However, this method required complex equipment with high maintenance costs and complex data processing.

Both stopping distance measurement (SDM), which is associated with [87], and deceleration rate measurement (DRM), which is associated with [88], require traffic lane closure. To do SDM, the wheels of the vehicle must be locked, and the distance the vehicle travels while reaching a full stop is measured. While for DRM, the brakes are applied to lock until deceleration rates can be measured.

The Dynamic Friction Tester (DFT) has the added advantage of being able to measure the speed dependency of the pavement friction by measuring friction at various speeds (Kazuo Saito et al., 1996). The DFT has three rubber sliders that are spring mounted on a disk at a diameter of 350 mm. The disk is initially suspended above the pavement surface, and it is driven by a motor with speed of 90 km/h. Water is then applied to the test surface. The friction force is measured by a transducer as the disk spins down. The Dynamic Friction Tester (DFT), which is in accordance with [89], is highly portable and easy to handle.

4.2.2.2. Texture based tests

Two tests based on texture are commonly used to measure the skid resistance are the British Pendulum Tester (BPT) and volumetric based spot test, which is called the Sand Patch Method (SPM) test.

BPT, which is in accordance with ASTM E303 [90], is firstly used in the 1960s. The device measures the frictional properties by determining the loss in kinetic energy of a sliding pendulum or rotating disc when in contact with the pavement surface. The loss of kinetic energy is converted to a frictional force and, thus, pavement friction. The typical slip speed for the BPT is usually assumed about 10 km/h. The test result is reported as the British Pendulum Number (BPN). This method provides a measure of microtexture and can be used either in the field or the laboratory. A minimum of five tests should be performed for each specimen.

The SPM test is a volumetric based spot test method which is based on [91] can be used to determine the (average) Mean Texture Depth (MTD) of pavement. This method is widely used as it is practical and inexpensive. The test procedure involves spreading a known volume of material (sand or glass bead) on a clean and dry pavement surface, measuring the area covered, and then calculating the average depth between the bottom of the pavement surface voids and the tops of surface aggregates. The method is significantly influenced by pavement macrotexture. Pavement aggregate particle shape, size, and distribution are not addressed in this method.

The average pavement macrotexture depth is then calculated by the following equation:

$$\mathrm{MTD} = \frac{4\mathrm{V}}{\pi \mathrm{D}^2} \qquad \text{(Eq. 8)}$$

Where: MTD = mean texture depth of pavement macrotexture, mm

V = sample volume, mm^3

D = average diameter of the area covered by the material, mm

Other tests to measure skid resistance based on texture are Outflow meter, Circular Texture Meter, Texture Depth Gauge, and Electro-optic method test. All of these tests are summarized in Table 0.3 (see Appendix D).

Land Transport Authority of Singapore conducts road condition surveys regularly to monitor the riding quality and skid resistance of major roads and expressways to provide a safe and smooth driving experience. LTA maintain their road network at an acceptable level of service. Three main parameters the structural, the functional, and the safety are checked. LTA use deflectograph to assess the residual life for the pavement by checking the road deflection. The deflectograph is operated with low speed of 2.5 kilometer per hour.

To check the road riding quality, LTA uses vehicle with multifunction road monitor, which has the main function of pavement roughness (IRI) measurement and the laser profilometer to determine the undulation of road surfaces. LTA uses a Sideway-force Coefficient Routine Investigation Machine (SCRIM) to measure the wet skidding resistance level of wet road surfaces.

4.2.3. Treatment methods to improve skid resistance

Various methods to improve the skid resistance of pavement can be done. It depends on the type of pavement either asphalt or concrete surface pavement. Examples of friction restoration are chip seal, micro-surfacing, HMA overlay, (longitudinal or transversal) tining, Next Generation Concrete Surface [92], and (longitudinal or transversal) grooving. However, it should be noted that any improvement method will be mainly determined by micro- and macrotextures. Details can be seen in Appendix D.

Flintsch [93] reported there are different impacts to the coefficient of friction and sliding velocity caused by the combination of micro- and macrotexture, whether its low texture and high texture. Furthermore, the size, the angularity, the shape and the texture of aggregate have a different impact on the pavement friction. According to NCHRP Report number 108 [78], on the surface, the angularity and the shape of fine aggregate defines its microtexture. The angularity and the shape of coarse aggregates affecting its macrotexture, while the texture defines its microtexture which makes some impacts on its friction.

Table 4.2 Effect on Pavement Friction

Aggregate Fraction	Aggregate Property	Effect on Pavement Friction	
		Asphalt Surface	Concrete Surface
Fine	Angularity and Shape	No effect (-)	Defines pavement microtexture, which highly impacts friction
	Texture	-	Little to no effect
Coarse	Angularity and Shape	Defines pavement macrotexture, which significantly impacts friction via hydroplaning potential	If exposed, helps define pavement macrotexture, which significantly impacts friction
	Texture	Defines pavement microtexture, which significantly impacts friction	If exposed, helps define pavement microtexture, which significantly impacts friction

Conforming to Fwa et al. [94], there are two aggregate types used in Singapore for road construction, i.e. granite and steel slag aggregate. Granite are used for asphalt roads since this material is the most common type of aggregates that can be found in the Southeast Asian region. However, the long-term skid resistance performance of granite is only marginally satisfactory. Therefore, since the early 1990s, steel slag has been introduced as an alternative material for road paving purpose. The test results revealed interesting insights into the skid resistance behaviors of the two aggregate types. It was found that water wetting, aggregate gap width, and wheel polishing action all had significant impacts on the skid resistance of the two aggregate types. The skid resistance behaviors of the two aggregates, however, were different under the influence of these factors. The skid resistance of the granite aggregate was affected more by wetting while the steel slag aggregate deteriorated more as the aggregate gap width widened. The effect of wheel polishing was affected by the aggregate gap width. Results show that steel slag produce a better skid resistance in comparison to granite, with maximum BPN of 46 and 35 (in wet condition) for steel slag and granite, respectively.

A study was conducted by Lee [95] to check the effectiveness of some common surface texturing methods adopted in Singapore. The methods were studied include troweling and brushing: soft and hard, both longitudinal and transversal direction. They found that troweling, hard, and soft brushing showed a significant improvement in providing skid resistance in dry and wet condition. However, hard and soft brushing methods provide a higher skid resistance than the trowelled surface, especially under wet condition.

Stated from the LTA's website, Kranji Expressway (KJE) was one of the first roads in Singapore (constructed in 1990 and was completed in 1994) that has been introduced to anti-skid surfacing. It has a total length of 8.4 km from the Bukit Timah Expressway (BKE) to the Pan-Island Expressway (PIE) [96]. The product has been used to improve the skid resistance in KJE was the use of a special tar-like asphalt substance as a surface material.

Furthermore, LTA mentioned that steel slag is their first choice for some road construction projects owing to its technical properties, and also because the lifetime road maintenance and replacement costs are minimized. LTA has been using steel slag aggregates since 1990. The reasons for using this aggregate are they provide significant advantages such as high skid resistance, better durability, and resistance to rutting. By having a long durable life of the road, it will also cut carbon emissions due to less road replacement and maintenance [97].

There are two different levels of improving skid resistance. The first level is texturing for new construction while the second one is re-texturing for maintenance or rehabilitation in order to improve the skid resistance. The table in Appendix D summarizes the texturing techniques, it is adopted and modified from NCHRP report number 108 [80].

4.2.4. Numerical models on skid resistance

The numerical model can be used as an additional tool to analyse the skid resistance. Time cost and resources can be significantly saved by developing a calibrated numerical model. Lee [98] explains many studies related to pavement surface texture were done before, with more studies related to the tire design and modeling compare to studies on the skid resistance.

Moore et al. [99] pioneers a simplified 3D elastic FEM in relation to rubber slider to study the skid resistance of grooved road pavements. The author concluded that in low sliding speeds, the comparison between experimental measurements of dry sliding friction and elastic theoretical predictions over the grooved pavement could be predicted. A 3D FEM simulates the BPT using ABAQUS. Three different pavement surface types were modelled, both for dry and wet condition. The kinetic energy loss during the test was calculated for comparison with experimental measurements. This model can be used to determine the skid resistance value and contact stresses between the rubber slider and pavement surface. However, the model cannot be used to analyze complex surface textures with non-symmetric patterns [100]. Lee [98] developed A 3D model using ABAQUS. The hyperelastic behavior of the rubber slider was modelled based on experimental test data. Three key issues associated with the BPT were addressed: effects of test surface curvature, effects of slider wear, and unreliable test behavior on coarse-textured surfaces. FEM was used to study the effect of pavement surface texture on BPT [101].

4.3. Surface water drainage performance

The pavement drainage factor is a crucial consideration in cross-section design because water depth has a critical influence on the skid resistance as well as tire hydroplaning resulting from the excess water on the surface pavement. Various parameters: average texture depth, pavement width, pavement super-elevation and grade, and rainfall intensity are affecting water depth above the pavement.

Rainfall excess which is not infiltrated into the pavement will comprise direct runoff to the shoulder lane and side drain eventually. It is common that any rainfall excess should be removed from the surface pavement quickly as the existence of any water above the surface might reduce the grip performance between the tire and the pavement. Two methods are used to define the response of a watershed to a rainfall event, a method based on time of concentration and quantity-based method (peak-flow and continuous flow models) [102].

Another factor is the flow of the water on pavements. When the rain falls on a sloped pavement surface, it forms a thin film which will increase in thickness as it flows to the edge of the pavement. As can be seen from Figure 4.4, the thickness of the water surface (water depth) relies on texture depth and the length of the flow path. As the length of the flow path increases, the water depth increases and eventually will cover the pavement macro-asperities. The flow can be considered as channel flow.

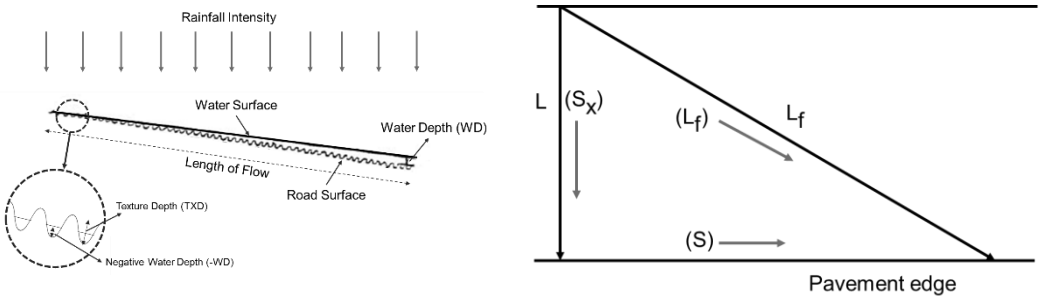

(a) (b)

Figure 4.4 Water flow path (a) over a pavement surface (b) the diagram [103]

The path that the runoff takes to the pavement edge is called the resultant flow path. The correlation between the resultant flow path, length of the flow path and the resultant slope can be determined from the following formula.

$$S_r = (S_x^2 + S^2)^2 \quad \text{(Eq. 9)}$$

and

$$L_f = L\left(\frac{S_r}{S_x}\right) = L(1 + \left(\frac{S}{S_x}\right)^2)^{0.5} \quad \text{(Eq. 10)}$$

Where:
- S_x = cross slope, m/m
- S = longitudinal gradient, m/m
- S_r = slope of resultant flow path, m/m
- L_f = length of flow path, m
- L = pavement width, m

Based on the diagram illustrated in Figure 4.4.a, the depth of water can be computed [104]. Rainfall intensity, length of the flow path, surface texture and the resultant surface slope are the inputs for the formula. As for the resultant surface slope, the parameter of the longitudinal grade significantly influences the flow path length. However, it does not appreciably affect the water depth. The formula can be seen below.

$$WD = 0.01485\left(TXD0.11^{{L_f}^{0.43}} I0.59^{{S_r}^{-0.42}}\right) - TXD \quad \text{(Eq. 11)}$$

Where: WD = the water depth above the top of the surface asperities, mm

TF = length of flow path, m

TXD = texture depth, mm

I = average rainfall intensity (mm/hr)

S_r = slope of resultant flow path, m/m

It can be seen from Figure 4.4.b, for a given cross slope (S_x), as the longitudinal grade (S) is steepened or as the pavement width (L) is increased, the flow path (L_f) is lengthened. The resultant flow path depends on the pavement width, cross slope and the longitudinal gradient. Guven and Melville [105] did a review on pavement cross slope design related to the surface drainage using climate conditions and design practice in Alabama. Based on his review, he concluded that the primary geometric factors which influence the water depth are the width of the pavement and the cross slope, while the longitudinal gradient has a small influence.

Gallaway et al. [106] study the effects of rainfall intensity, pavement cross-slope and surface texture in relation to the drainage length on pavement water depths. Based on the experimental study, they found that increasing the surface texture resulted in a decrease in water depth. Greater water depths can be caused by longer drainage lengths and higher rainfall intensities. While increasing pavement cross slope can reduce the water depths. Another conclusion is an increase in surface texture and pavement cross slope can decrease the water depth detention. The similar finding also mentioned in [107], that the increase of the cross slope of the drainage can help to increase the drainage ability of the pavement.

The Highway drainage guidelines [103] stated that good surface drainage of highway pavements is essential for traffic safety and reasonable maintenance of the roadway surface is necessary. Any water above the surface pavement might interrupt the traffic, reduce the grip, increase the risk of hydroplaning and limit the visibility due to splash and spray. Regarding traffic safety, the grip between the tire and the pavement needs to be optimally fulfilled to minimize the risk of skidding accident.

Yet, there is no research on surface water drainage performance on ECC pavement. As the ECC has a different matrix compared to the conventional concrete, its surface texture and grooves will affect the surface water drainage performance differently. Therefore, research is needed to study the performance on the surface pavement made of ECC.

More, the fact that Singapore receives high rainfall intensities brings additional reason to design the surface pavement more properly. Singapore experiences about 2400 mm of precipitation annually with up to 19 rainy days within a month with high rainfall intensity [108]. By 2012, the average of hourly rainfall intensities is about 120 millimeters which might increase to 140 mm by 2050. To deal with this issue, the post-development runoff have to be engineered efficiently [109].

4.3.1. Standard requirements of surface water drainage

Singapore is currently highly developed with many high-rise buildings, rail tracks, roadways, and parking lots, which bringing consequences of impervious surfaces. As a result, during the raining time, peak runoff from the urbanized (post-development) catchment may cause a flash flood. According to the Ministry of National Development of Singapore (2013), Singapore plans to use more than half of their land (58%) for housing, services, manufacturing jobs facilities, amenities, as well as green spaces and utilities by 2030. While 19% of their land will be used to support mobility and another 19% for defense needs [110]. Since infiltration may have limited performance, especially when pavement will be made of ECC material, then the runoff management should be well engineered. In accordance with the Drainage Handbook [111], Singapore through the Public Utilities Board (PUB) has established a Code of Practice (COP)

on Surface Water Drainage that regulates the minimum engineering requirements for the planning, design and construction of the drainage systems in Singapore. PUB has also developed the guidelines of the implementation of environmentally sustainable green features (including a strategic storm water management strategy) for users, called the Active, Beautiful and Clean (ABC) Waters. PUB uses the Rational Formula to compute the peak runoff. Runoff coefficient depends on the degree and the type of development within the catchment. For roads, highways, airport runways and paved up areas should use a value of 1.00 for C.

$$Q_r = \frac{1}{360} CIA \qquad \text{(Eq. 12)}$$

Where: Q_r = peak runoff at the point of design (m^3/s)

C = runoff coefficient

I = average rainfall intensity (mm/hr)

A = catchment area (hectares)

To calculate the time of concentration, PUB specifies time range from 5 minutes to 15 minutes for the overland flow time (to), depending on the overland travel distance, land topography and characteristics while the drain flow time (td) should be estimated from the hydraulic properties of the drainage channel.

Ideally, a runoff will be highly dependent on rainfall intensities, cross fall, longitudinal gradient, road surface texture and pavement width. To facilitate this issue, LTA (2010) specify a requirement for a cross slope or cross-fall at grade road, 1 in 36 and 1 in 30 for absolute minimum cross-fall and desirable cross-fall, respectively. The requirement for the grade of a carriageway can be seen in Table 4.3.

Table 4.3 Grade design criteria by LTA Singapore

Criteria	Express -way	Semi-Express way	Arterial road		Other road	
			Major	Minor	Primary access	Local access
Minimum grade (%)	0.4 [1)]	0.4 [1)]	0.4 [2)]	0.4 [2)]	0.4 [2)]	0.4 [2)]
Desirable max grade (%)	4	5	5	6	6	6
Absolute max grade (%)	5	6	6	8	8	8

Notes:

[1)] A road gradient of less than 0.4 % may be used for widening of expressway.

[2)] For built up area, a road gradient of less than 0.4 % may be used to tie in with existing access.

In other countries, not only they set a regulation regarding the cross-fall and grade, but also other parameters, such as flow path length. The flow path length is the distance of water flowing on the road, an important factor for road surface drainage. As an example, Japan requires a flow path length is not greater than 40 meters.

In regards to water (surface drainage) outflow, various standards in the USA specify a requirement for lower outflow times. The Texas DOT [112] and the State of North Carolina DOT [113] set a regulation of an average of 10 s or less shall be obtained for any lane mile section, while the Louisiana DOT [114] specifies that an average outflow reading of greater than 9.00 s. This study investigates various methods to improve surface water drainage. Tests with outflow meter were conducted.

Textured surfaces not only reduced the splash and spray but also help to diffuse the light to decrease the headlight glare from an oncoming vehicle. The headlight glare is increased at night during the wet condition. [115] recommended a minimum texture depth between 1 to 1.5 mm accordingly.

4.3.2. Test methods on surface water drainage

According to [116], outflow meter test can be conducted to evaluate the drainage performance of the pavement through its surface and subsurface voids. It measures the duration of a known quantity of water taken to run through voids in the pavement texture and intended to provide a measure of the ability of the pavement to relieve pressure from the surface of the tires, thus indicating hydroplaning potential under wet conditions. A faster run time indicates a thinner film of water may exist between the tires. Minimum five tests need to be performed for each sample.

4.3.3. Treatment methods to improve surface water drainage

According to a study done by Gallaway et al. [117], the surface water drainage is significantly affected by cross slope and texture depth, and it less significantly influenced by the direction of texturing. Thus, it is suggested to construct sufficient deep textures. Then secondly, it comes the direction as NCHRP study concluded that grooving could be an alternative for better drainage when the direction of the groove is in line with the gradient [72].

A proper design of sag-vertical curves can reduce hydroplaning. This design will support by maximum pavement width of 11 m, maximum inlet spacing (15 to 61 m), channelized curb flow encroachment, and increase in roughness coefficient by 0.005 with Manning's [117]. The splash and spray, which are closely related to water on surface drainage, are affected by macrotexture. Thus, by improving the macrotexture of the surface pavement, the surface water drainage will be improved. In details, the angularity and shape of coarse aggregate will help to improve the surface water drainage.

Several texture methods can be done to improve surface water drainage. Transverse grooving for concrete pavement is known as the most direct drainage channel of water of the pavement even though it is not common due to construction difficulties. Alternatively, longitudinal grooving also does provide a channel for water and produces a sufficient tracking effect on tires (vehicles), thus reducing the risk of skidding accidents [118]. Porous asphalt/concrete pavements are alternative for pavement application regarding water storm [119]. Porous pavements mixtures consist of binder, additives, and a high proportion of coarse aggregate with limited fines, resulting in a high percentage of permeable air voids (typically 15–20%) thus allow water to penetrate through the material. The high air void content creates permeability, which decreases the water on the roadway, help to reduce the splashing and spraying.

4.3.4. Numerical models on surface water drainage

Since there is no previous surface water drainage study on ECC, the numerical model can be utilized to study the rainfall loading on a highway in Singapore. Various textures, cross falls, and slopes will affect the surface drainage performance of the new pavement differently. The numerical model can be done by using fluid dynamics. However, until now, there are not many numerical models on water surface runoff. Many numerical models were developed on permeability and hydroplaning. Various investigations related to these three subjects are summarized in Table 4.4, Table 4.5, and Table 4.6.

Table 4.4 Numerical model on water surface runoff

Numerical model & Tool	Remarks
Pavement drainage Using Geoslope [107]	The FEM model were designed to evaluate the effect of (1) broken and seated concrete layer with or without a Superpave asphalt layer, (2) central collection pipe, (3) Superpave HMA surface, (4) pavement geometry, (5) cracks on pavement surface and (6) slope of drainage blanket.
Pavement surface runoff model using DUNE and DUMU, which were developed by University of Stuttgart. [120]	Flow resistance in the Pavement Surface Runoff Model is described by the Darcy-Weisbach equation based on the depth-averaged shallow water equations. The model includes a model road section with drainage facilities, an existing road section with irregular topography as well as a road section designed in CAD with a complex boundary.

Table 4.5 Numerical model on permeability

Numerical model & tool	Remarks
2D FEM analysis using GEOSLOPE. [107]	The analysis of permeability on Superpave surfaces had a moderate effect on the pavement drainage. While permeability of AC base had a significant effect on the pavement drainage.
3D FEM model of pavement subsurface drainage systems using FlexPDE program [121]	By conducting the unsaturated transient analyses, the drainage characteristics corresponding to various drainage design practices, geometry parameters and material properties were identified.
2D FEM model on pavement infiltration using HYDRUS-2D [122]	The simulation results of the volumetric water content θ in a pavement construction HYDRUS-2D has been applied on a pervious pavement with slots of 10 mm on a 40 cm base layer of gravel (0/45 mm) for a rain intensity of 100 l/(s·ha).
3D FEM model of pervious concrete pavement using ABAQUS [123]	The porosity distribution model was validated by comparing the results from EverFE. Three layers pervious concrete model developed with assumptions of linearly elastic material, the modulus of elasticity of pervious concrete is a function of the porosity, The Poisson's ratio is constant along the depth of the pervious concrete cross section, the porosity distribution is constant in the longitudinal and transverse directions of the pavement.

Table 4.6 Numerical model on hydroplaning

Numerical model & tool	Remarks
A rubber sliding on a two-dimensional smooth sinusoidal asperity separated by a thin fluid film is modeled. [124]	The first analytical treatment of the hydroplaning problem was proposed by Moore (1967). A one-dimensional Reynolds equation solution was obtained in which inlets, central and outlet regions for the fluid film were treated separately.
2D model on a tire deformation for hydroplaning [125]	Using the Navier-Stokes equations, inviscid, laminar, turbulent models and side flow were explored. However, the recovery factor is lower compare to NASA's experiment
3D FEM model of the dynamic aquaplane problem using ADINA [126]	Simulation of the fluid flow with the consideration of deformable tire structure

Numerical model & tool	Remarks
Simulation of hydroplaning through fluid-structure interaction using MSC.DYTRAN [127]	The simulation has a drawback in that the fluid flow was modeled using the potential flow theory. Pavement surface characteristics was not properly developed and its influence on hydroplaning was not analyzed.
3D simulation of effects of viscous hydroplaning using MATLAB for meshing and ABAQUS. [128]	Two different elasticity models of car tyre were modeled to simulate the viscous hydroplaning effects. Smooth surfaces were assumed, i.e. zero microtexture depth.
Simulation of hydroplaning based on 3D model using FLUENT (Finite volume method) [129]	Based on Navier-Stokes equation, the 3D model developed using pneumatic tire model, fluid flow model and the pavement surface model with consideration of tire-pavement contact and tire-fluid interaction.
Study of 3D model of hydroplaning risk on rolling and sliding car using ABAQUS [130]	Smooth tire was considered to roll and slide over plane pavement surface. Hydroplaning speed calculated using the developed simulation model was duly validated against the past experimental studies and the results show a good agreement with the experimental findings for both rolling and sliding cases and with the well-known NASA hydroplaning equation.

The numerical model with liquid dynamics tool can be used to study how material and textures can affect the surface water drainage performance. With numerical tools, a model with various textures can be created, therefore finding the optimum solution for safe pavement can be done without doing many experimental tests which need a lot of resources and costly.

4.4. Tire-pavement noise

Singapore has transformed into a highly developed city with most of the population live in urban areas. Due to limited space, the most residential area is developed close to expressways and major arterial roads with high traffic densities which cause noise pollution. Strait times [131] reported that communities have public complaints about noise pollution. According to [132], tire-pavement noise represents 75 to 90 percent of the total noise generated by passenger vehicles and the trucks. Tire-pavement noise is the main factor affecting the overall traffic that should be reduced to have quieter pavement systems. Three parameters of pavement properties are significantly affecting tire-pavement noise, namely texture, porosity, and stiffness [133].

4.4.1. Standard requirements for noise

The NEA of Singapore implemented residential noise limits for different periods of the day, which described below. The noise limit for 67 dB is applied to new roads and expressways.

Table 4.7 Noise limit in Singapore

Affected premise	Max noise limit (dB)		
	Day (07:00 – 19:00)	Evening (19:00 – 23:00)	Night (23:00 – 07:00)
Residential	65	60	55

4.4.2. Test methods on (tire-) pavement noise

Commonly, there are two ways to measure noise: wayside noise and source noise measurements. Wayside noise measurement is done at a fixed distance from the road (at the side of the road). The measurement is using microphones which is ideally placed between 7.5 to 15 m away from the road. Source noise measurements intended to study more about tire-pavement noise.

There are three common types of wayside testing. In instances where there is little traffic, statistical pass-by (SPB) testing can be done. In this case, a microphone at a fixed position is used to measure the maximum sound levels (Lmax) of hundreds of individual vehicles. Then, a calculation is made of the sound level from an “average” car, medium truck, and heavy truck travelling at a standardized speed. Second, known as test vehicle/tire combinations, which is called a controlled pass-by (CPB) test. Using SPB and CPB, pavements at different locations can be compared to one another. Some caution must be exercised, however, as there can always be differences in the “average” vehicle from site to site (for SPB) or unique interactions between a specific tire and pavement combination (for CPB). The third type of wayside testing that is commonly conducted is termed time-averaged, sometimes referred to as continuous flow traffic time-integrated model (CTIM). In this case, the microphone is set to record all of the traffic noise over a fixed time (commonly 5 to 30 minutes), and traffic levels and speeds are simultaneously recorded. An average equivalent sound level (Leq) over this period is calculated and is often reported as an average of repeat measurements. Concerning measurements of driving vehicles under well-controlled conditions, there are two types: (1) Pass-by situation where is characterized by the fact that the engine is on during the passing of the vehicle, and (2) Coast-by situation indicates the engine-off [134].

There are two principal techniques for measuring tire-pavement noise: close-proximity (CPX) and on-board sound intensity (OBSI). General Motors initially developed OBSI for tire evaluation at their test facilities. The technology was developed further by [135] of Illingworth & Rodkin as part of quiet pavement research for the Departments of Transportation in both California and Arizona. The CPX method uses single microphones that measure sound pressure. OBSI uses dual-microphone probes that measure sound intensity. The latter is directive, meaning that the measurements from each of the two microphones can be used to sort out the direction of the various sources. Currently, the CPX and OBSI methods specify different positions for the microphone including the height (from the ground), the spacing between the front and rear positions, and distance from the tire sidewall.

The Tire-Pavement Test Apparatus (TPTA), which pioneered at Purdue University, consists of a rotating arm with a tire assembly which is in contact with individual test panels that allow real pavement materials to be tested for tire-pavement noise at up to 30 mph. Microphones and probes can be positioned to collect CPX or OBSI style measurements. While large in size and used primarily for screening potential quieter pavement types in a research environment, the TPTA serves as a model for potential lab tests of the future to measure tire-pavement noise more directly prior to full-scale implementation. Noise absorption measurement can be considered to study the effect of texture and porosity, as this technology is reliable, handy, and it can be used in laboratory and in situ [136].

A research was conducted by Bhanap [137] in an apartment block adjacent to the East Coast expressway. The apartment block is 50 m away from the expressway. It is a major expressway (10-lane) linking the international airport and the eastern areas of the island with the central business district, port and the west coast of Singapore. Noise data was logged using a noise data sensor and data logging software. The noise sensor was mounted near an open window facing the expressway on the 11th floor apartment. Noise data was logged from 08:30 am to 10:00 pm every night for all days of the week. The logging software was set to sample noise data every minute. It was found out that most of the highways produced higher noise more than the limits specified by the Singapore government.

4.4.3. Treatment methods to reduce noise on (tire-) pavement

According to Rasmussen in the Little Book Quieter Pavements, there are three main parameters considered for quieter pavements: texture, porosity, and stiffness. Firstly, texture has to be remaining small (less than 5 mm) and negative. Secondly, it is better to have higher porosity as it does help to absorb noise and reduce the contact area. It works better when the porosity is more than 20%. However, air voids might affect durability. Thus, the porosity has to be carefully designed. Lastly, the stiffer the pavement, the quieter is [133].

For asphalt pavements, typically porous asphalt and gap-graded stone matrix asphalt (SMA) are used. In Europe, double-layer porous with maximum aggregate size 6 to 8 mm is one common type used for quieter pavement. In Arizona (USA), the asphalt rubber friction course (ARFC) used in many locations. It is an open-graded material with an additional binder. Research done by the National Concrete Pavement Technology Center has identified the quieter concrete pavement options that do not compromise on safety factor. Over than one thousand pavement test sections throughout the US and Canada have been tested. As results, drag surfaces (burlap and artificial turf) and diamond ground surfaces are among the quietest. Then, longitudinal tining also offers quieter pavement. In Europe, a common method used for concrete pavement surfacing is the exposed aggregate and porous concrete [138,139].

4.5. Texture durability

Texture durability is one of the critical points for the pavement to evaluate the effects of aggregate quality on micro- and macrotexture loss overtime/traffic. The study gives an understanding of how concrete mixtures with tougher, more durable aggregates retain higher friction values loss overtime/traffic. From the same study of texture durability, microtexture deterioration was investigated by using DF Tester. As an example, the usage of high-silica granite, which was used in Colorado, while granite was used in Minnesota shown high initial DFT(20) and it remains high after high traffic. The use of limestone in Kansas and Illinois shown a greater rate of microtexture deterioration. It was concluded that the use of higher quality aggregates in the concrete mixture helps to maintain the microtexture qualities needed for friction [80]. In conclusion, the most significant loss of macrotexture over traffic is experienced by diamond-ground textures. Meanwhile, the lowest loss is for longitudinally grooved and dragged textures. The geometric shape of the diamond ground textures results in more substantial loss than textures with no grooves.

4.6. Self-cleaning function on pavements

The projected Business-as-usual (BAU) emissions in Singapore are to reach 77.2 million tons in 2020. Thus, Singapore is aiming to reduce its carbon emissions up to 11% below business-as-usual-scenario levels by 2020. The primary emissions from traffic are nitrogen oxides (NO_x), hydrocarbons (HC), and carbon monoxide (CO) causing a significant impact on the urban quality such as urban smog, acid rain, fine particle pollution, and tropospheric ozone, which causing adverse issues for human health and the environment [140]. One way to fight the emission is through the innovative (material for) pavement application. The self-cleaning function on pavements can be enabled with the application of photocatalytic materials. Titanium dioxide (TiO_2) is used to provide an air-purifying surface to reduce air pollution from traffic. When it is used in urban areas, where the risk of smog formation is increased during hot sunny days, the air pollution will be decreased significantly. The commercialization of TiO_2-based photocatalytic products were started in the mid-1990s in Japan. Nowadays, the industry has grown rapidly as more than 2000 companies have emerged since 2003. [141] categorized the related industry into five: exterior construction materials, interior furnishing material, road construction materials, purification facilities, and household goods. Among those five categories, the self-cleaning exterior construction materials occupied the biggest market share.

4.6.1. Photocatalytic process

The photocatalytic process occurs in a way a semiconductor activated by light at a particular wavelength creates hydroxyl radicals (*OH) and superoxides (O_2^-) which accelerate the natural decomposition process of organic pollutants. In results, the pollutants are decomposed as non-hazardous waste products. Afterwards, the non-hazardous pollutants will be removed from the surface pavements by the washing rain.

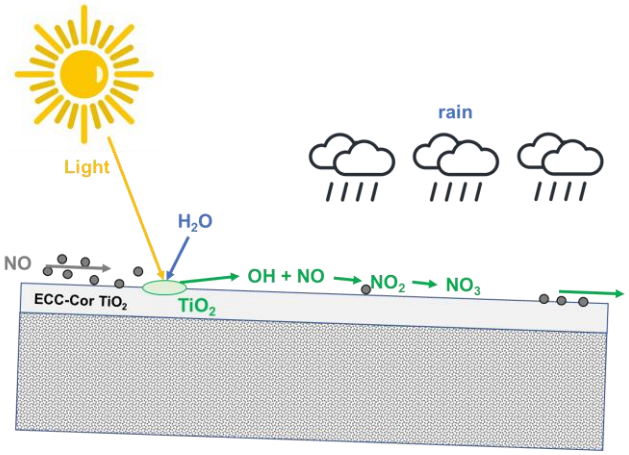

Figure 4.5 Photocatalytic process on concrete

Heterogeneous photocatalysis had shown promising results for NO_x abatement. Ultraviolet (UV)-light was commonly used to activate the photocatalyst. Recently, a new source of light, visible light (VL), is becoming a new way. Visible light composes the largest past of solar radiation which can be an advantage as the content of UV light in indoor is significantly smaller than that in sunlight environment because the fluorescent lamp mainly emits visible light. This means that photocatalytic application can also be applied in tunnels and indoor environments. It is worth to note that the air pollutants in tunnels are normally in high concentration.

Fujishima and Zhang [141] summarizes three methods on the utilization of visible light for photocatalysis: (1) utilization of semiconductors to absorb visible light, such as CdS, Cu_2O, Fe_2O_3, and WO_3, (2) doping of photocatalysts with metal ions (such as Cr^{3+}, Fe^{3+}) to create local energy levels within the band gaps of visible spectral range, and (3) by doping of photocatalysts with non-meal atoms, such as N, S, and C. From those three methods, the third one claimed to be the most efficient method for the development of photocatalysts utilizing visible light.

4.6.2. Test methods on photocatalytic performance

Test methods on photocatalytic performances are varied depending on the type and size of TiO_2, the source lights, and pollutant solutions. One example is examination via decomposition of Rhodamine B (RhB) which represents the pollutant solutions associated with dirt and stains, is one of the most common dyes used (UNI 11259:2008). Then the efficiency of photodecomposition of the sample can be observed with a spectrophotometer by measuring the light reflectance at a different wavelength. The reflectance of the sample is tested before and after it is exposed to dye and the lights. Cassar et al. [142] tested white cement containing TiO2 Degussa P25 with yellow dye (Phenantroquinone) under 400 W simulator lamps with λ > 290 nm. Vallee [143] investigated white cement mixed with T_iO_2 anatase with RhB dye under 300 W UV light Ultra-Vitalus. Bolte et al [144] was tested mortar made with cement mixed with Degussa P25a with RhB dye under 100 W mercury vapour lamp with λ < 320 nm filtered out to eliminate photolysis. Yuranova et al. [145] have investigated Cement based plates with T_iO_2/S_iO_2 surface layers as coating with TiO_2 rutile with red wine dye under suntest solar simulator (290 – 800nm). Bonafous et al. [146] has studied the effect of Mortar with both white

and ordinary cement mixed with T_iO_2 PC 105 with RhB dye under Bromocresol green 2.5 µg/cm2 300W lamp. Zhao [147] investigated White ECC mixed with P25 with RhB dye under 9W artificial UV and sunlight. Another test is the dirt pick-up resistance (DPUR) which is used to investigate the amount of dirt can be removed from the surface sample when the sample is exposed to the lights.

4.6.3. Research and application of photocatalytic pavements

Various studies have incorporated photocatalytic oxidation in pavement materials for NO_x reduction. Laboratory results indicate a good efficiency towards the abatement of NO_x in the air by using these innovative materials for pavement applications. Yet, real applications on a large scale are still showing inconsistency as there are many parameters cannot be fully controlled, such as humidity, light intensity, and wind speed [148].

The photocatalytic concrete paving blocks in Antwerp in 2004 was one of the first projects embedding photocatalytic function for pavements application. From this project, several insights were gained. Good durability of the efficiency towards NOx abatement was observed. The deposition of pollutants on the surface leads to a decrease in efficiency, which can be regained after washing. Measurements in 2010 indicate that even after more than five years of service life, the photocatalytic efficiency of the pavers is still present [148]. In 2007, [149] researched by incorporating T_iO_2 into a concrete paving block with different surface mix designs. The maximum aggregate size of the recycled fine aggregate used is 2.36 mm. Important results from the test show (1) the NO removal ability was increased when the porosity of the block was increased (lower density or material with less fine particles), (2) sample with a lower cement to aggregate ratio leads to higher efficiency rate for NO removal, (3) P-25 T_iO_2 shows a better photocatalytic performance compare to Rutile, but not in cost perspective [149].

In 2011, a photocatalytic function was embedded using cementitious coating materials in the Leopold II tunnel on project PhotoPAQ, which was funded by the European Life+. The lower result was gained from the expected performance. However, there are many interesting conclusions were drawn. The typical low average wind speed (~3 m s^{-1} during daytime), the cold, and low average relative humidity (70 -90% r.h.) inside the tunnel resulted in a reduction of the photocatalytic performance. Additionally, the UVA irradiance which was below the target (it only reached 0.6 to 1.6 Wm^{-2}, while the target is to produce more than 4 Wm^{-2}) is affected the photocatalytic performance [150].

Also, in 2011, two trial sections (each 30 m long and 3 m wide) of double-layered concrete have been built with photocatalytic materials. The bottom layer concrete was built with more than 50% of the large aggregates replaced by recycling concrete aggregates. Meanwhile, the top layer built with aggregate with a maximum aggregate size 6.3 mm. After conducting the test, it was found out that the curing compound has a negative effect on NO_x reduction. Different surface treatment has been performed: exposed aggregates, smooth (formwork side), and sawn surface. The results show that the surface of the exposed aggregates performs equally well as the smooth (formwork surface), but lower than the sawn surface. This caused by the combination of less photoactive cement at the surface and a higher surface porosity [151].

Three methods of application for T_iO_2 to concrete pavement were investigated: (1) a cementitious-based ultrathin coating, (2) a water-based titanium dioxide solution, and (3) sprinkling T_iO_2 to the fresh concrete surface before hardening [152].

4.7. Chapter discussion

This chapter about the functional performance is developed based on four main questions:

- Why functional performance for pavement (PUTW) is important?
- What important parameters in functional performance are? and why focus only on skid resistance and surface water drainage?
- How the functional performance of pavement made ECC (hypothetically) is?
- What can be improved on the functional performance of pavement made of ECC?

As it was discussed in chapter 3, PUTW offers great advantages in terms of structural performance. But on the other hand, PUTW has many downsides on functional performance. A study stated the importance of pavement safety is mainly affected by pavement surface, which is commonly characterized by friction, smoothness, tire-pavement noise, and texture [70]. Meanwhile, when it comes to road pavements, both structural performance and functional performance are important. The structural performance is needed to bear the traffic load and guarantee the durability of the roadway itself. While the functional performance of pavement is vital as it is directly related to the safety and yet comfort factor of driving experiences. AASHTO [1] points the importance of the functional performance of the pavement, which is based on its ability to serve the user. It consists major parameters of roughness, skid resistance, risk of hydroplaning, and appearance.

Many important design criteria parameters in functional performance must be considered and carefully designed in pavement engineering. However, all of parameters are not linearly correlated to each other. Therefore, it is very challenging to get a perfect solution for all design criteria parameters. Thus, the study will only focus on two main important parameters: skid resistance, and surface water drainage (which is related to splash and spray). These two parameters were chosen as they are known as the most important factors in functional performance [72].

ECC itself has naturally no textures due to no large size aggregates used in its mixture design. As consequences, unfinished ECC provides low skid resistance and low surface water drainage for surface PUTW pavement. Textures need to be embedded on ECC. The existence of textures will be possible by only adding aggregates and or introducing grooves into the surface. The addition of aggregates is only possible by modifying the mixture design of ECC through micromechanics approach. Thus, the mechanical properties will be not significantly affected. In addition, grooves can be introduced into the surface of PUTW pavement to increase surface water drainage performance. As for durability, the test needs to be performed to have a better understanding of whether PUTW with finished ECC can handle the designed load traffic.

Three main parameters are affecting tire-pavement noise: texture, porosity, and stiffness. By default, ECC has characteristics of low texture, low porosity, and high stiffness. Correspondingly, tire-pavement noise on PUTW will be relatively high. In addition to the conventional functional performance, a self-cleaning function can be embedded in PUTW as an innovative and green pavement. With self-cleaning function, pavements can reduce the NO_x in Singapore condition by integrating T_iO_2 material into mixture design of ECC.

5. Multi Criteria Decision Analysis on the Functional Performance of Pavement

5.1. Introduction

This chapter 5 explains the necessity of having a holistic understanding of the functional performance regardless of various standards as well as texturing methods available thus best decision can be made to fulfil design requirements. In real life, many decisions involve trade-offs, which is related to conflicting constraints. This is also the case in designing surface pavement to meet the functional performance required.

In many cases, a design (including pavements) requires coupled optimization of two or more parameters of performance. An example given by Ashby [153], a material was needed for a beam for bicycle component. The objective is to minimize the weight as well as the cost. The designer wants to have light material, but the marketing manager requires it to be as cheap as possible. Therefore, the material has constraint of stiffness, and yet price.

Surface of pavements have been studied for decades. Many surface treatments have been done by agencies to improve the functional performance of the pavements both for concrete and asphalt and: skid resistance, surface water drainage, pavement evenness, noise, and durability. However, there are so many different standards for those criteria applied, which might be causing misinterpretation when decision-makers are about to select the right surface treatment. As an example, is when they need to compare in which texturing methods are applied by different agencies who is using different standards. Firstly, there are various standards related to the functional surface performance of the pavement applied by different agencies. Secondly, there are many different measurement methods for the functional performance of the surface pavement. Thirdly, the surface treatment methods used to improve the surface pavement are varying. Therefore, it is not an easy task to understand, to compare one to another surface treatment method with different criteria, and then to select. Yet, fewer studies were found on comprehensive analysis on determining which surface treatment leads to better functional performance.

The objective of the research is to find a sophisticated method to define the functional performance of surface properties of such a type of surface pavement. The functional performance includes microtexture, macrotexture, pavement drainage (splash and spray), pavement unevenness, noise, cost, and durability.

One of many options decision support tools is the Multi-Criteria Decision Analysis (MCDA). MCDA is a decision-support tool for exploring issues and making decisions involving multiple criteria. The tool allows technical, economic, environmental, even social criteria, including setting up the priorities. It can be used to generate qualitative data about decision-making criteria, to rank decision options, and to discuss the background for rank positions.

Scores are defined based on references from existing research, guidelines, and standards. Scores are related to general action needed and the risk of accidents. Various criteria are then weighted to reflect the relative importance of different criteria. The weighted sum of the different chosen criteria is used to rank the options.

5.2. Functions, compound objectives, and multiple constraints within functional performance of surface pavements

Following an approach explained by Ashby [153], several functions, compound objectives, and multiple constraints can be found in design requirements on the functional performance of pavements. As functions, there are mainly two criteria related to surface pavements: a

design for new roads and design for retexturing roads. Design for new roads is needed when a new line or roadway is required and decided to be built. The retexturing road is mostly required when the existing roads have been built some time ago.

The objectives of road agency when they are considering such a design (texturing methods) for surface pavement can be different. Typical objectives are elaborated in Figure 5.1. It should be noted that in many cases, the road agency has more than one objective. As an example, an existing road located in the residential area needs to be treated. The objectives are to reduce the noise as well as to minimize the cost. However, the roads in highway need more objectives: quick to be opened for traffic, less noise, high skid resistance, and high comfort.

Ashby [153] explained that even from one objective might require more than one constraint. As consequences from different and compound objectives, multiple constraints need to be considered. As an example, if the objective is to improve the skid resistance, the constrains will include microtexture, macrotexture, and perhaps local material availability.

5.3. Scope of MCDA study

The scope of MCA needs to be defined as the functional performance can be extremely varied. For example, the design requirement of skid resistance is varying between roadway, roundabout, and pedestrian. Thus, in this study, the scope of MCA includes:

- Level of the road network: highway or main arterial road
- New roads or newly retextured
- Surface texture methods for concrete, and asphalt
- Seven criteria: microtexture, macrotexture, surface drainage, noise, pavement roughness, cost, and durability

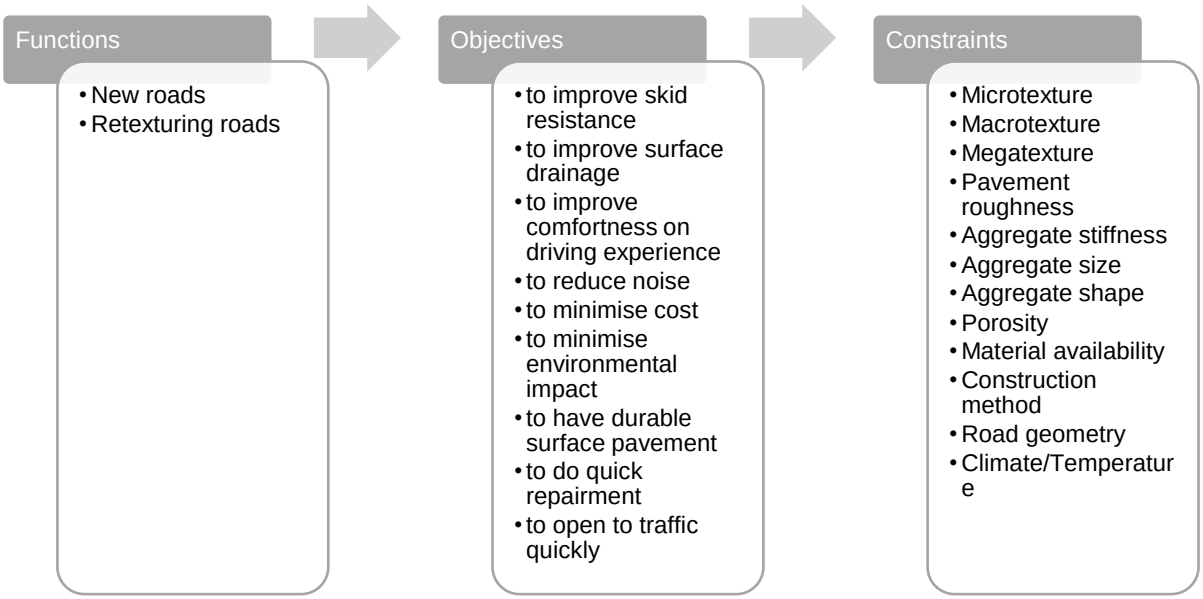

Figure 5.1 Functions, objectives, and constraints on functional performance

5.4. Methodology of MCDA

The objective of this study is to find an optimum solution for surface pavement from the safety aspect. An optimum solution for a safe pavement can be identified with the help of MCDA. MCDA has many advantages over informal judgement unsupported by analysis: it is open and explicit, the choice of objectives and criteria that any decision-making group may make are open to analysis and to change if they are felt to be inappropriate, scores and weights, when used, are also explicit and are developed according to established techniques.

The first step is data mining of functional performance from texturing methods. Data mining was done by collecting secondary data from previous research published in papers, reports, and any other reliable documents. It is expected to have many missing data of criteria for many texturing methods. Thus, an empirical formula with strong correlation is used to fulfil the gaps. Then it is statistically analyzed to check whether the quality of the data is good or should be categorized as an outlier.

MCDA techniques commonly apply numerical analysis to a performance matrix in two stages:

1. Scoring: the expected consequences of each option are assigned a numerical score on the strength of a preference scale for each option for each criterion. More preferred options score higher on the scale, and less preferred options score lower. Many studies apply scales extending from 0 to 5, where 0 represents a real or hypothetical least preferred option, and 5 is associated with a real or hypothetical most preferred option. All options considered in the MCDA would then fall between 0 and 5.

2. Weighting: numerical weights are assigned to define, for each criterion, the relative valuations.

Literature review on established guidelines and standards was done to develop the new score. Results have shown that various standards are applied. Therefore, general rules need to be created. Each value of the score will be highly dependent on the general actions needed to improve the functional performance of the pavement. It is also related to the risk of accidents. After the scoring was done, the next step is weighting. Weighting is important as not every criterion has similar importance or urgency level. In many cases, one criterion can be more important than others, e.g. most agencies are prioritizing safety more than comfort. With a combination of scoring and weighting, ranking can be done as a final step. The ranking can be used as a reference for a better or worse texturing method for overall criteria. However, in this study, ranking might be not critical, as this study will be focusing on skid resistance and surface water drainage. Flow chart of the methodology is illustrated in Figure 5.2.

$$\text{Weighted sum} = \sum_{j=1}^{n} w_j x_{ij}, \text{for } i = 1,2,3,\dots,m \qquad \text{(Eq. 13)}$$

Where: w = relative weight of importance (see Table 5.10)

x = performance value

n = decision criteria (microtexture, macrotexture, pavement roughness, noise, surface drainage, cost, and durability)

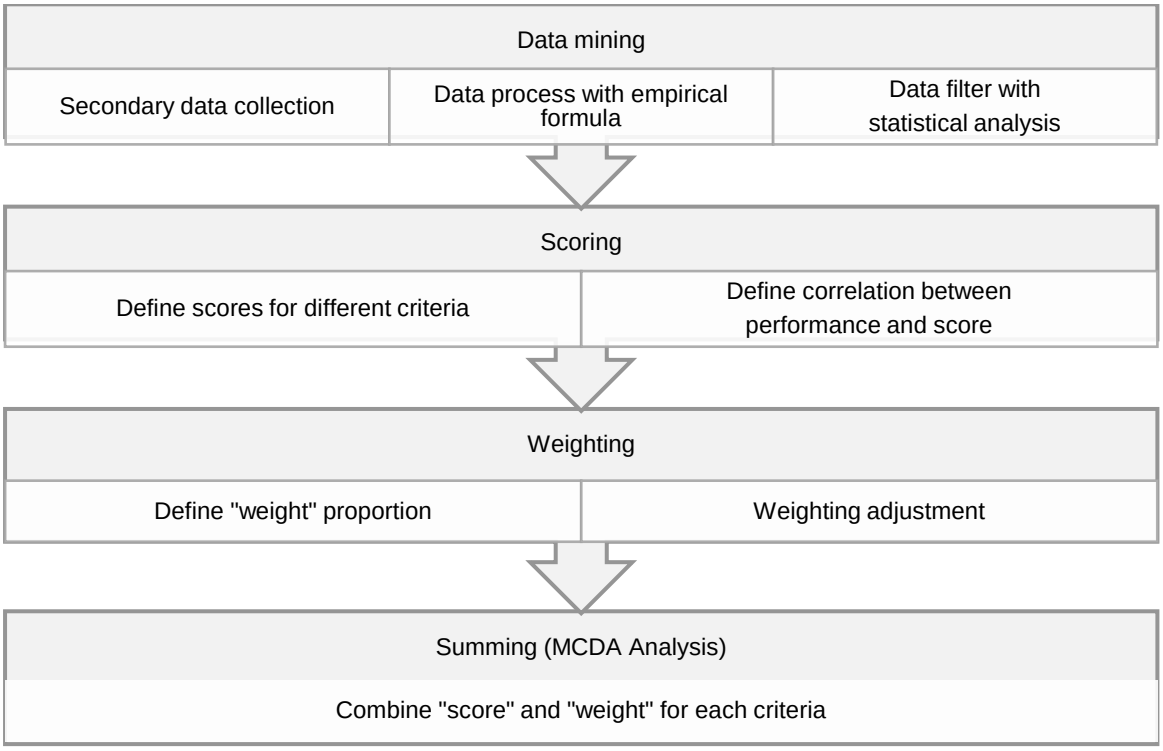

Figure 5.2 Methodology of MCA for Functional Performance of Pavement [154]

5.5. Data mining

5.5.1. Data collection

More than 10.000 data are collected for different texture methods based on different test standards. Five different criteria of functional performance are included: microtexture, macrotexture, surface pavement drainage, noise, pavement unevenness. Test methods for each criterion included in this MCDA study are summarized in Table 5.1. Additionally, two criteria: cost and durability are taken into account for the MCDA study, as these two criteria highly considered by most agencies.

Table 5.1 Data collection for MCA for functional performance of pavement

Criteria	Index	Test 1	Test 2	Test 3	Test 4
Microtexture	Microtexture	BPT (slider)			
	Friction	BPT (slider)	DFT (slider)	DFTester (Locked Wheel)	SCRIM (side force)
Macrotexture	MPD	Laser	CTM	SPM	
	MTD	Laser	CTM	SPM	
	RMS	CTM			
	ETD	Laser	CTM		
Surface pavement drainage	Water outflow	Outflow meter			
Noise	Wayside (traffic) noise	SPB	CPB	CTIM	

Criteria	Index	Test 1	Test 2	Test 3	Test 4
	Tire-pavement noise	OBSI	CPX		
	In-vehicle noise	microphone			
Pavement Roughness	IRI	Laser	profilometer		
	Profilograph index	Laser	profilometer		
	Ride Number	Laser	profilometer		

For asphalt pavement (coded as AC), there are about 35 different texturing methods found. Those texturing methods are then labelled with a code, as it will make it easier to be coded and to be visualized in charts later. On the other side, there are about 37 different texturing methods summarized for concrete pavements (coded as PCC). The texturing method can be categorized into two: New and or overlay (coded as NO), and retexturing or friction restoration (coded as RF). Examples of the meaning of the coding are given: ACNO means texturing method for Asphalt Pavement for New and Overlay. Meanwhile, PCCRF means texturing method for Concrete pavement for Retexturing and or Friction restoration.

5.5.2. Data process with empirical formula

Since many data are missing for some criteria from each texturing methods, there is need to find a solution on how to fulfil the data. One solution is by using an equation which has a close correlation (R^2) between each criterion. These equations are referred from previous research and mainly are based on empirical studies.

Table 5.2 Correlation between criteria of functional performance of pavement

Correlation	Micro-texture	Macro-texture	Friction	Rough-ness	Surface Drainage	Noise
Microtexture			(Eq. 14			(Eq. 27
Macrotexture		(Eq. 16, (Eq. 17	(Eq. 15, (Eq. 18		(Eq. 19 and (Eq. 20	(Eq. 21, (Eq. 22, (Eq. 23, (Eq. 24
Friction			(Eq. 25, (Eq. 26)			
Roughness				(Eq. 30		
Surface Drainage						
Noise						(Eq. 28, (Eq. 29

5.5.2.1. Correlation between microtexture/macrotexture and friction

Correlation between microtexture and friction has been mentioned by [72]. The equation given:

$$\mathrm{BPN} = 57.9 \times \mathrm{DFT}(20) + 23.1 \quad \text{(Eq. 14)}$$

Where: BPN = British Pendulum Number

DFT = DFTester

While correlation between macrotexture and friction is stated in report of NCHRP 634 [72] is shown below.

$$\mathrm{F}(60) = 0.081 + 0.732 \times \mathrm{DFT}(20) \times \mathrm{e}^{([20-60])/\mathrm{S_p}} \quad \text{(Eq. 15)}$$

Where: $\mathrm{F}(60)$ = Friction

DFT = DFTester

$\mathrm{S_p}$ = Speed number

5.5.2.2. Correlation in macrotexture

A correlation between CT meter MTD and CT meter MPD based on NASA/Wallops equation (Henry, 2000) is shown below.

$$\mathrm{MTD} = 0.952 \times \mathrm{MPD} + 0.091 \quad \text{(Eq. 16)}$$

Where: MTD = Mean Texture Depth

MPD = Mean Profile Depth

[155] elaborate formula for correlation between MTD from sand patch method and MPD from laser measurement as:

$$\mathrm{MTD(SPM)} = 1.0812 \times \mathrm{MPD(laser)} + 0.0697 \quad \text{(Eq. 17)}$$

Where: MTD = Mean Texture Depth

MPD = Mean Profile Depth

5.5.2.3. Correlation between macrotexture and friction

NCHRP illustrates the correlation between macrotexture and friction [72] as:

$$\mathrm{S_p} = 14.2 + 89.7 \times \mathrm{MPD} \quad \text{(Eq. 18)}$$

Where: MTD = Mean Texture Depth

MPD = Mean Profile Depth

5.5.2.4. Correlation between macrotexture and surface drainage

According to ASTM E2380, there is a correlation between MTD and OFT w with following Eq.:

$$\mathrm{MTD} = \frac{3.114}{\mathrm{OFT}} + 0.636 \quad \text{(Eq. 19)}$$

Where: MTD = Mean Texture Depth (mm)

OFT = Water Outflow Time (s)

Another formula proposed by Sarsam (2012) with correlation below:

$$\mathrm{OFT} = 2.647 \times \mathrm{MTD}^{-0.789} \quad \text{(Eq. 20)}$$

Where: MTD = Mean Texture Depth (mm)

OFT = Water Outflow Time (s)

5.5.2.5. Correlation between macrotexture and noise

The correlation between macrotexture (MPD) and tire-pavement noise ($\mathrm{R}^2 = 0.59$) was found by [156], it is shown in (Eq. 21.

$$\mathrm{Noise\ (OBSI)} = 3.13\mathrm{MPD} + 95.57 \quad \text{(Eq. 21)}$$

Where: OBSI = tire-pavement noise (on-board sound intensity)

MPD = Mean Profile Depth

[157] explained that macrotexture (MTD) has high correlation with tire-pavement noise ($\mathrm{R}^2 = 0.80$), but depends on the speed.

$$\mathrm{Noise\ (OBSI)} = 1826.2\mathrm{MTD} + 24809 \quad \text{(Eq. 22)}$$

$$\mathrm{Noise\ (OBSI)} = 1404.9\mathrm{MTD} + 17237 \quad \text{(Eq. 23)}$$

$$\mathrm{Noise\ (OBSI)} = 892.67\mathrm{MTD} + 9659.9 \quad \text{(Eq. 24)}$$

Where: OBSI = On-board sound intensity

MPD = Mean Profile Depth

MTD = Mean Texture Depth

5.5.2.6. Correlation in microtexture and friction

Researchers found out that British pendulum number of BPT and DFT(20) value of dynamic friction tester has a big correlation with $\mathrm{R}^2 = 0.86$. Equation below shows how we can use DFT(20) value to create BPN value and vice versa (NCHRP 2000).

$$\mathrm{BPN} = 57.9 \times \mathrm{DFT}(20) + 23.1 \quad \text{(Eq. 25)}$$

Where: BPN = British Pendulum Number

DFT = DF Tester

Another equation was found between F_{60} and FN40S during literature review. S_p means speed number and can be calculated from MPD value of pavement surface. It will be also explained below.

$$\mathrm{F_{60}} = 0{,}045 + 0{,}925 \times \mathrm{FN40S} \times \mathrm{e}^{5/\mathrm{S_p}} \quad \text{(Eq. 26)}$$

Where: $\mathrm{F_{60}}$ = Friction

$\mathrm{FN40S}$ = Friction Number

$\mathrm{S_p}$ = speed number

5.5.2.7. Correlation between microtexture/macrotexture and noise

It is mentioned in NCHRP 634 report, there is strong correlation ($R^2 = 0.61$) between macrotexture and noise on concrete pavement. The correlation can be seen in (Eq. 27).

$$\text{Log (SI)} = -0.35 + 0.37\text{x}\,\text{TD}_{\text{TRAN}} + 0.62 \times \text{GTI}_{\text{EAC}} + 0.20 \times \text{GTI}_{\text{LTi}} + 0.01 \times \#\text{Jts} + 0.06 \times \text{Ln(traffic)} + 0.53 \times \text{MPD}_{\text{HS}} \quad \text{(Eq. 27)}$$

Where:
- TD_{TRAN} = Transverse texture direction (1=transverse, 0=otherwise)
- GTI_{EAC} = GTI for Exposed Aggregate Concrete texture (1=EAC, 0=otherwise)
- GTI_{LTi} = GTI for longitudinal-tine texture (1=longitudinal-tine, 0=otherwise)
- $\#\text{Jts}$ = Number of joints per 305 m
- Ln(traffic) = Log normal cumulative traffic applications
- MPD_{HS} = MPD from high-speed profiler (mm)

5.5.2.8. Correlation in noise

According to Donovan (2009), there is a strong correlation between the wayside noise and tire-pavement noise. CPB and CPX have a correlation of 79% ($R^2 = 0.79$), while CPX and OBSI has a correlation of 93%. The equations are shown below.

$$\text{CPB} = 0.8 \times \text{CPX} - 2.3 \quad \text{(Eq. 28)}$$

Where:
- CPB = Controlled pass-by
- CPX = Close proximity

$$\text{CPX} = 1.04 \times \text{OBSI} - 6.52 \quad \text{(Eq. 29)}$$

Where:
- CPX = Close Proximity
- OBSI = On-Board Sound Intensity

5.5.2.9. Correlation in pavement roughness

According to [158], there is a correlation between PSR and pavement roughness which derived into following equation:

$$\text{PSR} = 5\text{e}^{-0.19(\text{IRI})} \quad \text{(Eq. 30)}$$

Where:
- PSR = present serviceability rating
- IRI = International roughness index

5.5.3. Data filter with statistical analysis

It is expected that a lot of data will be collected. Various data from different sources might create big differences (standard deviation). Therefore, this data will be statistically analyzed before it can be processed further. The boxplot is used to display the distribution of data based on minimum, first quartile, median, third quartile, the interquartile range, and maximum.

5.6. Scoring on criteria for functional performance

After the data process, the next step is the scoring. Scoring criteria is set up based on the literature review from guidelines and standards issued by agencies. Then, these scoring criteria will be used as a reference for categorizing functional performance.

5.6.1. Scoring criteria

Scoring criteria is set up based on the literature review from guidelines, standards, and related documents issued by agencies. The criteria are set from 1 to 5 (1=lowest performance, and 5=highest performance), and they are mainly based on the performance, required actions, and risk of accidents. Statistical analysis is used only when there are no similar scoring criteria found on existing standards, guidelines, and related documents issued by agencies. The scoring criteria is summarized in Table 5.3.

Table 5.3 Scoring category and their criteria for MCDA

Category	Scoring	Standard Related	Typical Action	Risk to accidents	Statistical Analysis
Excellent	5	Far beyond standard	No further action required	No	Above Q3
Good	4	Slightly above standard	Regular maintenance	No	Median to Q3
Fair	3	Meet the standard	Regular maintenance	No	Standard to median
Poor	2	Slightly below Standard	Maintain monitoring, data collection, and take corrective action as required	**Yes**	
Very Poor	1	Far below standard	Rehabilitation or reconstruction is needed	**Yes**	

5.6.2. Scoring on microtexture/friction

According to few existing standards and guidelines, the proposed scoring for microtexture/friction is summarized below:

Table 5.4 Scoring for microtexture/friction

Score (category)	BPT	DF Tester		Locked Wheel	
	Slider	DFT(20)	F(60)	FN40R	FN40S2
	BPN	-	-	-	-
5 (Excellent)	> 75	> 90	> 40	> 50	> 50
4 (Good)	65 to 75	70 to 90	35 to 40	45 to 50	40 to 50
3 (Fair)	55 to 65	50 to 70	28 to 35	35 to 45	28 to 40
2 (Poor)	45 to 55	40 to 50	24 to 28	26 to 35	20 o 28
1 (Very Poor)	< 45	< 40	< 24	< 26	< 20

5.6.3. Scoring on macrotexture

According to few existing standards and guidelines, the proposed scoring for macrotexture is summarized below:

Table 5.5 Scoring for macrotexture

Score (category)	Laser		CT Meter		Sand Patch
	MPD	MTD	MPD	MTD	MTD
	mm	mm	mm	mm	mm
5 (Excellent)	> 1,15	> 1,2	> 1,15	> 1,2	> 1,2
4 (Good)	0,9 to 1,15	1 to 1,2	0,9 to 1,15	1.0 to 1,2	1.0 to 1,2
3 (Fair)	0,8 to 0,9	0,8 to 1.0	0,8 to 0,9	0,8 to 1.0	0,8 to 1.0
2 (Poor)	0,35 to 0,8	0,4 to 0,8	0,35 to 0.8	0,4 to 0,8	0,4 to 0,8
1 (Very Poor)	< 0,35	< 0,4	< 0,35	< 0,4	< 0,4

5.6.4. Scoring on pavement surface drainage

According to few existing standards and guidelines, the proposed scoring for pavement drainage is summarized below:

Table 5.6 Scoring for pavement drainage

Score (category)	OFM
	OFT
	sec
5 (Excellent)	< 2
4 (Good)	2 to 5
3 (Fair)	5 to 10
2 (Poor)	10 to 50
1 (Very Poor)	>50

5.6.5. Scoring on noise reduction

According to few existing standards and guidelines, the proposed scoring for noise level is summarized below:

Table 5.7 Scoring for noise level

Score (Category)	Noise level	
	Tire-pavement	
	OBSI	OBSI
	dB(A)	dB(A)
5 (Excellent)	< 102	< 102
4 (Good)	102 to 104	102 to 104
3 (Fair)	104 to 106	104 to 106

Score (Category)	Noise level	
	Tire-pavement	
	OBSI	OBSI
	dB(A)	dB(A)
2 (Poor)	106 to 108	106 to 108
1 (Very Poor)	> 108	> 108

5.6.6. Scoring on pavement roughness

According to few existing standards and guidelines, there are many methods can be used. In this study, three methods are included: Profilograph Index, International Roughness Index, and Pavement Serviceability Ratio. The level for IRI and PSR directly derived from FHWA. The proposed scoring for pavement roughness is summarized below:

Table 5.8 Scoring for pavement roughness

Score (Category)	Pavement Roughness			
	PrI	IRI		PSR
	m/km	mm/m	In/mi	-
5 (Excellent)	< 110	< 0.95	< 60	> 4.0
4 (Good)	110 to 160	0.95 to 1.48	60 – 94	3.5 – 4.0
3 (Fair)	160 to 230	1.48 to 1.88	95 – 119	3.0 – 3.5
2 (Poor)	230 to 450	1.88 to 2.68	120 – 170	2.5 – 3.0
1 (Very Poor)	> 450	> 2.68	>170	< 2.5

5.6.7. Scoring on cost and durability

According to a few existing standards and guidelines, the proposed scoring for the cost of surface treatment and durability are summarized below in Table 5.9. The cost is presented in three different currencies. The conversion rates used are based on the date of 29 October 2018 issued by Bloomberg (www.bloomberg.com), which are: 1.3826 for USD/SGD and 0.8792 for USD/Euro. Meanwhile, durability presented in years.

Table 5.9 Scoring for cost and durability

Score (category)	Cost			Durability
	USD $ / m2	Euro € / m2	SGD $ / m2	years
5 (Excellent)	< 1.06	< 0.93	< 1.47	> 11
4 (Good)	1.06 to 1.98	0.93 to 1.74	1.47 to 2.74	9.5 to 11
3 (Fair)	1.98 to 3.86	1.74 to 3.39	2.74 to 5.34	7.5 to 9.5
2 (Poor)	3.86 to 10.60	3.39 to 9.32	5.34 to 14.66	4.6 to 7.5
1 (Very Poor)	> 10.60	> 9.32	>14.66	< 4.6

5.7. Weighting on criteria for functional performance

The next step of MCA is weighting. Weighting is a crucial consideration as not every criterion has similar importance or urgency level. One criterion can be more important than others, e.g.

most agencies are prioritizing safety more than comfort. The weight proportion use in this MCA based on a study done by NCHRP (see Chapter 4.1). On their study, it summarized that safety has more prioritization than other criteria (refer to Table 4.1). However, this MCA not using the same criteria with their study. Therefore, some adjustments are needed, including:

- The weight of durability in MCA study is 1.2, which is the average of durability for the USA and other countries.
- There is no criterion of cost from NHCRP reference. However, it is mentioned that the durability is highly important as it is related to budgeting consideration for the agency. Therefore, in this study, MCA is considered as important as durability, which is 1.2.
- The weight for both microtexture and macrotexture in MCA is similar to the weight of skid resistance from NCHRP study, as both micro- and macrotextures are a detailed factor of skid resistance. However, the weight is averaged.
- The weight of surface drainage in this MCA is the average of weight for the splash and spray for the USA and other countries.
- The weight of tire-pavement noise in this MCA is the average of weight for exterior noise for the USA and other countries.
- The weight of pavement roughness in this MCA is the average of weight rolling resistance and tire wear. The pavement roughness considered has similar weight as it is closely affected by rolling resistance and tire wear.

The next step is to inversely calculate the weight from “3 to 1 scale” into “1 to 5 scale”, with 1 is the lowest priority and 5 is the highest priority. Then, the last step is to convert all of the weight into ratio to 1, means the sum of weight for all seven criteria is 1. The summary of the previous study, the new weight proportion for MCA study, and the inversed ratio for related weight are summarized in Table 5.10.

Table 5.10 Weight proportion for MCA

Design Criteria	Reference Ranking		Proposed in MCA study	
	USA	Other Countries	Weight Proportion	Inversed weight (ratio to 1)
Durability	1,1	1,3	1.2	0.18
Cost			1.2	0.18
Skid resistance	1,2	1,4		
Microtexture			1.3	0.17
Macrotexture			1.3	0.17
Splash and spray	2,0	1,8		
Surface drainage			1.9	0.13
Exterior noise	2,4	2,2		
Tire-pavement noise			2.3	0.10
In-vehicle noise	2,4	2,4		
Rolling resistance	2,7	2,7		
Tire wear	2,7	2,9		
Pavement roughness			2.7	0.06

5.8. Results and Discussion

This chapter can be considered as the second important stage after literature review, as it gives a comprehensive understanding of the functional performance of surface pavement of many different texturing methods, regardless there are many different measurement methods and or standards were applied. More than 10.000 data from different texturing methods for asphalt and concrete pavements have been collected and analyzed for seven different criteria (constraint): microtexture and friction, macrotexture, water outflow, pavement roughness, and tire-pavement noise, cost, and durability.

Texturing methods for concrete pavements were checked closely, as concrete pavement considered closely related to PUTW, which both categorized as a cementitious material. Thus, typical texturing methods such as tining, grinding, and grooving can also be implemented in PUTW. Although texturing methods for asphalt pavement can also be considered if it is applied as a surfacing layer. However, the surfacing layer consequently adding more work, and cost.

In this study, the focus of functional performance lies on skid resistance and surface drainage, as they are closely related to the safety aspect. According to data, best practice of texturing methods for skid resistance and macrotexture include longitudinal diamond grooving, transverse diamond grooving, and turf drag. Additionally, exposed aggregate, longitudinal tining, and burlap drag can be used to improve skid resistance to the required safety standards. In terms of surface drainage, diamond grooving gives the best results. However, other texturing methods such as diamond grinding, tining, burlap drag, exposed aggregate resulting in a satisfactory performance for water outflow. The optimum texturing methods for both low tire-pavement noise and skid resistance include longitudinal tining, turf drag, broom drag, exposed aggregate, and followed by diamond grinding. The least solution for noise is transverse diamond grooving.

5.8.1. Radar chart analysis

The first analysis is done with the radar chart to evaluate each texturing method. Radar chart, also known as spider chart, web chart, polar chart, or star plot, is a two-dimensional chart to display multi-dimensional data structure. This spider chart is useful as it can be used to compare the average score of different characteristics of constraints (in this study includes: skid resistance, surface water drainage, tire-pavement noise, pavement roughness, durability, and cost). Further, the radar chart gives an overall picture of how each texturing method performs, as it gives the impression on how good or bad for each constraint. The weakness of this radar chart is, that it gives no clarity when the chart is used to compare different texturing methods. For comparison, a different type of analysis is needed, which is described in the next sub-chapters.

The functional performance of each texturing method for asphalt and concrete pavements are shown in Appendix F.1, respectively. Seven constraints (microtexture, macrotexture, pavement roughness, surface water drainage, tire-pavement noise, durability, and cost) are included in each texturing method which the value is scaled from 0 to 5. More results are elaborated in Appendix F.

5.8.2. Multiple two-constraints analysis on functional performance

The second analysis is done by plotting multiple constraints scenario. This analysis allows a comparison of many texturing methods. However, it is limited to two constraints. The plot is not determined to give a correlation between constraint (criterion). Instead, it gives a picture of what is the performance of two constraints for each texturing method.

Figure 5.3 gives an example of two-constraints combination between microtexture (BPN) and surface drainage (OFT, seconds). Within each graph, first and second frontier is included which gives identification for the first and the second-best options for those two constraints. However, it should be noted that they are not to be outside boundaries set by two lines for each constraint. As the boundary line have been set according to scoring criteria. It means any value outside the boundary lines gives bad results (Poor and Very Poor performance). More results for combination on macrotexture, microtexture, tire-pavement noise, pavement roughness, durability, and cost are elaborated in Appendix F.

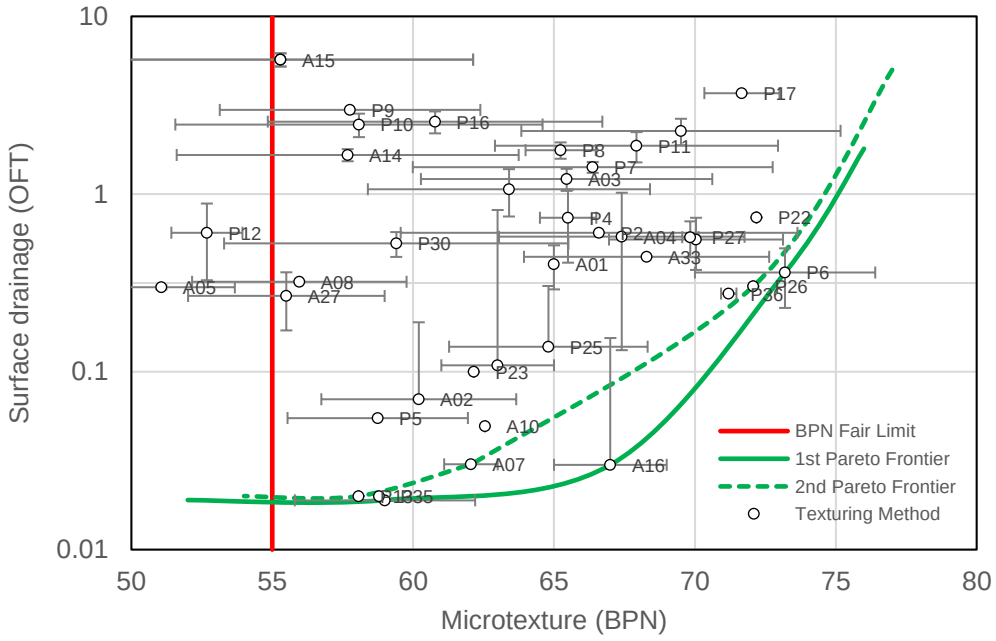

Figure 5.3 Two-constraints analysis

5.8.3. Multi Criteria Decision Analysis

The last analysis method is done by using MCDA. Every texturing method has been scored and weighted. As the final step, each value from seven constraints is summed. As results, each texturing method has a total value. The total value can be used as criteria for ranking the methods. The maximum value is 5. The weighted sum for all texturing methods for asphalt pavements and concrete pavements are summarized in Figure 5.4 and Figure 5.5, respectively.

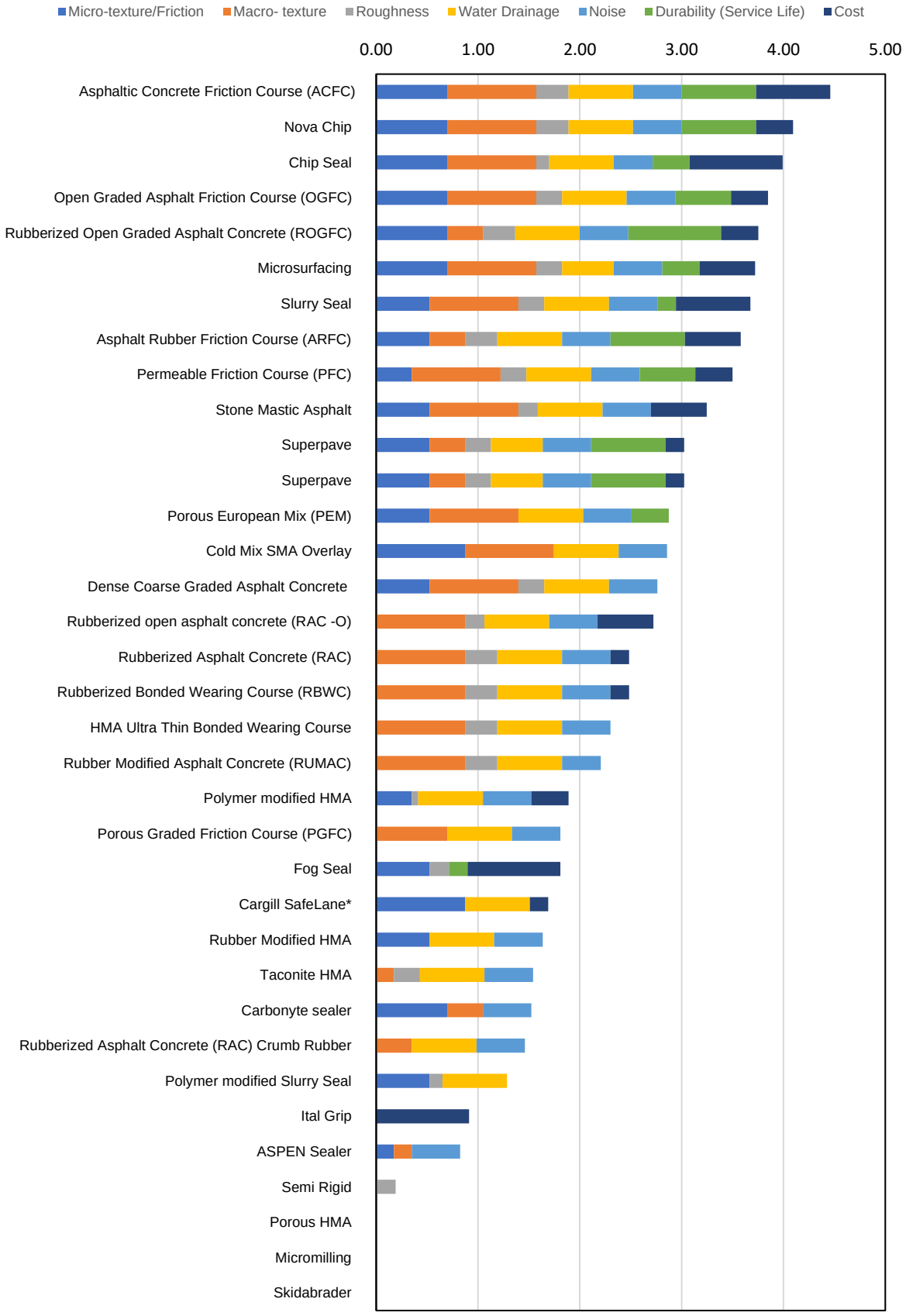

Figure 5.4 Weighted sum of texturing methods for asphalt pavement

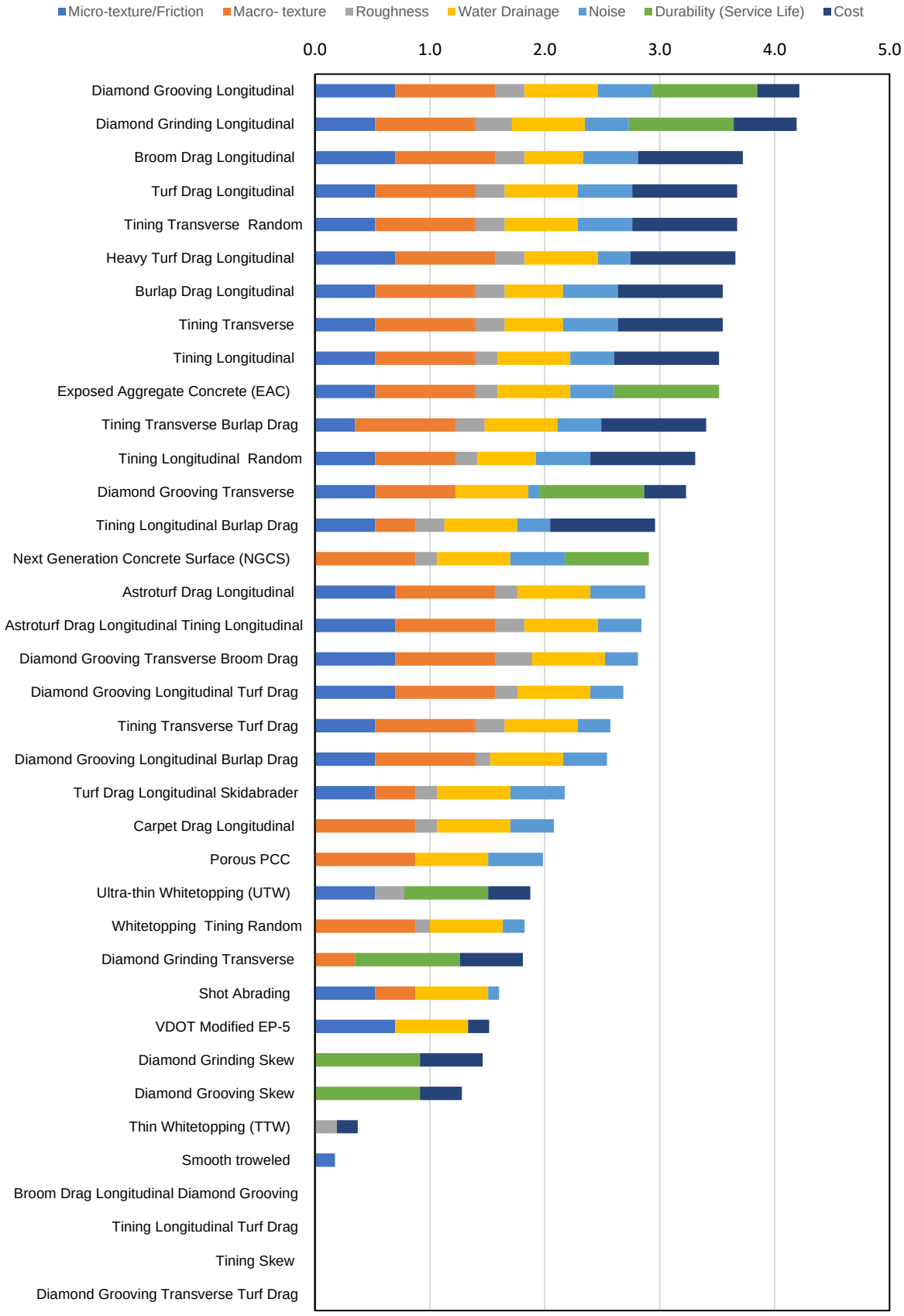

Figure 5.5 Weighted sum of texturing methods for concrete pavement

6. Study of Mechanical Properties

6.1. Introduction

The main objective of this study is to investigate the functional performance of pavement made of ECC material. However, it is required to study and then to understand the characteristics of ECC firstly before doing any modification for the existing mixture design. This chapter explains the mechanical properties according to the modification of the mixture design of ECC and if there is any effect to the structural performance of the applied pavement.

The non-existence of the aggregates is resulting in low skid resistance for ECC, as there are less micro- and macro- textures. The development of ECC design is ideally based on the performance-driven design approach (PDDA), which offers a systematic engineering solution rather than trial-and-error empirical experiments [45]. However, in this study, the methodology needs to be modified, as the functional performance has to be also fulfilled by improving the microtexture and macrotexture. Thus, aggregates need to be included in the modified mixture design. Consequently, there will be an adjustment needed on the micromechanics model, microstructure tailoring, and processing.

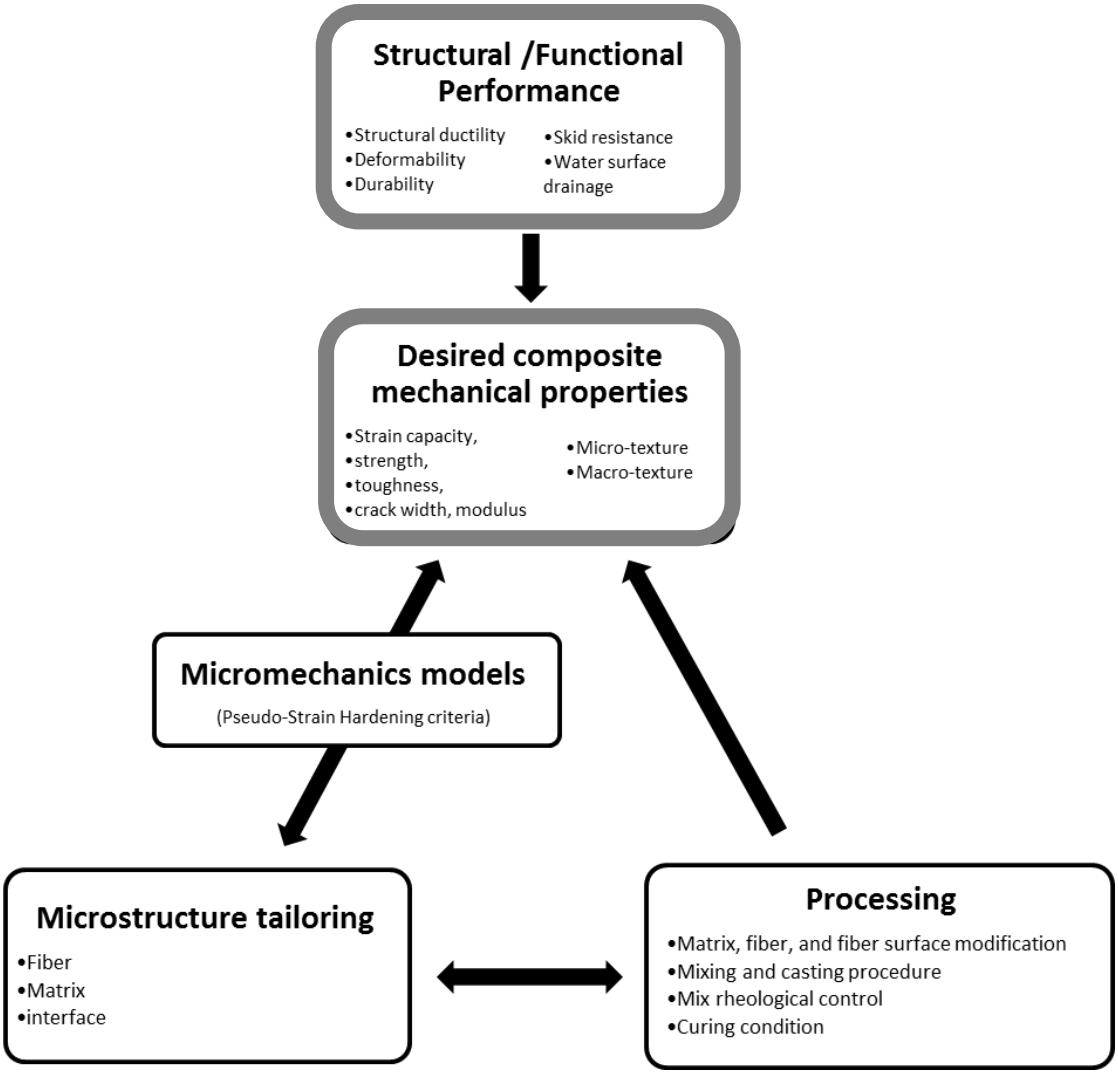

Figure 6.1 Modified PDDA to improve the functional performance of ECC material

6.2. Experimental program

6.2.1. Materials and mixture design

Two types of modified ECC have been developed in this study. The first one is the modified ECC mixed with corundum, namely ECC-Cor. And the second one is the modified ECC mixed with silica sand, named as ECC-SS. ECC-Cor is using Type I Portland cement, class F fly ash (FA), micro-silica sand (mean and maximum grain size of 110 μm and 200 μm, respectively), polyvinyl alcohol (PVA) fibers (length of 12 mm, diameter of 39 μm, nominal tensile strength of 1600 MPa), and a high-range water reducing (HRWR). To enhance skid resistance, corundum with a maximum particle size of 2.38 mm was used as fine aggregates for improving the surface textures of ECC. Table 6.1 summarizes the mixture design of ECC, incorporating a different amount of corundum (ECC-Cor). A control ECC mixture without the addition of corundum (ECC-Cor 0) was also prepared. All ECC-Cor mixtures have a low water-to-cementitious material ratio (w/cm) of 0.27. Micro-silica sand was replaced with corundum at different dosage, ranging from 50-100%, and the mixture was denoted as 'ECC-Cor #', indicating # with % of micro-silica sand was replaced with corundum.

Table 6.1 Mixture design of ECC-Cor (kg/m^3)

Mixture	Cement	Fly ash	Sand	Water	Super Plasticizer	PVA Fiber	Corundum
ECC-Cor 0	559	671	447	327	2.3	26	0
ECC-Cor 50	559	671	224	327	2.3	26	224
ECC-Cor 60	559	671	179	327	2.3	26	268
ECC-Cor 70	559	671	134	327	2.3	26	313
ECC-Cor 80	559	671	89	327	2.3	26	358
ECC-Cor 90	559	671	45	327	2.3	26	402
ECC-Cor 100	559	671	0	327	2.3	26	447

The second mixture is ECC-SS. Materials used include Type I white Portland cement, water, Polyester fibers (PE) 19 mm in length, oil coating: 1.2%, polycarboxylic-ether type high-range water reducing admixture plasticizer (ADVA 181), viscosity modifying admixtures (VMA) with type of Methyl Cellulose and aggregate silica sand with hardness is 7 Mohs' scale, density of 2.65 g.cm3, with maximum particle size of 2.38 mm as suitable aggregates. Table 6.2 summarizes the mixture design of ECC-SS.

Table 6.2 Mixture design of ECC-SS (kg/m^3)

Mixture	White Cement	Water	Super Plasticizer	PE Fiber (% by vol.)	VMA	Silica Sand
ECC-SS 00	1474	516	2.5	1.8	1.50	0
ECC-SS 01	1474	516	2.5	1.8	1.50	147
ECC-SS 02	1474	516	2.5	1.8	1.50	295
ECC-SS 03	1474	516	4.0	1.8	1.50	442

For full-scale, four 1000L-plus trial mixing were carried out. The mix proportion of the main raw materials, dimension of cast slab, slab surface treatment can be found in Table 6.3.

Table 6.3 Mixture of the additional four large-scale mixing trials

No	Mix	Mix proportions (kg/m^3 or g/L)						V (L)	Fiber dispersion and workability	Dimension of cast slabs
		OPC	FA	SS	Water	Fiber	Cor			
1	BC^	727	484	363	363	26	0	1244	Poor	dumped
	CBC^	755	482	115	348	15	303	150	Poor	
2	BC	488	780	432	291	28	0	1037	a bit bleeding	3.6m × 2.4m × 0.07m
	CBC	415	771	119	308	18	308	150	Good	
3	BC	504	756	454	291	26	0	1031	Good	Cast-in-site
	CBC	522	783	130	261	20	339	150	Good	
4	BC	620	676	468	279	26	0	1006	Good	3 of 0.9m × 1.2m × 0.07m
	CBC	415	771	119	250	18	334	150	Good	

6.2.2. Specimen preparation

Each of ECC-Cor and ECC-SS mixture was prepared in a planetary mixer. Cement, fly ash, and micro-silica sand are dried mixed first. Water was then added, followed by the addition of superplasticizer and mixed for 3-5 mins until the mix achieved the required consistency. Lastly, the PVA fiber and aggregates (corundum or silica sand) were added and mixed for another 3-5 mins. The fresh mixture was cast into a prism (280 mm x 70 mm x 50 mm) and plate (500 mm x 300 mm x 10 mm) moulds catered for various types of tests. Specimens were removed from the mould after 1 day and were cured at normal laboratory air (25±3^{o}C, 70%RH) for another 27 days before further testing. At the pre-determined age, either 1 d or 3 d, the top surface of plate specimens was treated with a steel brush to expose the aggregates (corundum or silica sand) on the surface.

6.2.3. Test program

The compressive test was carried out following ASTM C109/109M to determine the compressive strength of the cube specimens at the age of 28 days. The test was done under load with a loading rate of 25 kN/min. At least four specimens were tested for each mix. A uniaxial test was carried out to determine the tensile behaviour of ECC-TiO2 specimens. The coupon specimens were used. At least three specimens were tested for each mix. Tests were conducted with MTS machine loaded with 25 KN with a loading rate of 0.0025 mm/s. It is equipped with two external linear variable displacement transducers (LVDTs) to measure the displacement. Four-point bending tests were done in accordance with ASTM C78/78M were carried out on prism specimen to evaluate the flexural strength of specimens. The loading span (80 mm) is one-third of the support span (240 mm) and the rate of deflection at the loading points was controlled at 0.3 mm/min. At least three specimens were tested for each mix. Modulus of rupture (MOR) was calculated, and the ductility was estimated by means of a reverse calculation method.

The measurement of the real contact stresses gathered from the Tekscan I-Scan device. Various sets of loading and inflation pressure are applied to the apparatus. The vertical load is exerted on a single radial tire (Continental 315/80R22.5). Since only static loading is considered, only vertical contact stresses are acquired. Then, the measured data is analyzed and implemented into the verified 3D Finite Element (FE) model. Hence, the ANSYS is employed for numerical analysis. All contact stresses data is successfully imported into ANSYS [159]. Tire imprint in the FE model is totally identical to that from the measuring device. The same model used to study the effects of groove to the structural performance for pavement made of ECC.

The Wheel Tracking Slope (WTS) test was carried out to evaluate the long-term durability of the surface skid resistance. The test was done by following guidelines stated on TRL Report 176 [29]. The wheel tracking machine consists of a rubber wheel, which rotates at 42 cycles per minute while applying a load of approximately 520 N. The load traffic simulations run up to 100,000 wheel-passes, which is equivalent to about 3.7 million equivalent single axle loads (ESALS) according to Nichols (1997). During the traffic simulation, the tests were stopped in between to measure BPN and MTD by means of BPT and SPM, respectively. Two mixture formula, i.e., ECC-Cor 50 and ECC-Cor 100, were tested.

6.3. Results and discussion

This chapter gives the understanding of the characteristics of the modified ECC mixed with aggregates. Ideally, both structural and functional performance have to fulfil the requirements. Modification on the PDDA approach is needed as the original approach is not considering the functional performance in the desired mechanical properties, which are skid resistance and surface water drainage. Through some tests, it is proven that some modification on the processing and microstructure tailoring process allows the achievement of the desired mechanical properties. The modification includes the properties of aggregates, fibers, other materials, and the processing way. In summary, the inclusion of aggregates, which is needed to improve the micro- and macrotexture of ECC, does not negatively affect the mechanical behavior of ECC. Similar findings were also reported [160,161].

6.3.1. Effects of aggregates on the mechanical behavior

This study investigates the effects of aggregates on the mechanical behavior of the modified ECC. Table 6.4 summarizes the mechanical properties of the seven ECC-Cor mixes. First cracking strength and flexural strength were obtained directly from the four-point bending test results, while tensile strain capacity was inversely calculated from the load-deflection curve in accordance with ASTM C78/C78M [162]. The first cracking strength of ECC increases while the tensile strain capacity decreases when corundum is incorporated into the mix. This is attributed to the introduction of corundum with a high hardness which increases the matrix toughness and thus reduces the strain hardening and multiple cracking potentials [163]. Nevertheless, all ECC-Cor mixes still possess an adequate tensile strain capacity of around 1%, which is fulfilled the performance requirement for pavement application. Furthermore, the introduction of corundum does not seem to a have negative impact on the flexural strength of ECC-Cor as all mixes maintain high flexural strength between 10-12 MPa.

The workability was qualitatively measured, and it can be concluded that the workability of ECC is improved when corundum aggregate is added. This is because the existence of corundum creates more surface area, resulting less demand for water to wet the surface. Thus, the addition of the aggregates gives higher workability for similar water content. However, there are limits on aggregate particles size as it is affecting fiber dispersion, workability, and matrix toughness which may negatively affect the mechanical performance characteristics of ECC [160].

Table 6.5 summarizes the mechanical properties of the four ECC-SS mixes. The addition of fine size aggregate of silica sand does not significantly affect the mechanical properties of the modified ECC. All parameters compressive strength, flexural stress, and tensile strain capacity still in the performance range of conventional ECC (Li 2007), which are 20 to 95 MPa for compressive strength, 10 to 30 MPa for flexural strength, and 1 to 8% of tensile strain capacity.

Table 6.4 Mechanical properties of ECC-Cor

Specimen	First cracking strength (MPa)	Flexural strength (MPa)	Tensile strain capacity (%)
ECC-Cor 0	3.4 ± 0.4	11.1 ± 0.6	2.1 ± 1.0
ECC-Cor 50	6.0 ± 0.1	11.2 ± 1.1	0.8 ± 0.1
ECC-Cor 60	6.2 ± 0.2	12.1 ± 1.0	1.1 ± 0.2
ECC-Cor 70	6.0 ± 0.4	10.1 ± 1.2	1.1 ± 0.3
ECC-Cor 80	5.9 ± 0.2	11.3 ± 2.2	1.0 ± 0.3
ECC-Cor 90	5.6 ± 2.9	10.9 ± 1.7	1.0 ± 0.4
ECC-Cor 100	5.4 ± 1.2	10.7 ± 1.4	0.8 ± 0.1

Table 6.5 Mechanical properties of ECC-SS

Specimen	Compressive strength (MPa)	Flexural strength (MPa)	Tensile strain capacity (%)
ECC-SS 00	38.06 ± 0.06	9.13 ± 0.56	3.71 ± 1.50
ECC-SS 01	38.56 ± 1.00	9.01 ± 0.24	2.80 ± 0.52
ECC-SS 02	49.02 ± 1.74	10.20 ± 1.46	2.35 ± 0.10
ECC-SS 03	49.10 ± 2.86	4.21 ± 0.01	1.40 ± 0.34

In summary, the inclusion of aggregates into ECC mixture does not negatively influence the mechanical behavior in a significant way. The increase of the volume fraction of the aggregates slightly decrease the flexural strength and tensile performance. On the contrary, the increase of the volume fraction of aggregates increases the compressive strength.

6.3.2. Effects of aggregates on the first crack strength

Aggregates are affecting the first crack strength of the modified ECC. As can be seen in Table 6.4, the first crack strength of modified ECC mixed with aggregates is generally higher than normal ECC. This is due to more energy is needed to initiate the crack when aggregates are embedded inside the mixture. Illustration is given in Figure 6.2.

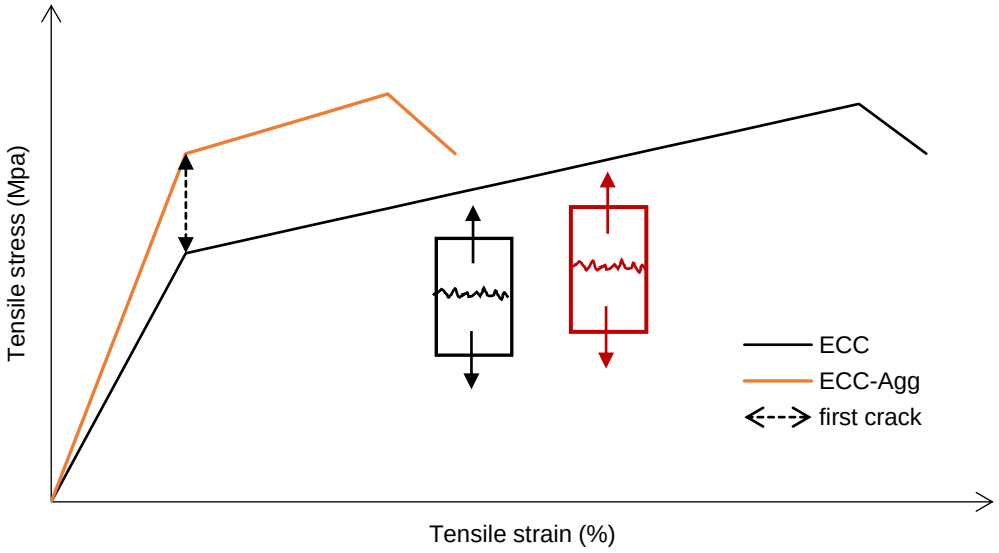

Figure 6.2 Effects of aggregates on the first crack strength

6.3.3. Effects of fibers to the mechanical behavior

ECC with PVA fiber produces good tensile behavior. PVA fiber results in a high interfacial chemical bond, frictional stress, and slip-hardening in a cementitious matrix. The test conducted shows robust pseudo-strain-hardening behavior with the ultimate strain exceeding 2%. It was achieved at a moderate fiber volume fraction of 2%.

Surface coating by oil on fiber is affecting the strain hardening behavior. As the oiling content increases, both frictional stress and interface fracture energy will decrease significantly. As results, the complementary energy of the fiber bridging stress increases with oil content given [50]. Test results have shown that ECC with PVA gives good results in compressive and flexural strengths, which is in line with previous research [52].

6.3.4. Effects of grooves to the structural performance of the slab

The effects of grooves to the structural performance of the slab needs to be study as the PUTW proposed has thickness design of only 70 mm. It is significantly different than conventional concrete slab, where commonly, concrete slab has thickness design for at least 250 to 300 mm.

Measurement of the contact pressures were done with the pressure mapping system device, called Tekscan I-Scan. It has sensor type of 7101 comprised of sensing elements arranged In 88 rows and 96 columns. The methodology was done base on similar study done by Bawono et al [159]. The data collected was then processed using numerical computing language tool. The magnitude of the contact stresses and their positions are located precisely based on the coordinate system. Different combinations of tire loading (10 to 50 kN) and tire inflation (600 to 900 KPa) were used.

Results from the Tekscan I-Scan shown that there is no significant impact by introducing grooves to the thin slab. The stresses produced are causing neither cracks nor failure for the slab. The results are shown in Figure 6.3.

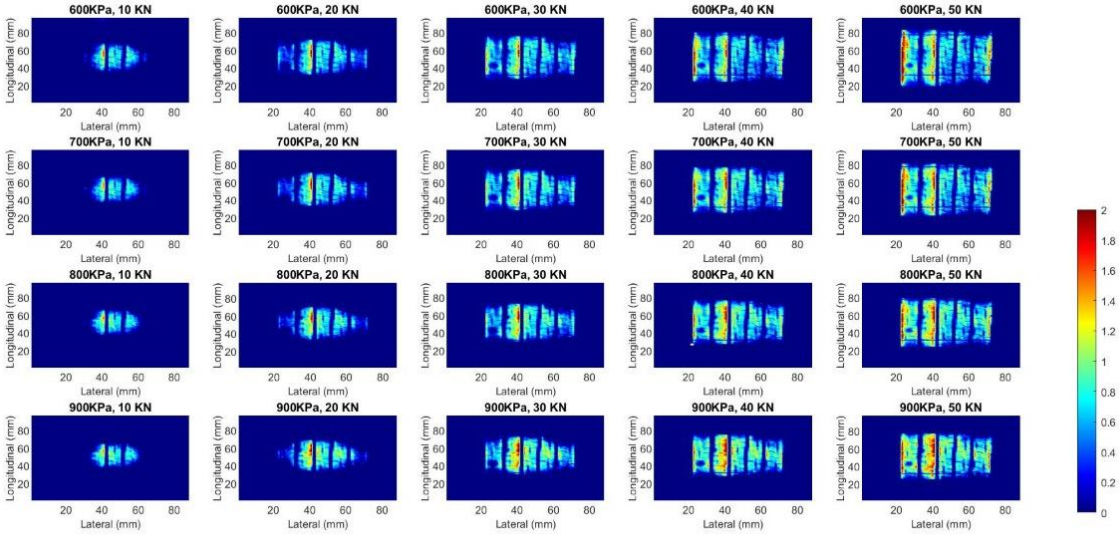

Figure 6.3 Tekscan results for stresses on grooved ECC slab

6.3.5. Large scale mix

Results from larger-scale mix have shown that there is no significant difference compare to laboratory scale. However, the temperature is one of the main factors that should be considered as a higher temperature leads to a faster curing process, which affects the casting and finishing process. Several important know-hows were learned from the additional four times of large-scale mixing: the quality of the fly ash is indeed very important for desirable fiber dispersion and workability; additional water (about 1-3 % of the binder, i.e. cement plus fly ash) is needed under a relatively dry weather; relatively good fiber dispersion may be maintained even with slightly over-dosage of the fibers. The mechanical properties of the mix were characterized by compression, tensile, and flexural test, after air curing of 28 days. The results were summarized in Table 6.6. The tensile stress-strain curve of the large-scale mixing specimen was compared with that of the lab-made specimens. The mechanical properties are comparable to the lab version and higher, leading to the conclusion that the technology of large-scaling mixing is mature and ready for field application.

Table 6.6 Mechanical properties of ECC-Cor from large-scale mixing

Specimen	Compressive strength (MPa)	Flexural strength (MPa)	Tensile strain capacity (%)
ECC-Cor	57.9 ± 5.1	9.9 ± 0.70	2.80 ± 1.90

6.3.6. Durability of surface texture

Figure 6.4 shows the BPN and MTD of ECC-Cor 50 and 100 after different load cycles. As can be seen, the trend shows BPN reduces while MTD remains unchanged with increasing load cycles. Even after 100,000 load cycles, the BPN is still above 65 BPN, and the MTD maintains at 0.34 mm. It can be concluded the surface texture and skid resistance made of ECC-Cor can last until the end of the pavement lifetime without any further intervention. This is mainly due to the hardness of corundum which makes the surface texture of ECC-Cor durable.

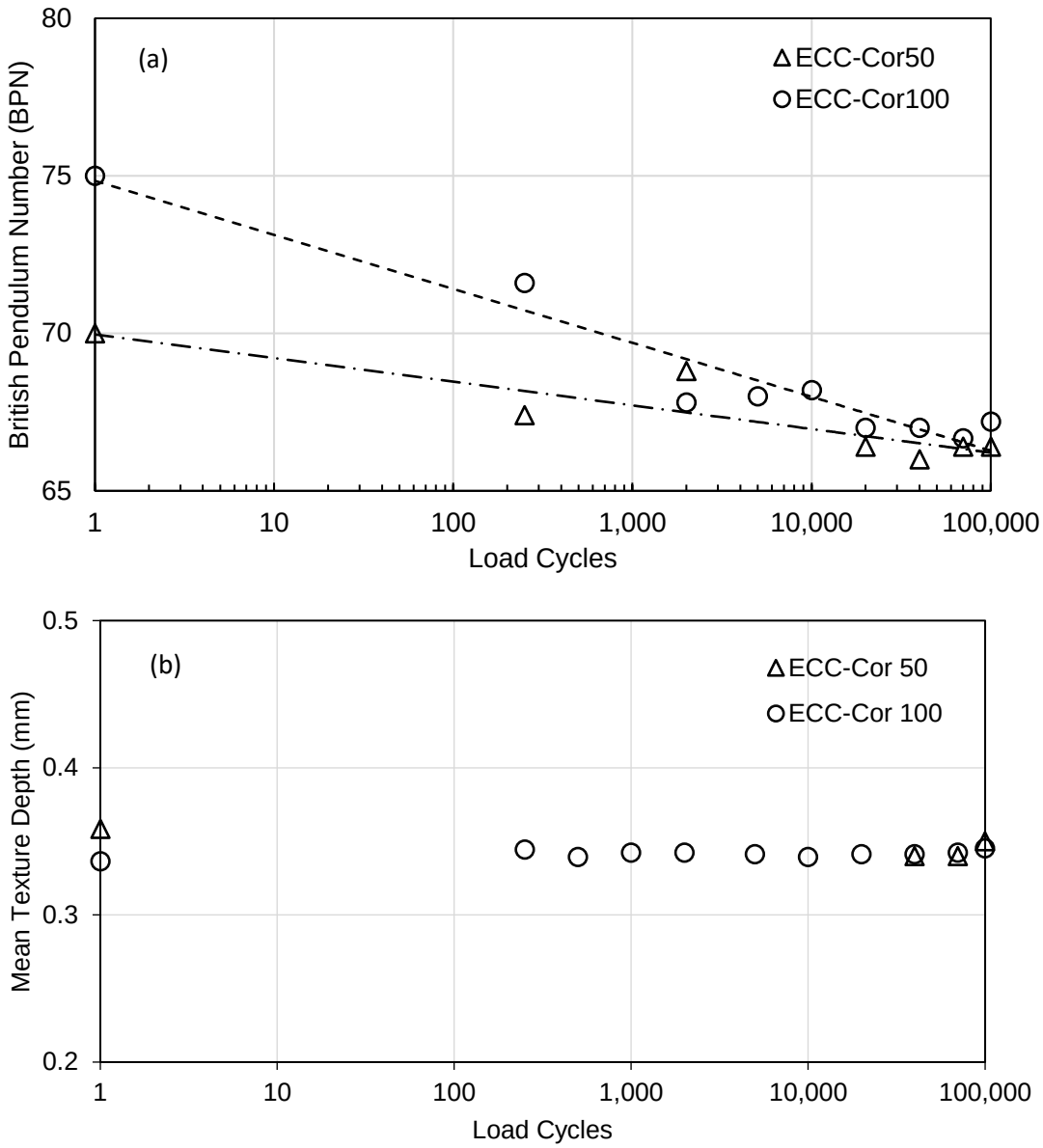

Figure 6.4 (a) BPN and (b) MTD of ECC-Cor 50 and 100 as a function of load cycles

7. Study of Skid Resistance: Laboratory Test

7.1. Introduction

This chapter presents the experimental research of the skid resistance for ECC material used for pavement. Data have been collected from various laboratory tests. The skid resistance tests include British Pendulum Test (BPT) for microtexture and Sand Patch Method Test (SPM) for macrotexture. Different surface treatment methods were evaluated to find the optimum solution to produce good surface properties. Laboratory results show that the skid resistance of the surface pavement can be improved by adopting hard fine aggregates into ECC mix, as it provides both the micro- and macrotextures. It is also shown that methods on laboratory scale tests can be further applied to full-scale application with results of a surface with good skid resistance.

7.2. Laboratory test program

The laboratory test is mainly designed to investigate whether ECC can be modified to improve the skid resistance for pavement application. The first part, which was to maintain the mechanical behavior was discussed in the previous chapter. Thus, this part mainly discusses the test and results related to skid resistance.

A normal ECC with neither aggregates nor surface treatment was investigated. As ECC does not use any aggregates, it is expected to have low results in terms of skid resistance. Therefore, the results will be used as a reference. Two primary types of mixture designs were designed and tested in this study. ECC mixed with corundum aggregate (ECC-Cor) and ECC mixed with silica sand (ECC-SS). The first mixture, ECC-Cor, was designed to achieve high skid resistance. Therefore, corundum, which has high hardness and abrasiveness, is used in the mixture. The second mixture design, ECC-SS, has a slightly different objective, as to find mixture design with not only offers good skid resistance but also brighter surface layer for less impact to Urban Heat Island (UHI) and better visualization. Thus, silica sand, which has a high hardness (slightly below corundum) and bright color, is used. Different surfacing methods were investigated: brushing the surface layer of ECC specimens, using exposed aggregates on ECC surface, and introducing grooves to the ECC specimens.

Microscopic skid resistance was evaluated by means of BPT followed ASTM E303-93. BPT is a dynamic pendulum impact-type test used to measure the energy loss when the rubber slider slides over the pavement surface. The test results are reported as British Pendulum Number (BPN). At least three specimens were evaluated for each mix, and a minimum of five tests was performed for each specimen. The tests were conducted in wet test conditions by spraying water on the specimens. BPT was also used to demonstrate the effects of macrotexture provided by the grooves. Previous studies mentioned that BPT is reliable for defining both microtexture and macrotexture [98,164,165]. However, the macroscopic skid resistance was mainly evaluated by means of SPM, a volumetric-based spot test method with sand patch. The method which is based on ASTM E965-96 can be used to determine the (average) Mean Texture Depth (MTD) of pavement which reflects the macrotexture characteristic of the surface.

As can be seen from Table 7.1, various methods of surface treatments have been studied in this study. To study the effects of surface macrotexture, grooves were manufactured with different experimental methods, including prefabricated and using grooves cutter. From the table, it is summarized whether one method is applicable for precast, cast in place, or both.

Table 7.1 Investigation on skid resistance for surface treatments on laboratory

No	Objective improvement	Method	Precast	Cast in place
1	Microtexture	Brushed ECC mixed with aggregates	Y	Y
2	Microtexture	Exposed aggregates on ECC surface	Y	Y
3	Macrotexture	Grooved ECC mixed with aggregates (precast with acrylic plate)	Y	
4a	Macrotexture	Grooved ECC mixed with aggregates (precast with Styrofoam)	Y	
4b	Macrotexture	Grooved ECC mixed with aggregates (precast with Styrofoam with larger gap)	Y	
5	Macrotexture and microtexture	Grooved ECC mixed with aggregates (precast with silicone rubber)	Y	
6	Macrotexture and microtexture	Grooved ECC mixed with aggregates (with concrete cutter machine)	Y	Y (requires heavy machinery)

7.2.1. ECC without any surface treatment

Typical ECC M45 mixture design is adopted. This ECC design has the characteristics of fly ash-cement (FA/C) ratio of 1.20 and water-cementitious (W/C) ratio of 0.27. The mixing procedure started with cementitious materials (cement and fly ash) being mixed with sand and corundum. The amount of cementitious materials, sand and corundum, were kept constant. Water was added after those materials were mixed. Later, the HRWRA was added to the mixture until the desired characteristics were achieved, which was decided visually, both the distribution of materials and the flow of the mixtures. Therefore, the HRWRA content was not kept in constant. As the last step, the fiber (PVA) added to the mixtures. The whole mixing process was done in 8-10 minutes. All the mixtures were prepared using a small size standard mortar mixer with maximum mixtures of seven liters. The mixture design of ECC M45, named as ECC-Cor 0 can be seen in Table 6.1.

(a) (b) (c)

Figure 7.1 Specimens of ECC M45

7.2.2. Method 1: Brushed ECC mixed with aggregates

The objective of this method is mainly to improve the microtexture of ECC by mixing ECC with aggregates together. This process can be applied for both “cast in situ” and “precast” method. Two aggregates are investigated: corundum and silica sand. ECC mixed with corundum is

named as ECC-Cor, while ECC mixed with silica sand is named as ECC-SS. The mixture designs for both can be seen in Table 6.1 and Table 6.2.

The ECC-Cor mixture was prepared in a planetary mixer. Cement, fly ash, and aggregates are mixed dry first. Water was then added, followed by the addition of superplasticizer and mixed for 3-5 mins until the mix achieved the required consistency. Lastly, the PVA fiber and aggregates were added and mixed for another 3-5 mins. Specimens were removed from the mold after 1 day and were cured at normal laboratory air (25±3^{o}C, 70%RH) for another 27 days before further testing. At the pre-determined age, either 1 d or 3 d, the top surface of plate specimens was treated with a steel brush to expose the aggregates on the surface. The second mixture, ECC-SS, is designed with a different objective. It offers good skid resistance with brighter surface layer for lesser impact to UHI and better visualization. Thus, fine aggregate, silica sand, which has a high hardness (slightly below corundum) and bright color, is used. The mixing process was done in a similar way to ECC-Cor.

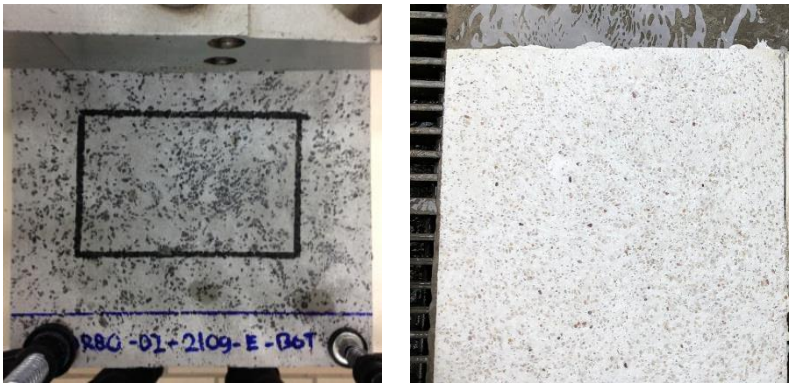

(a) (b)

Figure 7.2 Specimens of (a) ECC-Cor, (b) ECC-SS

7.2.3. Method 2: Exposed aggregates on ECC surface

The second method, exposed aggregates on ECC surface, is developed to maintain the original mechanical properties of ECC and to have good skid resistance by using fewer aggregates. Instead of mixing aggregates into the ECC mixture, the aggregate was first spread and distributed uniformly on the base of the plate molds, followed by casting normal ECC (M45) into the mold. Plate specimens were removed from the mold after 1 d, followed by curing at normal laboratory air (25±3^{o}C, 70%RH) for another 27 days before further testing.

(a) (b)

Figure 7.3 Specimens of exposed corundum aggregates on ECC surface

7.2.4. Method 3: Grooved ECC mixed with aggregates (precast with acrylic mold)

The third method is grooved ECC mixed with aggregates. The grooves made by using a precast by using a plate with space for the grooves. The plate is made of acrylic material with a thickness of 3.2 mm. The plate was made with two layers. The first layer is used as a base while the second layer made for designed grooves. Both layers are glued to each other using glue for acrylic. Advantages of using acrylic are the material is relatively easy to handle, easy to cut with the laser cutting machine, and is light. The plate is later to be placed inside the mold (see Figure 7.4) The ECC material is then to be poured afterwards.

However, the method was not successfully fabricating the grooves. The acrylic plate was stuck tightly on the grooves between the concrete. Due to this reason, the edges of each groove textures were broken when the acrylic demolded. Some acrylics were not able to be removed from the ECC samples. From the first experiment and its result, it can be concluded that acrylic should not be used to produce the grooves for ECC slabs as the material cannot be demolded easily. Therefore, BPT and SPM tests were not conducted on this method.

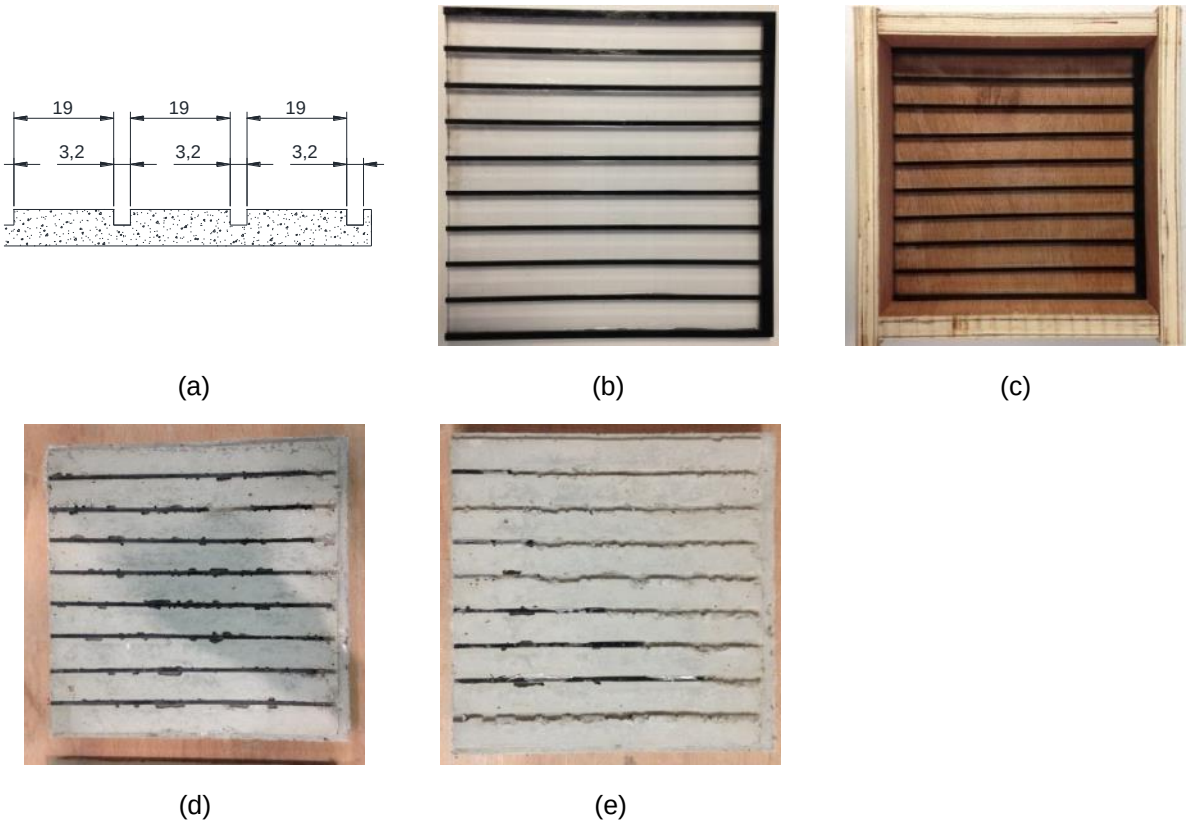

Figure 7.4 Method 3rd: prefabricated grooves with acrylic plate (a) dimension of the design of grooves (b) acrylic grooving plate (c) acrylic grooving plate fits into mold (d) acrylic was stuck on the grooves of the ECC sample (e) broken edges of ECC sample

7.2.5. Method 4: Grooved ECC mixed with aggregates (precast with Styrofoam mold)

The experimental test for the fourth method was done with the help of Styrofoam material used as a mat. The Styrofoam was cut according to the required design with the help of electronic hot wire foam cutting machine (see Figure 7.5). The Styrofoam mat is made of with a thickness of 3.2 mm. The mat consists of two bonded layers. The first layer used as a base, and the second layer made for designed grooves. Styrofoam material was chosen as an alternative due to its flexibility, so it should be easily demolded. The cut Styrofoam then glued to another Styrofoam material resulting in a mat with tailored grooves.

Two different designs were prepared so they can be used as a comparison. The first design was made to imitate the design of pavement with grind (small land area), which is illustrated in Figure 7.6. The second design, as shown in Figure 7.7, was prepared to imitate the design of grooved pavement (larger land area).

Figure 7.5 Electronic hot wire foam cutting machine

As results, not all ECC samples were cast successfully. In particular, the results from the first design, grinding texture (small land area) were not come up as expected. As the Styrofoam was too thin, it was moving all the time when the ECC was poured (please see Figure 7.6).

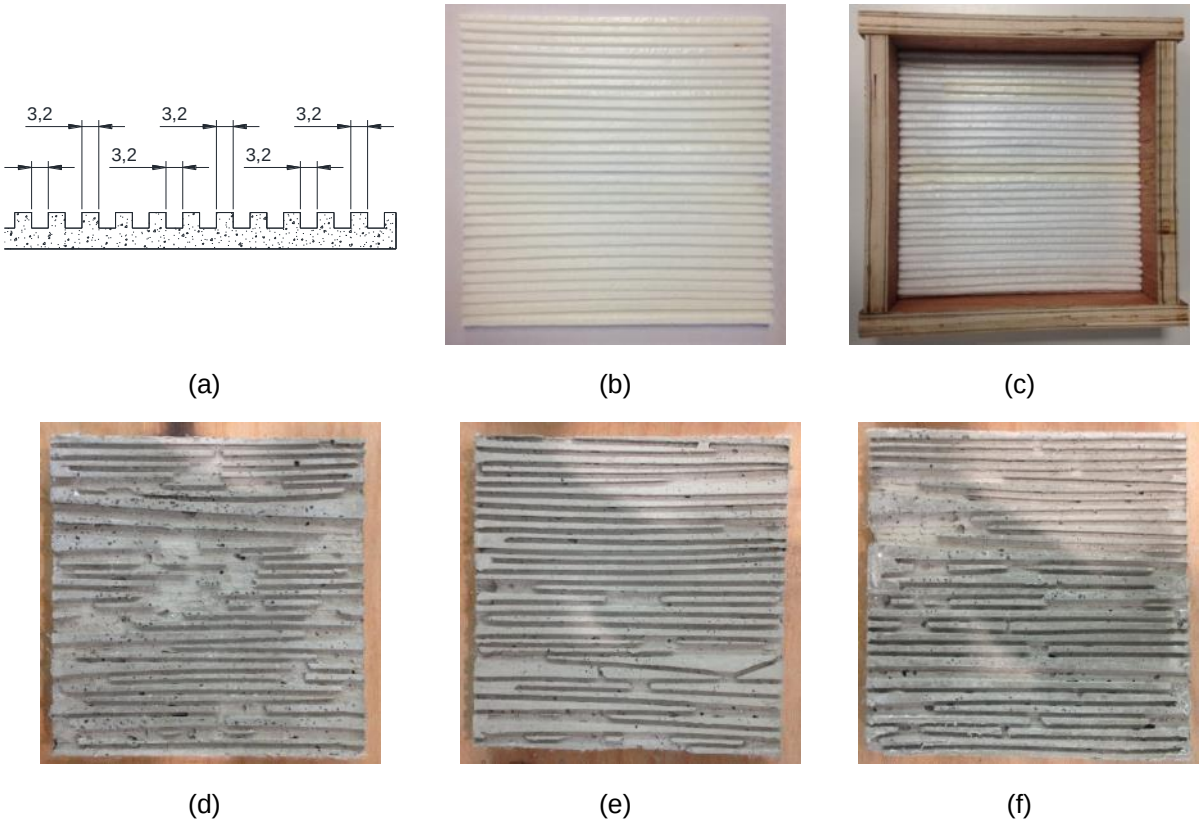

(a) (b) (c)

(d) (e) (f)

Figure 7.6 Method 4th (1st design): prefabricated grooves with Styrofoam (a) design of grooves (b) styrofoam plate (c) styroforam plate fits into the mould (d), (e), and (f) sample results

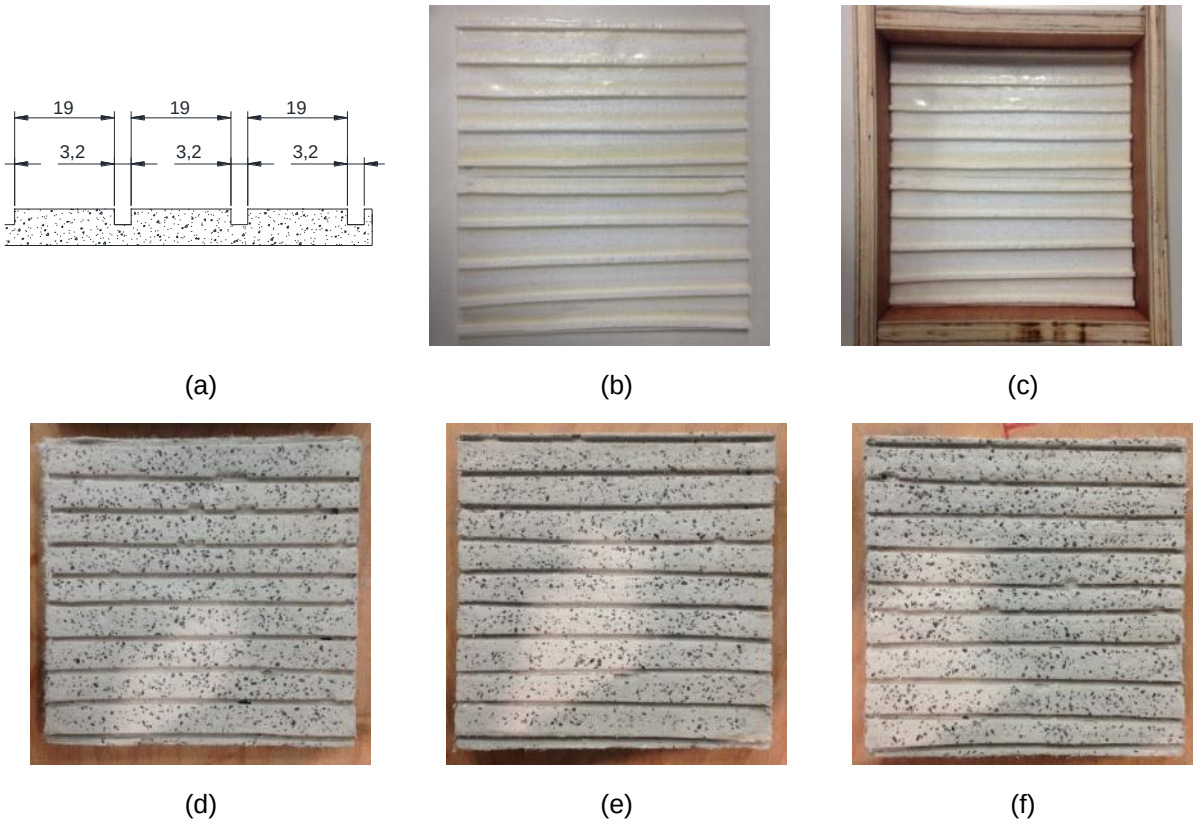

Figure 7.7 Method 4th (2nd design): prefabricated grooves with Styrofoam (a) design of grooves (b) styrofoam plate (c) styroforam plate fits into the mould (d), (e), and (f) results

The second design with the fourth method has better results than the first design (grinding texture). The bigger land area between grooves makes it more stable, as the Styrofoam were less moving when the ECC was poured. Later, the Styrofoam can be easily removed by using Acetone. However, the results are not precisely done as some dimensions of the land area, and the groove is different from the original plan.

In summary, using Styrofoam material as a mat to produce grooves has a limitation when it comes to a smaller land area as the ECC material has denser and heavier property it will easily move the Styrofoam itself. However, using Styrofoam for wider land area results in a better sample. Yet, the grooves made of Styrofoam mat were not perfectly straight. Thus, the test of BPT and SPM only conducted on the second design. Results are summarized in Table 7.3. The third method, with acrylics, shows no results as the specimens were not cast successfully. Thus, no tests were conducted. On the other hand, the fourth and fifth methods show promising results. Both Styrofoam and silicone rubber can be used to create precast grooves for ECC specimens. However, it should be noted that precast with silicone rubber offers more advantages as it is easy to be made, more stable compare to styrofoam, and it can be used repetitively. As results, BPN for longitudinal grooves is considered to remain the same, while BPN for transversal grooves increases. MTD for ECC with grooves is also increased about three times compared to the specimen without grooves.

7.2.6. Method 5: Grooved ECC mixed with aggregates (precast with silicone rubber)

The experiment with method number 5 was done by preparing a silicone rubber mat. The first step is to prepare the wooden mold plate, which was cut with a laser cutting machine to produce precise holes as a negative mold for the silicone rubber. The thickness of the wooden plate should be chosen similar to the designed thickness of grooves, which is 3.2 mm at this case. After wooden plate is ready, silicone flowable liquid and curing agent (with a mix ratio of 100:2) is then mixed and prepared. The mixed silicone liquid then to be cast into mold with a

wooden plate inside. The mixed silicone liquid will be hardened after 3-4 hours at room temperature. The hardened silicone rubber is then placed into another mold, and it is ready to be used to cast the ECC.

(a) (b) (c)

Figure 7.8 Method 5th prefabricated grooves with silicone rubber: (a) negative wooden mold plate grooves with Styrofoam (b) casting silicone rubber for the prefabricated mold (c) results of grooved ECC sample by using mold made of silicone rubber

7.2.7. Method 6: Grooved ECC mixed with aggregate (with concrete cutter machine)

The last method is grooved ECC mixed with aggregate with the grooves were successfully implemented by using a concrete cutter machine. Parallel grooves were created on the surface of ECC-Cor 80 specimens (500 mm x 300 mm x 10 mm) by means of a concrete cutter machine. The concrete cutter was equipped with a blade of 350 mm in diameter and 3.2 mm in thickness. The blade position is adjustable, so it can slide forward and backwards, while the level can be fixed to make a groove with the specified depth. Four macrotextures were evaluated, and the corresponding groove dimensions are summarized in Table 37.

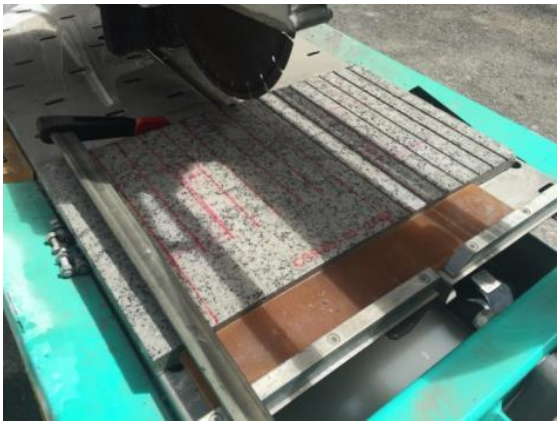

Figure 7.9 Method 6th: Grooving with concrete cutter machine

Table 7.2 Groove dimensions for grooved ECC-Cor

Type	Land Area (mm)	Groove (mm)	Height (mm)	Illustration
ECC-Cor 80-Gro 01	25.0 ± 0.5	3.2 ± 0.2	3.2 ± 0.3	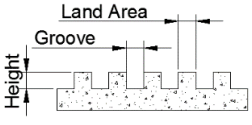
ECC-Cor 80-Gro 02	20.0 ± 0.5	3.2 ± 0.2	3.2 ± 0.3	
ECC-Cor 80-Gro 03	15.0 ± 0.5	3.2 ± 0.2	3.2 ± 0.3	
ECC-Cor 80-Gro 04	7.5 ± 0.5	3.2 ± 0.2	3.2 ± 0.3	

7.3. Results and discussions

7.3.1. Skid resistance performance of ECC and modified ECC

BPN of ECC M45 (ECC-Cor 0) and ECC-Cor # specimens with brushing and exposing aggregate methods are presented in Figure 7.10. As can be seen, without the addition of corundum, ECC-Cor 0 has a BPN of 53±9.1 which is lower than the required skid resistance of 55 for new roadways in accordance with the local standard set by the Land Transport Authority of Singapore. This suggests ECC-Cor 0 cannot be used for road application unless surface treatments are introduced.

ECC mixed with corundum (i.e., ECC-Cor 50 to 100) with surface exposure after three days shows some improvement in skid resistance as most of the results are above 55 BPN on average, except ECC-Cor 90. The moderate improvement may be attributed to delayed surface exposure process at day 3, where the matrix, a fiber-reinforced paste, was very hard to be removed and thus fewer corundum aggregates were exposed on the surface. It can be seen from the same figure, that there is no clear correlation between the amount of corundum aggregates and skid resistance of ECC-Cor. This again may be attributed to delayed surface exposure process at day 3, which is not able to expose the surface corundum evenly as evidenced by the large variation of the BPN results.

A significant improvement of skid resistance of ECC-Cor with exposing process one day after casting was observed (BPN above 65). From Figure 7.10, it can be observed that skid resistance (BPN) increases with an increasing amount of corundum used in the ECC-Cor mix. The ECC-Cor 100 possesses a BPN of 75, about 40% improvement compared to ECC-Cor 0. This is because the surface exposure process was carried out at day 1, and the paste can be removed easily and evenly as evidenced by the reduced variation of the BPN results.

High skid resistance is also observed for the ECC-Cor specimens with the exposed method (BPN around 75, comparable to the ECC-Cor 100). Even with much less corundum was included in the ECC-Cor 0-S specimen (150 kg/m^3) as compared to other ECC-Cor mixes (e.g., 225 and 450 kg/m^3 for ECC-Cor 50 and 100 mixes, respectively). Since skid resistance is a surface property, ECC-Cor 0-S represents a potential approach to strategically use corundum to improve the surface property while keeping the superior mechanical performance of the original ECC. Ultimately, this approach may be applied to both cast-in-situ and precast construction. BPN and MTD results can be seen in Figure 7.10 and Figure 7.11, respectively.

As shown in Figure 7.11, the MTD of ECC-Cor 0 is very low with the surface texture of only 0.09±0.005 mm. Replacement of 50% corundum (ECC-Cor 50) remarkably increases the MTD to 0.36±0.02 mm. Further increment of corundum dosage does not lead to continuous enhancement of MTD. On average, the MTD of ECC-Cor # is about 0.35±0.05 mm, which is three times that of ECC-Cor 0.

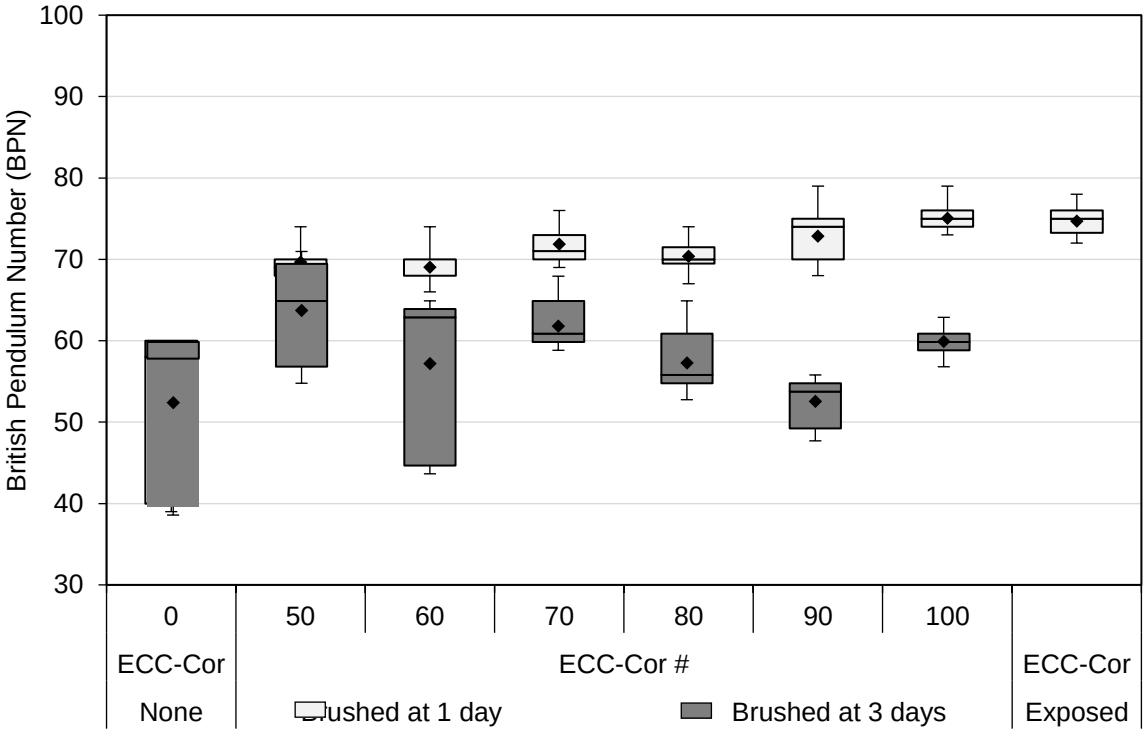

Figure 7.10 BPN of ECC-Cor

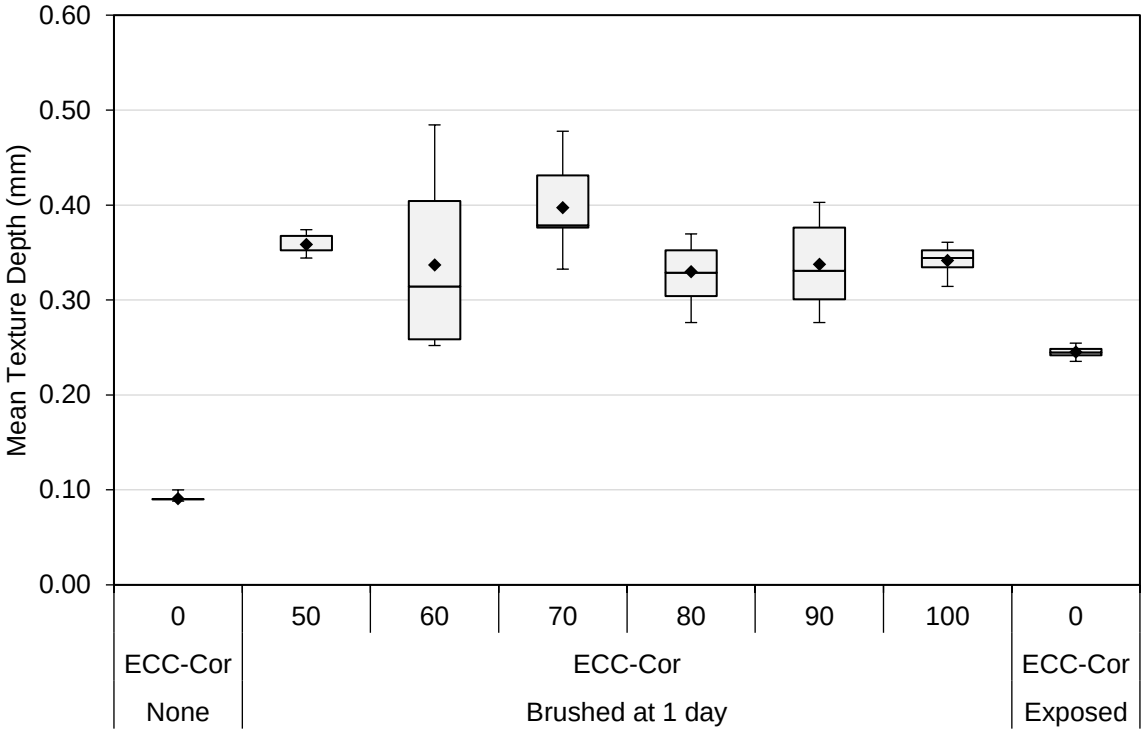

Figure 7.11 MTD of ECC-Cor

BPN of ECC-SS specimens with brushing method is presented in Figure 7.12. As can be seen, without the addition of fine aggregate silica sand, ECC-SS 00 has a BPN of 54±6.6 lower than the required skid resistance of 55 for new roadways in Singapore. This suggests ECC-SS 0 cannot be used for road application unless surface treatments are introduced.

A significant improvement of skid resistance of ECC-SS with exposing process one day after casting was observed (BPN above 65). The ECC-SS 01 possesses a BPN of 66, and ECC-SS 02 possesses a BPN of 79, about 20% and 45% improvement, respectively, compared to ECC-SS 00. However, more silica sand (ECC-SS 03) does not significantly improves the results, compared to ECC-SS 02 anymore. As shown in Figure 7.13, the MTD of ECC-SS 00 is very low with the surface texture of only 0.09±0.002 mm. Additional 10% of fine aggregate silica sand (ECC-SS 10) remarkably increases the MTD to 0.22±0.04 mm. While with 20% of fine aggregate silica sand will lead the MTD to 0.37±0.04 mm Further increment of fine aggregate silica sand dosage does not lead to continuous enhancement of MTD.

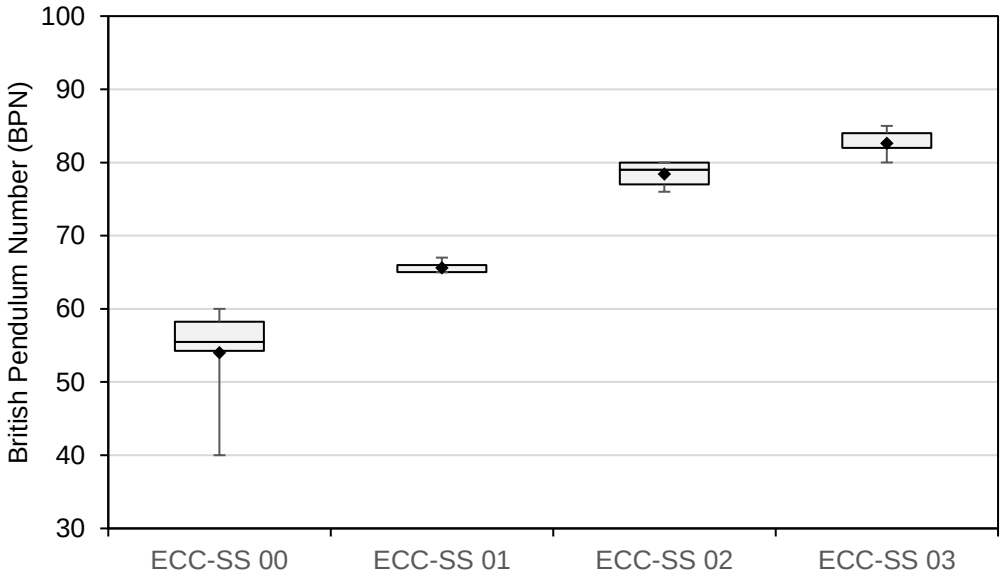

Figure 7.12 BPN of ECC-SS

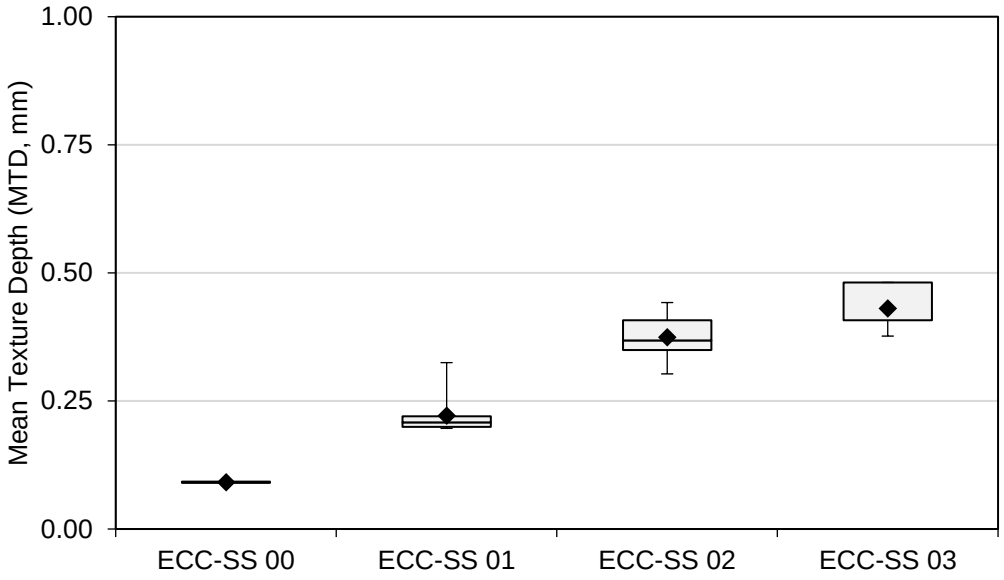

Figure 7.13 MTD of ECC-SS

During the laboratory tests, it was found that the fines are affecting the skid resistance. When the fines are covering the surface of the non-exposed specimens, the results of BPT on the wet condition are sometimes higher than the dry condition. But when the fines are washed away during the test on the wet condition, the results are decreasing.

In summary, the brushed ECC mixed with aggregates method comes with its advantages and disadvantages including:

- It can fulfil the requirements of skid resistance, which means it enhances the safety factor of surface pavement being used by the motorist. Both mixture designs of ECC-Cor and ECC-SS can achieve high BPN (more than 55 BPN).
- It gives good skid resistance only when the brushing/exposing process done by 1 day. As longer than 1 day leads to hardened condition causes difficulties in removing fine material.
- It is trade-offs with mechanical behavior. As there is a certain volume of fine silica sand replaced by aggregates, the behavior of ECC is affected. Therefore, the amount of aggregates needs to be carefully designed.
- It is durable. The aggregates are well distributed in the matrix. Since the aggregates embedded inside the matrix of ECC, there will be another layer of aggregates once the aggregates on the surface is starting to wear off together with the mortar.
- It is a relatively easy procedure to cast ECC mixed with aggregates followed by a brushing process.
- It means additional cost for adding aggregates into the mixture of ECC. As 50% replacement of fine silica sand, that covered around 225 kilograms per cubic meter of corundum.

The advantages and disadvantages of the exposed aggregates method include:

- It offers a solution for high skid resistance without affecting the mechanical behavior of ECC. As it is a separate layer between the ECC the aggregates.
- It can fulfil the requirements of skid resistance, which means it enhances the safety factor of surface pavement being used by the motorist.
- It offers lower cost compared to the previous method (mixing aggregates with ECC). The aggregate needed for this method is much less (150 kg/m3) in comparison to the first (mixing aggregate with ECC) method, which requires at least 225 kg/m3 (ECC-Cor 50) to 450 kg/m3 (ECC-Cor 100).
- It could offer lesser texture durability in comparison to the mixing aggregate with ECC method ass the aggregates are only on the surface. Once the aggregates removed along with time/traffic, there will be no other aggregates that appear on the surface.

7.3.2. Skid resistance performance on grooved ECC

Table 7.3 summarizes the BPN and MTF of ECC-Cor specimens with grooves with different precast methods. The third method, with acrylics, shows no results as the specimens were not cast successfully. Thus, no tests were conducted. On the other hand, the fourth and fifth methods show promising results. Both Styrofoam and silicone rubber can be used to create precast grooves for ECC specimens. However, it should be noted that precast with silicone rubber offers more advantages as it is easy to be made, more stable compare to Styrofoam, and it can be used repetitively. As results, BPN for longitudinal grooves is considered to remain the same, while BPN for transversal grooves increases. MTD for ECC with grooves is also increased about three times compared to the specimen without grooves.

Table 7.3 Effect of grooves to microtexture and macrotexture with precast method

Specimen	Microtexture – longitudinal (BPN)	Microtexture – transversal (BPN)	Macrotexture, MTD (mm)
ECC-Cor 0	54.15±2.50		0.09±0.005
ECC-Cor 80	71.43±2.02		0.36±0.019
ECC-Cor 80-Gro (3rd method)	N/A	N/A	N/A
ECC-Cor 80-Gro (4th method)	67.93±2.79	87.67±4.78	1.03±0.130
ECC-Cor 80-Gro (5th method)	72.00±0.89	89.20±0.75	0.86±0.018

Table 7.3 summarizes the BPN and MTD of ECC-Cor 80 specimens with different surface grooving treatment (i.e., ECC-Cor 80-Gro 1 to 4) and compared with that of ECC-Cor 0 and ECC-Cor 80 as the control. As can also be seen from Figure 7.16, the average texture depth increased for the ECC mixed with corundum compared to the conventional ECC with MTD of 0.09 and 0.36, respectively. Macrotextures are much improved with additional grooves, ranging from 0.70 to 1.41 depending on the dimensions of the grooves. With a land area of 25.0 ± 0.5 mm, the MTD is 0.74 mm, which doubles the result for ECC-Cor. When the spacing (land area) of the grooves are shortened, the MTD of the macrotexture improved accordingly. For a land area of 20.0 ± 0.5, 15.0 ± 0.5, and 7.5 ± 0.5 mm, the results of MTD are 0.85, 1.08 and 1.33 respectively.

Table 7.4 Effect of grooves to microtexture and macrotexture

Specimen	Microtexture – longitudinal (BPN)	Microtexture – transversal (BPN)	Macrotexture, MTD (mm)
ECC-Cor 0	54.15±2.50		0.09±0.005
ECC-Cor 80	71.43±2.02		0.36±0.019
ECC-Cor 80-Gro 1	71.40±1.43	77.50±1.57	0.74±0.030
ECC-Cor 80-Gro 2	72.10±0.83	88.60±1.28	0.85±0.030
ECC-Cor 80-Gro 3	72.60±0.92	90.50±1.28	1.08±0.054
ECC-Cor 80-Gro 4	74.10±0.70	92.80±1.60	1.33±0.059

The BPN of the grooved ECC-Cor 80 tested in the transversal direction (i.e., the grooves are perpendicular to the BPT swing direction) is higher than that of the ECC-Cor 80. Furthermore, the BPN increases with reducing the land area. ECC-Cor 80-Gov 4 with a land area of 7.5 ± 0.5 mm shows the highest BPN of 92.80±1.60, which represents a 71% and 30% enhancement as compare to that of ECC-Cor 0 and ECC-Cor 80, respectively. This may be attributed to the increased macrotexture on the surface, which holds the movement of the rubber slider on the pendulum. The BPN of the grooved ECC-Cor 80 tested in the longitudinal direction (i.e., the grooves are parallel to the BPT swing direction); however, it remains similar to ECC-Cor 80.

The results of the SPM test are represented in Figure 7.16. The test results are described with a box plot statistical method. There are six types of results. The “ECC” represents the results for conventional ECC. “ECC-Cor” represents specimens of ECC mixed with corundum. “Gro” represents the results for grooved specimens of ECC mixed with corundum while the number after “Gro” indicates the groove dimensions which are specified in Table 7.2.

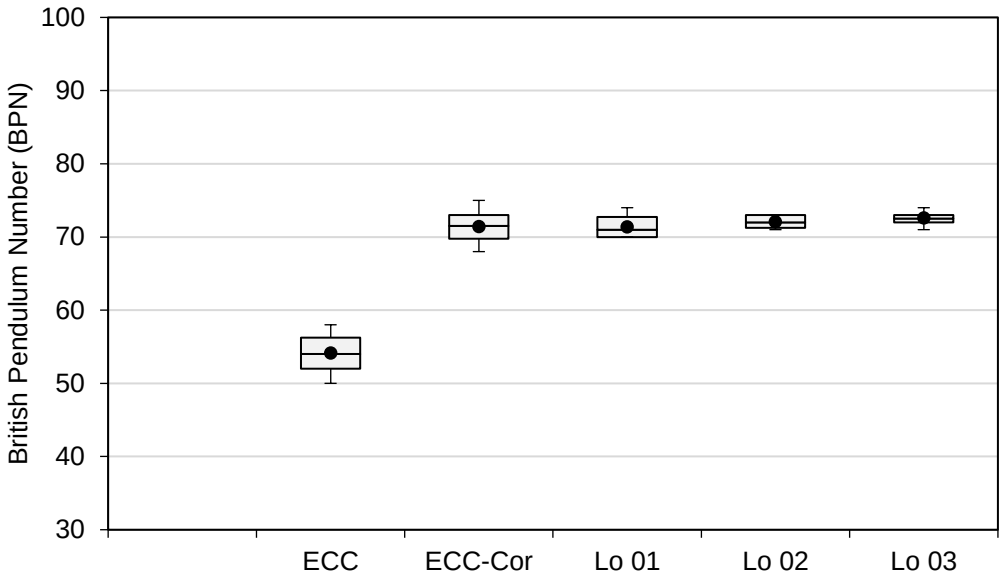

Figure 7.14 BPN of ECC, ECC-Cor, and longitudinally grooved ECC-Cor specimens

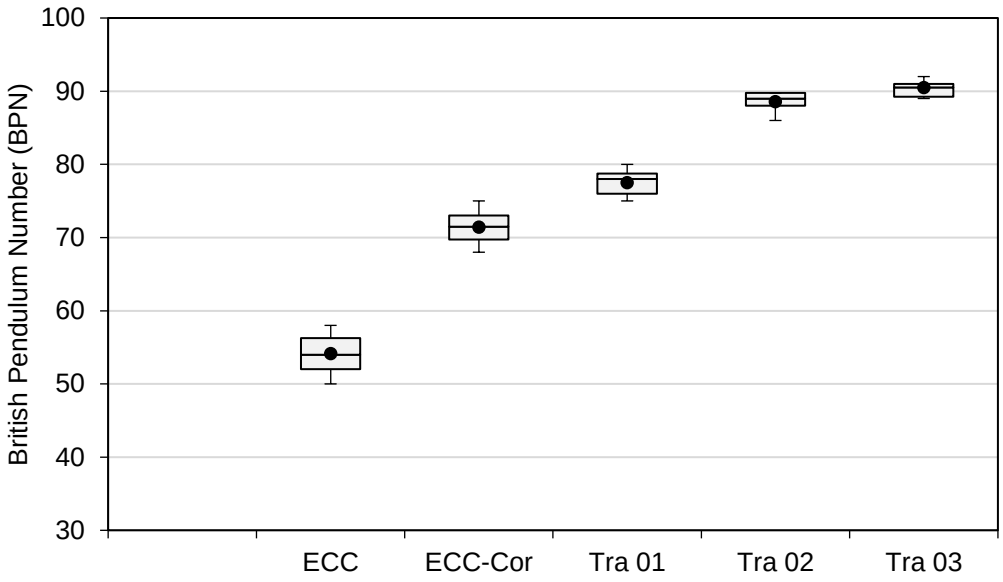

Figure 7.15 BPN of ECC, ECC-Cor, and transversally grooved ECC-Cor specimens

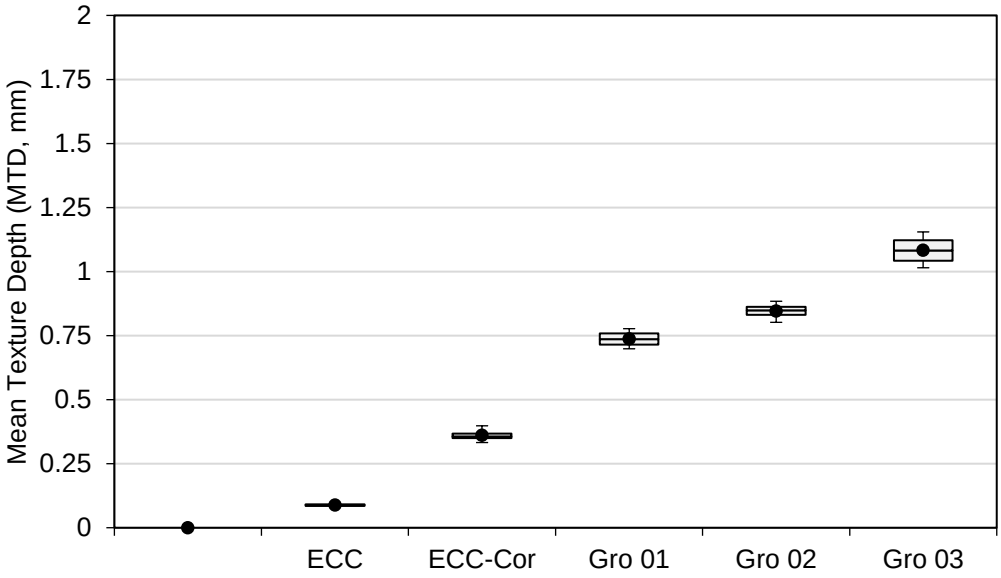

Figure 7.16 MTD of ECC, modified ECC-Cor, and modified ECC-Cor with grooves

In summary, the grooved ECC mixed with aggregates method comes with its advantages and disadvantages including:

- It can fulfil the requirements of skid resistance, which means it enhances the safety factor of surface pavement being used by the motorist. Both mixture designs of ECC-Cor and ECC-SS can achieve high BPN (more than 55 BPN).
- It is durable. The aggregates are well distributed in the matrix. Since the aggregates embedded inside the matrix of ECC, there will be another layer of aggregates once the aggregates on the surface is starting to wear off together with the mortar.
- It is a relatively easy procedure to cast ECC mixed with aggregates followed by the grooving process. The grooves can be made by both precast or groove in situ methods.
- It means additional cost for grooving pavement made of ECC.

8. Study of Skid Resistance: Field Investigation

8.1. Introduction

Chapter 8 presents the investigation on the full-scale application of modified ECC for pavement application. Data from various texturing methods applied in the field have been investigated and analyzed. The skid resistance tests include British Pendulum Test (BPT) for microtexture, and volumetric based Sand Patch Test (SPT) for macrotexture. Various tests were performed on the field to evaluate the surface properties of pavement made of ECC. Different texturing methods applied to find the optimum solution to produce good surface properties for pavement application.

In comparison to laboratory scale, there are more variables that need to be considered for full-scale application of modified ECC i.e. temperatures, mixing method, and finishing work. Test results show that the skid resistance of the surface pavement can be improved by adopting hard fine aggregates into ECC mix, as it provides both the micro- and macrotextures. It is also shown that texturing methods which was studied on laboratory scale tests can be further applied to full-scale application with consistent results.

8.2. Full-scale field investigation program

Microscopic skid resistance was evaluated by means of BPT followed ASTM E303-93, Standard Test Method for Measuring Surface Frictional Properties Using the British Pendulum Tester. BPT is a dynamic pendulum impact-type test used to measure the energy loss when the rubber slider slides over the pavement surface. The test results are reported as British Pendulum Number (BPN). BPT was also used to demonstrate the effects of macrotexture provided by the grooves. Previous studies mentioned that BPT is reliable for defining both microtexture and macrotexture [98,164]. However, the macroscopic skid resistance was mainly evaluated by SPT, which is based on ASTM E965-96 to determine the Mean Texture Depth (MTD).

A full-scale application can be completely different from the laboratory test. Many ideal conditions which can be found in the laboratory is simply not existing in the field. The type of mixer, duration of mixing, temperature, way of casting, way of demolding are just some examples of factor that can simply change the method which has been established in laboratory scale. Various methods of surface treatments investigation in full-scale are summarized in Table 8.1.

Table 8.1 Investigation on skid resistance for surface treatments on field application

No	Method	Precast	Cast in place
1	Brushed ECC mixed with aggregates (casting in place)		Y
2	Exposed aggregates on ECC surface	Y	Y
3	Precast modified ECC slabs (with wooden formwork)	Y	
4	Precast modified ECC slabs (with steel formwork)	Y	
5	Reverse precast modified ECC slabs	Y	

8.2.1. Method 1: Brushed ECC mixed with aggregates (casting in place)

The first trial was done to check the workability of ECC material on a bigger scale as the main objective. The method chosen is casting in place, as this method considered as the simplest one. Most of the area is done by normal ECC (M45), with only a quarter of the total area was treated with surface treatment by mixing aggregates, corundum together with ECC mixture.

Two mixtures have been designed and prepared. A 1000 liter of ECC was casting in situ on an area with a size of 6.0 meter of length times 2.5 meter of width. Another 80 liters of ECC mixed with corundum was also mixed and then cast as a surface treatment on the smaller part. Two different mixers used. The 1000 liters of ECC was mixed with the main mixer in the batching plant (Figure 8.1a). The ECC with corundum was mixed with a smaller mixer with 100 liter of capacity (Figure 8.1b). The application of the modified ECC-Cor was made in two ways: mixed together with other components of ECC (illustrated in the green box) and exposed corundum aggregates on fresh ECC (illustrated in the yellow box). The finished surface was then levelled manually with trowels. The brushing process for the aggregates was done in three different times. The first brushing process was done after four hours. The exposed aggregates method will be discussed in the next subchapter.

(a) (b)

Figure 8.1 Concrete mixer (a) plant drum with 3000 L capacity, (b) with 100 L capacity

(a) (b)

Figure 8.2 Finishing stage (a) surface levelling, (b) results with cast in situ

Similar results to laboratory investigation, the corundum on the ECC surface is still covered with fibers and fine materials when they are mixed for the first time. Therefore, the corundum needs to be exposed. The exposing process can be done by using a brushing machine with a hard-plastic brush pad. The brushing machine specification can be seen in Table 8.2. Illustration of the brushing machine and brushing plastic pad can be seen in Figure 8.3.

Table 8.2 Brushing machine specification

Voltage	Power	Speed	Weight	Disc diameter	Pad Material
220V/50Hz	2 HP	175 RPM	55 Kg	430 mm	Hard plastic

(a) (b)

Figure 8.3 (a) Brushing machine, and (b) brushing pad

8.2.2. Method 2: Exposed aggregates on ECC surface

The second method, exposed aggregates, which is done by spreading aggregates onto the ECC surface, was investigated. The main objective of this method is to produce a structural component made of ECC material which has a good skid resistance but not bothering to change the prevailing mechanical properties of ECC. In this method, normal mix design of ECC is used as a first layer (Figure 8.5a). Aggregates are then spread onto the ECC surface to enhance the skid resistance (Figure 8.5b). Less density of aggregates (kg/m^3) is used in this method compared to the previous method where aggregates mixed together with other ECC material. This method is applied to two applications: slab for pavement, and footpath. The difference between mixing aggregates with ECC and spreading aggregates onto the surface of ECC can be seen in Figure 8.4.

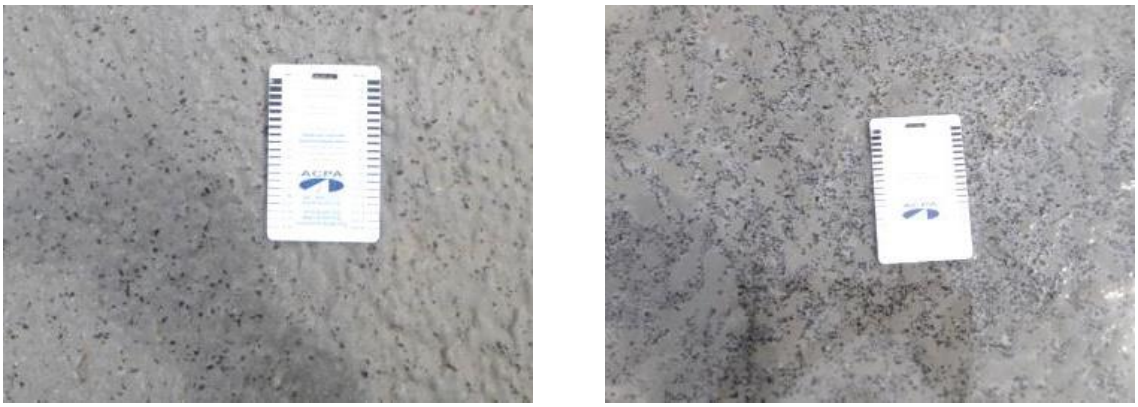

(a) (b)

Figure 8.4 Texture of (a) of ECC-Cor, and (b) exposed corundum on ECC surface

The first application, which is for the slab, was done with method cast in place. A 1000 liters of ECC was cast on an area with a size of 6.0 meter of length times 2.5 meter of width. The 1000 liters of ECC was mixed with the main mixer in the batching plant (Figure 8.1a). On top of ECC, corundum aggregates (100 kg/m^2) were spread.

This method was also applied to a footpath. In this application, corundum aggregates (150 kg/m^2) were distributed on the surface, and being exposed on 30 m length and 1.5 m width of the existing footpath was demolished and reconstructed with ECC and normal concrete with compressive strength of 45 MPa (used as a comparison). The concrete was treated with transverse tining. Reinforcement (M5) is used in some part of ECC and normal concrete as this is the standard applied by LTA. In ECC, the first 15 m is reinforced, and the second 15 m is not reinforced. Meanwhile, the full length of the normal concrete part is equipped with reinforcement. Detail design can be seen in Figure 8.6.

(a) (b)

(c) (d)

Figure 8.5 Spreading aggregates onto ECC for footpath application (a) casting normal ECC, (b) spreading aggregates onto ECC surface, (c) SPM test, and (d) BPT test

The application is followed with skid resistance tests: BPT and SPM for both ECC-Cor and concrete material, located at five random spots. As can be seen from Figure 8.18, both BPN and MTD for ECC-Cor with the spreading method is higher than conventional concrete due to corundum aggregates are well distributed on the surface.

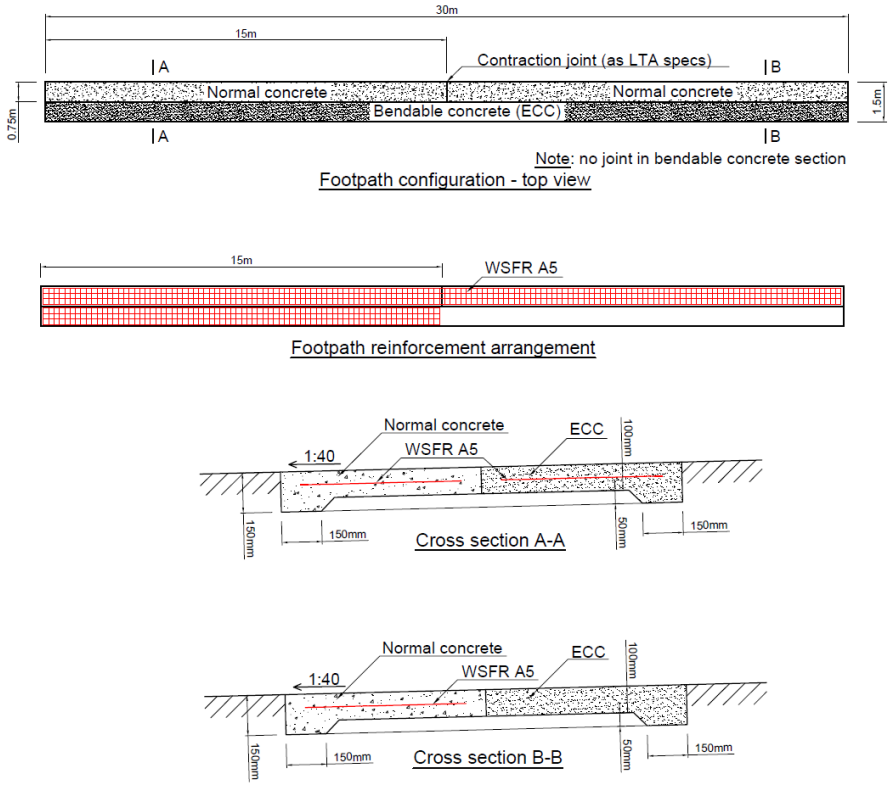

Figure 8.6 Method 2: spreading aggregates onto ECC surface for footpath application

8.2.3. Method 3: Precast modified ECC slab (first trial with wooden formwork)

The objective of method 3 is to investigate the workability, the mixture design, and the end results of the prefabricating method. Wooden formwork with the inner size of 3.6 m by 2.4 m has been prepared to fabricate the ECC slab (Figure 8.7a). Two mixtures were prepared: the first mixture (normal ECC) is designed as a structural layer, while the second layer is modified ECC-Cor designed as a surface layer. A 1000 liter of ECC was mixed in the batching plant and then cast into the wooden formwork. Another 80 liters of modified ECC-Cor was also mixed and then cast as a surface layer (Figure 8.7b). It is mixed with a smaller mixer with 100 liters of capacity. The second layer must be done immediately with no more than 30 minutes after the first layer when the material is not hardened yet to produce better chemical bonding between layers. The finished surface of the slab was then levelled manually with vibrator steel plate and trowels (see Figure 8.7 c). It is important to ensure that the surface to be flat. After one day, the surface layer of modified ECC-Cor was then brushed so the corundum will be exposed. The exposing process was also done by using brushing machine with a hard-plastic brush pad (see Figure 8.19 d).

Due to the difference of temperature between in the night (the trial) and the morning (by the time precast slab is prepared), there was a need to add a significant amount of plasticizer for the second batch. According to the weather.gov.sg, the minimum temperature at Tuas South area on 30th August was 25.1ºC, while the maximum temperature reached 31.3ºC.

(a)

(b)

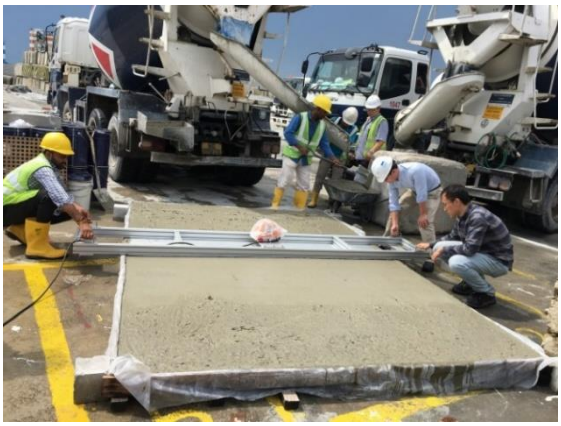

(c)

(d)

Figure 8.7 Precast modified ECC mixed with aggregates (a) Wooden mold 3.6 x 2.4 m^2, (b) pouring ECC into the wooden formwork, (c) leveling ECC-Cor surface, and (d) brushing process

8.2.4. Method 4: Precast modified ECC slabs with steel formwork

Method 4 is designed with the objective to improve the expecting results of previous method 3. Steel formwork is used to avoid the slab is becoming bent.

Two steel molds were designed and ordered for the manufacturing of the bendable concrete slabs (Figure 8.8a and Figure 8.8b). Dimensions of the steel molds are 3.4 m x 2.4 m x 0.075 m and 1.7 m x 2.4 m x 0.075 m, respectively. The molds were designed such that the sidewalls can be removed right after the material harden to prevent the formation of shrinkage cracks. Silicone mattresses with circular holes (Figure 8.8c) were also manufactured to be used in combination with the steel molds to create circular convex nodes on the bottom of the slabs, as shown in Figure 8.8d. This is to increase the bonding of the interface between the bendable concrete slab layer and the underneath asphalt layer.

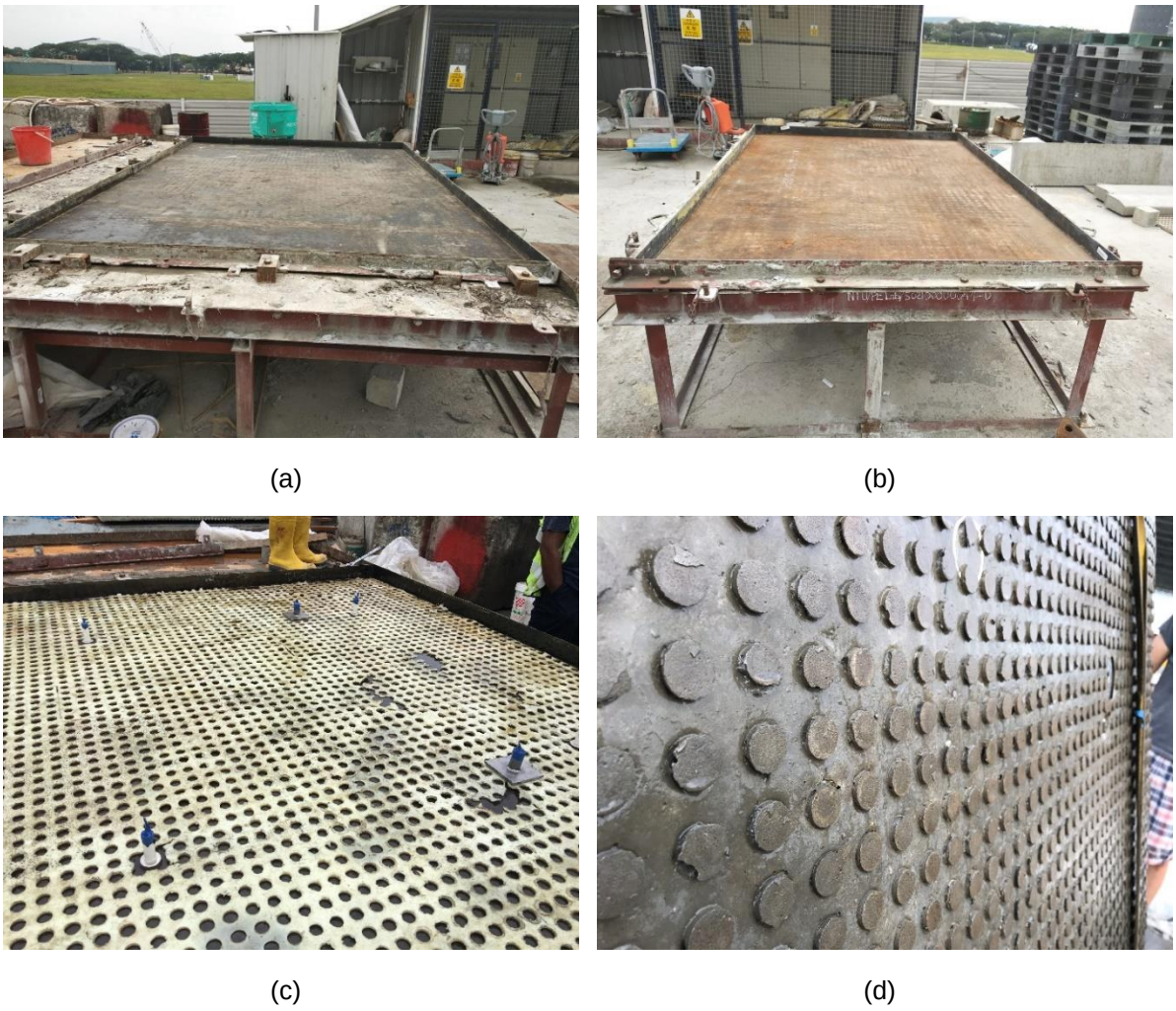

(a) (b)

(c) (d)

Figure 8.8 Precast method (a) steel mold used for large slab, (b) steel mold used for small slab, (c) silicone mattress with circular holes and (d) circular convex nodes on the bottom surface of slab.

Seven large-scale mixings were conducted. Brushing process of the slab was done with the brushing machine. But the time of brushing process was not always the same due to the effect of temperature. In the beginning, the brushing process was always done after one day, but then it found out for bigger scale, the curing process needs more time, so the slab is hardened enough to be dry. When the slab is cast during a rainy day, more days are needed for the slab to be in dry condition. The mixing procedures were identical to that of previous large-scale mixing trials as introduced previously. As it has been discovered during previous trials, the water amount required to reach desired workability may be affected by the weather of the day of casting. Table 8.3 summarizes the water to binder (w/b) ratio of each mix and the meteorological condition of each day of mixing. As can be seen, the w/b ratio varies from 0.236 to 0.302 under different weather. The identification slab number can be seen in Figure 8.9.

Table 8.3 Mix designs and weather conditions

Date	Temperature (ºC)	Rainfall on the previous day (mm)	Water/b ratio	Brushin g (after x day)	Identific ation No. of slab (Half size)	ID No. of slab (Full size)
March 6, 2018	26.0-31.7, very dry	0.0	0.302	1	6	Failed
March 8, 2018	25.7-30.5, dry	5.4	0.269	1	4	11
March 13, 2018	26.1-33.3, dry	1.0	0.274	3	3	Back up
March 20, 2018	26.5-32.6, rainy	0.0	0.236	5	Back up	10
March 22, 2018	27.0-34.5, very dry	0.2	0.283	3	5	7
March 27, 2018	24.0-26.8, rainy	57.2	0.260	5	2	9
April 3, 2018	27.0-34, very dry	0.0	0.283	2	1	8

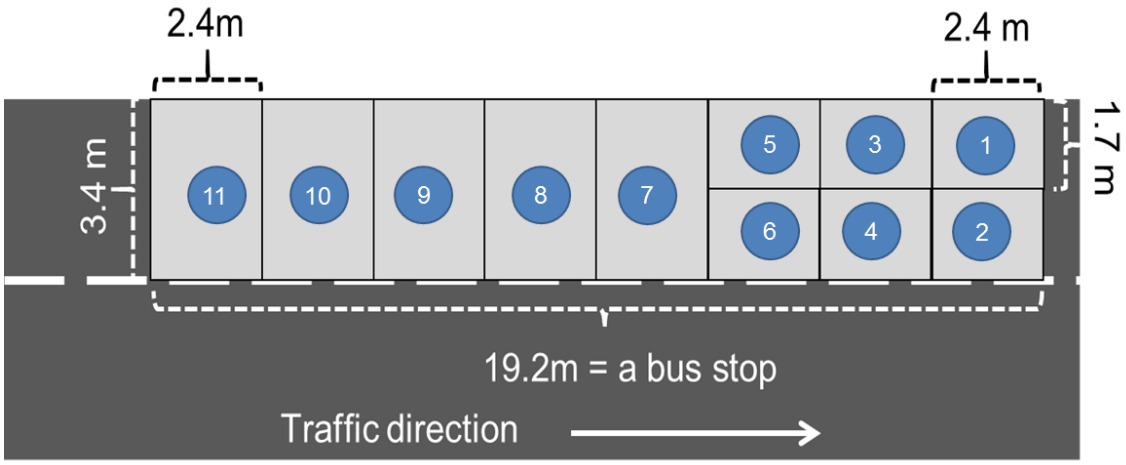

Figure 8.9 Plan for modified ECC slabs on busbay application

The process of producing and installation of a prefabricated modified ECC slab can be seen in Figure 8.10. The first layer of ECC is cast into the formwork, then the second layer 10 mm ECC-Cor cast as a surface layer. After one day, the slab is demolded from the formwork, and then it is brushed to expose the aggregates. After the modified ECC slab is hardened, it can be deployed. Then, BPT and SPM tests were taken on site.

(a)

(b)

(c)

(d)

(e)

(f)

Figure 8.10 (a) casting first layer, (b) casting second layer ECC-Cor, (c) brushing process, (d) placing modified ECC slab, (e) SPM test, and (f) BPT test

8.2.5. Method 5: Reverse Precast modified ECC

The main purpose of the fifth method is to produce a better surface, which is flatter and smoother. By having a surface layer facing the formwork, it will create an ideal surface, which is found to produce the surface layer much better than the conventional precast method.

A half-size slab was made with the fifth method by using steel formwork with a dimension of 1.7 m x 2.4 m x 0.075 m. The molds were designed such that the sidewalls can be removed right after the material harden to prevent the formation of shrinkage cracks. Silicone mattresses with circular holes were also used to create circular convex nodes on the bottom of the slabs.

On the contrary to the previous method (normal prefabricate), the reverse method starts with the surface layer first. Apart from the reverse process differences, the lifting levelling device needs to be modified. The previous design of lifting device (Figure 8.11a) was mainly and can be only used for one direction, which is why the plate only embedded in the bottom area. The function of the plate is to hold the bear the weight of the slab when the slab is lifted. The plate is then working similarly when the slab needs to be levelled. However, the same design will be not working if the reverse casting is proposed. For the reverse method, the lifting device should be able to work on both directions (going upwards and downwards). Two alternative designs can be used: using two plates which embedded on both ends (Figure 8.11b), or one plate embedded in the middle (Figure 8.11c). As the surface layer on the bottom when the slab is cast, the plate of the lifting device needs to be on the bottom (surface layer) to bear the weight of the slab when it is lifted for the first time from the formworks. Then the slab needs to be rotated, so the surface layer will be on to facing upwards as there is another plate holding the slab from another surface, which is needed when the slab is then lifted and placed to the working site. This plate will also be needed for the levelling work.

The modified lifting and levelling device together with the pipe for grouting are placed in the steel formwork (Figure 8.12a). The modified ECC-Cor with a thickness of 10 mm is poured first onto the steel formwork. Then, the second layer, ECC material with a thickness of 60 mm, is poured on top of the ECC-Cor. The silicone rubber mat is then pressed onto the wet ECC (Figure 8.12b). After the rubber mat is laid on the wet ECC, it is important to ensure that ECC material filled the holes, vibrator machine can be used to help this process (Figure 8.12c). The end results of the convex nodes can be seen in Figure 8.12d. After the slab is hardened, the slab needs to be lifted and rotated. The surface needs to be brushed to expose the aggregates. End results of the surface layer can be seen in Figure 8.12f.

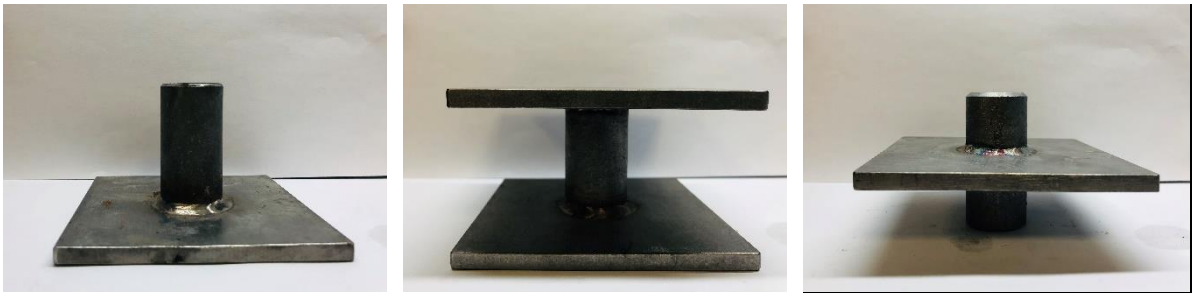

(a) (b) (c)

Figure 8.11 Lifting leveling (a) conventional device for conventional precast, (b) and (c) modified device for reverse precast slabs

(a) (b)

(c) (d)

(e) (f)

Figure 8.12 Procedure of reverse prefabricating method (a) placing modified lifting leveling device, (b) silicone rubber mat place after material is poured, (c) vibrating silicone rubber mat, (d) end results of convex nodes, (e) lifting hardened slab (f) end results of surface layer for reverse method.

8.3. Results and discussions

8.3.1. Skid resistance of ECC in large scale

The results from casting in situ ECC in large scale does not satisfy the requirement for pavement application. Not only the skid resistance is considerably low, but also it results in wrinkles as shown in Figure 8.13. The wrinkles due to the low workability of the ECC itself. The existence of fiber inside the mixture combined with low water-cement ratio causing difficulties when levelling works need to be done on the field. Therefore, material ECC is not recommended for pavement application, except there is an improvement in the mixture design to improve the workability for the material.

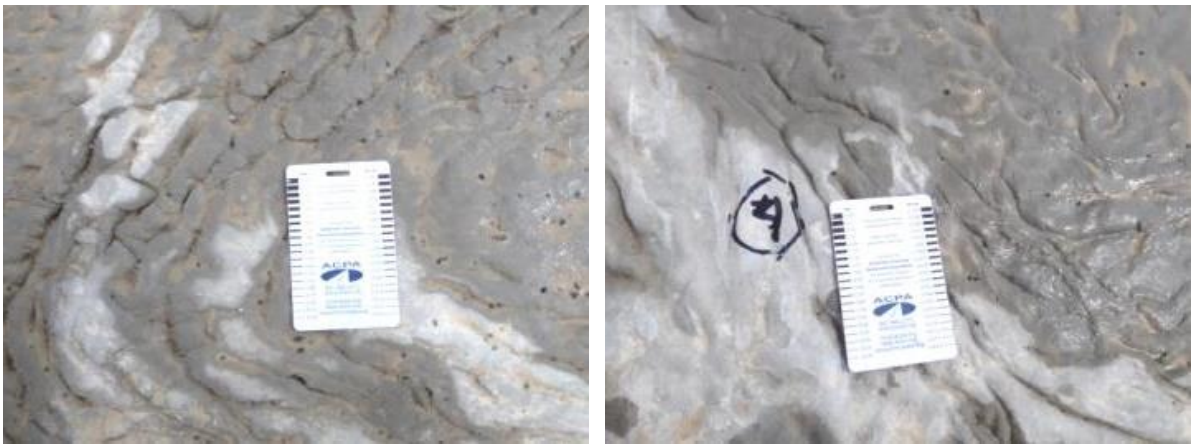

Figure 8.13 Wrinkles on surface layer of normal ECC with cast in situ method

8.3.2. Skid resistance of brushed modified ECC in large scale

Based on the workability, working ECC mixed with corundum on the surface layer was found to be much easier compared to normal ECC. Two reasons for the improvement of the workability are the higher density of the corundum material and the existence of the corundum as intermediate material between fine materials and fibers.

The brushing process for the aggregates was done in three different times. The first brushing process was done after four hours. The work was relatively easy as the material was not completely hardened. However, in results, many corundum materials were found to be removed easily. The second brushing process was done in five to six hours after the casting process. The fine materials can be removed easily, and corundum aggregates were exposed as a result. After six hours, the material is hardened enough. Therefore, the corundum materials were staying in their places. The last brushing process trial was done after 21 hours. The fines still can be removed, but more efforts and times are required to get similar results as exposing process after six hours. The surface treatment with brushed ECC mixed with aggregates seems to work well. Time to expose between 6 to 12 hours is suggested.

(a) (b) (c)

Figure 8.14 Cast in situ ECC-Cor after (a) four hours, (b) six hours, and (c) 21 hours

Inspections and test measurements were conducted to check the performance of ECC with the cast in situ method. The inspections were done visually to check whether any cracks or deformation occur after some time. The performance of ECC was monitored after three days, seven days, 14 days, and 30 days.

The second inspection was based on visual only, which was done after seven days. Similar condition as third days, neither cracks nor any deformation have been found after seven days.

The third inspection was done after 14 days consists of visual inspection and test measurements on functional performance. Based on visual inspection, the structure performance of the pavement is in good condition as there is no crack, shrinkage, or deformation found on the site. Three tests on the functional performance have been performed: skid resistance related to the microtexture with British Pendulum tester, macrotexture with sand patch method test, and outflow with outflow meter.

The fourth visual inspection was done after 30 days. Crack has been found in the middle of the slab, which is the location of the wheel trucks. The size of the crack is approximately 0.35 mm with a length of one meter. The crack occurred due to there is no bond between the ECC layer and the layer below resulting a hanging slab.

Figure 8.15 Cracks on first trial cast in situ of ECC-Cor

Brushing ECC-Cor after four hours causes many corundum were being removed easily. As results (shown in Figure 8.16), the BPN is not improved significantly (average BPN is 56). Convincing results were acquired with exposing process after six hours. Fines materials were easily removed without removing the corundum as the matrix is sufficiently hardened. As consequences, BPN increased up to 80 with 72 as the average. The third trial of exposing process was done after 21 hours resulting average BPN of 64 with 69 as the maximum BPN.

Based on the results, it is concluded that working on the surface after 21 hours is still working but need more effort to reach similar results. A different method with pouring corundum on top of ECC material increases the BPN to 60 as the average with 64 as the maximum. The microtexture results from field investigation are quite consistent with laboratory tests. 71.43±2.02 BPN while the average from field investigation is 72 BPN.

As can be seen from Figure 8.17, results of SPM test of macrotexture on brushed ECC mixed with aggregates after four hours, six hours and 21 hours are 1.26 mm, 1.19 mm, and 1.22 mm respectively. The results from the field test are more than double in comparison to laboratory test, which is 0.36±0.019 mm. The inconsistency occurs due to in large scale, the finishing of the ECC-Cor was not as smooth and flat as the specimens in sample. Therefore, small waviness of the large-scale slab has higher macrotexture.

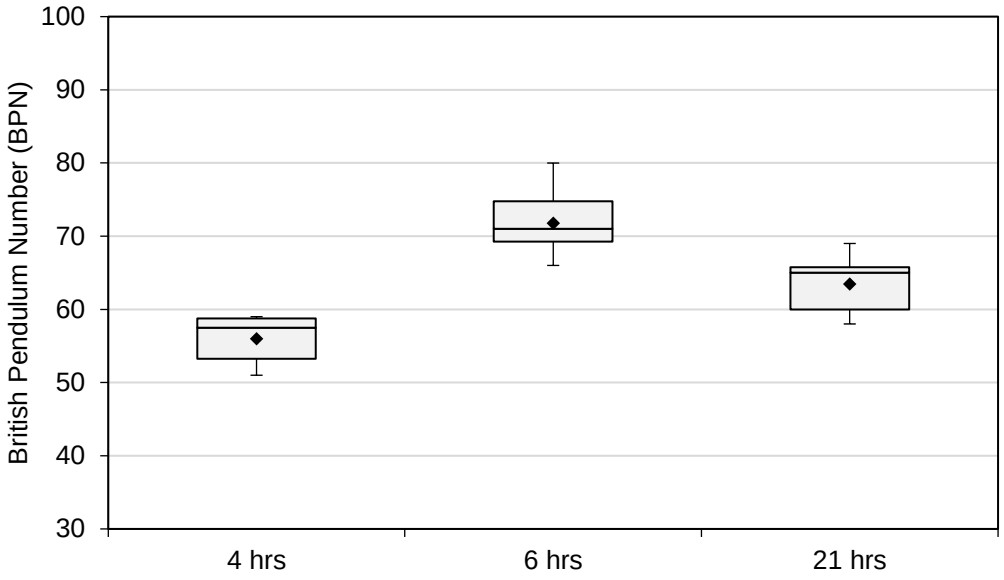

Figure 8.16 BPN of brushed ECC mixed with aggreggates (method 1)

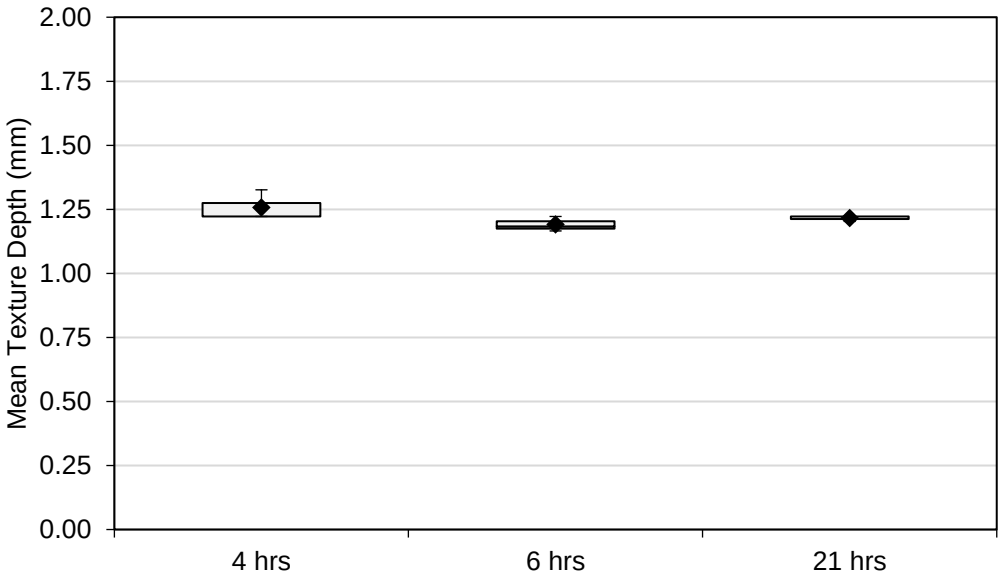

Figure 8.17 MTD of brushed ECC mixed with aggregate methods (method 1)

In summary, the brushed ECC mixed with aggregates method in large scale comes with its advantages and disadvantages including:

- It can fulfil the requirements of skid resistance, which means it enhances the safety factor of surface pavement being used by the motorist. Both mixture designs of ECC-Cor and ECC-SS can achieve high BPN (more than 55 BPN).
- It gives good skid resistance only when the brushing/exposing process done by 6-12 hours. The latest of brushing process will be 24 hours. As longer than 1 day leads to hardened condition causes difficulties in removing fine material. The faster process needs to be done in larger scale due to the effect of ambient temperature.
- It is trade-offs with mechanical behavior. As there is a certain volume of fine silica sand replaced by aggregates, the behavior of ECC is affected. Therefore, the amount of aggregates needs to be carefully designed.
- It is durable. The aggregates are well distributed in the matrix. Since the aggregates embedded inside the matrix of ECC, there will be another layer of aggregates once the aggregates on the surface is starting to wear off together with the mortar.
- It is a relatively easy procedure to cast ECC mixed with aggregates followed by a brushing process. However, a slight improvement on the mixture might result in a flatter and smoother surface.

8.3.3. Skid resistance of exposed ECC-Cor in large scale

The results of the exposed aggregates on ECC surface can be seen in Figure 8.18. The first trial was done for slab application. The second trial was done for footpath application, and it has comparison with concrete M45 as both constructed in the same manner and time. The exposed aggregate on ECC for slab application results in lower BPN compare to the footpath as it is finished with fewer aggregates on the surface. On the contrary, the MTD for the slab is higher than footpath due to the waviness of the un-flattened surface for the slab. In comparison to concrete with tining, the exposed aggregate results in higher BPN and MTD (mm).

In summary, the advantages and the disadvantages of the exposed aggregates on ECC in large scale include:

- It offers a solution for high skid resistance without affecting the mechanical behavior of ECC. As the corundum lays on the ECC layer. Further, it offers lower cost compared to method of mixing aggregates with ECC. The aggregate needed for this method is much less (100-150 kg/m^3) in comparison to the first (mixing aggregate with ECC) method, which requires at least 225 kg/m^3 (ECC-Cor 50) to 450 kg/m^3 (ECC-Cor 100).
- It could offer lesser texture durability in comparison to the mixing aggregate with ECC method. As the aggregates only on the surface. Once the aggregates removed along with time/traffic, there will be no other aggregates that appear on the surface.
- It should be taken into account that both full-scale applications were made manually. This results in inconsistency for BPN, MTD, and visual/physical appearance. Proper machinery for distributing aggregates can be used to get more consistent results.

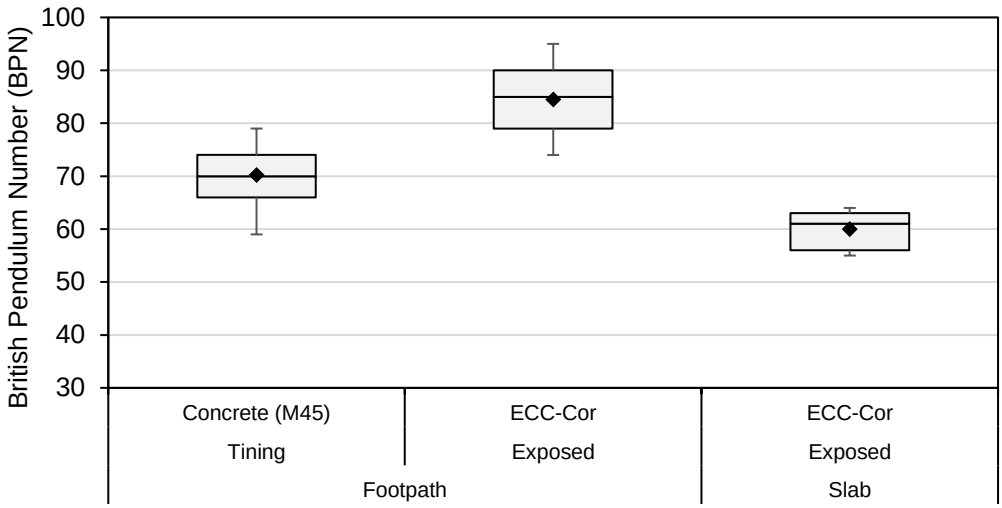

(a)

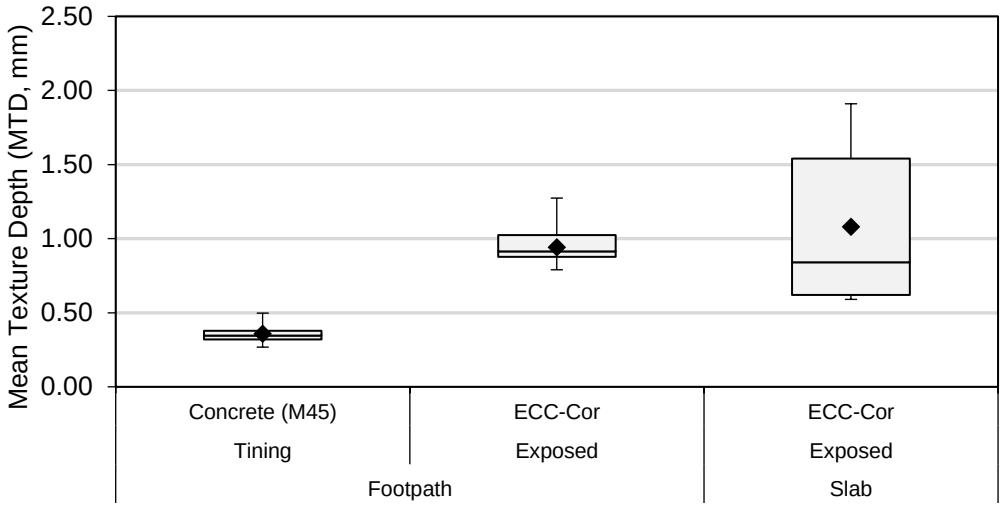

(b)

Figure 8.18 Test results from exposed aggregates on ECC in large scale (a) microtexture in BPN (b) macrotexture in MTD, mm

8.3.4. Skid resistance of precast modified ECC-Cor slabs in large scale

The first trial of the precast method for the modified ECC slabs on a large scale was done by using wooden formworks. BPT and SPM tests were conducted (Figure 8.19e and Figure 8.19f) on six random spots on the precast modified ECC-slab. As results, this application gives microtexture of 71±4.7 BPN and macrotexture of 0.59±0.08 mm, shown in Figure 8.20.

The surface layer property coming from this method has better results compared to cast in situ or spreading aggregates (Figure 8.19a and Figure 8.19b). However, the results are not well distributed as ECC material is hard to work on. Some spots were identified to have minor roughness, as shown in Figure 8.19c. A further reason, the slab was not ideal as the slab is bent due to the wooden formwork which was not able to bear the load of the slab itself. Not to mention that there are imperfect forms due to shrinking on the edge of the slab (Figure 8.19d).

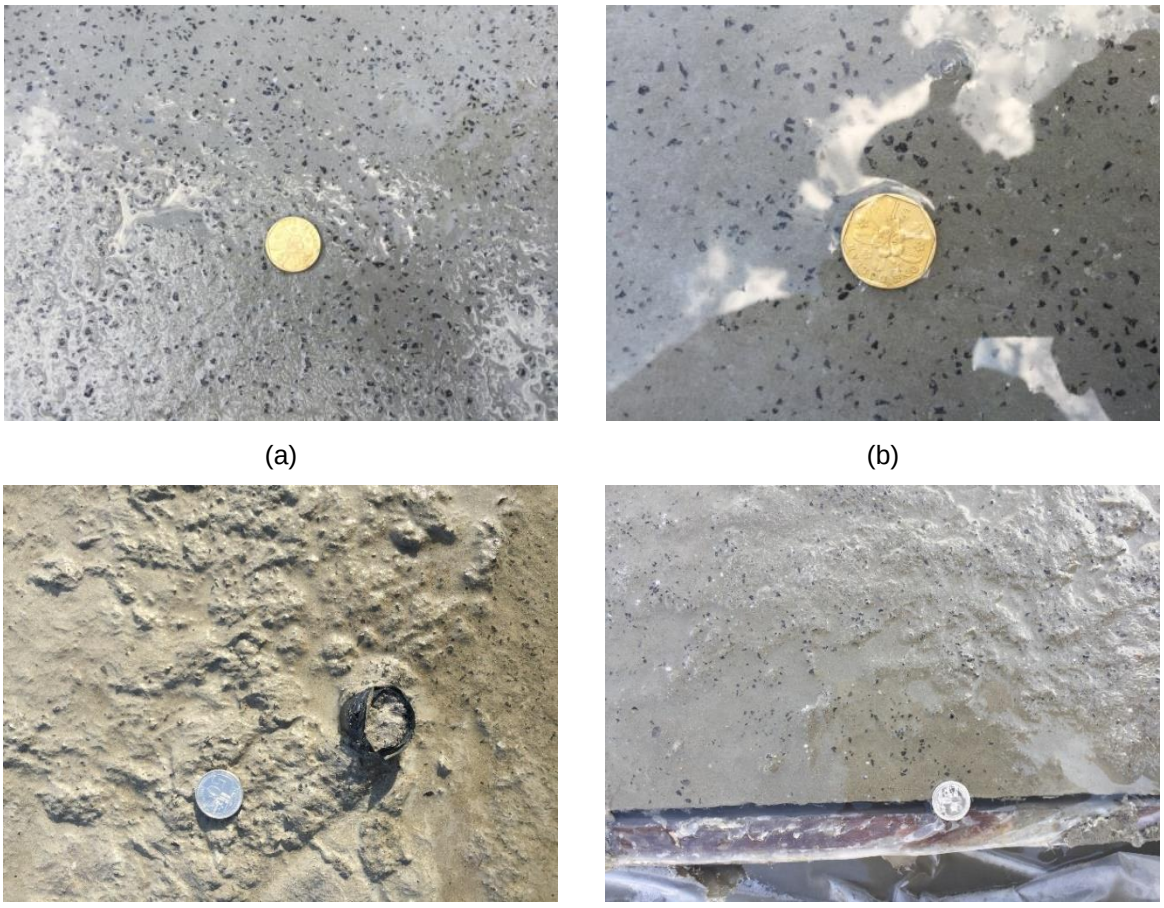

(a) (b)

(c) (d)

Figure 8.19 Appearance of (a) ECC-Cor texture, (b) ECC-Cor texture (close look), (c) rough surface, and (d) gap between slab and wooden formwork

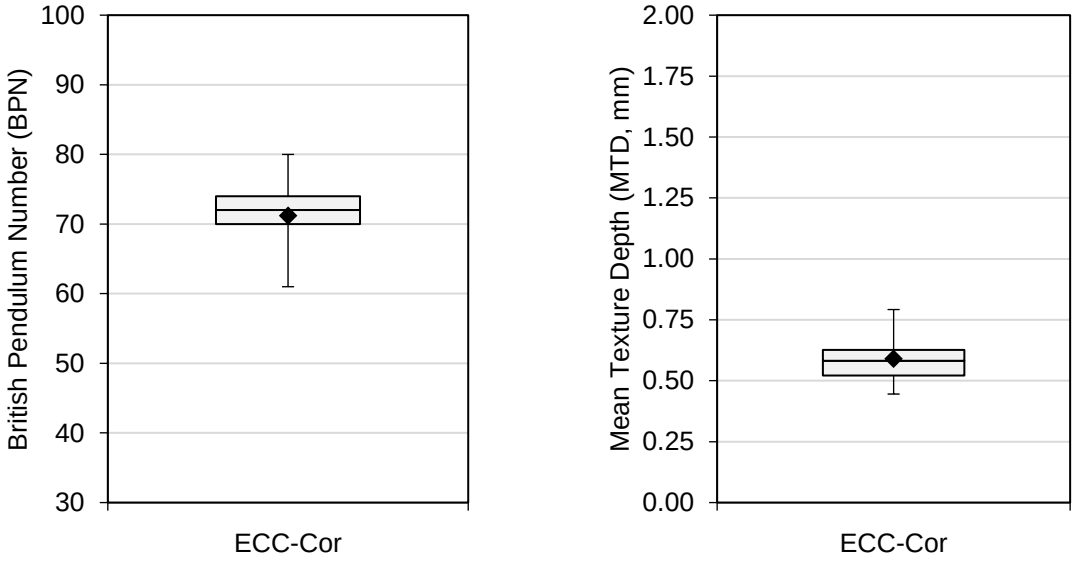

(a) (b)

Figure 8.20 Test results from precast modified ECC slab with wooden formwork (a) microtexture in BPN (b) macrotexture in MTD, mm

More slabs of modified ECC were made with the precast method by using steel formworks to avoid unnecessary deformation, which was occurred on the first trial with wooden formwork. About 12 slabs (details in Table 42) were cast. Five full-size slabs and six half-size slabs were installed on busbay in Jurong Island. BPT and SPM tests were taken on site. As can be seen in Figure 8.21, various results are observed due to differences during mixing, casting, and finishing work. However, all slabs with precast method result in more than 55 BPN, with an average of 68±6.5 BPN for slab 02 to slab 11. The average for macrotexture is 0.44±0.09 mm.

As has been mentioned, the reverse precast method is designed to solve previous issues faced, including deformation in the early stage, as well as inconsistency in a flat and smooth surface. As shown in Figure 8.21 (slab 01), the reverse precast method for modified ECC gives results in microtexture 68±2.45 BPN and macrotexture MTD 0.24±0.02 as an average value. Further, this method improves the end-result of physical appearance as the surface is flatter and smoother compare to other previous methods.

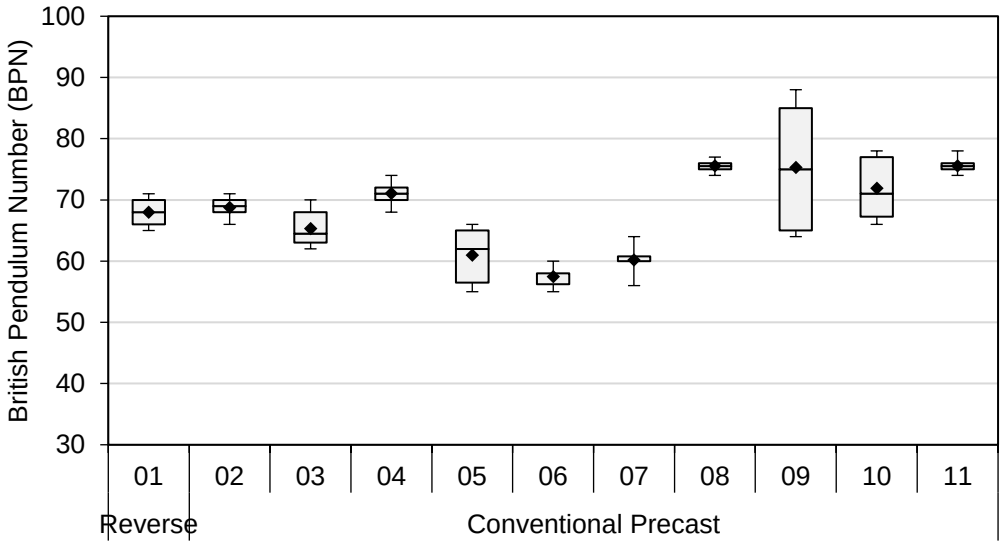

(a)

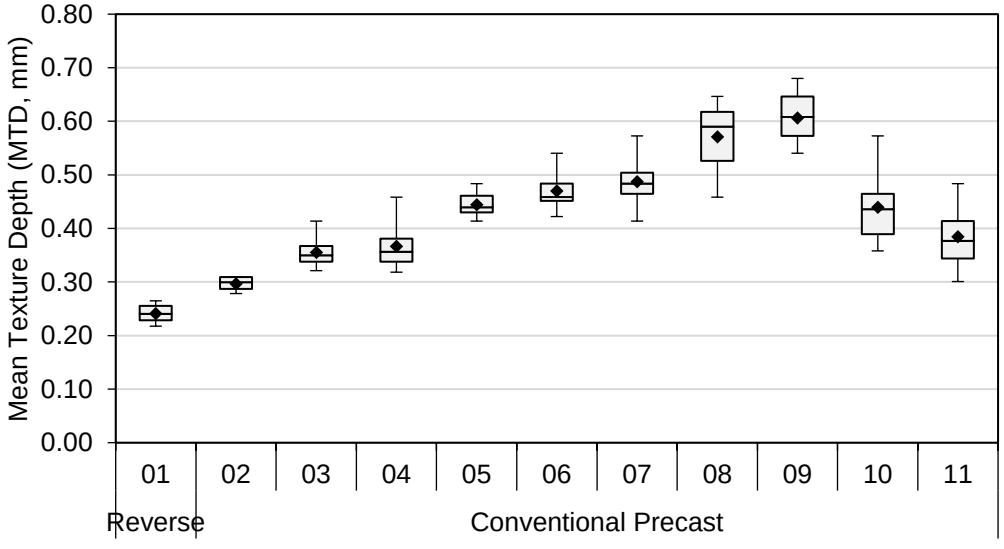

(b)

Figure 8.21 ECC-Cor with precast and reverse precast method (a) microtexture in BPN, (b) macrotexture MTD in mm

In summary, the precast ECC mixed with aggregates method gives conclusions including:

- It can fulfil the requirements of skid resistance, which means it enhances the safety factor of surface pavement being used by the motorist. This method gives high BPN (more than 55 BPN).
- Precast should be done with rigid-based material, such as steel. Wooden material allows deformation at an early stage.
- Precast with steel formwork gives good results and no deformation in an early stage. However, inconsistency is occurred due to several reasons: temperature during mixing and casting process and the way of finishing works. The temperature issues can be easily solved if the mixing and casting process is done in an indoor environment when the temperature is considered stable. As for the finishing work issue, several solutions can be sought including improving the workability of the modified ECC by changing the mixture design, using standardized machinery to flatten the surface, or using the reverse precast method.
- Reverse precast method gives a flatter, and smoother surface compared to conventional precast. Further, it gives the consistency for slab manufacturing process. In consequence, the manufacture process of the slab needs to be adjusted, i.e. improvement for the lifting and levelling design.

8.3.5. Comparison of “cast in situ” and “precast” method for modified ECC

Cast in situ method for modified ECC slab has its advantages and disadvantages, including:

- It gives good skid resistance performance. However, the consistency might be low when manual work is done. Thus, machinery for finishing work is suggested.
- It offers a direct process. There are no requirements for formwork, handling and storage for the slabs, transport logistics. Consequently, it might less cost compare to the precast method.
- It does not need joints. In results, higher comfort and less traffic noise.
- It best for new construction as there is no consideration needed for curing time. However, for reconstruction work, this method might be less efficient compared to precast as it needs curing time, causing a longer time to open to traffic. Consequently, a higher life cycle cost is incurred.

Precast method for modified ECC slab has its advantages and disadvantages, including:

- It gives good skid resistance performance with good consistency.
- It offers an indirect process. There are many requirements for formwork, handling and storage for the slabs, transport logistics. Consequently, it might boost the cost compare to cast in situ method.
- It is equipped with joints. In results, lesser comfort and higher traffic noise.
- It best for roadway reconstruction as there is high consideration for the timing to be open to traffic. Consequently, lower life cycle cost is incurred.

9. Study of Skid Resistance: Numerical Modelling 3D FEM

9.1. Introduction

Chapter 9 describes FEM model development on analyzing and evaluating texturing methods to improve the skid resistance for pavement made of ECC material. Finite Element Method (FEM) model can be used to solve mathematical problems by translating partial different equation into algebraic equations by representing the real structure into subdivision or parts called finite elements.

ANSYS as finite element software offers several computational algorithms for dynamics analysis. The development of the model is using ANSYS Version R17.2 Academic License. The objective is to develop a 3D FEM model according to BPT test to measure the skid resistance of ECC material for PUTW. BPT mechanism is based on a dynamic movement to measure the friction of the sample. Therefore, a dynamic analysis is needed. ANSYS offers various analyses such as Explicit Dynamics, Transient Structural, and Rigid Dynamics.

Explicit dynamics analysis is used to determine the dynamic response of a structure due to stress wave propagation, impact or rapidly changing time-dependent loads. Momentum exchange between moving bodies and inertial effects are usually important parameters. Furthermore, this analysis can also be used to model mechanical movements that are highly nonlinear. Explicit dynamics analysis can be used to model both rigid and flexible bodies. However, this type of analysis cannot be used to model complicated mechanisms and joints which are offered by transient structural analysis and rigid dynamics analysis. Explicit dynamics analysis is more efficient to study model on time scales less than one second. For a longer time of duration events, the transient structural analysis should be considered.

The transient structural analysis which is also called time-history analysis can be performed for both rigid and flexible bodies. This type of analysis is used to determine the dynamic response of a structure under the action of any general time-dependent loads. It can be used to determine the time-varying displacements, strains, stresses and forces in a structure. The time scale of the loading is such that the inertia or damping effects are important. This analysis can be used either for linear or nonlinear.

Rigid dynamics analysis can be used to determine the dynamic response of an assembly of rigid bodies which is linked by joints, springs, and other body interactions. This analysis is suitable to study the kinematics of pendulum movement. However, rigid dynamic analysis has the limitation that both inputs and outputs are only related to forces, moments, displacements, velocities and accelerations. While all parts are rigid that there are no stresses and strain results produced. In this research, rigid dynamics analysis is used.

Inputs are needed for 3D FEM Model of the BPT simulation. Those inputs include: material properties, spring damping, friction, body contact and body interaction, and mesh design. Data for inputs are collected from samples as well as references from another research. Through significant number of simulations, results from BPT model are collected and analyzed: sliding distance, time, and position. Those data will be analyzed further to get BPN as ultimate result. Inputs and outputs from 3D FEM model are summarized below.

Table 9.1 Inputs and outputs for 3D FEM model of BPT

Input parameters	Output variables
Material properties and element dimension	Sliding distance
Spring damping and stiffness	Time
Friction	Position (probe)
Body contact and interaction	BPN
Mesh design	

9.2. Material properties

Material properties are determined in early stage in ANSYS development. Materials used for the BPT model includes aluminum for the pendulum, rubber for the rubber plates and ECC for the sample tested. Those are the inputs in Engineering Data module in ANSYS software.

Aluminum material is used for the pendulum of the BPT. It has properties of elastic modulus of 72.400 MPa, Poisson's ratio of 0.33, and density of 2700 kg/m^3.

The rubber slider is specified according to [90] The rubber was modeled as a hyperelastic material. According to [166], even though rubber categorized as a viscoelastic material with a non-linear stress-strain relationship, during the test, it is reasonable to assume that the rubber remained wholly elastic with one compression modulus due to small deformation. A recommended rubber modulus is from 3.22 to 3.29 MPa. On this model, the rubber modulus value of 3.29 MPa was used. The other properties for rubber slider recommended [99] for a Poisson's ratio (μ) value of 0.47. While in the analysis, it was modeled that for the density of the rubber is 1100 kg/m^3, which is based on measurement in the laboratory [98].

ECC has Elastic Modulus of 18 to 34 GPa with Poisson's ratio of a range from 0.15 to 0.20 [51,167]. In this 3D FEM model, the value of 22 GPa and 0.15 were adopted for elastic modulus and Poisson's ratio respectively. The densities of ECC samples were calculated: 2040 kg/m^3 and 2190 kg/m^3 for the ECC mixed corundum with Pour and Precast Method. Therefore, for this model an average value of 2100 kg/m^3 has been used for the density of the specimen. This is complying with typical Portland cement mortar which normally has the density around 2000 to 2200 kg/m^3. However, on this model analysis, the density might not affect much for the results.

Table 9.2 Material properties for BPT model

Material	Aluminum	Rubber	ECC
Elastic modulus (MPa)	72.400	3.29	22.000
Poisson ration	0.33	0.47	0.15
Density (kg/m^3)	2700	1100	2100

9.3. Geometric model

As has been mentioned in the preliminary design, a simplified three-dimensional model of the British Pendulum Tester and sample of ECC surface were created with DesignModeler tool in ANSYS [168]. The dimension of every parts of BPT model are set accordingly to the actual BPT tester. The 3D FEM model of BPT is illustrated in Figure 9.1.

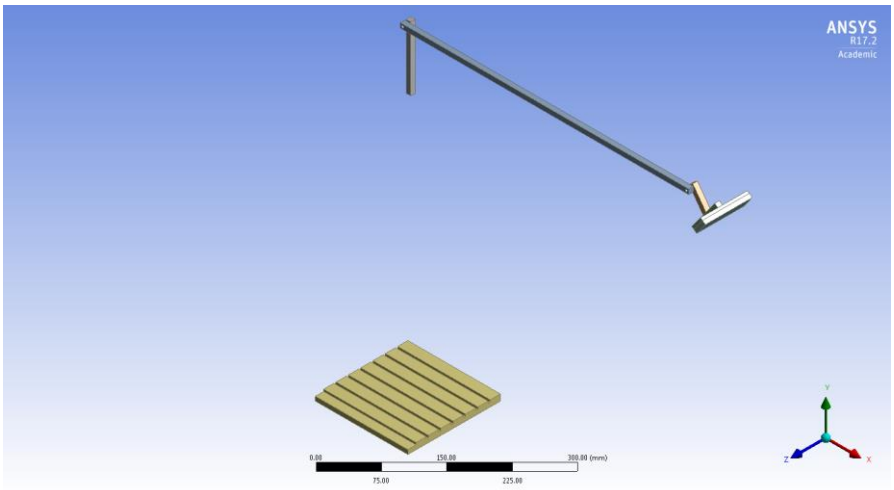

Figure 9.1 3D FEM model of British Pendulum Tester

The pendulum arm and the supporting arm are made of aluminum, which are designated as a beam. There are a lever arm and a lever system connecting the pendulum arm and the slider. The lever arm and the lever system also made with the aluminum material. While the lever arm and the lever system connected by the spring. The spring behavior can be determined by its stiffness and damping coefficient, which have to be adjusted. The stiffness and the damping were adjusted through verification of laboratory measurement and results obtained from the finite element simulation.

The cap of the rubber slider is also made of aluminum. While the rubber slider was modeled with rubber with the approximate dimension of 76 mm by 25 mm by 6 mm (length x width x thickness). The total mass of the aluminum including the rubber is 1.486 kg.

The ECC specimen model has the dimension of 150 mm x 150 mm x 10 mm. As specified in [90], the tester shall be capable to provide a slider contact path of 125 ± 1.6 mm for tests on flat surfaces .Therefore, the position of the sample can be and it has to be adjusted in order to achieve a sufficient contact length between the slider and the sample.

9.4. Mesh design

Mesh design in finite element analysis plays an important role on results. According to ANSYS, bad quality mesh can cause convergence difficulties, bad physic description, and diffuse solution. Therefore, a mesh design for FEM model should be carefully designed. The main objective of this 3D FEM model is to simulate the behavior of the friction on the surface sample. Therefore, mesh design is specifically designed only for the sample surface. The meshing was created with the help of Body Sizing and Face meshing tools to create a rectangular shape with maximum element size of 2 mm. This dimension was chosen considering the size of Maximum Aggregate Size in ECC mixture design. A dense mesh is selected for the rubber slider, especially at areas along the edge where contact was created between the rubber slider and the ECC. The meshing comprised 57370 nodes and 18312 elements. The meshing for smooth and grooved samples can be seen in Figure 9.2 and Figure 9.3, respectively. While meshing for rubber slider is shown in Figure 9.4.

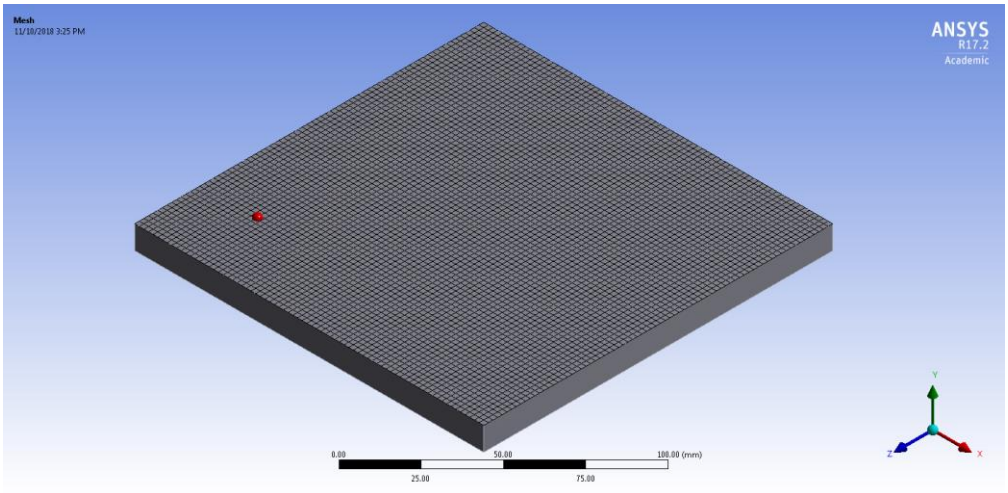

Figure 9.2 Mesh design for smooth (ECC) sample

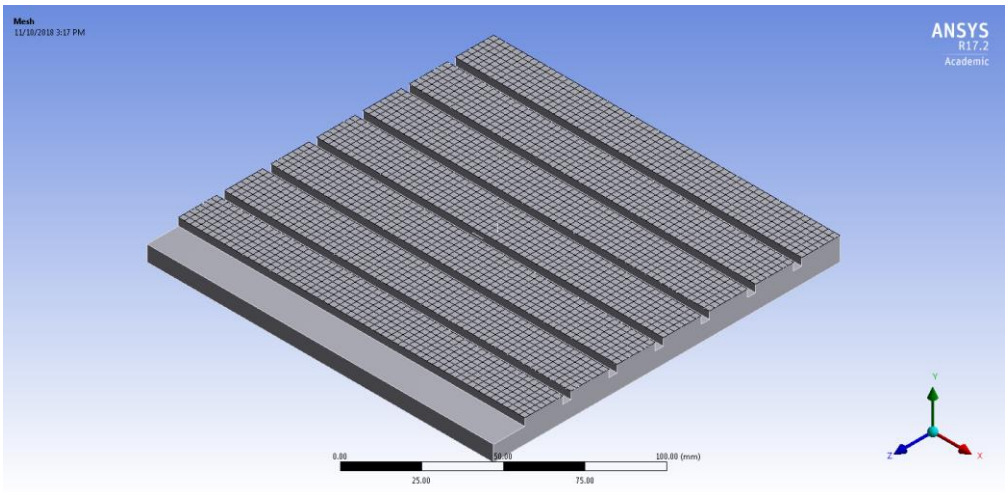

Figure 9.3 Mesh design for grooved (ECC) sample

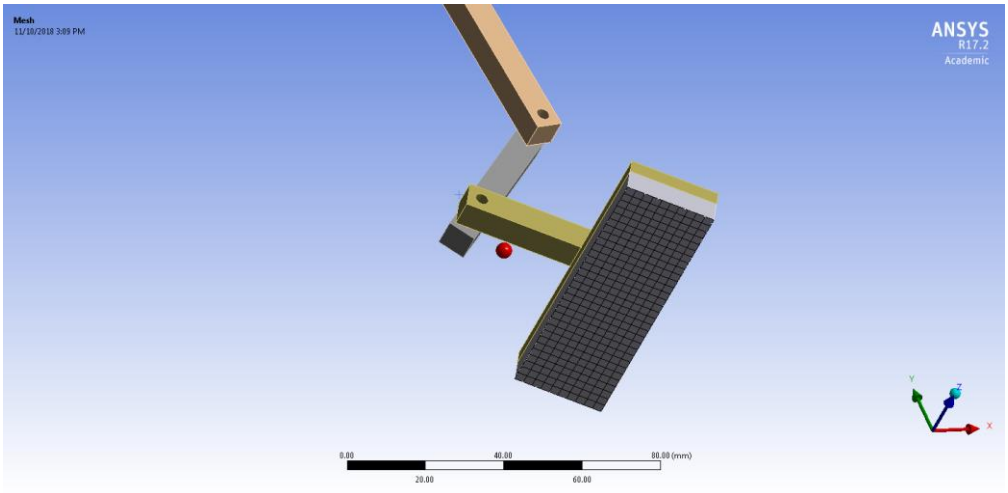

Figure 9.4 Mesh design for rubber slider

The quality of the mesh has been checked in ANSYS program. ANSYS recommend is to keep minimum orthogonal quality above than 0.1. Another parameter is the aspect ratio, which can be calculated by the length divided by the height. This model has the aspect ratio of 1.0024 as average. Based on the results from these parameters, the model shows a good quality. The results for meshing are summarized in Table 9.3.

Table 9.3 Quality of meshing for 3D FEM model of BPT

Criteria	Value	Standard criteria
Element quality	0.99895 ± 0.0043	0 to 1 0 is worst, 1 is best
Orthogonal quality	0.99996 ± 0.0012	0 to 1 1 indicates a perfect cube or square; while 0 indicates element has a zero or negative volume
Aspect ratio	1.00308 ± 0.0353	The best possible quadrilateral aspect ratio is 1

9.5. Contact and body interaction

The slider contact path between rubber slider and (ECC) sample surface is simulated with setting of manual contact with type of Force Frictional Sliding. The ECC sample surface is set as contact bodies while rubber slider is set as target bodies. The target surface is intended as rigid surface while the contact surface as deformable surface. However, on rigid dynamics analysis, the results might have not significant differences.

9.6. Model validation

The 3D FEM model of BPT has been validated with few parameters including: (1) the validation of the mass of the model, (2) the validation of the distance from the center of gravity of the pendulum to the center of the oscillation, (3) the validation of sliding contact path distance, and (4) the calibration of correlation between the BPN measurement with real BPT tester and BPN measurement with FEM model.

The validation of the mass of the model. According to the standard (ASTM E303), the spring and the lever arrangement shall give an average normal slider load of 1500 ± 100 g. On this 3D FEM model, the pendulum together with the slider and the mount slider has total weight of 1500 g.

The validation of the distance from the center of gravity of the pendulum to the center of the oscillation shall be 411 ± 5 mm, which is accordance to the [90]. While on this developed 3D FEM Model, the distance from the center of gravity of the pendulum to the rotation center is 411.2 mm.

The validation of sliding contact path distance between the rubber slider and the sample surface according to the required standard of BPT test, which is 125 ± 1.6 mm. The verified result is shown in Figure 6 6. In a real situation, this condition can be achieved by adjusting the position of the slider with the vertical height control knobs. On this 3D FEM model, parameters are considered to achieve this condition: the position (height) of the slider, the angle of the rubber slider and the spring coefficient for the rubber slider.

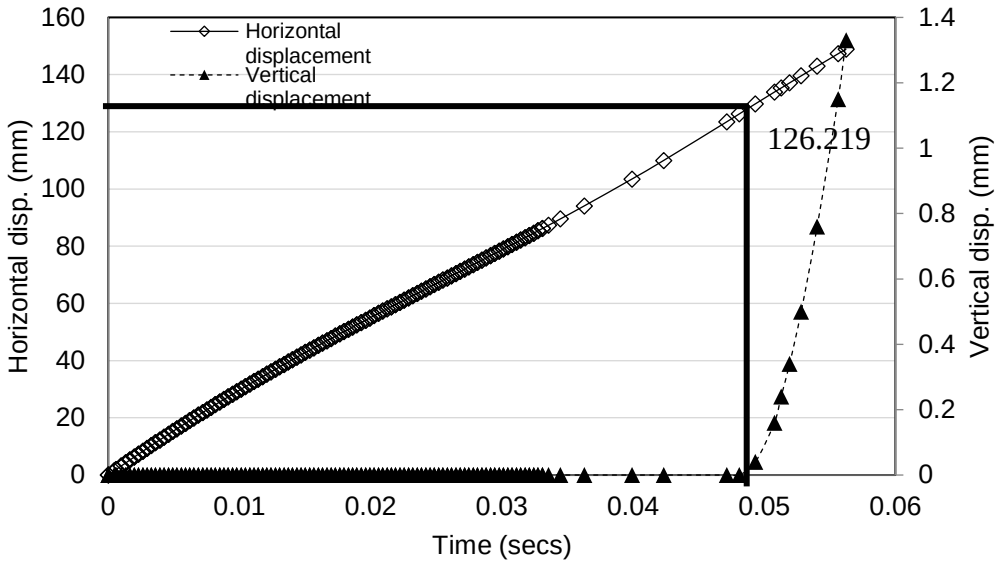

Figure 9.5 Verification of sliding contact path distance for FEM model

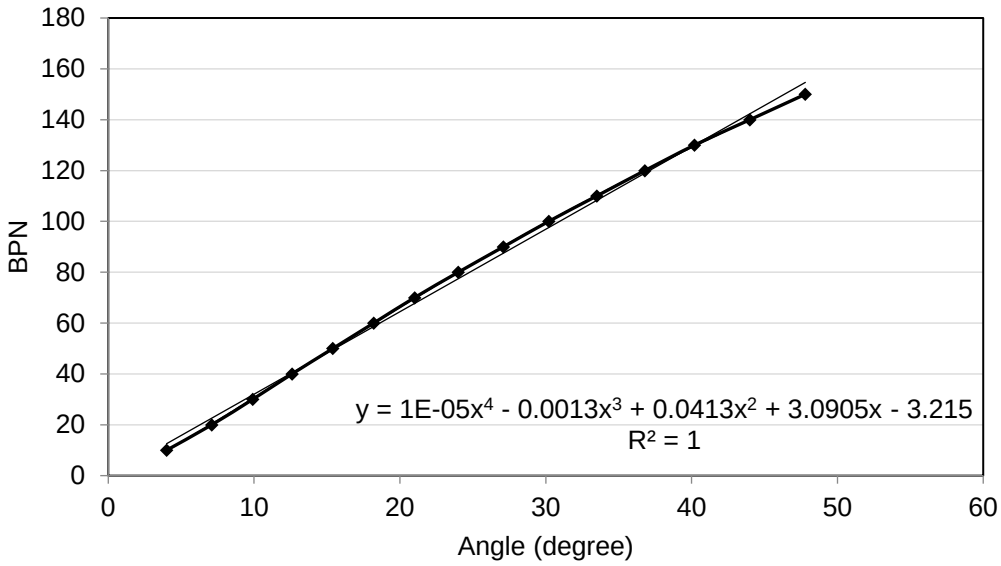

Figure 9.6 Correlation between degree of angle of the pendulum and BPN

The calibration of correlation between the BPN measurement with real BPT tester and BPN measurement with FEM model. A method was proposed by comparing the energy loss between laboratory measurement and finite element analysis [100]. However, slight differences ~ 10 % for results are expected. On this FEM model, the analysis is done by using the correlation between the degrees of the angle of the pendulum of BPT with the BPN values. Therefore, the BPN is calculated based on the position where the pendulum stops during the simulation. The correlation is derived to an equation below:

$$PN = 0.00001xdeg^4 - 0.0013xdeg^3 + 0.0413xdeg^2 + 3.0905xdeg - 3.215 \quad \text{(Eq. 31)}$$

Where: $\mathrm{BPN_r}$ = British Pendulum Number

deg = angle

9.7. Results and discussion

The angle of the pendulum can be easily calculated by using probe tools in ANSYS. Then, the BPN can be determined with the proposed equation. The results are summarized in Table 9.4.

Table 9.4 Results of BPN from the finite element analysis

Mixture	Condition	Texture	FEA results		
			Position	Angle	BPN
ECC - Cor	Dry	No texture	-405.56	29	97
		Longitudinal grooving	-411.9	28	92
	Wet	No texture	-432.83	21	70
		Longitudinal grooving	-435.59	20	67

The FEM model was validated by comparing the BPN results from the FEM analysis with BPN results from laboratory tests. The sample used for validation is from sample with mixture design of ECC-Cor 80. Samples were prepared for both flat and grooved texture. This mixture design was chosen due to their skid resistance was one of the highest compared to another specimens. The comparison is summarized in Table 9.5. From the results, it can be seen the difference between FEM model and laboratory test is below 5%, considerably good model.

Table 9.5 BPN results comparison between experimental measurement and FEM model

Mixture	Test condition	Texture	BPN results		Percentage difference
			Laboratory measurement	Finite element analysis	
ECC - Cor	Dry	No texture	97	97	0%
	Dry	Longitudinal grooving	96	92	4.17%
	Wet	No texture	70	70	0%
	Wet	Longitudinal grooving	68	67	1.47%

The 3D FEM model was conducted to predict the BPN of ECC samples. Validation and calibration of the model were performed with consideration of key parameters of the BPT mechanism: the mass, the center of gravity of the model and the sliding distance of the rubber slider. The simulation results show a good correlation with laboratory measurements.

The development 3D FEM model of BPT was done by using a Rigid Dynamic analysis. This type of analysis can be used to determine the dynamic response of an assembly of rigid bodies linked by joints and springs, which are also the main parts of the BPT. However, Rigid Dynamics analysis has some limitation consist of: (1) inputs and outputs are limited to forces, moments, displacements, velocity and accelerations, (2) all parts are rigid, that the system cannot analyze the stresses and the strain. It can only analyze forces, moments, displacements, velocities and accelerations, (3) viscous damping can be taken into account through springs, (4) another advantage is the solver is tuned to automatically adjust the time step.

10. Study of Surface Water Drainage: Laboratory Test

10.1. Introduction

Surface water drainage is another important consideration in pavement design. Water pond on the pavement surface produces excess water which leads to hydroplaning effect and endangers driver. Further, any water on the surface pavement might interrupt the traffic, reduce the grip, and limit the visibility due to splash and spray [125], which are amplified on area with high rainfall intensity [62,106]. Inclusion of coarse aggregates in concrete mix design introduces macrotexture which significantly reduces the risk of hydroplaning effects on tire-pavement [124]. Besides surface texture, pavement geometry, i.e., cross-slopes and grades, can also affect surface water drainage performance [61]. While many literatures reported the correlation between water outflow and (macro)-texture, few studies investigated the effect of pavement geometry on the surface water drainage. Furthermore, effects of surface texture and pavement geometry on water drainage performance of ECC pavement are still not clear and no model has been reported.

The test results of skid resistance show that the surface of pavement made of ECC can be improved by adopting hard fine aggregates into ECC mix, as it provides both the micro- and macrotextures. However, there is still a risk of hydroplaning. Surface texturing methods can be introduced to reduce the risk of hydroplaning by improving the drainage performance as well as the skid resistance of ECC pavement. Therefore, studies on the functional performance of ECC on roadway application needs to be extended, particularly on the surface water drainage performance since high rainfall intensity may lead to hydroplaning [124,125].

Ideally, the drainage performance of pavement is divided into two mechanisms [108]: water surface runoff (water flowing above the surface pavement) and water infiltration (water infiltrates through the pavement).

For further consideration, Singapore is a tropical city that receives approximately 2400 mm of precipitation annually, and up to 19 high rainfall intensity days a month [169], which is much higher compared to those three states. Data provided by the NOAA National Climatic Data Center which is collected by weather stations throughout each state from 1971 to 2000 specified that Texas, North Carolina, and Louisiana experience average annual precipitation of roughly 734 mm, 1279 mm, and 996 mm, respectively [170].

Singapore does not have standard related to the measurement of surface water drainage. However, several standards by the Department of Transportation (DOT) in the USA specify a requirement for outflow times which can be used as a baseline. Neither standard on water film thickness (WFT) can be found in Singapore. However, according to Austroad [171], the requirement for water film thickness is:

- maximum water film depth of 2.5 mm (desirable) to 4.0 mm (absolute) for:
    - Sections where design speed ≥80 km/hr,
    - Approaches to and exits from intersections and roundabouts,
    - Intersections, roundabouts, and steep downhill sections,
    - Merge and diverge sections for entry ramps/ overtaking lanes/climbing lanes,
    - Superelevated curves (particularly those approaching limit curve speed).
- Maximum water film depth of 5mm (desirable and absolute) for all other situations.

This chapter investigates the surface water drainage performance of pavement made of ECC. ECC incorporating hard aggregates is first developed. Standard test with outflow meter was utilized to investigate the surface water drainage performance. Subsequently, a tailored experimental was set to investigate the water depth/water film thickness on the surface of the pavement. Finally, an improvement on the surface of ECC is proposed to enhance the surface water drainage performance.

10.2. Laboratory test program

10.2.1. Materials and mixture design

Type I Portland cement, class F fly ash (FA), micro-silica sand (mean and maximum grain size of 110 μm and 200 μm, respectively), polyvinyl alcohol (PVA) fibers (length of 12 mm, diameter of 39 μm, nominal tensile strength of 1600 MPa), a high-range water reducing (HRWR) were used to prepare the mix. Corundum with a maximum particle size of 2.38 mm was used as fine aggregates for improving the surface textures of ECC. The material size distribution of corundum is given in Figure 13.1.

10.2.2. Specimen preparation

The objective of this method is mainly to improve the micro- and macrotexture of ECC by mixing aggregates together. As the aggregates are mixed together with other material during the mixing process, it makes this process can be applied for both “cast in situ” method and “prefabricating” method. Two aggregates are investigated: corundum and silica sand. ECC mixed with corundum is named as ECC-Cor, while ECC mixed with silica sand is named as ECC-SS. Both specimens are shown in Figure 7.2.

ECC and ECC-Cor mixture was prepared in a planetary mixer. Cement, fly ash, and micro-silica sand are dried mixed first. Water was then added followed by the addition of superplasticizer and mixed for 3 to 5 mins until the mix achieved the required consistency. Lastly, the PVA fiber and corundum were added and mixed for another 3-5 mins. The fresh mixture was cast into prism (280 mm by 70 mm by 50 mm) and plate (500 mm by 300 mm by 10 mm) moulds catered for various types of tests. Specimens were removed from the mould after 1 day and were cured at normal laboratory air (25±3^{o}C, 70%RH) for another 27 days before further testing. At the pre-determined age, either 1 d or 3 d, the top surface of plate specimens was treated with a steel brush to expose the corundum on the surface.

The second mixture, ECC-SS, designed with different objective. It offers good skid resistance with brighter surface layer for lesser impact to UHI and better visualization. Thus, fine aggregate, silica sand, which has high hardness (slightly below corundum) and bright color, is used. The ECC-SS mixture was prepared in similar way to ECC-Cor.

The specimens were prepared for two different tests: outflow and water film thickness. For outflow test, the flat and grooved specimens were made. Both have a dimension of 500 mm x 300 mm x 10 mm. The flat specimens were reverse cast to ensure the surface is flat. The grooved specimens were also made with a reverse method. The grooves were successfully implemented by using a concrete cutter machine. The concrete cutter was equipped with a blade of 350 mm in diameter and 3.2 mm in thickness. The blade position is adjustable, so it can slide forwards and backwards, while the level can be fixed to make a groove with the specified depth. Four macrotextures were evaluated, and the corresponding groove dimensions are summarized in Table 37. Five minimum tests were conducted for each sample (see Figure 10.1). As for the water film thickness test, flat and grooved specimens were also prepared but with different dimension. It has a dimension of 2 m x 0.5 m x 0.07 m in thickness. Both specimens were cast with a reverse method. For the grooved ECC-Cor specimens, the grooves were made by using rubber silicone mat as a negative mould (see Figure 10.1).

(a) (b)

Figure 10.1 Grooves preparation with (a) concrete cutter (b) silicone mould

10.2.3. Test program

Outflow meter tests were conducted to evaluate the surface water drainage performance of the pavement specimens made of modified ECC through its surface and subsurface voids. It measures the duration of a known quantity of water taken to run through voids in the pavement texture and intended to provide a measure of the ability of the pavement to relieve pressure from the surface of the tires, thus indicating hydroplaning potential under wet conditions. A faster run time indicates a thinner film of water may exist between the tire [116]. The duration measured with digital timer with an accuracy of 0.00 sec. Minimum five tests were conducted with a water temperature of 28 ºC in an outdoor environment (air temperature of 30 ºC). It is important to ensure the sample level is zero to avoid the effect of pavement geometry, the cross slope and the grades. The grade and the cross slope of the specimens were measured using a digital inclinometer (Figure 10.2).

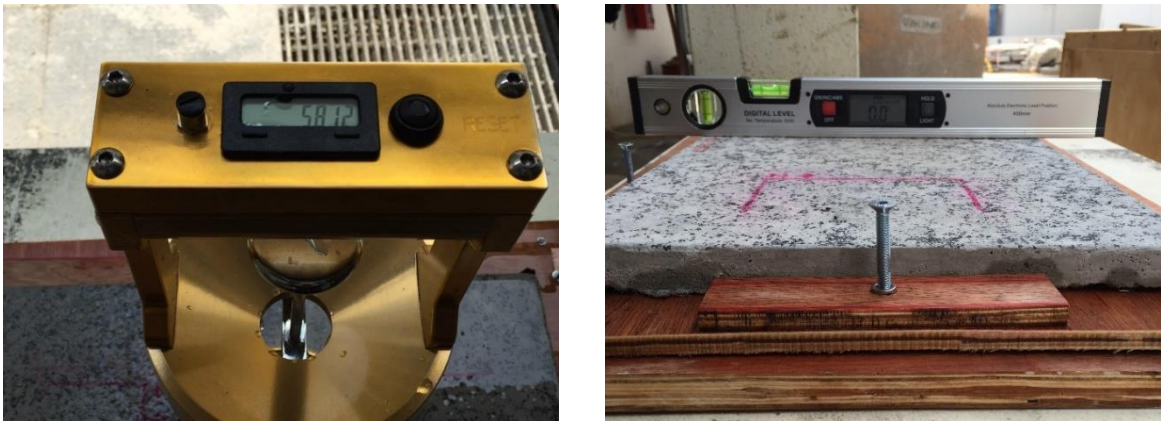

(a) (b)

Figure 10.2 Water outflow measurement (a) with digital timer, (b) specimen level

Water film thickness or water depth above the top of the specimen surface was also measured. According to Gallaway [117], water depth is affected by many variables (e.g. texture, pavement geometry, and environmental conditions) has a strong correlation with hydroplaning and skid resistance. Therefore, it must be minimized.

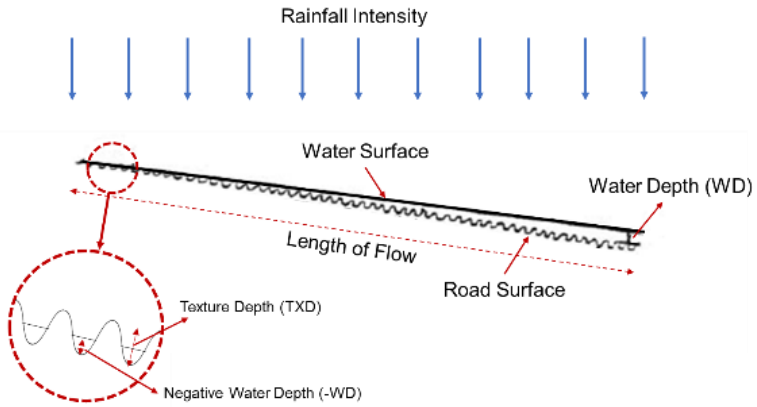

Figure 10.3 Water depth (water film thickness) above the specimen surface [117]

The equation of water depth [117] shown as:

$$WD = 0.01485\left(TXD0.11^{Lf^{0.43}}I0.59^{Sr^{-0.42}}\right) - TXD \qquad \text{(Eq. 32)}$$

Where:

WD	=	the water depth above the top of the surface asperities, mm
TF	=	length of flow path, m
TXD	=	texture depth, mm
I	=	average rainfall intensity (mm/hr)
S_r	=	slope of resultant flow path, m/m

In this study, the water depth is measured based on the difference of water volume between the input and the output within the system itself. The system is illustrated in the figure below. The water will be flowing from the inbox (input of the system) and then going on top of the specimen. Then the water will be caught again in the outbox. The water pump which placed in the outbox will pump back the water again into the inbox via pipes. The flow rate of the water can be controlled with the valve as well as monitored with the flow meter.

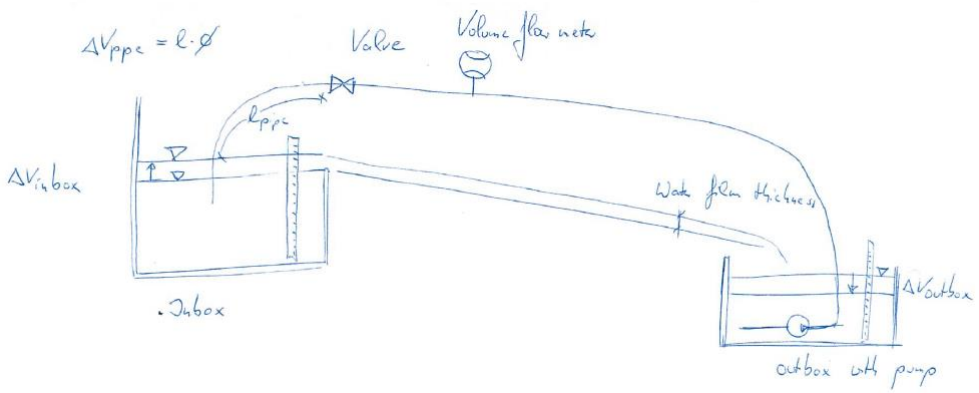

Figure 10.4 The average water depth above the surface of specimen (Lechner B. & Bawono A.A)

To do the investigation, according to the theory mentioned above, a tailored apparatus was designed and made accordingly. The investigation on the water depth was done on a different flow rate of water and grade of the slab specimen. The flow rate of the water is varying: 1, 3, 5 and 9 liter/minute. While two grades: 1% and 5% are selected. The 1% grade is commonly used as the minimum grade in the pavement geometry design. Meanwhile, a grade of 5% is considered as the maximum. Even though, in some geometry pavement guidelines states that grade more than 5% can be used in specific road segments.

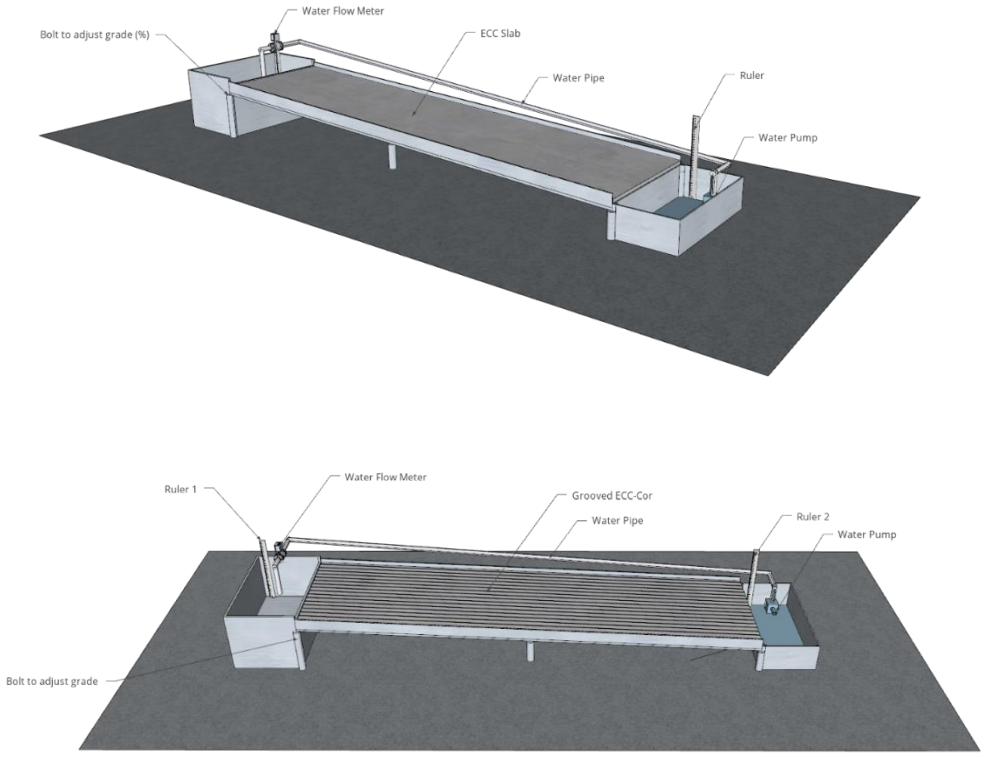

Figure 10.5 The 3D illustration of the surface water drainage test setup (a) on ECC-Cor (b) on grooved ECC-Cor

The equation of the average water depth can be seen below. The proposed experiment, as well as the equation, gives a different perspective in comparison to the method developed by Gallaway et al. The proposed equation gives the average water depth on the whole surface of the specimen, while Gallaway et al. gives the water depth above the surface only at the edge of the specimen.

$$WD_{average} = \frac{\Delta V_{outbox} - \Delta V_{inbox} - \Delta V_{pipe}}{Area_{pavement}} \quad \text{(Eq. 33)}$$

Where: $\mathrm{WD}_{\mathrm{average}}$ = Water depth or water film thickness

V = Water Volume

The intrinsic water permeability of a typical structural concrete is very low; it lies within a range of 5 x 10^{-19} to 2 x 10^{-17} m/s [172]. The water permeability of ECC is even lower compared to conventional concrete. Research was done on the permeability of ECC material by using two experimental setups: a falling head test which was used for specimens with low permeability, and a constant head test which was used for samples with higher permeability. Both tests done with the tensile specimen edges were sealed with epoxy to facilitate unidirectional flow. As results from the experimental tests, ECC M45 produced micro-cracks with crack widths ranging from 40 to 70 µm, and in the loaded state, the results are lower than the limit of 100 µm. In the unloaded scenario, ECC micro-cracks are observed to have crack widths from 5 µm to 10 µm. This led to water permeability of approximately 8.18 x 10^{-12} m/s and 7.74 x 10^{-10} m/s for un-cracked ECC, and ECC subjected to 3% strain, respectively. This means the water permeability remained very low for both conditions: cracked and un-cracked. Water permeability does not change significantly when the number of cracks increases because it is maintained by the micro-cracks [37]. Therefore, water infiltration was ignored in this research and focused on the water surface runoff.

As can be seen from Table 10.1, various methods of surface treatments have been studied in this study. Each surface treatment is evaluated with outflow test. Then, it is followed by a test on the water film thickness for specimens of ECC with corundum. As a reference, the outflow test was done on normal ECC samples.

Table 10.1 Laboratory test on the surface water drainage for surface treatments

No	Specimen	Water outflow	Water film thickness
1	ECC	Y	
2	Brushed ECC-Cor	Y	Y
3	Brushed ECC-SS	Y	
4	Grooved ECC-Cor	Y	Y

10.3. Results and discussion

10.3.1. Water outflow performance of ECC, ECC-Cor, and ECC-SS

The outflow times on normal ECC cannot be measured as the surface is very smooth that the rubber ring of the Outflow meter device is stick to the surface tightly. This condition makes the water flowing out at a very slow rate. As can be seen in Figure 10.6, the outflow times on ECC mixed with corundum is improved as the corundum provides a microtexture on the surface pavement which allows the water to find a gap between the aggregates. The average outflow time result of ECC-Cor is 62.11±4.99 s. A similar result is observed in ECC-SS 01 with 65.06±3.51 s.

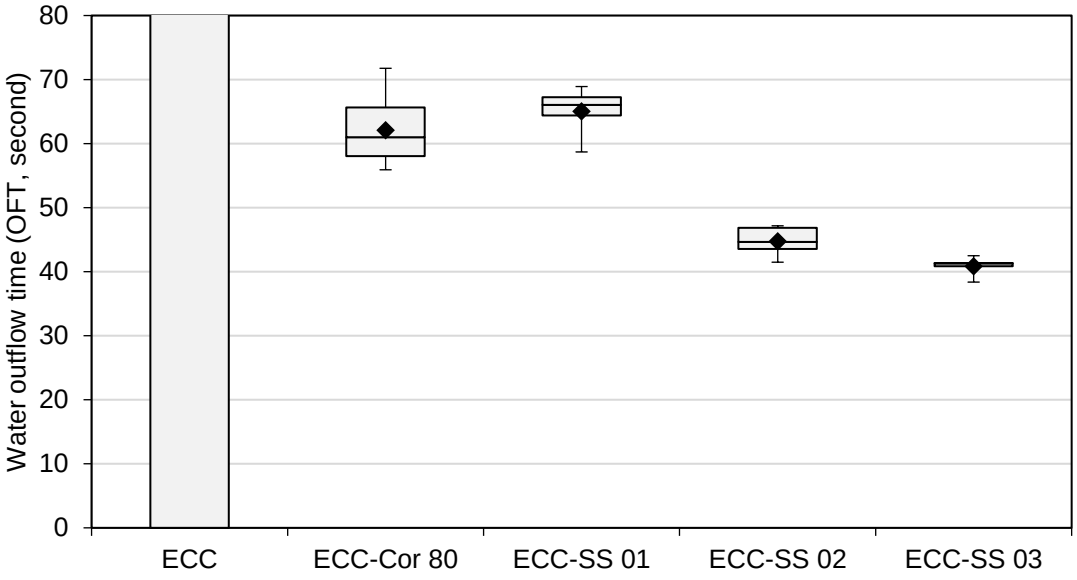

Figure 10.6 OFT of ECC, ECC-SS #, and ECC-Cor 80

10.3.2. Water outflow performance on grooved ECC-Cor

As expected, the outflow times for the grooved ECC-Cor are even shorter. The combination of the microtexture provided by the corundum and the macrotexture provided by the grooves makes the space between the rubber ring of the Outflow Meter device and the surface pavement specimens even bigger, which results in a lower value of outflow times. The outflow times of grooved ECC-Cor with a land area of 25.0 ± 0.5, 20.0 ± 0.5, 15.0 ± 0.5, and 7.5 ± 0.5 mm is 7.73 s, 7.30 s, 5.83 s and 3.38 s, respectively. Detail results are shown in Figure 10.7.

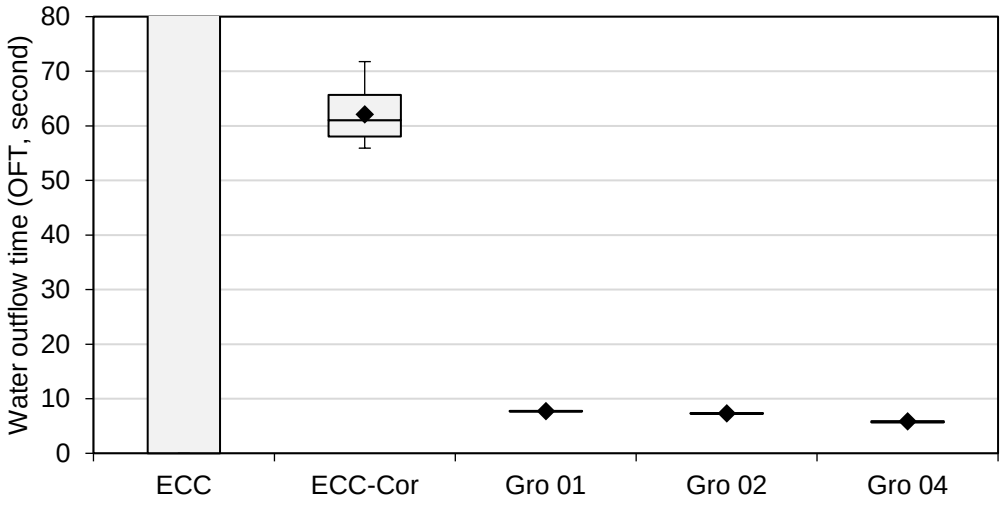

Figure 10.7 OFT of ECC, ECC-Cor 80, ECC-Cor Gro #

10.3.3. Water film thickness on ECC-Cor

It can be seen in Figure 10.8, the average WFT on ECC-Cor for water drained above the ECC-Cor surface pavement (grade 1%) with a flow rate of 1.0, 3.1, 5.1, and 8.9 liter/minute, are 1.33, 1.91, 2.66, and 4.10 mm, respectively. It can be seen in Figure 10.9, the average WFT on ECC-Cor for water drained above the ECC-Cor surface pavement (grade 5%) with a flow rate of 1.0, 3.1, 5.1, and 8.9 liter/minute, are 1.03, 1.18, 1.93, and 2.78 mm, respectively. It is not much difference between the average WFT results derived from the equation and direct measurement (less than 10%).

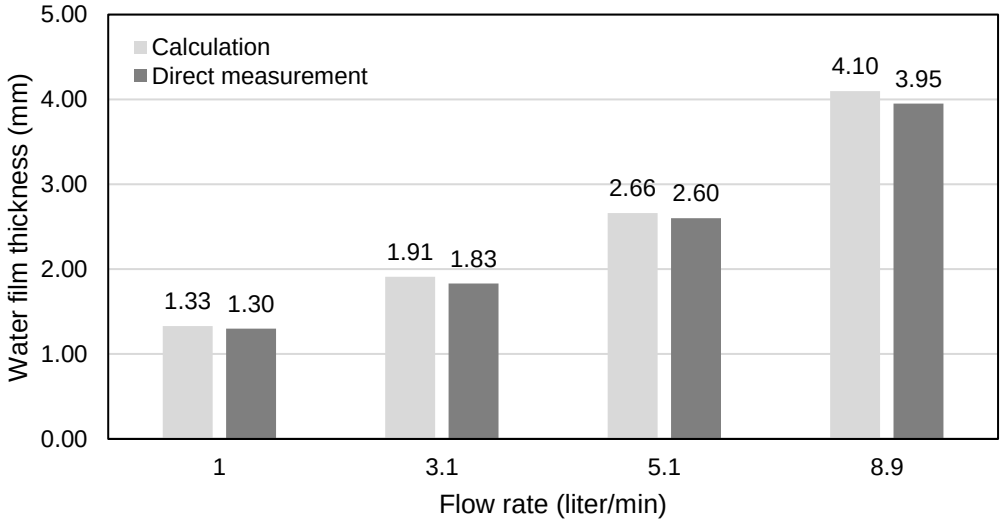

Figure 10.8 Average WFT on flat ECC surface (grade 1%)

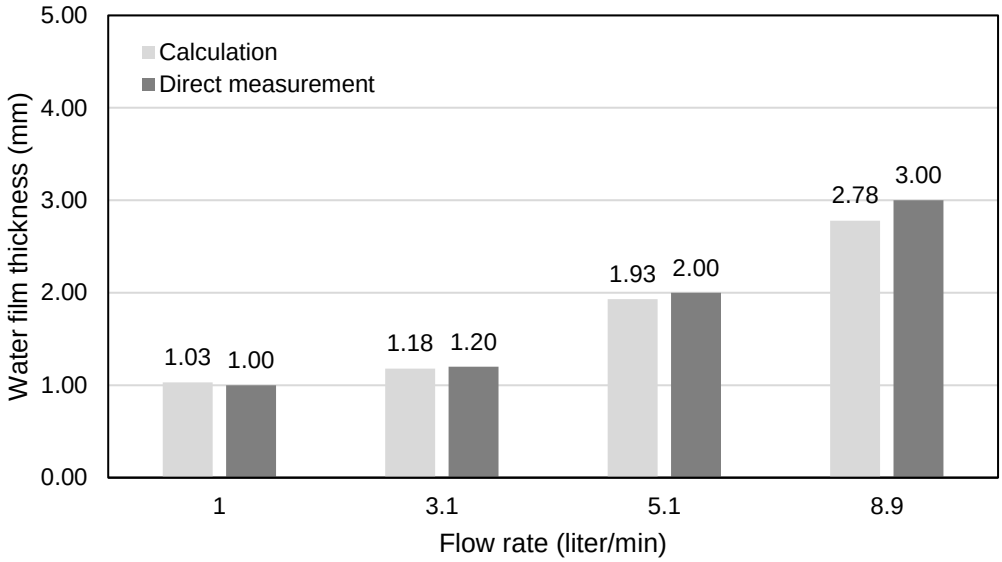

Figure 10.9 Average WFT on flat ECC surface (grade 5%)

The difference between the average WFT of ECC-Cor with a grade of 1% and 5% can be seen in Figure 13.2. Meanwhile the WFT on the edge the of pavement can be seen in Figure 10.11. As depicted from these figures, when the grade of the slab increased, the average WFT will be reduced.

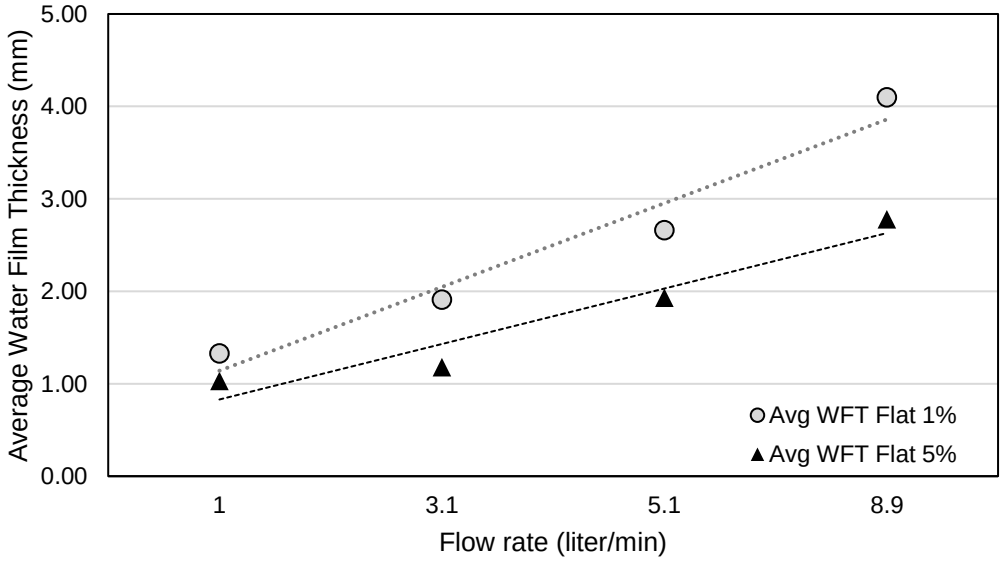

Figure 10.10 Average WFT on flat ECC surface (grade 1% vs 5%)

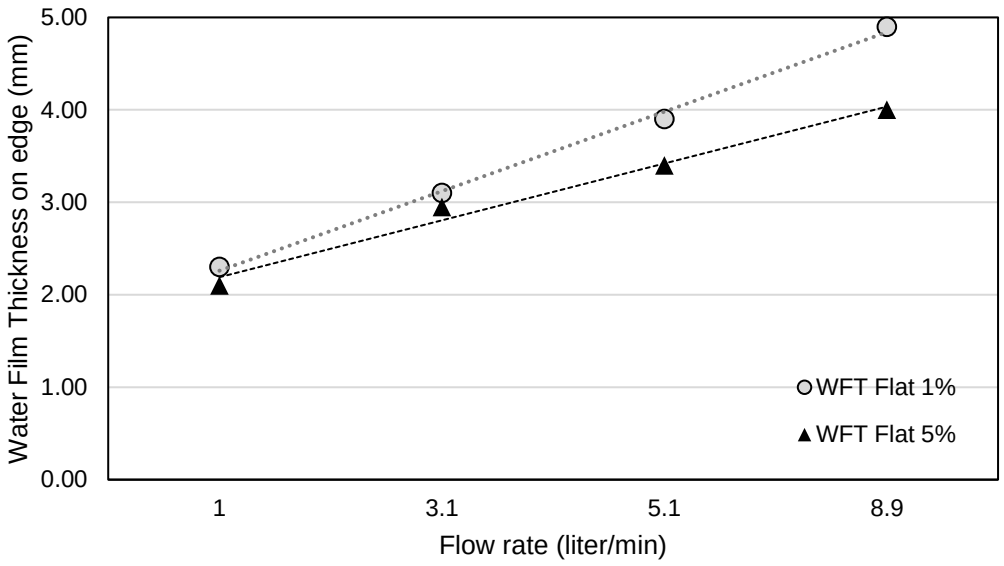

Figure 10.11 Average WFT on edge for flat ECC surface (grade 1% vs 5%)

10.3.4. Water film thickness on grooved ECC-Cor

It can be seen in Figure 10.12, the average WFT on grooved ECC-Cor for water drained above the ECC-Cor surface pavement (grade 1%) with a flow rate of 1.0, 3.1, 5.1, and 8.9 liter/minute, are 0.09, 0.15, 0.22, and 0.35 mm, respectively. It can be seen in Figure 10.13, the average WFT on grooved ECC-Cor for water drained above the ECC-Cor surface pavement (grade 5%) with a flow rate of 1.0, 3.1, 5.1, and 8.9 liter/minute, are 1.03, 1.18, 1.93, and 2.78 mm, respectively. It is not much difference between the average WFT results derived from the equation and direct measurement (less than 10%).

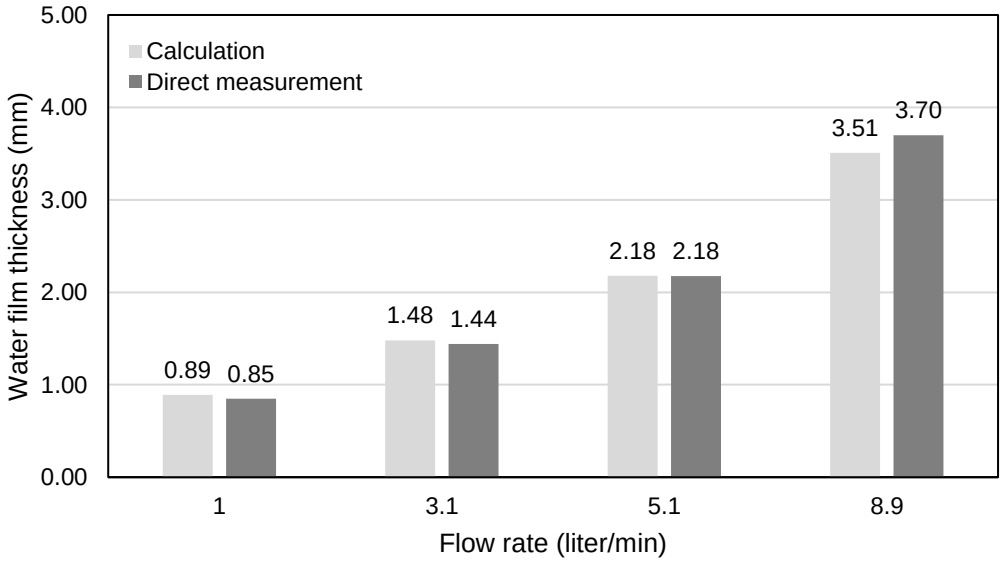

Figure 10.12 Average WFT on grooved ECC surface (grade 1%)

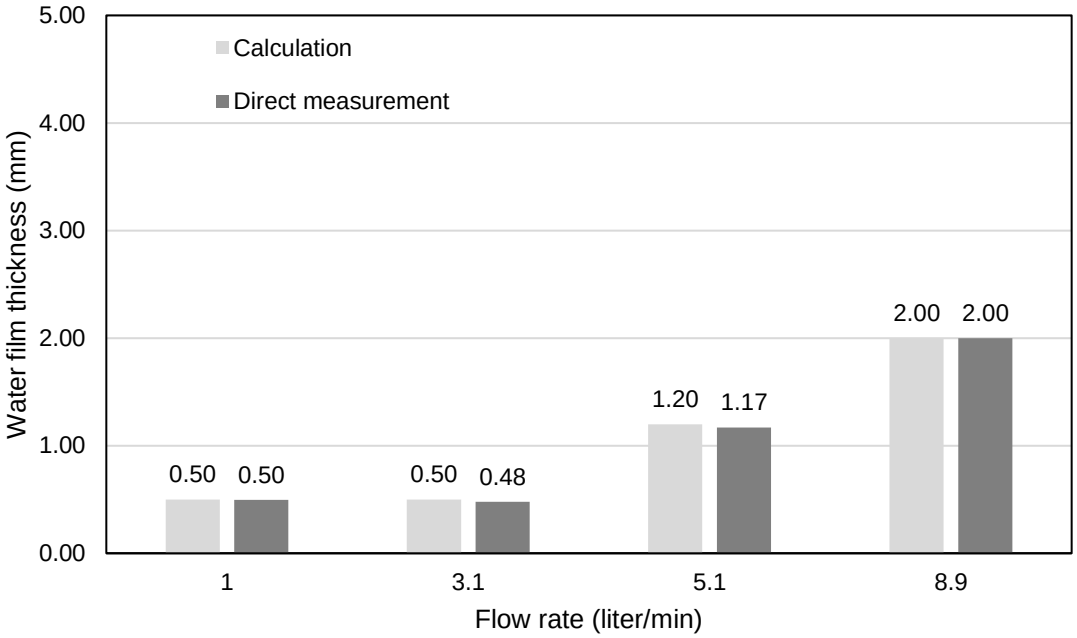

Figure 10.13 Average WFT on grooved ECC surface (grade 5%)

The difference between the average WFT of ECC-Cor with a grade of 1% and 5% can be seen in Figure 10.14. The WFT on the edge of the pavement can be seen in Figure 10.15. As depicted from these figures, when the grade of the slab increased, the average WFT will be reduced.

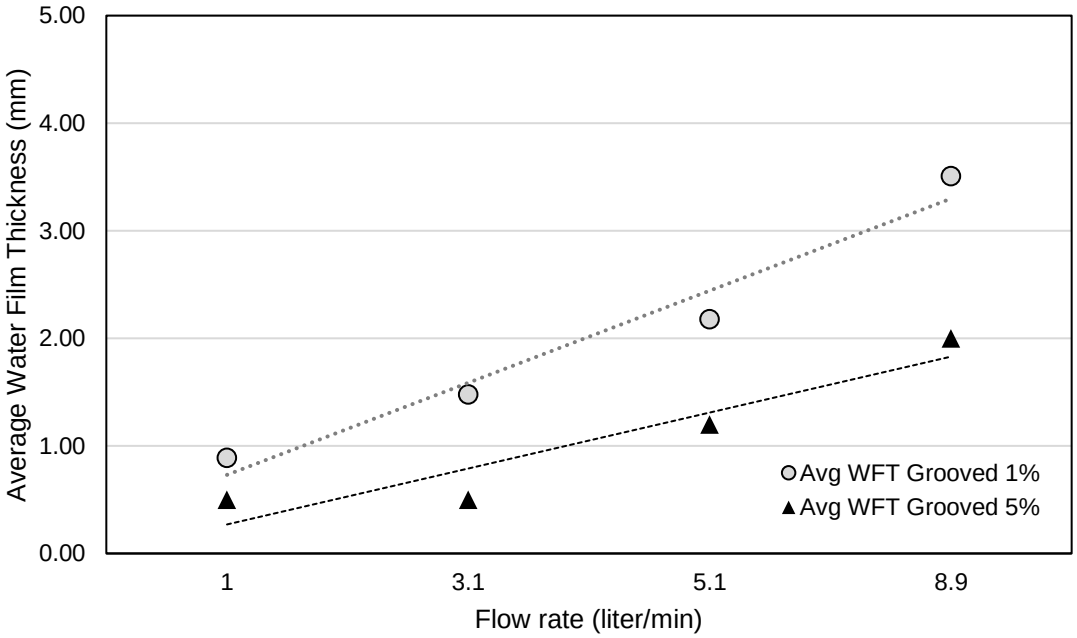

Figure 10.14 Average WFT for grooved ECC surface (grade 1% vs 5%)

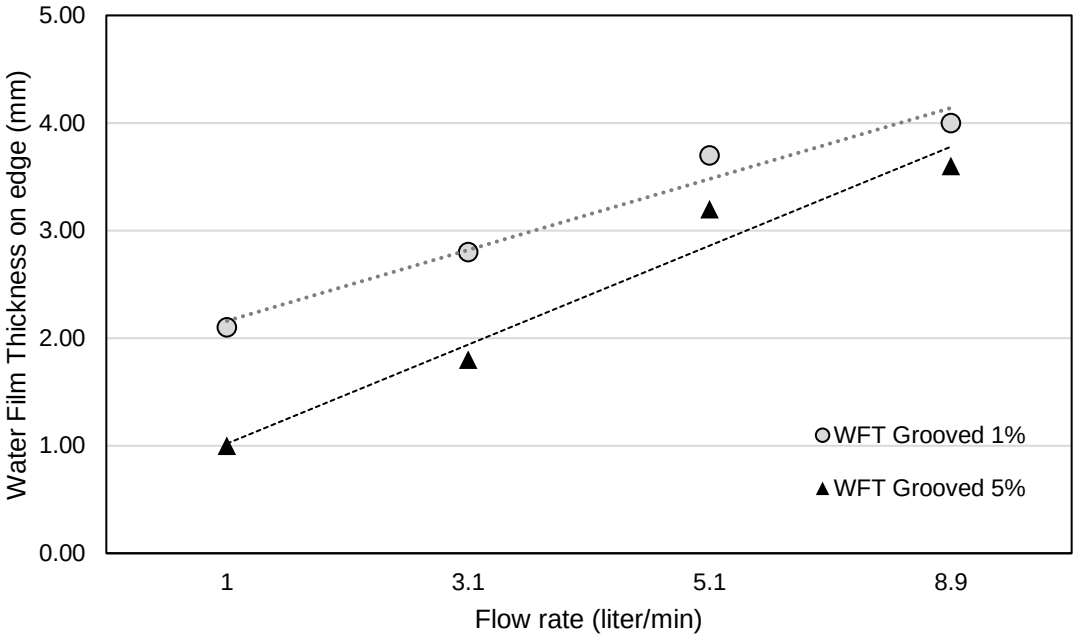

Figure 10.15 WFT on edge for grooved ECC (grade 1% vs 5%)

10.3.5. Water film thickness comparison between flat and grooved ECC-Cor

The WFT will be significantly decreased when such a surface pavement equipped with grooves. The comparison results between the flat and grooved ECC-Cor specimens can be seen in Figure 10.16 and Figure 10.17 for average WFT and WFT on edge, respectively.

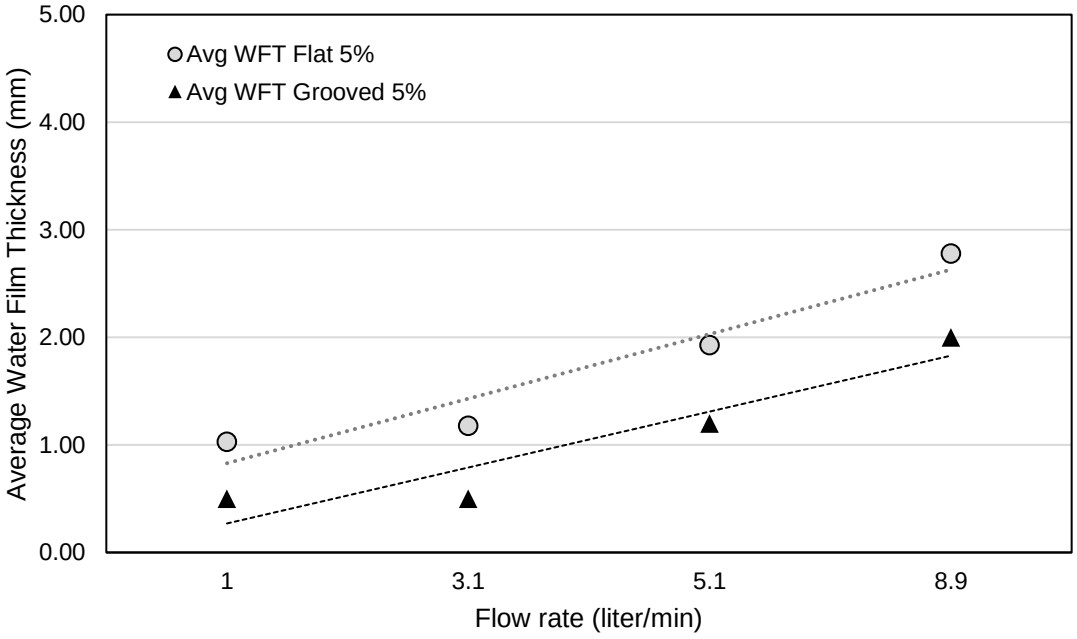

Figure 10.16 Average on WFT on flat vs grooved ECC-Cor (grade 5%)

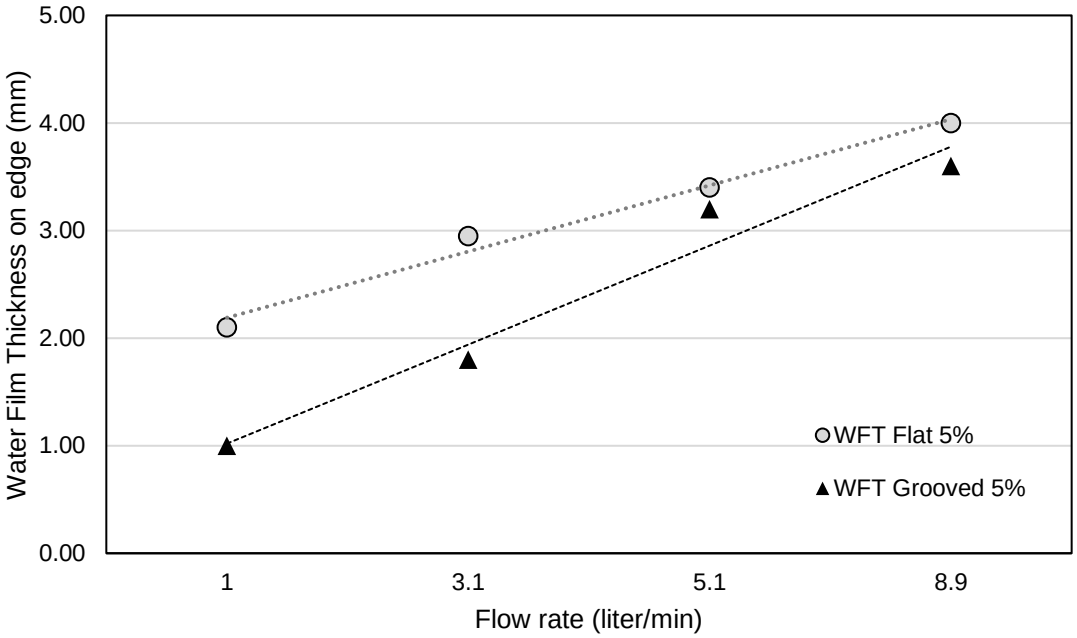

Figure 10.17 WFT on edge for flat vs grooved ECC-Cor (grade 5%)

In summary, conclusions can be drawn, including:

- The WFT will be significantly decreased when such a surface pavement equipped with grooves. As the water will fill the grooves immediately when it drained above the surface. Once, the grooved filled with water, the remaining water will only then drained along the original surface of the pavement.
- The grooves can reduce the WFT up to 50% of its original thickness, depends on the dimension of the grooves, as well as the grade of the pavement.
- The higher the grade, will result in more reduction of the WFT. With a similar dimension of grooves, the WFT is reduced up to 30% between the flat and grooved ECC-Cor with 1% grade. While the WFT can be reduced up to 50% between the flat and grooved ECC-Cor with 5% grade.

11. Study of Surface Water Drainage: Field investigation

11.1. Introduction

This chapter presents the investigation of surface water drainage on the full-scale application of modified ECC for pavement application. Data from various texturing methods applied in the field have been investigated and analyzed. The test includes water drainage performance with outflow meter. Different texturing methods applied to find the optimum solution to produce good surface properties for pavement application.

In comparison to laboratory scale, there are more variables that need to be considered for full-scale application of modified ECC i.e. temperatures, mixing method, and finishing work. Test results show that the surface water drainage of the surface pavement can be improved by adopting hard fine aggregates into ECC mix, as it provides both the micro- and macrotextures. It is also shown that texturing methods which was studied on laboratory scale tests can be further applied to full-scale application with consistent results.

11.2. Full-scale field investigation

11.2.1. Test program

Outflow tests have been performed on the field to investigate surface water drainage performance on full-scale application. Many ideal conditions which can be found in the laboratory is simply not existing on the field. The type of mixer, duration of mixing, temperature, casting process can be the factors which can simply change the results compare to results acquired from laboratory test scale. Various methods of surface treatments investigation in full-scale are summarized in Table 11.1.

Table 11.1 Site Investigation on surface water drainage based on surface treatments

No	Surface treatment method	Precast	Cast in place	Reference
1	Brushed ECC mixed with aggregates		Y	Ch. 8.2.1
2	Exposed aggregates into ECC surface	Y	Y	Ch. 8.2.2
3	Prefabricating modified ECC slabs with steel formwork	Y		Ch. 8.2.4
4	Reverse prefabricating slabs of ECC mixed with aggregates	Y		Ch. 8.2.5

The first method, brushed ECC mixed with aggregates, was done by using the same method mentioned in 8.2.1. Meanwhile, the second, third, and fourth methods are done according to the same method mentioned in chapter 8.2.2, 8.2.4, and 8.25, respectively.

Outflow meter tests were conducted to evaluate the drainage performance of the pavement through its surface and subsurface voids. It measures the duration of a known quantity of water taken to run through voids in the pavement texture and intended to provide a measure of the ability of the pavement to relieve pressure from the surface of the tires, thus indicating hydroplaning potential under wet conditions. A faster run time indicates a thinner film of water may exist between the tire [116]. The duration measured with digital timer with an accuracy of 0.00 sec. Minimum five tests were conducted with water with a temperature of 28 ºC in an outdoor environment (air temperature of 30 ºC). The grade and the cross slope of the specimens were measured using a digital inclinometer.

11.3. Results and discussions

11.3.1. Water outflow of brushed ECC-Cor

As can be seen from Figure 11.1, the outflow results of brushed ECC mixed with corundum improved when there is more corundum on the surface as they have been exposed (see after six hours and 21 hours). When the matrix is not fully hardened, more corundum aggregated have been removed away in the process. This phenomenon can be seen on the “after four hours exposed” part.

The difference between the time of processing does not affect water outflow results as all of them are below 10 s. It should be noted that based on microtexture and macrotexture, good results are coming from brushing time in the range between 6 to 12 hours. However, it should be mentioned that the results from field investigation are faster than results acquired in laboratory tests where outflow times are approximately more than 60 s and less than 10 s for laboratory tests and field investigation results, respectively. This occurs because the levelling process of ECC in a full-scale application is considerably difficult, resulting in rougher surface.

11.3.2. Water outflow performance of exposed ECC-Cor

OFT results for the exposed aggregates on ECC method, which is applied for slab and footpath application are shown in Figure 11.2. Additional results from concrete M45 which was applied on a footpath is also added for comparison. In comparison to the concrete surface with tining surfacing method, the modified ECC with exposed aggregates (both for footpath and slab) results in faster water outflow (less than 10 s). Thus, exposed aggregates on ECC surface shown as a good potential method to improve the surface water drainage.

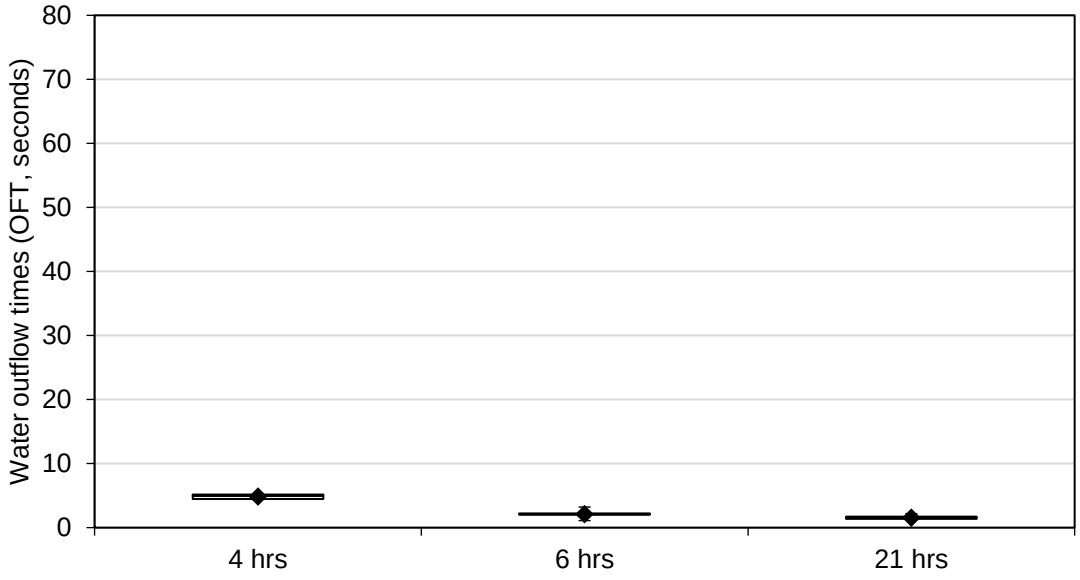

Figure 11.1 OFT of brushed ECC-Cor with cast in situ method

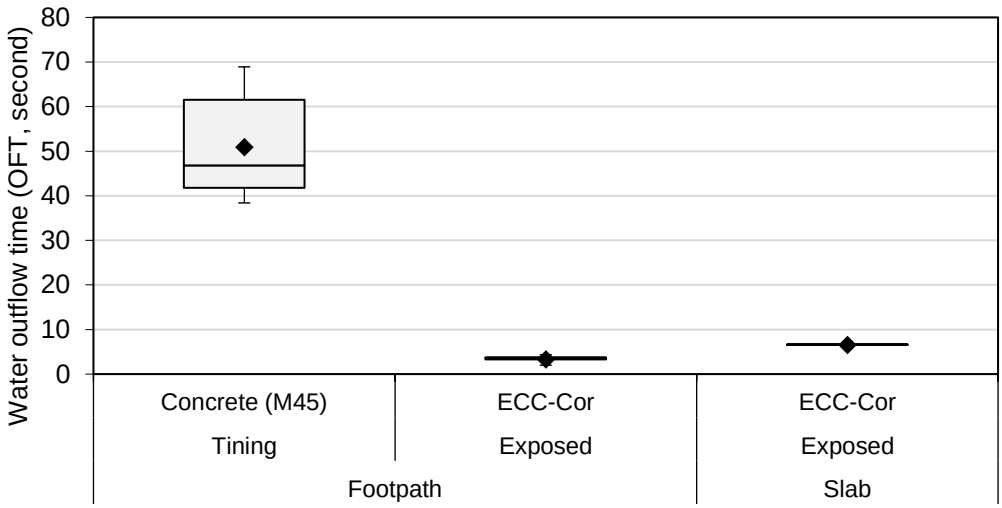

Figure 11.2 OFT of exposed aggregates on ECC

11.3.3. Water outflow performance of pavement made of ECC-Cor with precast method

OFT tests were taken on site at the busstop for slabs made with precast method, both with reverse and conventional precast. According to the results, which are shown in Figure 11.3, ECC-Cor with reverse precast method (method 4th), which is slab 01, results in a slower rate of outflow times compared to the conventional precast method (slab 02 to 11). This occurred due to ECC which made with reverse precast method produce a flat surface in comparison to conventional precast method. As we know, the flat state of the surface leads to lesser gap between surface of ECC and the rubber of the outflow meter.

Various results can be seen from ECC slabs made with conventional precast method (slab no 02 to 11). The results are range between 3 to 19 s, with an average of 7 s, in which again may happen due to unstandardized casting process. Less variety can be expected when slabs can be manufactured with more proper machines and human resources. The number of the slab is in accordance to the plan illustrated in Figure 8.9.

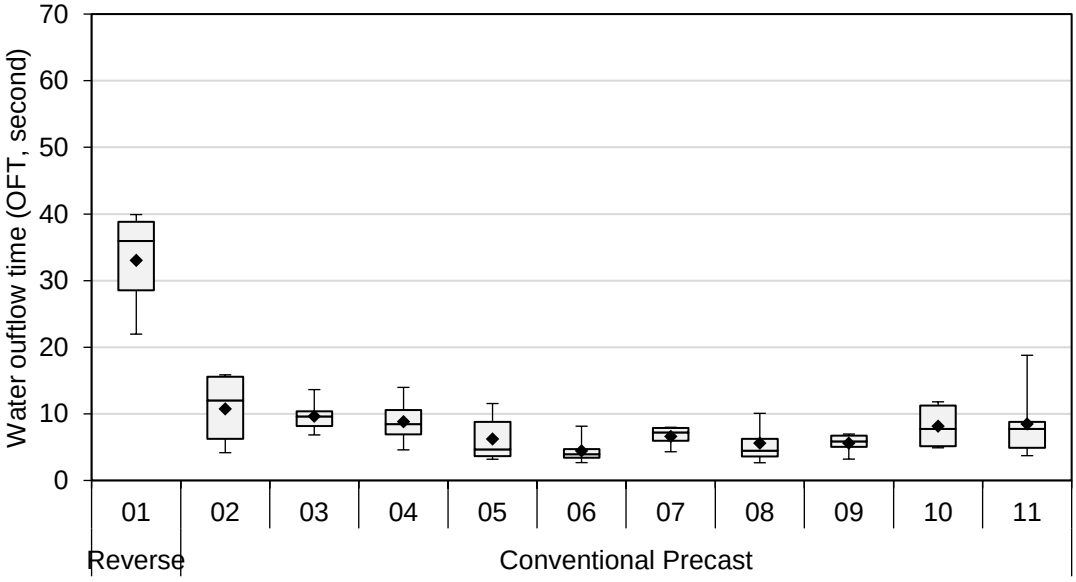

Figure 11.3 OFT of precast and reverse precast ECC-Cor (busbay application)

In summary, the brushed method can be used as a surface treatment for pavement made of ECC if the surface can be produced in a flat way. It is important to do the brushing not more than 24 hours to avoid the cementitious material is becoming completely hardened. Thus, it sticks to the surface while the surface of the pavement is expected to have some texture.

From the same results, another conclusion can be drawn that reverse precast method may produce much flatter surface compare to conventional precast method. However, the brushed method may produce a slower outflow rate in comparison to the exposed method.

12. Study of Surface Water Drainage: Numerical 3D CFX

12.1. Introduction

Chapter 12 describes the numerical study that employed by using ANSYS Fluent (Fluid Dynamics Analysis) in the study. The numerical study consists of the development of the 3D model for the simulation of surface water drainage. The 3D model includes the geometry development, mesh design, material properties, conditions, model validation and analysis. The objective of the model is to simulate how surface texture and geometry of pavement made of ECC will affect water surface runoff.

It has been highlighted that doing an analysis using a numerical model on water surface runoff will be helpful to study the rainfall loading on the highway in Singapore. Various textures, cross falls, and slopes which affect the surface drainage performance of the pavement can be studied by using fluid dynamics. However, until now, there is no numerical model on water surface runoff in Singapore condition where rainfall loading is considerably high. Such a study will be quite useful to determine the surface properties of pavement design for SRT.

12.2. Overview of CFD model by using ANSYS CFX

Computational Fluid Dynamics (CFD) is a software-based tool used for simulating behavior such as fluid flow, heat transfer, and other related physical processes. It works by solving the equations of fluid flow over a region with designed boundary. The equation is in conjunction with the Navier-Stokes. There are methods that can be used to solve CFD model. However, the most common one is the finite volume technique or also known as Finite Volume Model (FVM). In this FVM, the region of interest will be divided into small sub-regions, called control volumes. The equations are discretized and solved iteratively for each control volume. As results, an approximation of the value of each variable at specific points throughout the domain can be obtained [173].

Regarding CFD, ANSYS CFX provides comprehensive modelling capabilities for a wide range of incompressible and compressible, laminar and turbulent fluid flow problems. Steady-state or transient analyses can be performed. In ANSYS CFX, a broad range of mathematical models for transport phenomena (like water transfer) is combined with the ability to model complex geometries.

Simulation of water transport can be done using the Volume of Fluid (VOF) Model. The VOF model can model two or more immiscible fluids by solving a single set of momentum equations and tracking the volume fraction of each of the fluids throughout the domain. ANSYS CFX can model the effects of open channel flow (for example, rivers, dams, and surface-piercing structures in unbounded stream) using the VOF formulation and the open channel boundary condition. These flows involve the existence of a free surface between the flowing fluid and fluid above it (generally the atmosphere). In such cases, the wave propagation and free surface behavior becomes important. Flow is generally governed by the forces of gravity and inertia. This feature is mostly applicable to marine applications and the analysis of flows through drainage systems.

Free surface flow refers to a multiphase flow situation where the phases are separated by a distinct interface. Examples of free surface flows include open channel flow, flow around ship hulls, tank filling problems, Pelton turbines, and many others. Free surface flow with the homogeneous model should be used when possible.

Free surface flow model criteria:

- For the Buoyancy Reference Density, choose the density of the light fluid (air). This simplifies the definition of pressure, and hence the specification of pressure initial and boundary conditions. In the hydrostatic limit:
- At pressure outlets, the elevation of the water must usually be known as part of the problem definition. The mechanism used to enforce this elevation is to set a pressure profile consistent with the known elevation. In some circumstances, the elevation is not known in advanced. In this case, it is best to specify a pressure profile consistent with an estimate for the outlet elevation. This assumption should not affect the flow other than possibly inducing a small kink in the flow just upstream of the outlet condition.
- The initial conditions for the pressure field and volume fraction must be consistent (that is, the pressure field is hydrostatic in the heavy phase and uniform in light phase). This is easily done using CEL step functions. For example, the functions:

(a) (b)

Figure 12.1 Liquid phase of fluid dynamic model [173]

12.3. Material Properties

Material properties are determined in the early stage in ANSYS development. Materials used for the CFX model includes ECC for the sample tested, water and air. Those are the inputs in Engineering Data module in ANSYS software. ECC has an Elastic Modulus of 18 to 34 GPa with Poisson's ratio of a range from 0.15 to 0.20 [51,167]. In this 3D FEM model, the value of 22 GPa and 0.15 were adopted for elastic modulus and Poisson's ratio, respectively. The densities of ECC samples were calculated: 2040 kg/m^3 and 2190 kg/m^3 for the ECC mixed corundum with Pour and Precast Method. Therefore, for this model, an average value of 2100 kg/m^3 has been used for the density of the specimen. This is complying with typical Portland cement mortar which normally has the density around 2000 to 2200 kg/m^3. However, in this model analysis, the density might not affect much for the results. Normal material properties for water and air has been used.

Table 12.1 Material properties for CFX model on surface water drainage

Material	Water	ECC
Elastic modulus (MPa)	N.A	22.000
Poisson ration	N.A	0.15
Density (kg/m^3)	997	2100

12.4. Geometry Model

A 3D model of the surface water drainage test on ECC surface was created with DesignModeler tool in ANSYS. As can be seen in Figure 12.2, the dimension of the ECC specimen is set accordingly to the actual measurement. The model consists of two parts: (1) the main body, with a dimension of 2 m by 0.5 m by 0.05 m, made of ECC material is where the water and air can flow on top of the surface. The angle of the body can be adjusted according to needs. In this study, it was designed for an angle of 1^o and 5^o. In Figure 12.2b, it can be seen that the main body angle is adjusted to an angle of 1^o, (2) the second body is attached to the main body, as it was designed as the output of the water from the main body. The second body is fixed (its angle cannot be adjusted).

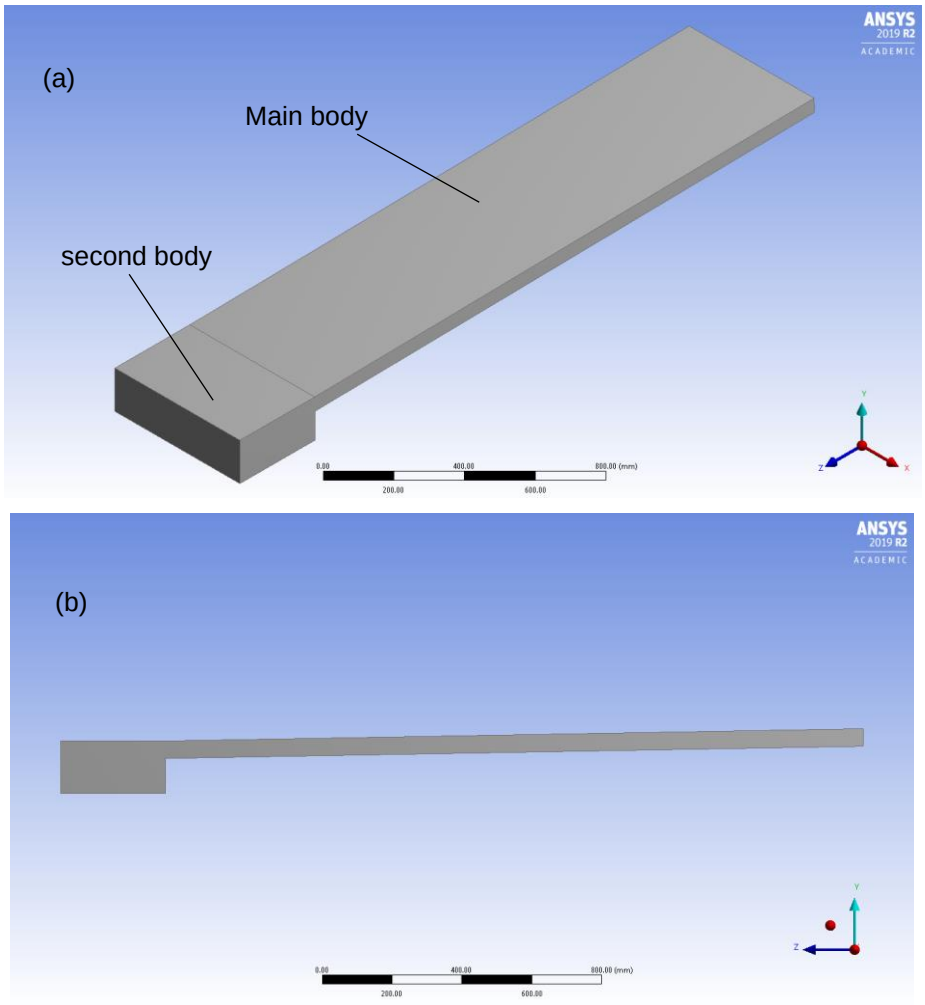

Figure 12.2 3D CFX model on surface water drainage (a) bird view (b) side view

12.5. Mesh Design

The main objective of this 3D CFX model is to simulate the surface water drainage performance on the ECC sample. The meshing was created with the help of Sweep Method and Face Sizing tools to create a rectangular shape with a maximum element size of 0.5 mm. The meshing comprised of 1589367 nodes and 375000 elements.

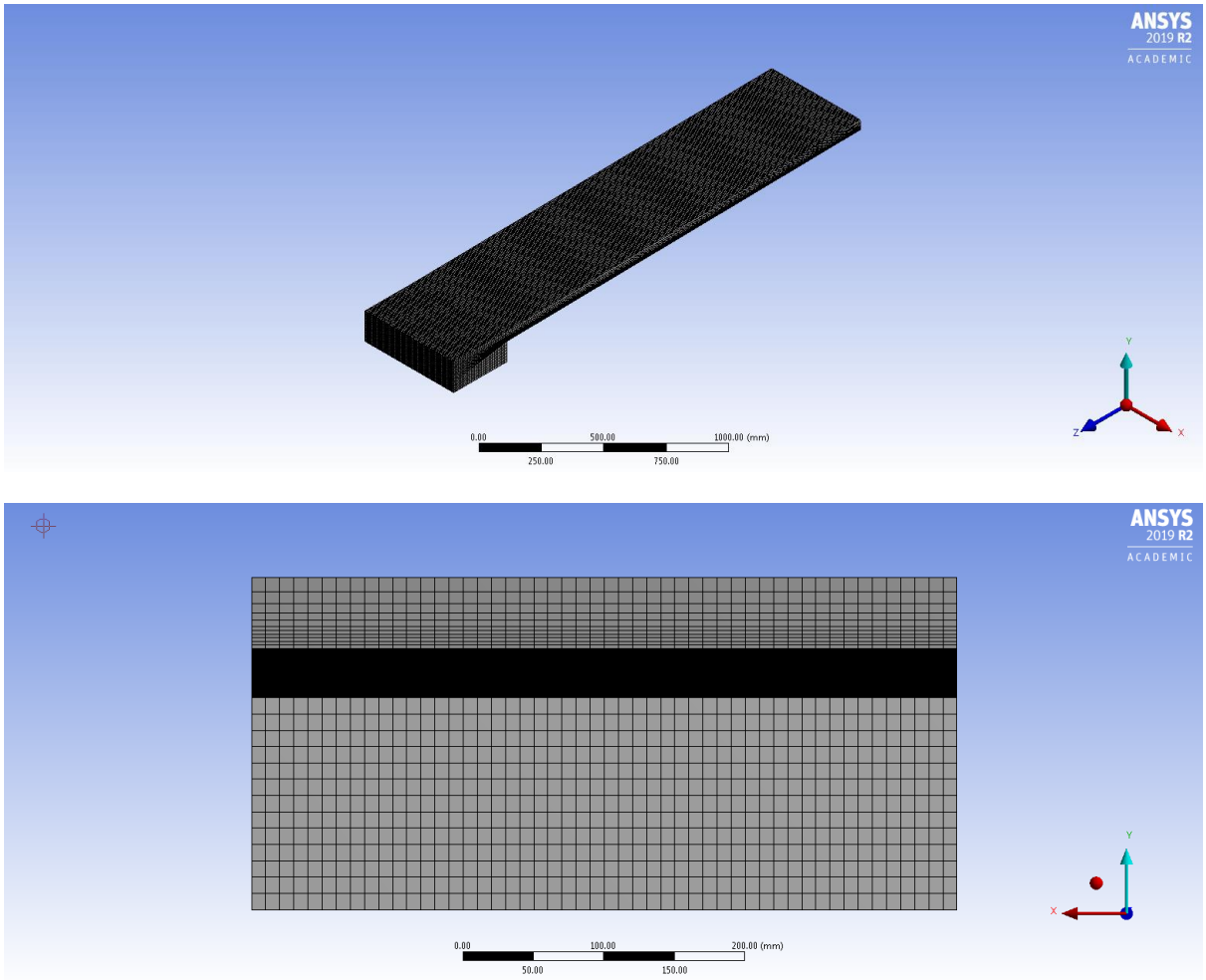

Figure 12.3 Meshing design on 3D CFX model (a) from general view, (b) with denser mesh at “inlet”

The quality of the mesh has been checked in ANSYS program. ANSYS recommend keeping minimum orthogonal quality above than 0.1. Another parameter is the aspect ratio, which can be calculated by the length divided by the height. This model has the aspect ratio of 5.99 as average. Even though the Element Quality and Aspect Ration showing the rather low-quality meshing, but it is still acceptable as these values are generated from the average of the whole system. More importantly, it is the meshing where the water is flowing where the meshing was designed denser. The results for meshing are summarized in Table 12.2.

Table 12.2 Quality of meshing for 3D FEM model of surface water drainage test

Criteria	Value	Standard criteria
Element quality	0.38 ± 0.21	0 to 1 0 is worst, 1 is best
Orthogonal quality	0.79 ± 0.17	0 to 1 1 indicates a perfect cube or square; while 0 indicates element has a zero or negative volume
Aspect ratio	5.99 ± 3.3	The best possible quadrilateral aspect ratio is 1

12.6. Surface Water Drainage 3D CFX Model

The 3D CFX surface water drainage model is designed based on the steady-state model. A flow that is not a function of time is called steady flow. Steady-state flow refers to the condition where the fluid properties at a point in the system do not change over time. Time-dependent flow is known as unsteady (also called transient). Whether a particular flow is steady or unsteady, it can depend on the chosen frame of reference. For instance, laminar flow over a sphere is steady in the frame of reference that is stationary with respect to the sphere. In a frame of reference that is stationary with respect to a background flow, the flow is unsteady.

Turbulence is flow characterized by recirculation, eddies, and apparent randomness. Flow in which turbulence is not exhibited is called laminar. It should be noted, however, that the presence of eddies or recirculation alone does not necessarily indicate turbulent flow—these phenomena may be present in laminar flow as well. Mathematically, turbulent flow is often represented via a Reynolds decomposition, in which the flow is broken down into the sum of an average component and a perturbation component.

The Reynolds number (Re) is an important dimensionless quantity in fluid mechanics used to help predict flow patterns in different fluid flow situations. It has wide applications, ranging from liquid flow in a pipe to the passage of air over an aircraft wing. With respect to laminar and turbulent flow regimes: laminar flow occurs at low Reynolds numbers, where viscous forces are dominant, and is characterized by smooth, constant fluid motion. While, turbulent flow occurs at high Reynolds numbers and is dominated by inertial forces, which tend to produce chaotic eddies, vortices and other flow instabilities. The Reynolds number is defined as:

$$R_e = \frac{\rho u L}{\mu} = \frac{u L}{v} \qquad \text{(Eq. 34)}$$

Where:
- ρ density of the fluid (SI units: kg/m^3)
- u velocity of the fluid with respect to the object (m/s)
- L characteristic linear dimension (m)
- μ dynamic viscosity of the fluid (Pa·s or N·s/m^2 or kg/(m·s))
- ν kinematic viscosity of the fluid (m^2/s).

There are at least four boundaries need to be set up in this model, namely as (1) inlet, (2) outlet, (3) free, and (4) ECC. Boundary needs to be set up as it functioned as artificial walls in order to prevent the water (fluid) flowing from the system to outside. The inlet was set up as “inlet”, which produces a low intensity of turbulence. The volume fraction of water is 1, while air is 0. The outlet was set up as “outlet” with option Average Over Whole Outlet to get distributed output. The free-body was set up as “opening”, which produces a low intensity of turbulence. The volume fraction of air is 1, while water is 0. And then ECC was set up as “wall”.

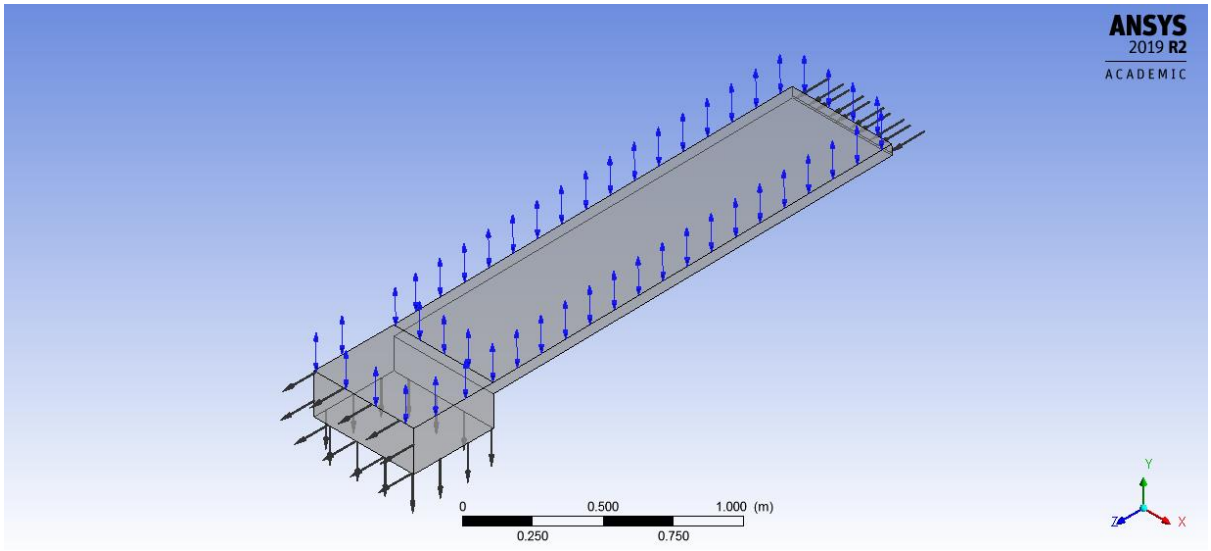

Figure 12.4 Boundary set up in CFX model system

12.7. Model Validation

The 3D CFX surface water drainage model has been calibrated and validated including (1) roughness properties, (2) the calibration of correlation between WFT measurement in a laboratory test with WFT results generated from CFX 3D model.

The ECC surface property in the 3D model has been calibrated accordingly as a rough wall with sand grain roughness set up based on the macrotexture property of ECC, which is 0.36 mm. This means the study considered the effect of surface roughness on the flow of the water. The roughness of the surface, which is set as a wall in the model, will add an additional term to the equation that reduces the mean velocity of the water along the wall [174,175]. In this CFX model, the conversion from a real roughness height (K) of ECC material can be safely assumed to an equivalent roughness height (K_s), which then derived as ($K = K_s$) [176]. In results, the ECC wall is physically displaced in upwards direction by $K_s/2$ (ANSYS).

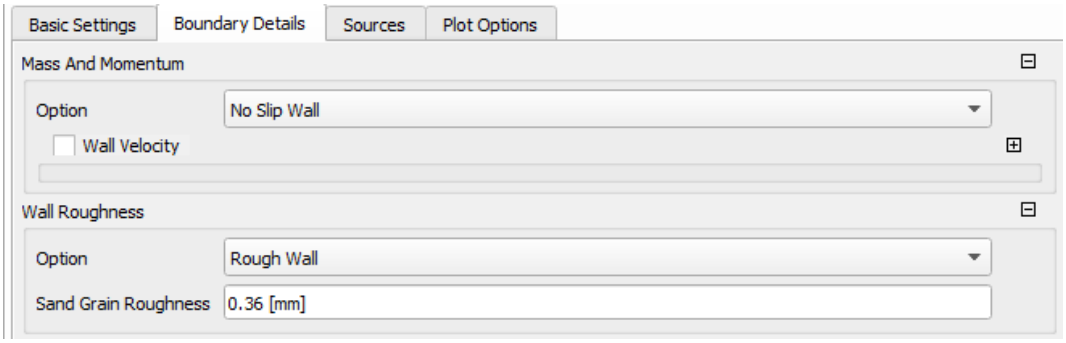

Figure 12.5 Wall roughness in CFX model

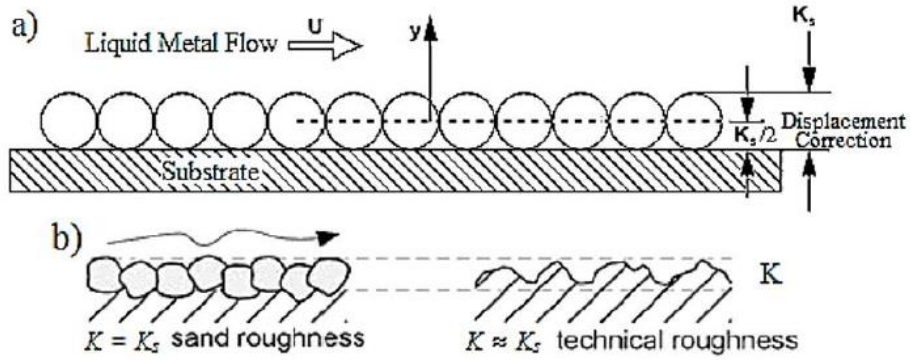

Figure 12.6 Equivalent sand grain roughness (a) monolayer of spheres as rough layer in the CFX model, (b) compaison of real roughess and its equivalent sand roughness (ANSYS)

In order to validate the model, two full-scale of ECC specimens were built with a dimension of 2 m by 0.5 m by 0.1 m. One ECC specimen is with a smooth surface, and the other one is equipped with grooves. Then the water flowing above the ECC surface with a steady flow rate. The angle of the ECC specimen is adjusted to a certain angle (1%). Then the water film thickness above the ECC specimen is measured with minimum nine measurements (three measurements on 1/3 length of the specimen, three measurements on ½ length of the specimen, and the rest three measurements on 2/3 length of the specimen). The average value is then taken and then used to validate the CFX model.

12.8. Results and Discussions

The results will be derived after the solution can be converged through simulation. Convergence control was set up with 2500 maximum iterations with residual target 0.0001, meaning the solution will stop and derived when the residual RMS reach this value. This value is taken as it is considered as good results with very minimum standard deviation (ANSYS).

Two methods are used to show the results of the 3D CFX model. Firstly, by using isosurface where the surface of the water can be generated automatically. The input used for the isosurface is the water volume fraction with water velocity as a variable. Secondly, the results can be generated by using streamline or isoclip, where several lines are representing the surface of the water. The isosurface meant more for visualization, as it produces better image and or video for the animation of the water above the ECC specimen itself. This method can be used for quick analysis, whether the model and results generated are properly working. Once the model is working, more detail results can be generated with streamline. With streamline / isoclip, the water flow will be generated in the shape of lines. Both results of isosurface and streamline can be seen in Figure 12.7. More results can be seen in Appendix H.

As can be seen in Figure 12.8 and Figure 12.9, the elevation of the water and the concrete lines are plotted in the same chart. The elevation is a relative value. The only important parameter is the difference in the elevation between the water and concrete lines, which is then calculated as the water film thickness. In this study, the average value of the water (surface) lines is taken and considered as the main value which will later use as a comparison to the results from the laboratory tests. Both results from 3D CFX model and laboratory measurement (including results from the proposed equation) are summarized in Table 12.3.

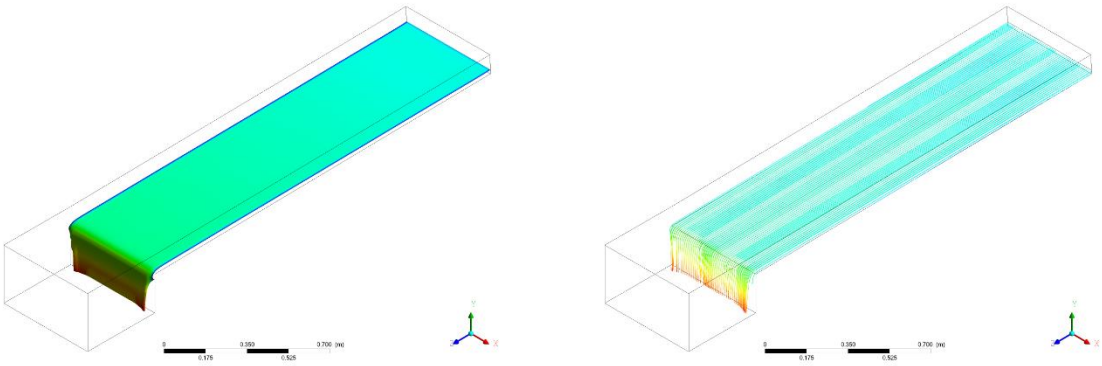

Figure 12.7 CFX results of WFT on ECC-Cor with (a) isosurface, (b) isoclip

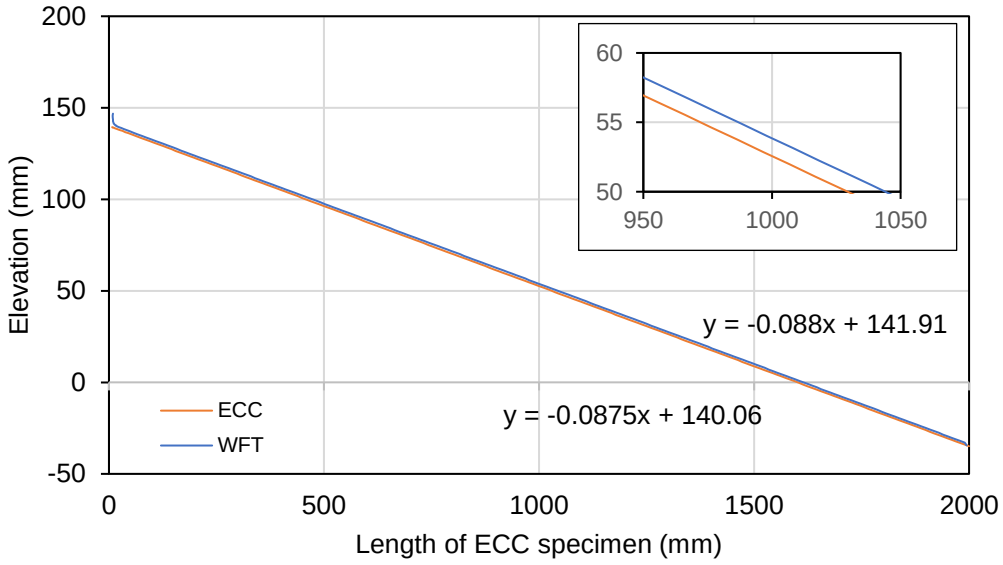

Figure 12.8 Elevation of water and ECC-Cor based on isoclip method with CFX

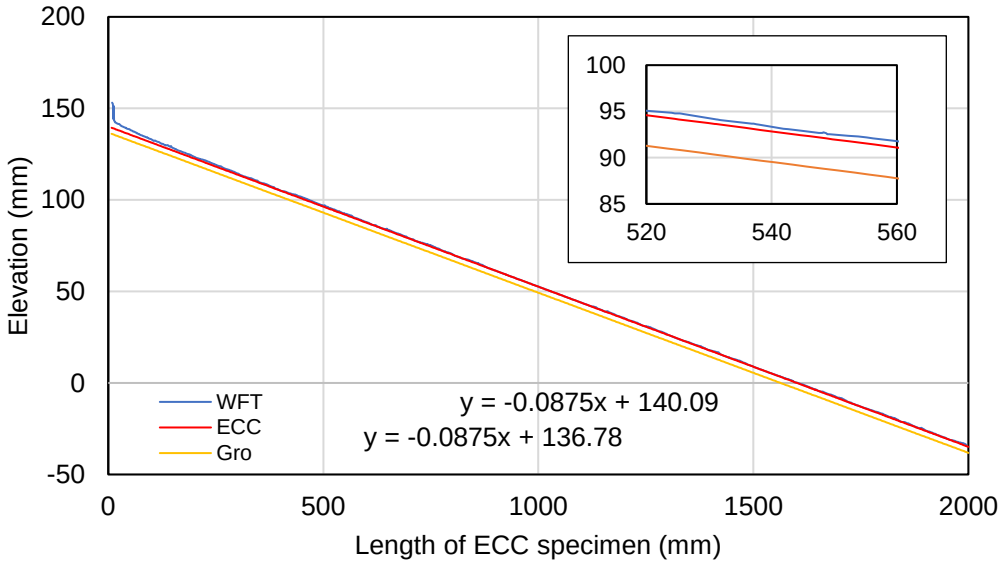

Figure 12.9 Elevation of water and ECC-Cor Gro based on isoclip method with CFX

Table 12.3 WFT results comparison between lab tests and CFX model

Mixture	MTD	Grade (%)	Water Film Thickness (mm)			Difference (%)	
			CFX	Lab Test	Eq. 33	CFX vs Lab	CFX vs Eq. 33
ECC-Cor	0.36	1	1.26	1.33	1.30	5.6%	3.4%
		5	1.00	1.03	1.00	3.3%	0.5%
ECC-Cor Gro	0.36*	1	0.88	0.89	0.85	1.1%	3.5%
		5	0.53	0.50	0.50	5.6%	5.6%

*on the surface only

As can be seen from the results summarized in Table 12.3, a validated 3D CFX model gives good correlation in comparison to results from the laboratory tests as well as results derived from the (Eq. 33 for water film thickness on ECC-Cor. Maximum and minimum differences are 5.6% and 3.3%, respectively, is observed between results from CFX model and laboratory test. Meanwhile, the difference of results between CFX model compares to the equation are about 3.4% (maximum) and 0.5% (minimum). The validated 3D CFX model also gives a strong correlation with a lab test and equation results. In comparison to lab tests, the 3D CFX model gives 1.1% and 5.6% differences for 1% and 5% grades, respectively. While in comparison to (Eq. 33, the 3D CFX model gives 3.5% and 5.6% differences for 1% and 5% grades, respectively. This means 3D CFX model can be used to study and to design a surface water drainage. Several parameters can be studied with this model, including the effect of macrotexture, effect of grade, and the effect of grooves to water film thickness.

Higher grade of a specimen, which correlates to the grade or the cross slope of pavement design, leads to thinner WFT. On flat ECC-Cor specimen, the increase of the grade from 1% to 5% will reduce the WFT up to 21%. While for grooved ECC-Cor, the WFT of 5% grade specimen is 44% thinner compared to 1% grade specimen.

Grooves on ECC-Cor specimens reduce the WFT on the surface. With the same total area (2 m x 0.5 m), the WFT on grooved ECC-Cor surface will be more than 50% decreased in comparison to ECC-Cor surface. The number is, however, might be varied on the dimension of the grooves (width, length, and thickness). In consequence, thinner WFT will cause a higher safety for motorists/vehicles as it creates smaller risks of hydroplaning effect between tire of vehicles and pavement in wet condition.

The roughness of the material, which is sand grain roughness in the CFX model, is negatively affecting the velocity of the water flow. The higher roughness of the material applied, the slower is the water flow in results. This means surface water drainage model must be designed carefully. When the wall is designed to have roughness, it will reduce the water flow, especially on the wall parts. In results, the water flow in the middle part will flow faster compare to the water in the wall area part.

13. Study of Correlation between Skid Resistance and Surface Water Drainage Performance

13.1. Introduction

This chapter elaborates the correlation between the skid resistance and the surface water drainage performance based on analysis from data collected and numerical simulation modelled. It has been discussed in previous chapters, that the safety on riding experience is mainly related to skid resistance and surface water drainage. Previous study [177] mentioned one case where there is one method which is able to provide good skid resistance but not surface water drainage. This fact emphasizes that those two criteria should be designed well that they are contributing to the safety comprehensively.

In this study, corundum as fine aggregate is first incorporated into ECC mix (ECC-Cor) to improve the surface microtexture. The resulting ECC-Cor possesses satisfactory mechanical performance and high skid resistance (BPN > 70). ECC-Cor also shows good durability as the microtexture and macrotexture can last for more than 100,000 load cycles. While the addition of corundum significantly enhances the microtexture and skid resistance, improvement on macrotexture and surface drainage is marginal. Further surface treatment with grooves successfully improves the functional performance, not only by minimizing the risk of hydroplaning (water outflow time < 4 s) but also by improving the skid resistance (BPN > 90). An empirical model, which correlates water drainage to macrotexture and pavement geometries of ECC, is proposed.

13.2. Experimental program

13.2.1. Materials and mixture design

Type I Portland cement, class F fly ash (FA), micro-silica sand (mean and maximum grain size of 110 μm and 200 μm, respectively), polyvinyl alcohol (PVA) fibers (length of 12 mm, diameter of 39 μm, nominal tensile strength of 1600 MPa), a high-range water reducing (HRWR) were used to prepare the mix.

To enhance skid resistance, in this study, corundum with maximum particle size of 2.38 mm was used as fine aggregates for improving the surface textures of ECC. The material size distribution of corundum is given in Figure 13.1. Corundum is a crystalline form of aluminum oxide (Al2O3) with extremely high hardness [178]. It is rated at nine on Mohs scale of mineral hardness, where diamond rated as 10, whereas the most common mineral in aggregates, quartz, only rated as 7 [179,180]. Based on field experience in Swiss, corundum was used to ensure high skid resistance for the surface of concrete pavement [178].

Table 13.1 summarizes the mixture design of ECC incorporating different amount of corundum (ECC-Cor). A control ECC mixture without the addition of corundum (ECC-Cor 0) was also prepared. All ECC-Cor mixtures have a low water-to-cementitious material ratio (w/cm) of 0.27. Micro-silica sand was replaced with corundum at different dosage, ranging from 50-100%, and the mixture was denoted as ‘ECC-Cor #’, indicating # with % of micro-silica sand was replaced with corundum.

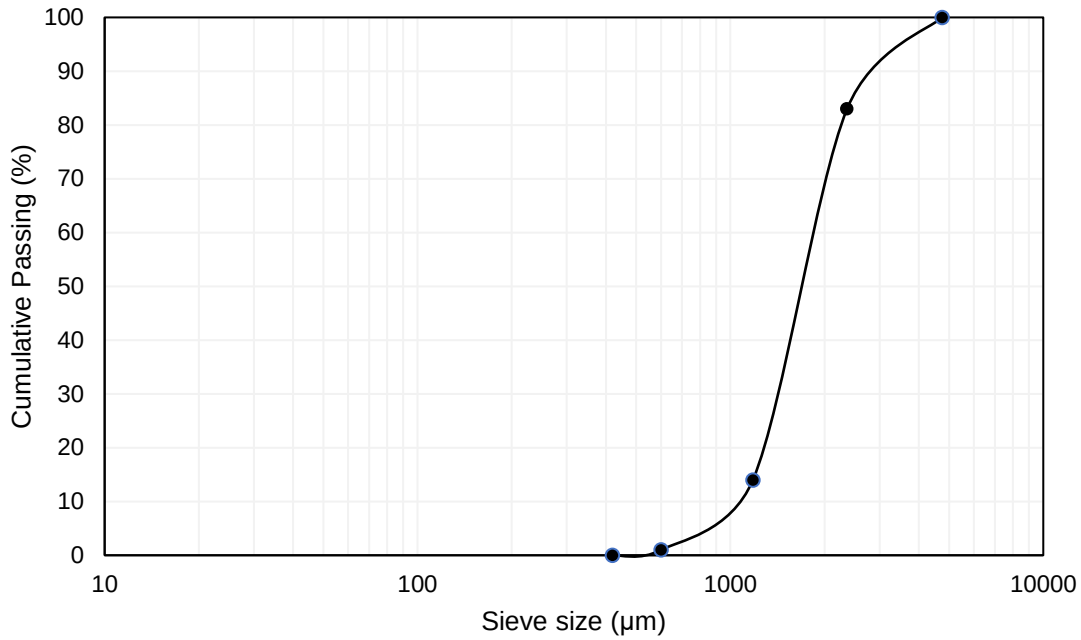

Figure 13.1 Size distribution of corundum aggregate

Table 13.1 Mixture design of ECC-Cor (kg/m^3)

Mixture	Cement	Fly ash	Sand	Corundum	Water	PVA	HRWRA
ECC-Cor 0	559	671	447	0	327	26	2.3
ECC-Cor 50	559	671	224	224	327	26	2.3
ECC-Cor 60	559	671	179	268	327	26	2.3
ECC-Cor 70	559	671	134	313	327	26	2.3
ECC-Cor 80	559	671	89	358	327	26	2.3
ECC-Cor 90	559	671	45	402	327	26	2.3
ECC-Cor 100	559	671	0	447	327	26	2.3

13.2.2. Specimen preparation

ECC-Cor mixture was prepared in a planetary mixer. Cement, fly ash, and micro-silica sand are dried mixed first. Water was then added followed by the addition of superplasticizer and mixed for 3-5 mins until the mix achieved the required consistency. Lastly, the PVA fiber and corundum were added and mixed for another 3-5 mins. The fresh mixture was cast into prism (280 mm by 70 mm by 50 mm) and plate (500 mm by 300 mm by 10 mm) moulds catered for various types of tests. Specimens were removed from the mould after 1 day and were cured at normal laboratory air (25±3^{o}C, 70%RH) for another 27 days before further testing. At the pre-determined age, either 1 d or 3 d, the top surface of plate specimens was treated with a steel brush to expose the corundum on the surface.

An alternative specimen preparation method was also investigated in the current study. The alternative method has the objective to have a sufficient skid resistance with less corundum used. Instead of mixing corundum into the ECC mixture, corundum (150 kg/m3) was first spread and distributed uniformly on the base of the plate moulds, followed by casting ECC-Cor 0 into the mould. The specimen is named ECC-Cor 0-S. Plate specimens were removed from the mould after 1 d, followed by curing at normal laboratory air (25±3oC, 70%RH) for another 27 days before further testing.

To study the effects of surface macrotexture on skid resistance and surface water drainage performance of ECC-Cor, parallel grooves were created on surface of ECC-Cor 80 specimens (500 mm by 300 mm by 10 mm) using a concrete cutter machine. The concrete cutter was equipped with a blade of 350 mm in diameter and 3.2 mm in thickness. The blade position is adjustable, so it can slide forward and backward, while the level can be fixed to make a groove with the specified depth. Four macrotextures were evaluated, and the corresponding groove dimensions are summarized in Table 37.

13.2.3. Test program

Table 13.2 summarizes the test program of the current study. Mechanical properties, skid resistance, surface water drainage performance, and durability were evaluated using the four-point bending test (FPBT), the British Pendulum test (BPT) and the sand patch method (SPM), the outflow meter test, and the wheel tracking test (WTT), respectively.

Table 13.2 Test Program

Mixture	Mechanical Properties		Skid Resistance		Surface water drainage performance	Durability
	MOR	Ductility	Microtexture	Macrotexture		
	FPBT	Inverse	BPT	SPM	OFT	WTT
ECC-Cor 0	Y	Y	Y	Y		
ECC-Cor 50	Y	Y	Y	Y		Y
ECC-Cor 60	Y	Y	Y	Y		
ECC-Cor 70	Y	Y	Y	Y		
ECC-Cor 80	Y	Y	Y	Y	Y	
ECC-Cor 80-Gro 1			Y	Y	Y	
ECC-Cor 80-Gro 2			Y	Y	Y	
ECC-Cor 80-Gro 3			Y	Y	Y	
ECC-Cor 80-Gro 4			Y	Y	Y	
ECC-Cor 90	Y	Y	Y	Y		
ECC-Cor 100	Y	Y	Y	Y		Y
ECC-Cor 0-S			Y	Y		

Microscopic skid resistance was evaluated following ASTM Standard Test Method for Measuring Surface Frictional Properties Using the British Pendulum Tester [90]. The test results are reported as British Pendulum Number (BPN). Plate specimens for BPT have a dimension of 500 mm by 300 mm by 10 mm. The tests were conducted in wet test conditions by spraying water on the specimens. At least three specimens were evaluated for each mix and a minimum of five tests were performed for each specimen. BPT was also used to demonstrate the effects of macrotexture provided by the grooves. Previous studies mentioned that BPT is reliable for defining both microtexture and macrotexture [98,164]. However, the macroscopic skid resistance was mainly evaluated using SPM, a volumetric-based spot test method with sand patch. The method is based on ASTM Standard [91,181] and can be used to determine the Mean Texture Depth (MTD) of pavement, which reflects the macrotexture characteristic of surface.

Surface water drainage performance was evaluated using the outflow meter (OFM) test in accordance with ASTM E2380M-15, Standard Test Method for Measuring Pavement Texture Drainage Using an Outflow Meter. The OFM consists of a transparent cylinder rests on a rubber which placed on the surface of specimen. It measures the duration of a known quantity of water taken to run through voids in the pavement texture (i.e., water outflow time, OFT) and intends to provide a measure of the ability of the pavement to relieve pressure from the surface of the tires, thus indicating hydroplaning potential under wet conditions. A faster run time indicates a thinner film of water may exist between the tire and pavement surface [116]. Surface water drainage performance of ECC-Cor 80 specimens with different groove dimensions was evaluated and ECC-Cor 0 was also tested as the control. The cross slope and the grade of the specimens were confirmed to be on a zero-grade using a digital inclinometer to avoid external effect. A minimum of three specimens were prepared with minimum five tests were performed for each specimen. The test used water with temperature of 28ºC in an outdoor environment with air temperature of 30ºC.

Effects of geometrical road design with different cross slope and grade to the surface water drainage performance were studied. A tool with two layers of wooden plate was made to evaluate the effects of geometrical design on surface water drainage as shown in Figure 13.2. The purpose of the top plate is to simulate the grade of the pavement. The top plate can be adjusted from 0.0 % to 4.0 % grade using hex bolts. The bottom plate, which can be adjusted from 0.0 % to 5.0 %, was designed to evaluate the effect of the cross slope to the surface water drainage. The concrete specimens were placed on top of the wooden plate tool when the OFTs were conducted to check the surface drainage with different cross slope. The cross slope was checked using an inclinometer in units of mm/m with a 0.10 mm/m error. It is important to measure the inclination by putting the inclinometer above the specimens rather than above the wooden plates, as the wooden plates might be bent due to the weight of the specimen. Afterwards, measurements of the water outflow time with different slopes were conducted. Minimum of three specimens were prepared with a minimum of five tests were performed for each specimen. The test was done using water with temperature of 28ºC in an outdoor environment with air temperature of 30ºC.

(a) (b)

Figure 13.2 Adjustment mechanism for (a) grade and (b) cross slope of the specimen

13.3. Results and Discussion

13.3.1. Skid Resistance

BPN of ECC-Cor specimens are presented in Figure 13.3. As can be seen, without the addition of corundum, ECC-Cor 0 has a BPN of 53±9.1 which is lower than the required skid resistance of 55 for new roadways in accordance with the local standard set by the Land Transport Authority of Singapore. This suggests that ECC-Cor 0 cannot be used for road application unless surface treatments are introduced.

ECC mixed with corundum (i.e., ECC-Cor 50 to 100) with surface exposure after three days shows some improvement in skid resistance as most of the results are above 55 BPN on average, except for ECC-Cor 90. The moderate improvement may be attributed to delayed surface exposure process at day 3, where the matrix, a fiber-reinforced paste, was very hard to be removed and thus less corundum aggregates were exposed on the surface. It can be seen from the same figure, that there is no clear correlation between amount of corundum aggregates and skid resistance of ECC-Cor. This again may be attributed to delayed surface exposure process at day 3, which is not able to expose the surface corundum evenly as evident by the large variation of the BPN results.

A significant improvement of skid resistance of ECC-Cor with exposing process one day after casting was observed (BPN above 65). From Figure 13.3, it can be observed that skid resistance (BPN) increases with increasing amount of corundum used in the ECC-Cor mix. The ECC-Cor 100 possesses a BPN of 75, about 40% improvement compared to ECC-Cor 0. This is because the surface exposure process was carried out at day 1 and the paste can be removed easily and evenly as evident by the reduced variation of the BPN results. High skid resistance is also observed for the ECC-Cor 0-S specimen (BPN of around 75, comparable to the ECC-Cor 100). Even with much less corundum was included in the ECC-Cor 0-S specimen (150 kg/m3) as compared to other ECC-Cor mixes (e.g., 225 and 450 kg/m3 for ECC-Cor 50 and 100 mixes, respectively). Since skid resistance is a surface property, ECC-Cor 0-S represents a potential approach to strategically use corundum to improve the surface property while keeping the superior mechanical performance of the original ECC. Ultimately, this approach may be applied for both cast-in-situ and precast construction.

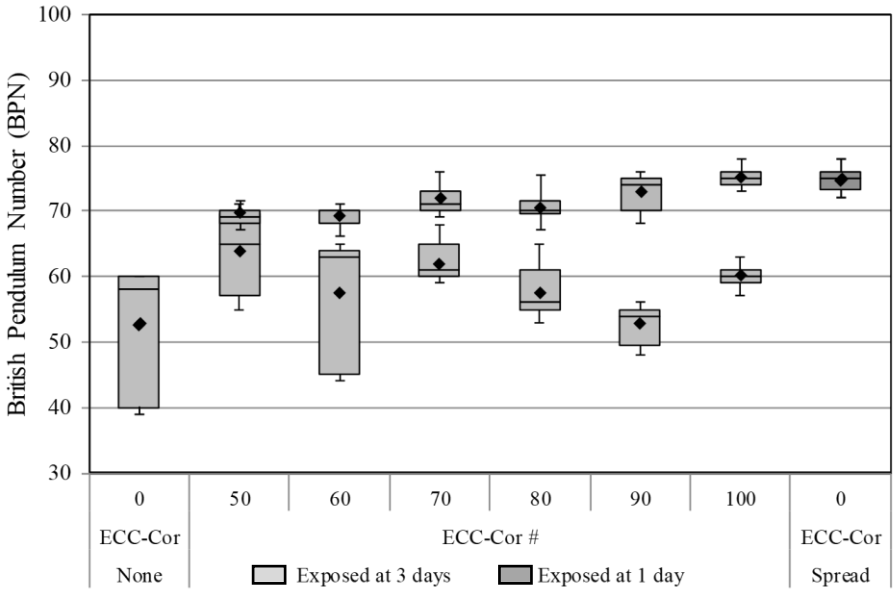

Figure 13.3 BPN of ECC-Cor

As shown in Figure 13.4, the MTD of ECC-Cor 0 is very low with surface texture of only 0.09±0.005 mm. Replacement of 50% corundum (ECC-Cor 50) remarkably increases the MTD to 0.36±0.02 mm. Further increment of corundum dosage does not lead to continuous enhancement of MTD. On average, the MTD of ECC-Cor # is about 0.35±0.05 mm, which is 3 times that of ECC-Cor 0. The variance of MTD results may be due to the fact that many results were drawn from at least three specimens for each mix, and minimum five tests were performed for each specimen. Arguably, sand patch test procedures have shown poor to fair repeatability [182].

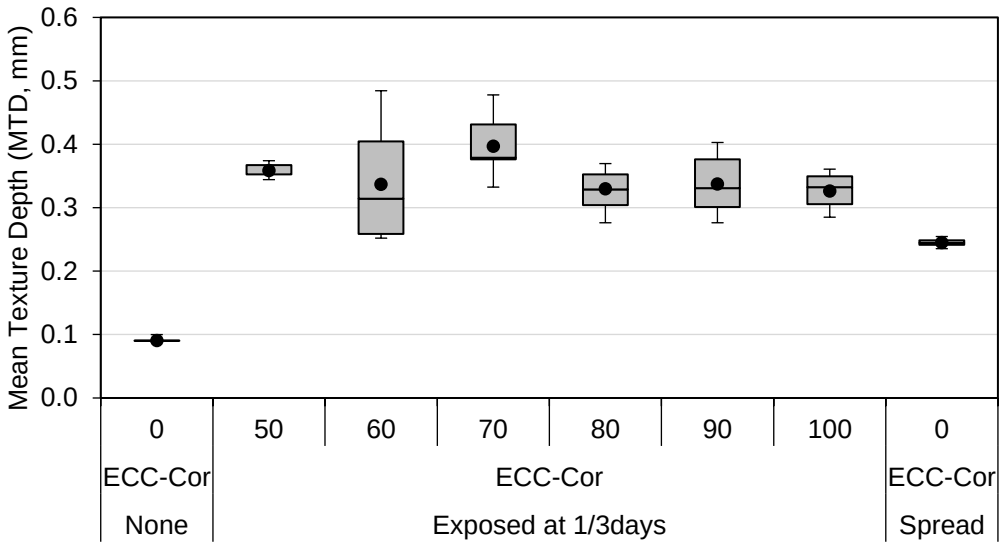

Figure 13.4 MTD of ECC-Cor

13.3.2. Surface water drainage performance

Surface water drainage performance is governed by the surface macrotexture [155]. A long OFT is indicative of smooth macrotexture surface, while short OFT indicates rough macrotexture surface textures. Since ECC-Cor 50 to 100 have similar MTD, only ECC-Cor 80 was measured using OFM to evaluate its surface water drainage performance and compared with ECC-Cor 0. As can be seen in Figure 13.5, OFT of ECC-Cor 0 cannot be measured as the surface is very smooth without the inclusion of corundum. The absence of macrotextures creates no gaps between the rubber of the OFM and the surface of the specimen. As a result, the water stays inside the OFM device. The average OFT for ECC-Cor 80 is 62.11±4.5 s. While the macrotextures created by the inclusion of corundum indeed improves the surface water drainage performance to a certain level, the OFT is still remarkably high, which may lead to risk of hydroplaning effect. In fact, several Department of Transportation for states in the US requires OFT of 9-10 seconds as the maximum limit [177]. Therefore, further treatments are necessary to fulfil the surface water drainage performance requirement for ECC-Cor 80.

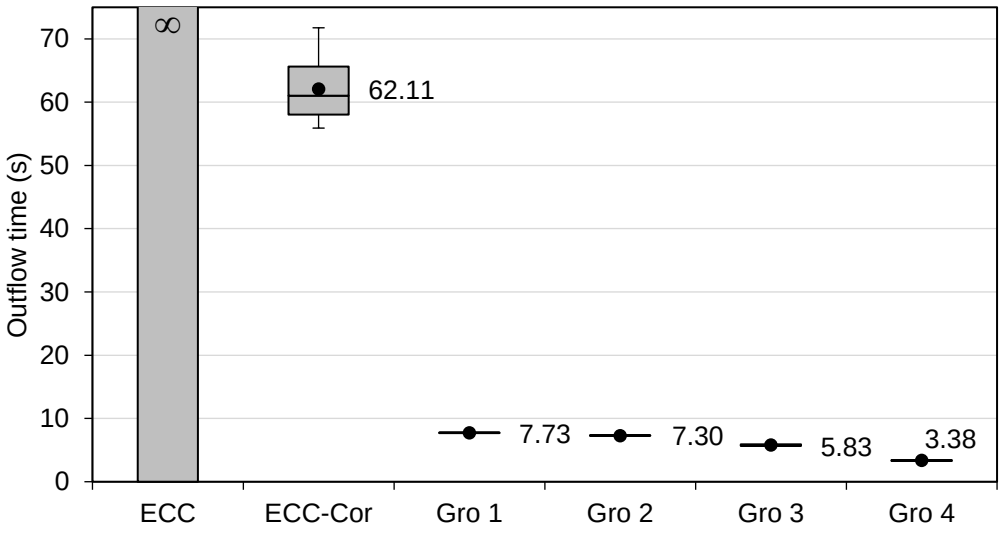

Figure 13.5 OFT of ECC-Cor

13.3.3. Effects on grooving treatment on surface water drainage performance and skid resistance

Table 56 summarizes the OFT, MTD, and BPN of ECC-Cor 80 specimens with different surface grooving treatment (i.e., ECC-Cor 80-Gro 1 to 4) and compared with that of ECC-Cor 0 and ECC-Cor 80 as the control. As can be seen, the OFTs for the grooved ECC-Cor 80 specimens are further reduced from 62.11±4.5 s to 7.73±0.05 s (ECC-Cor-Gro 1). With reduced land area, the surface water drainage performance further increases. ECC-Cor 80-Gro 4 with a land area of 7.5 ± 0.5 mm shows the shortest OFT of only 3.38±0.08 s. This is because grooving treatment greatly enhances the macrotexture of the specimen and MTD increases significantly with reducing land area (Figure 13.6). The combination of the microtexture provided by the corundum and the macrotexture provided by the grooves remarkably enhances the drainage of water through the space between the rubber ring of the OFM device and the specimen surface.

Table 13.3 Effect of grooves to water outflow

Specimen	Microtexture – longitudinal (BPN)	Microtexture – transversal (BPN)	Macrotexture, MTD (mm)	Water Outflow, OTF (s)
ECC-Cor 0	54.15±2.50		0.09±0.005	>500
ECC-Cor 80	71.43±2.02		0.36±0.019	62.11±4.99
ECC-Cor 80-Gro 1	71.40±1.43	77.50±1.57	0.74±0.030	7.73±0.05
ECC-Cor 80-Gro 2	72.10±0.83	88.60±1.28	0.85±0.030	7.30±0.05
ECC-Cor 80-Gro 3	72.60±0.92	90.50±1.28	1.08±0.054	5.83±0.18
ECC-Cor 80-Gro 4	74.10±0.70	92.80±1.60	1.33±0.059	3.38±0.08

The BPN of the grooved ECC-Cor 80 tested in the transversal direction (i.e., the grooves are perpendicular to the BPT swing direction) is higher than that of the ECC-Cor 80. Furthermore, the BPN increases with reducing land area. ECC-Cor 80-Gro 4 with a land area of 7.5 ± 0.5 mm shows the highest BPN of 92.80±1.60, which represents a 71% and 30% enhancement as compare to that of ECC-Cor 0 and ECC-Cor 80, respectively. This may be attributed to the increased macrotexture on the surface which holds the movement of the rubber slider on the pendulum. The BPN of the grooved ECC-Cor 80 tested in the longitudinal direction (i.e., the grooves are parallel to the BPT swing direction); however, remains similar to ECC-Cor 80.

13.3.4. Effects of cross slope and grade on surface water drainage performance

Figure 13.6 plots the OFTs of ECC-Cor 80 with and without grooves at different cross slope and grade. The general trend shows that surface water drainage performance increases with increasing cross slope and grade. This is particularly true for surface without grooving treatment, i.e., ECC-Cor 80. As shown in Figure (a), OFT decreases by 9.7% and 17.2% with 4% incremental change of cross slope and 5% change of grade, respectively. The OFT decreases by 30% when both cross slope and grade increases by 4% and 5%, respectively. However, it is observed that effects of cross slope and grade are much less pronounced for grooved surface (Figure 13.7). For example, OFT of ECC-Cor 80-Gro 1 specimen decreases by 1.2% only when the cross slope increases by 4%, and the OFT decreases by 0.9% only when the grade increases by 5%. Further, OFT decreases by 2.2% when both cross slope and grade increases by 4% and 5%, respectively. This is because grooving treatment has already provided an effective means to drain water and to greatly shorten the OFT. Further reduction of OFT by increasing the cross slope and grade is less pronounced. This is particularly true for specimen with larger land area, i.e., ECC-Cor 80-Gro 4.

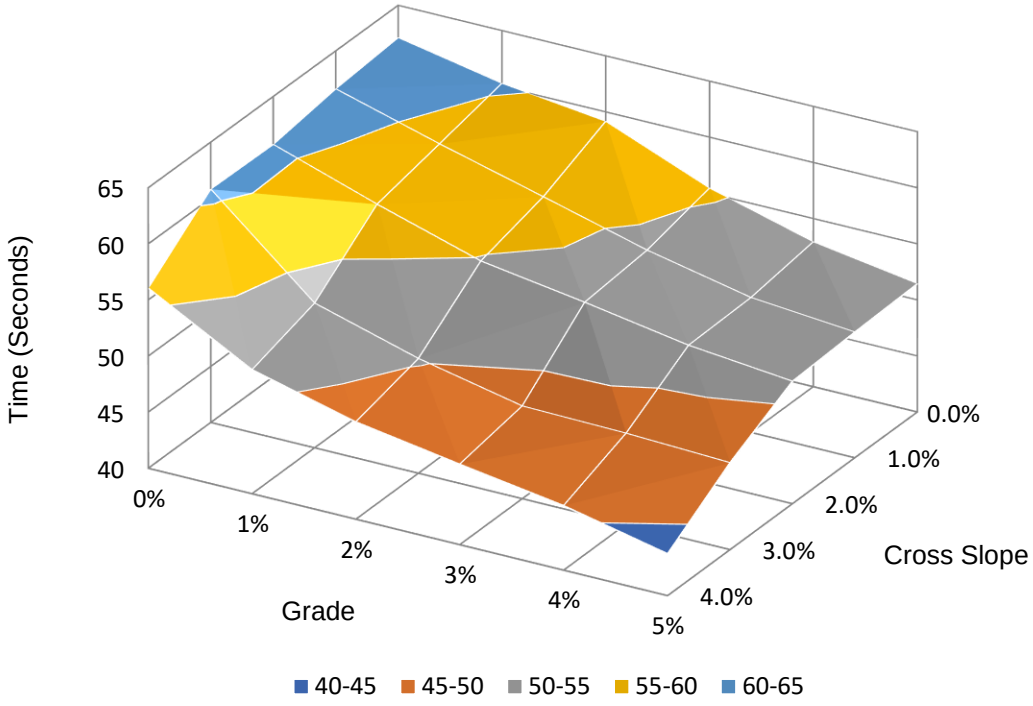
Time (Seconds)
65
60
55
50
45
40
0%
1%
2%
3%
4%
5%
Grade
0.0%
1.0%
2.0%
3.0%
4.0%
Cross Slope
40-45
45-50
50-55
55-60
60-65

(a)

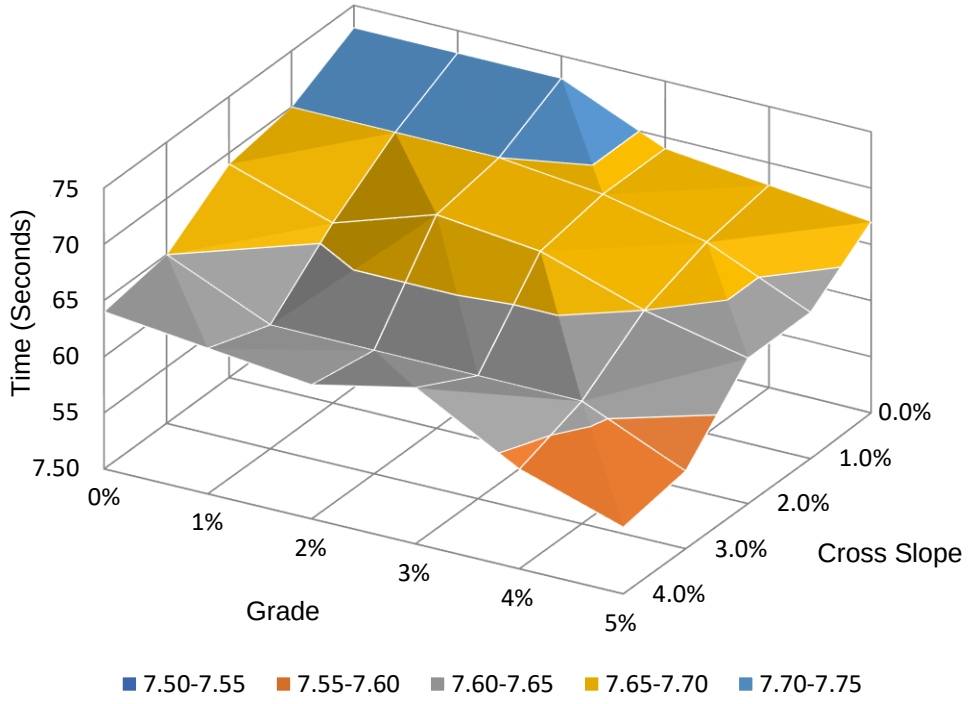
Time (Seconds)
75
70
65
60
55
7.50
0%
1%
2%
3%
4%
5%
Grade
0.0%
1.0%
2.0%
3.0%
4.0%
Cross Slope
7.50-7.55
7.55-7.60
7.60-7.65
7.65-7.70
7.70-7.75

(b)

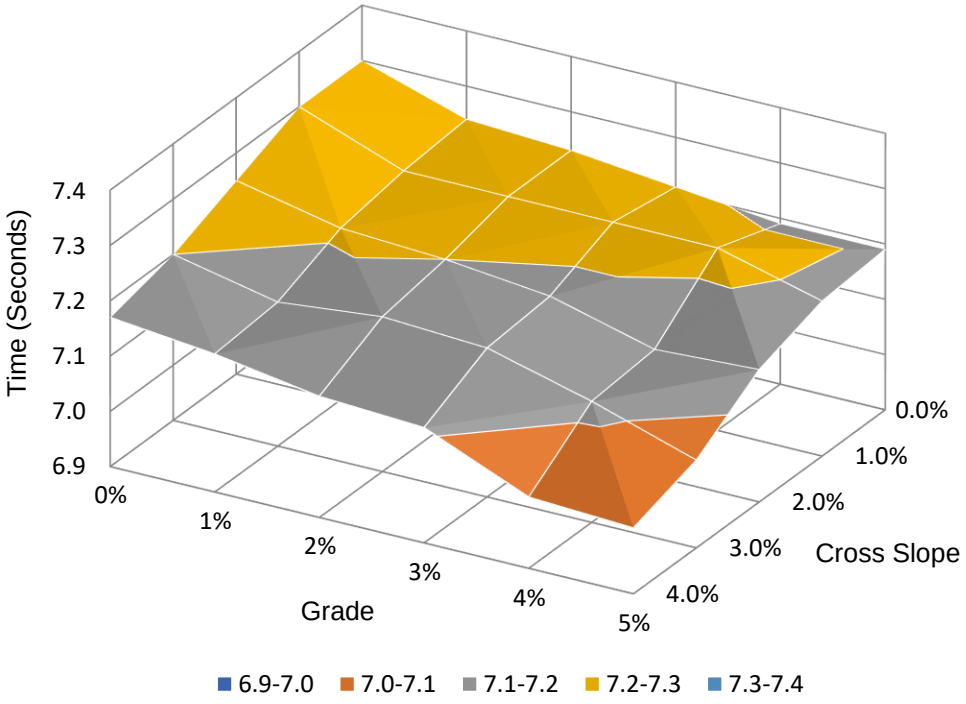
Time (Seconds)
7.4
7.3
7.2
7.1
7.0
6.9
0%
1%
2%
3%
4%
5%
Grade
0.0%
1.0%
2.0%
3.0%
4.0%
Cross Slope
6.9-7.0
7.0-7.1
7.1-7.2
7.2-7.3
7.3-7.4

(c)

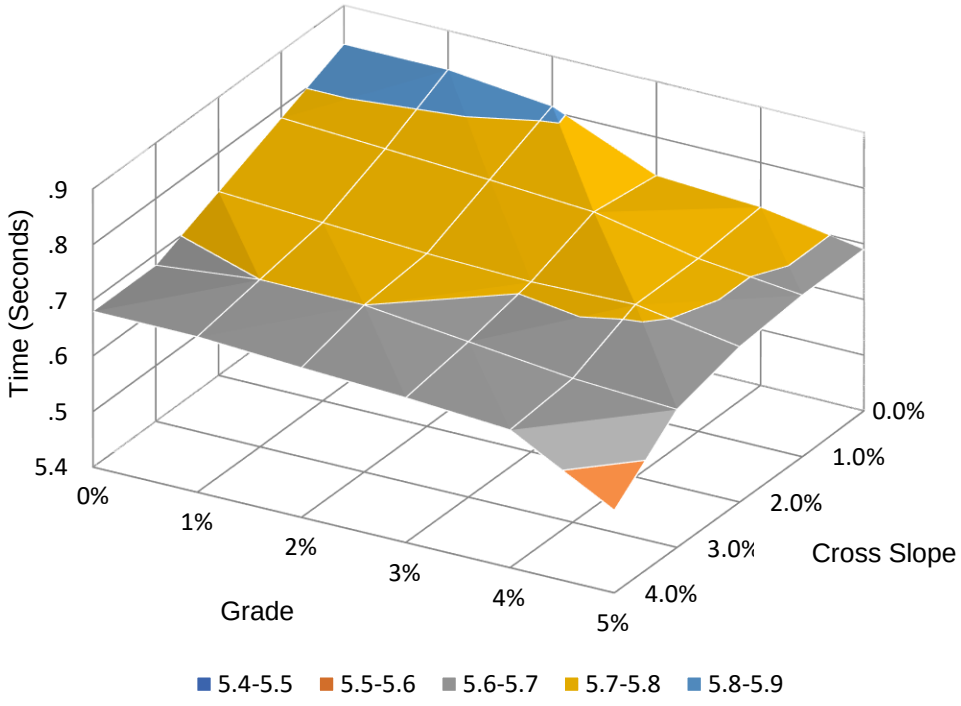
Time (Seconds)
.9
.8
.7
.6
.5
5.4
0%
1%
2%
3%
4%
5%
Grade
0.0%
1.0%
2.0%
3.0%
4.0%
Cross Slope
5.4-5.5
5.5-5.6
5.6-5.7
5.7-5.8
5.8-5.9

(d)

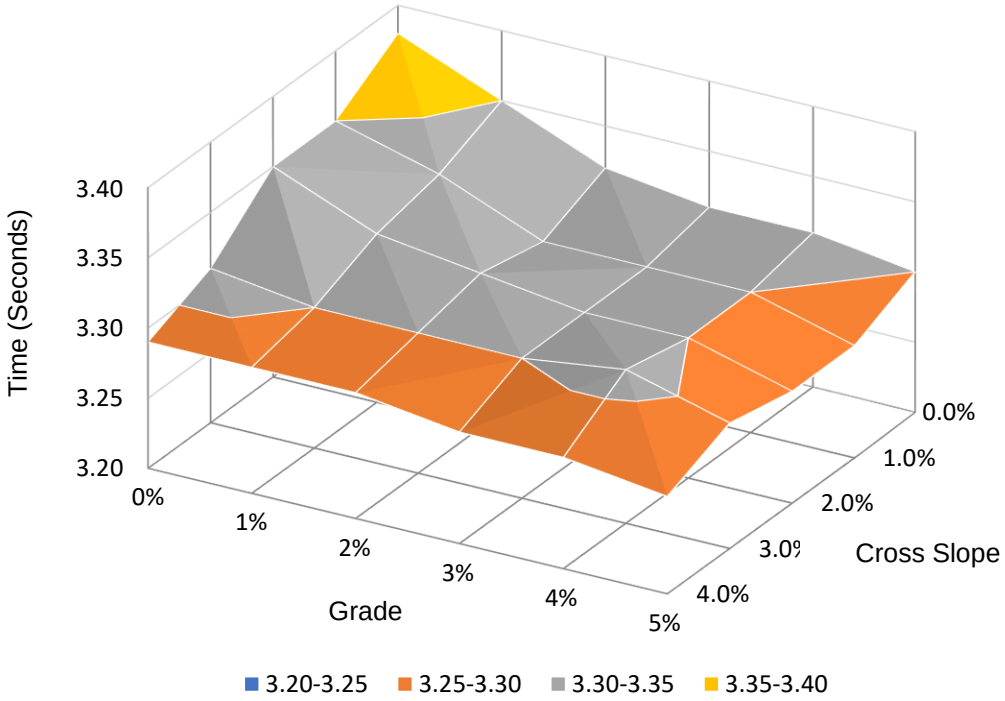

(e)

Figure 13.6 OFTs for (a) ECC-Cor 80, (b) ECC-Cro 80-Gro 1, (c) ECC-Cro 80-Gro 2, (d) ECC-Cro 80-Gro 3, and (e) ECC-Cro 80-Gro 4 as a function of cross slope and grade

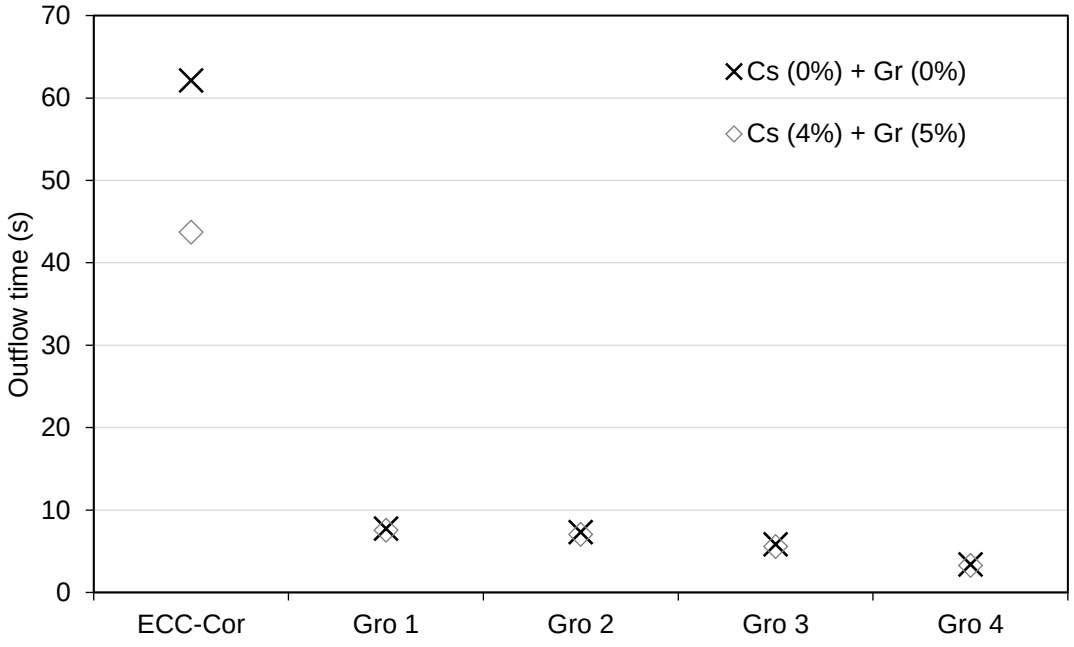

Figure 13.7 Effects of 4% cross slope and 5% grade on OFT of ECC-Cor 80 with and without grooving treatment

13.3.5. The correlation between skid resistance and surface water drainage with effect of cross slope and grade

Based on the experimental results, an empirical formulation associating OFT with MTD and grade and cross slope are proposed by curve fitting.

$$OFT = \frac{5.88\ MTD^{-2.31}10^{-0.4403\ MTD^{-1.955}\ Cs} + 5.88\ MTD^{-2.31}10^{-0.4403\ MTD^{-1.955}\ Gr}}{2} \quad \text{(Eq. 35)}$$

where OFT is the outflow time in s; MTD is the Mean Texture Depth in mm; Gr is the grade of pavement in %; and C_S is the cross slope of pavement in %. As shown in Figure 13.8, the results from Equation (Eq. 35) was compared with experimental results as well as formula proposed in [183] and by Sarsam [182], as can be seen in (Eq. 19 and (Eq. 20, respectively.

From the experimental results, it can be seen that in general, OFT of ECC reduces with MTD exponentially. Slab with higher cross slope and grade possesses lower OFT at a given MTD. This is particular true for slab with low MTD. Current model prediction fits well with the experimental results for both with and without cross slope and grade. The ASTM and Sarsam models, however, deviate significantly with the experimental results, OFT for ECC with low MTD in particular. At higher MTD (> 1.2 mm), all three models give good prediction of the OFT. This is because cross slope and grade play important role and govern water drainage at low MTD, and the effects of cross slope and grade diminish with increasing MTD. The ASTM and Sarsam models are developed based on water drainage on conventional concrete and asphalt pavement surfaces which often have higher MTD and thus effects of cross slope and grade are not considered in these two models. However, due to the absence of coarse aggregates in ECC mix, low MTD for un-grooved ECC surface is often expected. The proposed model takes cross slope and grade of pavement into account and is able to predict surface water drainage performance (OFT) for any given MTD and pavement geometries.

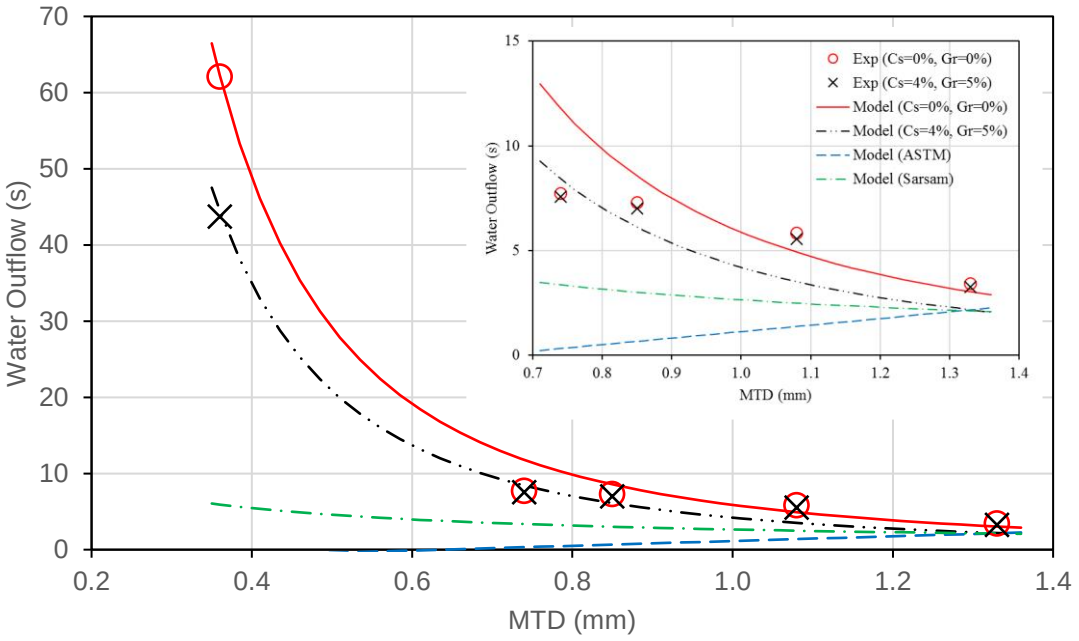

Figure 13.8 OFT as a function of MTD

14. Study of Noise

14.1. Introduction

Singapore have transformed into a highly developed city with most of the population live in urban areas. Due to a limited area, the most residential area is developed close to expressways and major arterial roads with high traffic densities which cause noise pollution. Strait times (Goh Chin Lian 2010) reported that communities have public complaints about noise pollution. Quieter pavements were considered as one of solutions that should be provided by authorities.

Three main material properties are affecting noise, namely density, porosity, and texture. Thus, it was expected that ECC material may produce higher noise due to its high density and less porous properties. However, there is a need to study the noise caused by pavement made of ECC as a reference for future usage as well as identification for an improvement. Corundum is incorporated as fine aggregates into ECC mixture (ECC-Cor) to improve the surface microtexture. The ECC-Cor results in satisfactory performance of high skid resistance (BPN > 70). Further surface treatment with grooves successfully improves the functional performance, not only by minimizing the risk of hydroplaning (water outflow time < 4 s) but also by improving the skid resistance (BPN > 90). The noise comes from the same texture on ECC-Cor is further investigated. Yet, no studies have been reported on noise level for pavement made of ECC. This chapter elaborates the investigation of noise on pavement made of ECC.

The contact-free measuring method applied on the specimens, allows for a non-destructive determination of the surface roughness (macro texture) of slab surfaces. The noise level is then simulated and predicted by using SPERoN software which is based on the approach that pre-processed input data are used [184].

14.2. Experimental Program

14.2.1. Materials and mixture design

The mixture design used in this study is mixed ECC with corundum (ECC-Cor), as has been discussed in Chapter 6. ECC-Cor is using a Type I Portland cement, class F fly ash (FA), micro-silica sand (mean and maximum grain size of 110 μm and 200 μm, respectively), polyvinyl alcohol (PVA) fibers (length of 12 mm, diameter of 39 μm, nominal tensile strength of 1600 MPa), a high-range water reducing (HRWR) were used to prepare the mix.

To enhance skid resistance, corundum with maximum particle size of 2.38 mm was used as fine aggregates for improving the surface textures of ECC. The material size distribution of corundum is given in Figure 13.1. A control ECC mixture without the addition of corundum (ECC-Cor 0) was also prepared. All ECC-Cor mixtures have a low water-to-cementitious material ratio (w/cm) of 0.27. Micro-silica sand was replaced with corundum at 80% dosage.

14.2.2. Specimen preparation

ECC-Cor mixture was prepared in a planetary mixer. Cement, fly ash, and micro-silica sand are dried mixed first. Water was then added followed by the addition of superplasticizer and mixed for 3-5 mins until the mix achieved the required consistency. Lastly, the PVA fiber and corundum were added and mixed for another 3-5 mins. The fresh mixture was cast into steel formwork with dimension of 2000 mm by 500 mm by 80 mm. Specimens were removed from the mould after 1 day and were cured at normal laboratory air (25±3^{o}C, 70%RH) for another 27 days before further testing. At the pre-determined age, 1 d, the top surface of plate specimens was treated with a steel brush to expose the corundum on the surface.

To study the effects of surface macrotexture on skid resistance and surface water drainage performance of ECC-Cor, parallel grooves were created on surface of ECC-Cor 80 specimens by using a silicone rubber. The design used ECC-Cor Gro 01 which can be seen in Table 7.2. Three slab specimens were prepared: ECC, ECC-Cor 80, and ECC-Cor 80-Gro 1.

14.2.3. Test program

This study consists of three stages: laboratory measurement, numerical study with finite element analysis (FEA), and noise prediction analysis. Firstly, is to determine the actual tire contact stresses and contact area using Tekscan I-Scan measuring device. The output will be used for the input to FEA to comprehensively study pavement response. Finite element (FE) tools ANSYS will be employed in this study. The results, however, are already discussed in the chapter of study of mechanical properties, showing there is no significant effect of grooves to the ECC slab.

Secondly, the contact-free measuring method applied allows for a non-destructive determination of the surface roughness (macro texture) of slab surfaces. The measurement and description of the surface texture is carried out by using a profilometer, which set according to ISO 13473 “Characterization of pavement texture by use of surface profiles”, Parts 1 to 4. The slab surface is scanned using a laser triangulation measuring system over the whole length according to the method of continuous measurements. The profilometer is connected to the power source and a computer which has the controls and software to record and save the measurements done by the laser. The mean profile depth of the slab is measured by the equipment based on triangulation laser measurement system. The percentage of the laser beams which fail to reflect is called the dropout rate. This determines the accuracy of the measurement. According to ISO 18743, a dropout percentage of 5% is allowed for one trial. The texture of three slabs: ECC, ECC-Cor, and ECC-Cor Gro 1 were measured with the surface profilometer, which can be seen in Figure 14.1, to evaluating the tyre-road-noise. The results, which is measured as texture depth, is required as an input for the software. The measured data must contain at least six parallel measurement lines with a length of at least 2 m each. Therefore, the tested ECC-Cor slabs were made with a minimum length of 2 m.

Figure 14.1 Surface profilometer measuring the texture of ECC slabs

As can be seen in Figure 14.1, the laser scanning equipment is aligned parallelly over the slab. Slopes or slants in both the vertical and horizontal directions are avoided to allow the movement of the laser scanner in a straight line. Once the setup is done, a trial run is conducted over the full length of the slab to ensure the laser runs on a straight line. A total of 96-line areas are scanned along the length of the slab with an offset of 2mm. The total run time for 96-line areas on one slab is approximately 20 minutes. The process is repeated for all the three slabs.

The resolution of the applied measuring system is 200 µm horizontally and 8 µm vertically. Data will be then processed to predict the noise level by evaluating the MPD-value (according to ISO 13473-1) and the shape factor of the profile; these two values give a good indication whether the road surface is suitable to reduce the tire-road noises.

The tyre-road noise is predicted by using SPERoN (Statistical Physical Explanation of Rolling Noise) software, which is based on the pre-processed input data of texture. SPERoN is developed by the Müller-BBM [184]. The SPERoN model calculates the coast-by noise of a vehicle by considering four parameters tyre vibrations, the aerodynamic sound sources, the tire cavity modes, and the residual sound sources [184], which then followed with the statistical model [185]. The equation can be seen below.

$$p^2{}_{coast-by} = p^2{}_{vib} + p^2{}_{air} + p^2{}_{cav} + p^2{}_{res} \quad \text{(Eq. 36)}$$

$$p^2{}_{vib} = aF_c^2\Gamma^{\alpha 1}B^{\alpha 2}S^{\alpha 3} \quad \text{(Eq. 37)}$$

$$p^2{}_{air} = b(F_c^2\Gamma^{-1.5}S^{-2})^{\beta 1}B^{\alpha 2}V^4 \quad \text{(Eq. 38)}$$

$$p^2{}_{cav} = cG_{pattern}^{y1} \quad \text{(Eq. 39)}$$

$$p^2{}_{res} = dV^{\delta 1} \quad \text{(Eq. 40)}$$

Where: $a, \mathrm{b}, \mathrm{c}, \mathrm{d}$ are regression coefficients per 3rd octave band; α_1, α_2, $\alpha_3, \mathrm{b}_1, \gamma_1, \delta_1$ are exponents; $\mathrm{F_c}$ is contact force in N; Γ is tyre/road contact air flow resistance in Pa s/m; B tyre width in m; S is tyre tread stiffness in N/m; $\mathrm{G_{pattern}}$ is spectral power of the tread pattern variation; V is spectral power of the tread pattern variation driving speed in m/s.

Thus, the input characteristics of road surface is necessary to obtain results on the coast-by noise including: road texture (roughness of the road surface), acoustical impedance (a measure for the sound reflection and absorption properties of a road surface with 0% as totally reflecting and 100% as totally absorbing), air flow resistance, and mechanical impedance (as the ratio of the input force and vibration velocity measured at a certain point of the structure. The SPERoN calculations were performed with a tyre called “Michelin Energy Saver”, which used as a standard tyre, with speed of 50 km/h [186]. The SPERoN model has been validated by comparing to eight coast-by measurement results. The results show that the total sound levels for all of the investigated road surfaces have a mean precision of 1.5 dB [187,188].

14.3. Results and Discussion

14.3.1. Texture depth based on profilometer measurement

Surface texture depth from three slabs: ECC, ECC-Cor, and ECC-Cor Gro have been measured. As can be seen Figure 14.2, the texture depth of ECC is flatter in comparison to the other surfaces with only less than 100 µm deviation. Meanwhile, ECC-Cor has rougher texture depth with about 350 µm deviation as it has a rougher texture because of the corundum. Lastly, ECC-Cor Gro has similar rough texture with ECC-Cor with additional spikes due to the grooves. The texture depth results from the laser profilometer are in line with results drawn from the sand patch test where ECC-Cor has more macrotexture than ECC, and ECC-Cor Gro has more texture than ECC-Cor.

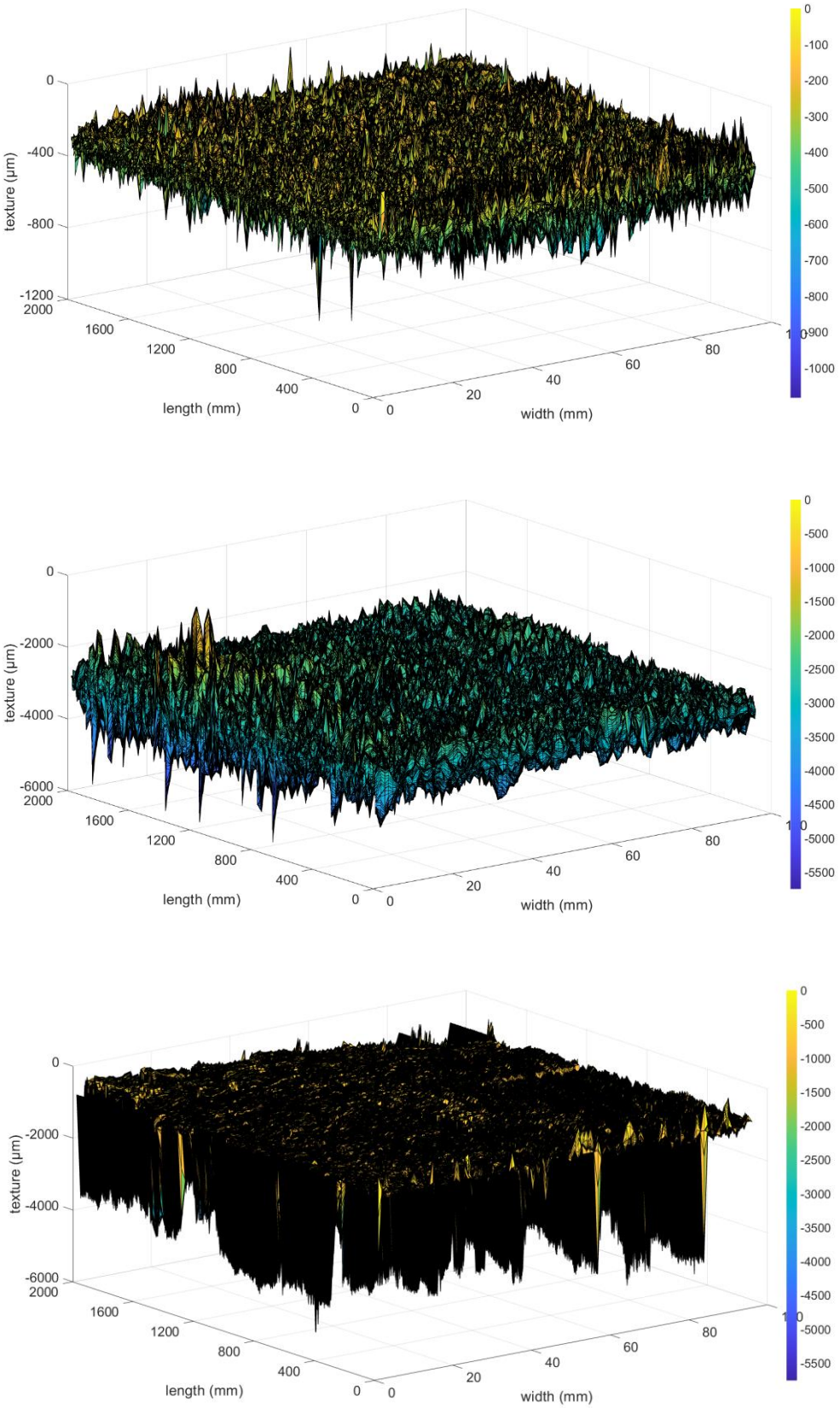

Figure 14.2 Texture depth of (a) ECC, (b) ECC-Cor, and (c) ECC-Cor Gro

14.3.2. Macrotexture (MPD) and shape factor

Throughout the measurement with the laser profilometer, two parameters were measured including macrotexture, in mean profile depth (MPD), and the shape factor for each slab. These two parameters are necessary as then later used for the calculation of the total sound level. Previous studies mentioned that two road surfaces with identical texture amplitude spectra do not necessarily show identical acoustical behavior. Therefore, the shape factor needs to be considered as it corresponds to the percentage contact length within the characteristics profile length [185,189].

Table 14.1 MPD and Shape factor of ECC, ECC-Cor, and ECC-Cor-Gro 1

Texture	MPD	G
	[mm]	[%]
ECC	0.10±0.03	69.8±0.19
ECC-Cor 80	0.61±0.22	55.4±0.17
ECC-Cor 80 Gro 1	0.21±0.20	59.1±0.20

14.3.3. Sound Level

The calculation with SPERoN was done for three slabs based on texture depth as one of main inputs [186]. In results, there are four different noise level are produced with different parameters including vibration, air, cavity, and residual noise. Those four noise parameters have been explained in (Eq. 36. The results of sound pressure level, which are summarized from Table 14.2 to Table 14.5, are explained based on the octave band center frequency, reported in Hertz (Hz). Hertz in this noise known as the frequency of a sound as how fast the small air pressure changes are occurring. Similar to sound level, the perception of frequency is also non-linear.

Table 14.2 Sound level (vibration) of ECC, ECC-Cor, and ECC-Cor-Gro 1

Texture	L vibration in dB(A) – based on the octave band center frequency (Hz)									
	315	400	500	630	800	1000	1250	1600	2000	Tot
ECC	27.9	27.9	41.4	49.2	44.0	44.8	32.0	29.2	22.4	51.9
ECC-Cor 80	45.9	40.1	52.3	59.8	63.3	61.4	47.9	44.9	37.9	66.8
ECC-Cor 80-Gro 1	30.4	28.9	40.8	47.9	44.9	45.5	32.0	29.1	21.4	51.6

Table 14.3 Sound level (air) of ECC, ECC-Cor, and ECC-Cor-Gro 1

Texture	L air in dB(A) – based on the octave band center frequency (Hz)									
	315	400	500	630	800	1000	1250	1600	2000	Tot
ECC	35.6	38.7	39.5	42.6	48.2	53.5	54.1	52.0	52.2	59.6
ECC-Cor 80	38.8	40.9	44.1	47.1	54.3	56.6	56.4	53.0	52.5	62.1
ECC-Cor 80-Gro 1	36.0	38.8	39.2	42.0	48.5	53.6	54.1	52.0	52.1	59.6

Table 14.4 Sound level (cavity) of ECC, ECC-Cor, and ECC-Cor-Gro 1

Texture	L cavity in dB(A) – based on the octave band center frequency (Hz)									
	315	400	500	630	800	1000	1250	1600	2000	Tot
ECC	39.9	44.4	55.4	50.8	56.0	56.2	56.0	19.2	12.4	62.3
ECC-Cor 80	39.9	44.4	55.4	50.8	56.0	56.2	56.0	34.9	27.9	62.4
ECC-Cor 80-Gro 1	39.9	44.4	55.4	50.8	56.0	56.2	56.0	19.1	11.4	62.3

Table 14.5 Sound level (residual) of ECC, ECC-Cor, and ECC-Cor-Gro 1

Texture	L residual in dB(A) – based on the octave band center frequency (Hz)									
	315	400	500	630	800	1000	1250	1600	2000	Tot
ECC	37.9	44.7	42.9	42.1	38.8	38.6	37.6	35.3	35.6	50.0
ECC-Cor 80	37.9	44.7	42.9	42.1	38.8	38.6	37.6	35.3	35.6	50.0
ECC-Cor 80-Gro 1	37.9	44.7	42.9	42.1	38.8	38.6	37.6	35.3	35.6	50.0

The two main source of sound level [190], vibration and air, are shown in Figure 14.2. As can be seen, the sound level for ECC-Cor is higher than ECC. The higher sound level of ECC-Cor occurred because of the lower shape factor (G) due to a rougher surface as results from the existence of corundum aggregate on the ECC surface. The shape factor as well as the MPD for each design mixture are summarized in Table 57.

Throughout the measurement with the laser profilometer, two parameters were measured including macrotexture, in mean profile depth (MPD), and the shape factor for each slab. These two parameters are necessary as then later used for the calculation of the total sound level. Previous studies mentioned that two road surfaces with identical texture amplitude spectra do not necessarily show identical acoustical behavior. Therefore, the shape factor needs to be considered as it corresponds to the percentage contact length within the characteristics profile length [180,183].

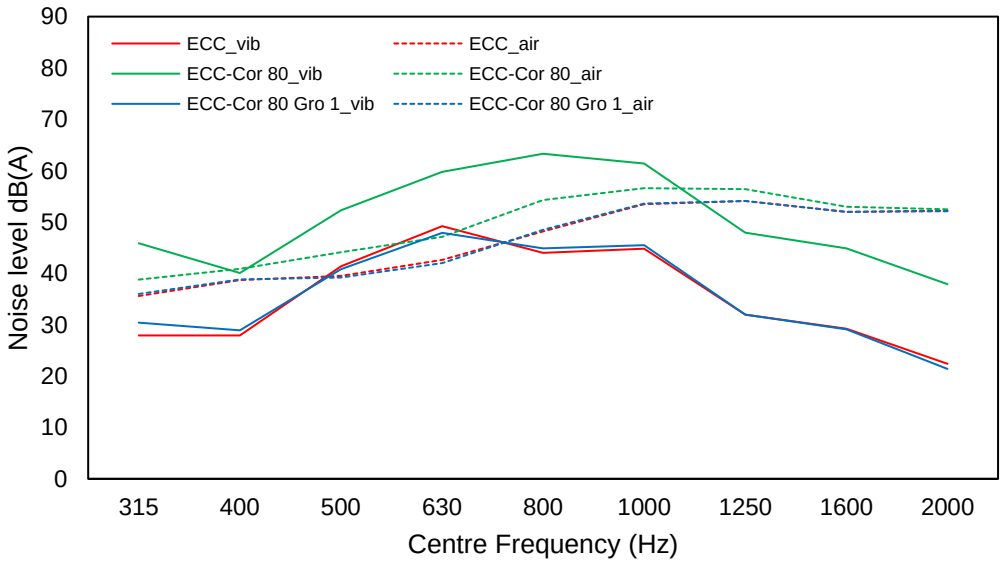

Figure 14.3 Noise level of ECC, ECC-Cor, and ECC-Cor-Gro 1 based on vibration and air

The other parameters, tyre cavity, is mainly determined by the tyre pattern and less affected by the road surface. Due to the use of same standard tyre, there is no notable differences. The residual component is the cumulation of all air flow noises caused by the frame of the vehicles which is statistical and only dependent on the velocity. Therefore, all results of the noise level for the slabs are the same.

In results, as can be seen in Table 62, the total sound level of ECC-Cor is higher than ECC, with 69.2 compare to 64.6 dB for ECC-Cor and ECC, respectively. The modification of ECC-Cor by introducing grooves (ECC-Cor-Gro 1) has been successfully reduce the sound level coming from the vibration. The sound level from the air parameter is slightly reduced, mainly in the frequency from 315 to 1250 Hz. The shape factor is then increased for ECC-Cor-Gro 1. In results, the total sound level for ECC-Cor-Gro 1 is reduced significantly from 69.2 (ECC-Cor without grooves) to 64.6 dB, which is lower than the NEA limits of 67 dB for new roads and expressways.

Table 14.6 Sound level (total) of ECC, ECC-Cor, and ECC-Cor-Gro 1

Texture	L Total in dB(A)									
	315	400	500	630	800	1000	1250	1600	2000	Tot
ECC	43.0	48.1	55.9	53.8	56.9	58.3	58.2	52.1	52.3	64.6
ECC-Cor 80	48.0	49.0	57.5	60.6	64.5	63.6	59.5	53.7	52.7	69.2
ECC-Cor 80-Gro 1	43.2	48.2	55.9	53.3	57.0	58.4	58.2	52.1	52.2	64.6

In summary, some findings from the study of noise on pavement made of ECC can be drawn. Those findings including:

- The evaluation of the MPD-value (acc. to ISO 13473-1) and the shape factor of the profile; are giving a good indication whether the road surface is suitable to reduce the tire-road noises.
- The noise level coming from the pavement made of ECC can be up to 65 dB(A), which is quite safe as it is below of many standard values regulated by the authorities. However, from the perspective of skid resistance and surface water drainage performance, the ECC slab is not safely to be used for roadways.
- The noise level for ECC-Cor-Gro 1 increased up to 69.2 db(A) because of the lower shape factor (G) due to a rougher surface as results from the existence of corundum aggregate on the ECC surface. The shape factor at ECC-Cor is at 55% which is very low for dense surfaces.
- It can be seen from the analysis of the different formation mechanism, that the biggest differences can be found in the vibrational noises, meaning that ECC-Cor has a rough surface that stimulates the tire to vibrate more. The aeroacoustics parts are as well increased compared to ECC slab.
- The modification of ECC-Cor by introducing grooves (ECC-Cor-Gro 1) has been successfully reduce the sound level coming from the vibration. The sound level from the air parameter is slightly reduced, mainly in the frequency from 315 to 1250 Hz. The shape factor is then increased for ECC-Cor-Gro 1.
- The ECC-Cor with grooves can be a solution for the (electrified or normal) roadways with pavement made of ECC in Singapore condition, where the NEA regulates the noise limit for 67 dB to new roads and expressways.

15. Study of Self-cleaning and Slip-proof ECC

15.1. Introduction

Currently, Singapore is embracing the sustainable development of the land transport to improve the living environment. Emission from the transport sector is one of the main issues in Singapore. Efforts to tackle this issue not only can be done through the improvement of the vehicles wise but also from the pavement infrastructure wise. A self-cleaning pavement can be a good alternative for solution.

Pavement in tunnels should be designed differently than pavement for other outdoor applications. Visibility is a critical consideration to ensure safety in use and during accidents for pavement in tunnels [191–195]. The brighter pavement was found to have fewer accidents according to studies done in the UK [196,197]. By having high surface reflectance of pavement, lower luminance is required, and thus both energy and life cycle cost can be reduced [196]. Another comparison study in the tunnel was done with the conclusion that the power and flux required for tunnel depend strongly on the reflection properties of the road pavement [198,199]. By changing the road pavement from asphalt (black) to concrete (grey), it allows 6-10% and 6-8% savings on required flux and power, respectively [199]. Furthermore, concrete is known to have better fire resistance and durability when compared to asphalt. For this reason, more pavements in tunnels are built with concrete nowadays. In fact, some regulations including European Directive state that concrete pavements shall be used for tunnels longer than 1,000 m [192].Few studies have reported potential use of ECC for rigid pavement applications. Compared to conventional concrete and hot mix asphalt (HMA) overlay systems, ECC overlay offers lower life-cycle cost over a 40-year service life with reduced total life cycle energy by 14%, greenhouse gas (GHG) emissions by 43%, and costs by 40% [42]. Recently, ECC has been applied on an 80 m jointless test track and shows that this material can be produced in large quantity and high quality. The long-term monitoring showed that the material could handle high traffic loads and the abrasion was low [44]. On top of that, the reflective cracking failure which commonly occurred in an overlay can be eliminated due to the high ductility of ECC material [42].

ECC can be a potential alternative for concrete pavements. However, the critical shortcoming of ECC material, in particular for roadway application, is on the surface texture. As the mix design of ECC omits coarse aggregates and often includes only micro silica sand with particle size less than 300 μm to reduce matrix toughness and to ensure good ductility, it decreases the skid resistance of ECC pavement, which is of great concern for roadway applications with respect to required grip levels [177]. Skid resistance is one of the most important functions in pavement, as this parameter is responsible for the safety aspects for motorists. Many agree that safety should be prioritized in designing pavement [72,155]. The skid resistance of pavement is mainly characterized by its micro- and macrotextures. Bawono et al. [200] engaged hard corundum particles into ECC mix to enhance the skid resistance. However, due to the black color of corundum particles, the surface of the resulting ECC is very dark with low surface reflectivity.

It is very desirable to impart additional functions, i.e., self-cleaning and air purification, into concrete for pavement in tunnels. Self-cleaning helps to maintain the brightness and reflectivity of the surface [142,201,202], while air purification improves the air quality in tunnels [203]. These two functionalities are often imparted into cement-based materials through engaging ingredients with photo-catalysis properties. Titanium dioxide (T_iO_2) as photo-catalyst was firstly introduced by Fujishima and Honda [204]. Then, in 2003, Cassar [142] did experimental study in engaging photocatalytic function into concrete by adding T_iO_2 and reported that the resulting concrete is capable to photo-decompose the organic compound sticking on the surface and then to photo-catalyze the transformation of NO_x to NO_3. In 2011, Awadalla et al. [205] concluded that concrete panel incorporating T_iO_2 has the ability to

decompose CO_2. At the same time, a study on photocatalytic de-pollution in tunnel irradiated by artificial UV light was reported in Brussels using commercially available TX Active®. UV lamps were used to activate the photocatalytic reaction. However, the field results showed there is no observable reduction of NOx in the tunnel [150,206]. The current photocatalytically active cement coating, such as TioCem® and TX Active® can effectively remove various pollutants including volatile organic compounds by exposing the cement surface to UV light. Zhao et al. [147] incorporated a commercial T_iO_2 into a white ECC mix to engage photo-catalysis property. However, the photo-catalysis property is activated only under UV irradiation. This is because TiO2 used in those studies can only be photoactivated by UV irradiation due to its wide bandgaps (3.0-3.2 eV) which lie in UV region [207,208].

This chapter reports the development of a bright and slip-proof ECC with visible light activated photocatalysis property for pavement in tunnels. Different T_iO_2 nano-particles were tested first to evaluate their photocatalysis property under visible light irradiation. The selected T_iO_2 nano-particle was used to develop the bright and slip-proof ECC with the inclusion of white fine aggregates. Effects of fine aggregate content on the mechanical properties and skid resistance of the resulting ECC were investigated. Influences of T_iO_2 dosage on the mechanical properties of ECC were tested and self-cleaning performance and dirt pick-up resistance (DPUR) of ECC under visible light irradiation were studied.

15.2. Experimental Program

15.2.1. T_iO_2 screening, characterization and performance evaluation

Four commercial T_iO_2 were tested in the screening stage: Aeroxide P25 (Evonik, Germany), KRONOClean K7000 (KRONOS, USA), T_iO_2-anatase (Shijiazhuang Kailing, China) and T_iO_2-rutile (Shijiazhuang Kailing, China). Commercially available methylene blue (Sigma-Aldrich, Singapore) and Rhodamine B (Sigma-Aldrich, Singapore) were used for photo-decomposition of dye and self-cleaning experiment, respectively.

The morphology of T_iO_2 was investigated by a field emission scanning electron microscope (FESEM, JSM-7600F). The FESEM combines an electron column with semi-in-lens detectors and an in-the-lens Schottky field emission gun, which is able to deliver ultra-high-resolution secondary electron images with a wide range of probe currents from 1 pA to more than 200 nA. X-ray powder diffraction (XRD) for quantitative phase analysis (QPA) of T_iO_2 was carried out by using a θ/θ diffractometer (XRD Bruker D8 Advance). T_iO_2 samples in round sample holders were placed on the spring plate. The XRD diffractograms were recorded using a Cu Kα radiation at 40 kV and 40 mA with a scan range from 10° to 110° in 2θ at 0.01°/step and exposure time of 0.1 sec/step. X-ray photoelectron spectroscopy (XPS) was utilized to characterize the elemental composition of T_iO_2 as well as the chemical state of titanium, oxygen and carbon species. N_2 adsorption-desorption test was utilized to determine the specific surface area of T_iO_2 nanoparticles using Brunauer-Emmett-Teller (BET) theory. The optical properties of T_iO_2 were evaluated by an UV-vis spectrophotometer equipped with diffuse reflectance accessory (Shimadzu UV-2600). From reflectance spectra, the optical bandgap of commercial T_iO_2 was calculated using the Kubelka-Munk equation. Surface charge of T_iO_2 was assessed by measuring their electro-kinetic potential (zeta potential) via a zeta potential analyzer (Malvern Zetasizer, Nano ZS).

The photo-decomposition of methylene blue was observed based on the absorption spectroscopic technique. In a typical procedure, 50 mg of T_iO_2 was dispersed in 50 ml of methylene blue solution (10 μM) in a 100 mL Pyrex beaker. The mixture was then stirred under the dark condition for 30 min to reach the adsorption equilibrium. After which, the solution was irradiated under visible light for up to 4 h with incessant stirring. A 500 W long arc xenon lamp with a UVIRCUT420 optical filter was used to provide the visible light source. The dye solution was sampled periodically to check the degree of adsorption (in the first 30 min) and photo-

decomposition (after the light source is on) of methylene blue. The sample was first centrifuged to separate the T_iO_2 particles from the solution. The light absorption of photo-reacted solution at 660 nm (i.e., the wavelength corresponding to the maximum light absorption of methylene blue) was measured using an UV-visible spectrophotometer (Varian Cary 5000) and compared with that of the pristine methylene blue solution to evaluate the degree of adsorption (in the first 30 min) and decomposition (after the light source is on). A control test (i.e., same methylene blue solution without the addition of T_iO_2 underwent the same adsorption and irradiation exposures) was also performed to evaluate potential decomposition of methylene blue due to direct photolysis.

15.2.2. Material

Type I white Portland cement, high strength and high modulus polyethylene (PE) fibers (Spectra® 1000, Honeywell), high-range water reducer (HRWR, ADVA® 181, GCP Applied Technologies), methycellulose-based viscosity modifying agent (VMA), white silica sand, and T_iO_2 nano-particles were used to formulate white ECC. Based on the results of T_iO_2 screening tests in Section 2.1, KRONOClean K7000 (KRONOS, USA) was selected to impart visible light photo-catalysis property into ECC for pavement applications. KRONOClean K7000 has a density of 2.9 g/cm^3 with no pigmentary property [209]. The PE fiber has a diameter of 23 µm, a length of 19 mm, a tensile strength more than 3000 MPa, and an elastic modulus beyond 100 GPa (Table 15.1). The high tensile strength and elastic modulus are achieved due to the use of ultra-high molecular weight PE resin through a gel spinning process during the manufacturing of the PE fiber.

Table 15.1 Properties and geometry of the PE fibers (Spectra® 1000, Honeywell)

Diameter (µm)	Length (mm)	Tensile strength (MPa)	Elastic modulus (GPa)	Density (g/cm^3)
23	19	3250	113	0.96

White silica sand is engaged to enhance the skid resistance while maintaining the surface brightness. The white silica sand has a density of 2.65 g/cm^3, a hardness of 7 Mohs, and a maximum particle size of 2.38 mm. Figure 15.1 shows the gradation curve of the white silica sand used in the current study.

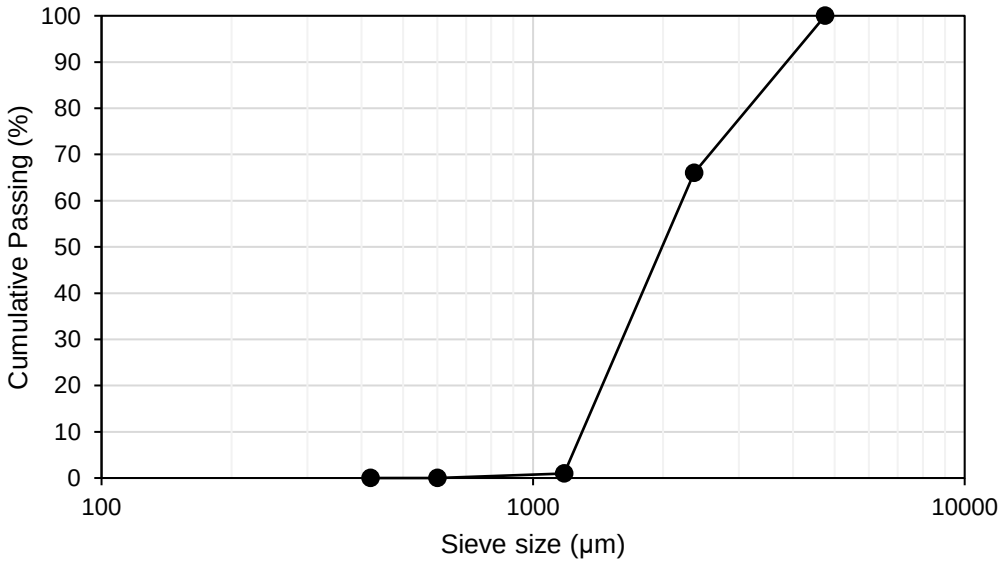

Figure 15.1 Gradation curve of silica sand

15.2.3. Mix design and specimen preparation

Different amounts of silica sand (10%, 20%, 30%) and T_iO_2 (1%, 2%, 5%) were incorporated into the white ECC mix to enhance the skid resistance and to impart the photocatalysis property, respectively (Table 15.2). A reference ECC mixture (S00-T0) without the addition of silica sand and T_iO_2 was also prepared.

Table 15.2 Mixture design of white ECC with visible light photocatalysis property for pavement applications (kg/m^3)

Mixture	White cement	Silica sand	T_iO_2	Water	HRWRA	VMA (vol.%)	PE fiber (vol.%)
S00-T0	1.0	None	None	0.35	0.02	1.5	1.8
S10-T0	1.0	0.1	None	0.35	0.02	1.5	1.8
S20-T0	1.0	0.2	None	0.35	0.02	1.5	1.8
S30-T0	1.0	0.3	None	0.35	0.03	1.5	1.8
S20-T1	1.0	0.2	0.01	0.35	0.02	1.5	1.8
S20-T2	1.0	0.2	0.02	0.35	0.03	1.5	1.8
S20-T5	1.0	0.2	0.05	0.35	0.03	1.5	1.8

ECC mixtures were prepared in a planetary mixer. White cement, silica sand, and T_iO_2 were dried mixed first. Water was then added followed by the addition of HRWR and VMA and mixed for 3-5 mins until the mixture achieved the required consistency. Lastly, the PE fibers were slowly added and mixed for another 3-5 mins until the fibers were uniformly dispersed. The fresh mixture was cast into cubes (50 mm by 50 mm by 50 mm) for compressive tests, coupon plates (300 mm by 75 mm by 12 mm) for flexural tests, dog-bone shaped molds with gauge length zone 120 mm (length) by 85 mm (width) tapering to 35 mm with thickness of 15 mm for uniaxial tensile tests, large plates (300 mm by 300 mm by 10 mm) for skid resistance related tests, and small plates (50 mm by 50 mm by 10 mm) for self-cleaning related tests. Specimens were removed from the mold after 1 day and were further cured at normal laboratory air (25±3^{o}C, 70%RH) for another 27 days before further testing. For the skid resistance related tests, the top surface of the large plate specimens were treated with a steel brush after the specimens were removed from the mold (i.e., at age of 1 d) to expose the silica sand on the surface.

15.2.4. Test program

The mechanical properties of white ECC incorporating a different amount of silica sand and T_iO_2 were evaluated. The compressive test was carried out following ASTM C109/109M [210] to determine the compressive strength of the cube specimens at the age of 28 d. The test was done under load control with a loading rate of 25 kN/min. At least four specimens were tested for each mix. The uniaxial tensile test was carried out on dog-bone specimens to determine the tensile behavior of specimens. The test was done under displacement control at 0.0025 mm/s. Two external linear variable displacement transducers (LVTDs) were attached to the dog-bone specimen with a gauge length of 100 mm to measure the specimen deformation. At least three specimens were tested for each mix.

Microscopic skid resistance of white ECC incorporating a different amount of silica sand was evaluated using the British pendulum test (BPT) followed ASTM standard [90]. BPT is a dynamic pendulum impact-type test used to measure the energy loss when the rubber slider slides over the pavement surface. The test results are reported as the British pendulum number (BPN). This method provides a measurement of microtexture and can be used either in the field or laboratory. At least three specimens were evaluated for each mix and a minimum

of five tests were performed for each specimen. The tests were conducted in wet test conditions by spraying water on specimens' surface. The macroscopic skid resistance was evaluated using the sand patch test (SPT), i.e., a volumetric-based spot test method with a sand patch. The method which is based on ASTM standard [91] can be used to determine the (average) mean texture depth (MTD) of pavement surface which reflects the macrotexture characteristic of the surface. This method is widely used as it is practical and considerably inexpensive.

Photocatalytic activity of white ECC samples incorporating a different amount of TiO2 was evaluated by measuring the degradation of dyes under visible light irradiation. Rhodamine B (RhB) dye which shows a strong red colour was used for this test. RhB has been extensively used to study the photocatalytic performance of T_iO_2-based cementitious composites for the following reasons. Firstly, the structure of RhB is similar to the structure of anthracene, an example of polycyclic aromatic hydrocarbons compounds (PAH compounds) [211]. PAHs are an example of soiling agents found in urban environments and mainly produced by incomplete combustion of organic matter. Secondly, RhB is relatively stable in the alkaline environment of the cementitious surface [212]. Lastly, RhB is water-soluble and hence can be spread easily on the surface of cement samples. As the photodecomposition of RhB occurs, the red color will be diminished, and in this case used as an indication of self-cleaning performance [47,202]. The procedure is commonly used and standardized in the Italian standard (UNI 11259:2008). RhB solution was prepared with a concentration of 0.05 g/L. The RhB solution was then applied to the surface of white ECC specimens with a total area around 4 cm2 in a circular shape. The dyed specimens were placed into a chamber equipped with a 0.55 W/m2 visible light lamp for irradiation. The reflectance of the specimen before and after the different duration of irradiation (i.e., 2 and 4 h) was captured with a UV-Vis spectrophotometer (UV-2600).

Accelerated dirt pick-up resistance (DPUR) of white ECC incorporating a different amount of T_iO_2 was also carried out. The surface brightness of the specimen was measured before and after the application of synthesized dirt which is a carbon black-based formula synthesized following ASTM D7898-18. The specimens were first sprayed 50 times with the synthesized dirt. The specimens were then rinsed with flowing water for 30 s. The sample surface was dried out and the brightness was determined with a reflected color measurement spectrophotometer. At least two specimens were tested, and the average brightness is reported for each mixture designs.

15.3. Results and Discussions

15.3.1. T_iO_2 characterization

Four commercial T_iO_2 samples were evaluated in this screening test. Figure 15.2 shows the morphologies of the four T_iO_2 nanoparticles. As can be seen, the T_iO_2 particles show a spherical shape with strong flocculation to form larger-size clusters. The primary particles size of P25 and K7000 is estimated to be about 20-40 nm in diameter, while the particle size of T_iO_2-anatase and T_iO_2-rutile is in the range of hundreds nanometer. However, the primary particles of K7000 tend to agglomerate to form larger secondary particles (> 500 nm) giving raise to the porous structure.

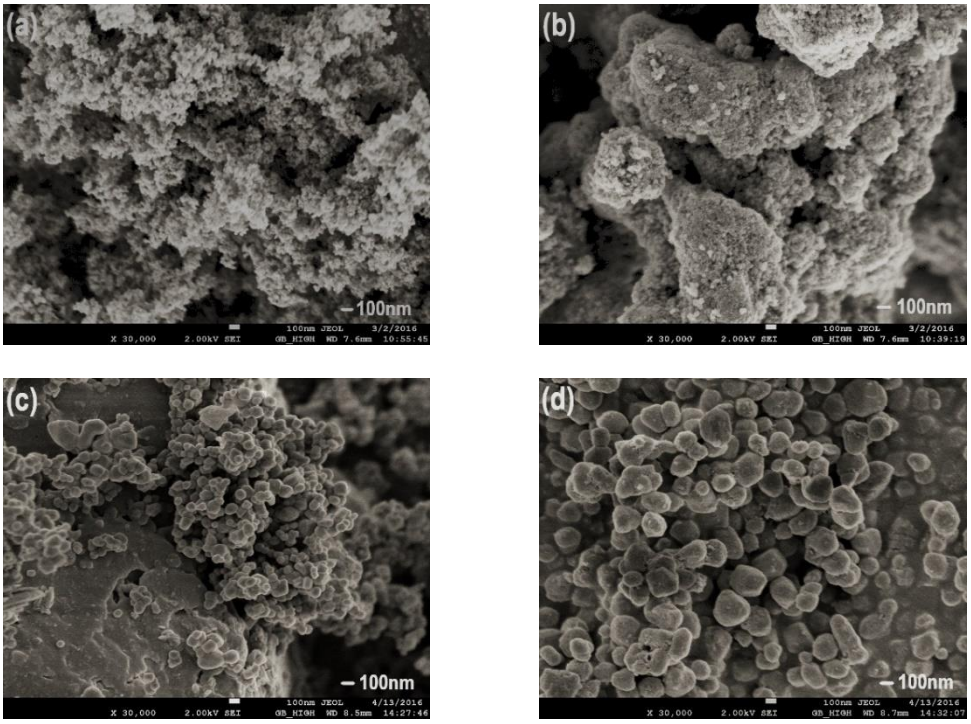

Figure 15.2 Scanning electron microscope (SEM) images of (a) P25, (b) K7000, (c) T_iO_2-anatase and (d) T_iO_2-rutile

The specific surface area and pore structure were evaluated by N2 adsorption experiment. Figure 15.3 presents the physi-sorption isotherm of the four T_iO_2. As can be seen, the physi-sorption isotherm for K7000 shows a hysteresis effect indicating it is mesoporous. In comparison, the observed isotherms for P25, T_iO_2-anatase, and T_iO_2-rutile suggest that these particles are non-porous. The Brunauer-Emmett-Teller (BET) theory was adopted to calculate the surface area (Table 15.3). As can be seen, the calculated BET shows that K7000 has the highest specific surface area of 252 m2/g followed by P25 (46.9 m^2/g). The high surface area for K7000 was strongly correlated to the meso-pore volume [213]. In contrast, the surface area for T_iO_2-anatase and T_iO_2-rutile samples is only 8 and 10 m2/g, respectively.

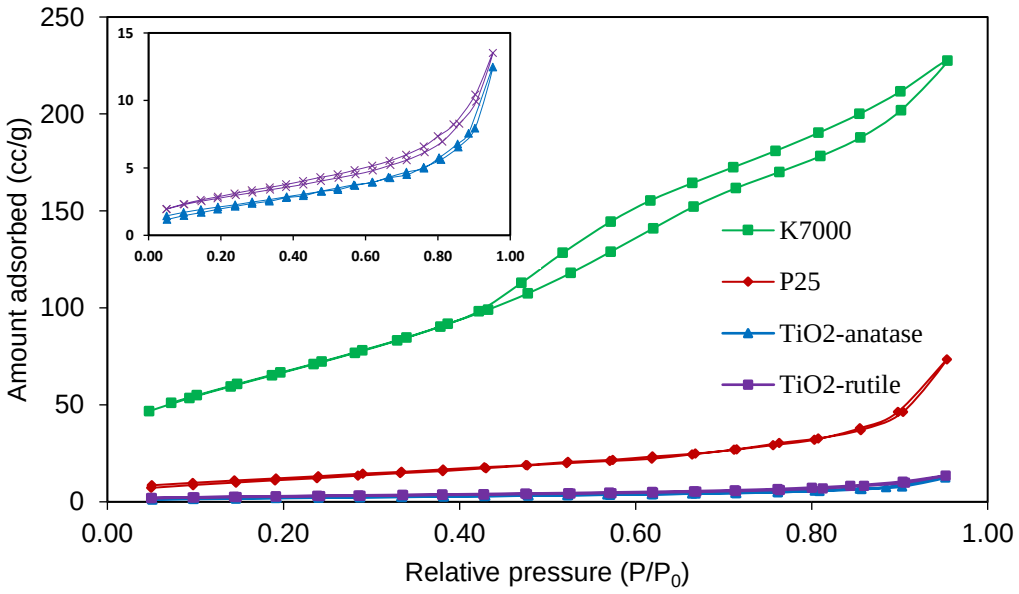

Figure 15.3 N_2 adsorption isotherms of P25, K7000, T_iO_2-anatase, and T_iO_2-rutile

Table 15.3 Properties of P25, K7000, T_iO_2-anatase, and T_iO_2-rutile

TiO2 sample	Crystalline phase	Bandgap energy (eV)	BET-surface area (m2/g)	Surface charge* (mV)	Methylene blue	
					Adsorption (%)	Photo-decomposition (%)
P25	80% Anatase 20% Rutile	3.21	46.9	33.20±0.26	5%	21%
K7000	Anatase	3.25	252	20.00±0.10	8%	43%
TiO2-anatase	Anatase	3.20	8	-28.70±2.21	51%	17%
TiO2-rutile	Rutile	2.95	10	21.13±0.38	6%	18%

* Measured in deionised water. Statistical significance differences (t test): $P < 0.01$.

The crystal structures of T_iO_2 were investigated through the XRD analysis. Figure 15.4 shows the XRD patterns of P25, K7000, T_iO_2-anatase, and T_iO_2-rutile. As can be seen, XRD analysis confirms that K7000 and T_iO_2-anatase samples consist of anatase phase, while T_iO_2-rutile sample consists of the rutile phase. P25 is the only sample consisting of both anatase and rutile phases, in the ratio of 80% to 20% (Table 15.3).

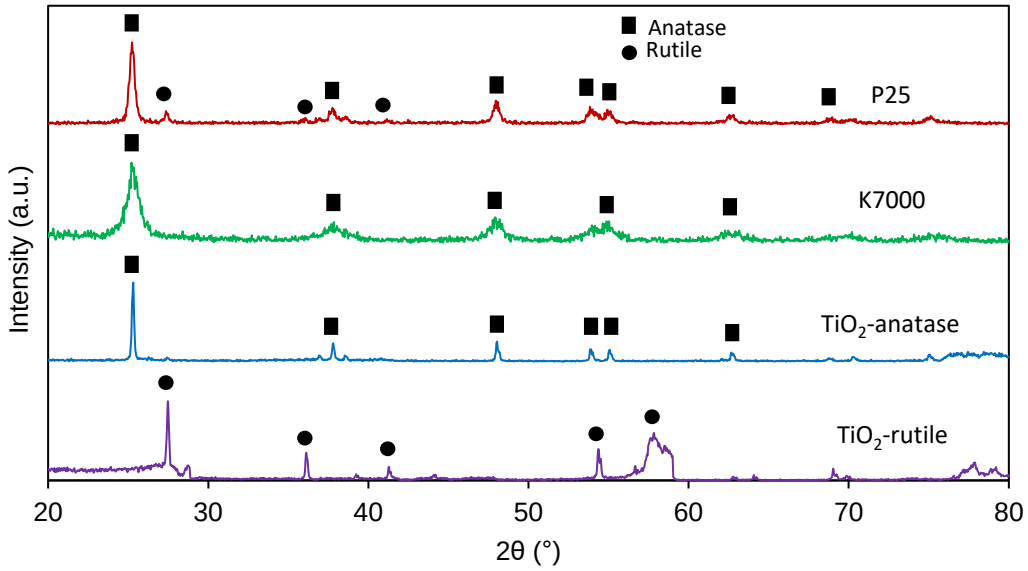

Figure 15.4 XRD spectra of P25, K7000, T_iO_2-anatase, and T_iO_2-rutile

The optical properties of the four T_iO_2 were examined using diffuse reflectance spectroscopy. Figure 15.5 presents the absorption spectra and bandgap energy calculation of P25, K7000, T_iO_2-anatase, and T_iO_2-rutile. The bandgap of T_iO_2 can be estimated from the absorption spectra using the Kubelka-Munk model and plotted using Tauc's relation.

$$\alpha h\nu = const\ (h\nu - Eg)^r \qquad \text{(Eq. 41)}$$

where hν represents the energy of the incident photon and the exponent r denotes the nature of the transition. The Tauc's plot ((αhν)1/r vs. hν) has a distinct linear regime which indicates the onset of absorption. Linear extrapolation of this regime to the energy axis at (αhν)1/r = 0 yields the bandgap energy of a material. Assuming the value of r is 2 (indirect allowed transition) for T_iO_2 [214,215], the Tauc's plot ((αhν)1/2 vs. hν) is illustrated in Figure 15.5(b).

The calculated bandgap of P25, K7000, and T_iO_2-anatase is around 3.2 eV, which that of rutile is slightly less than 3.0 eV (Table 15.3).

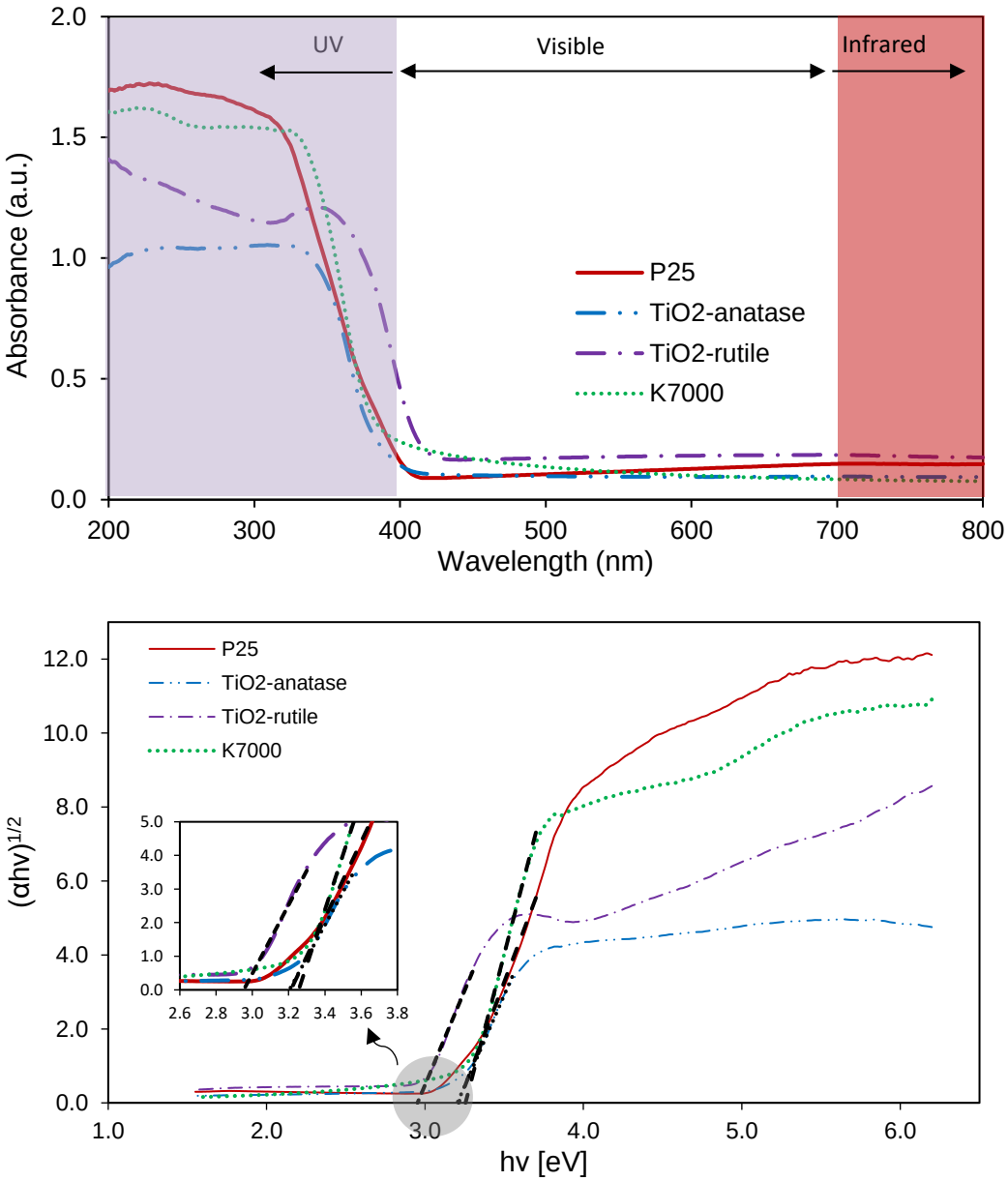

Figure 15.5 (a) Absorption spectra of P25, K7000, T_iO_2-anatase, and T_iO_2-rutile and (b) the corresponding Tauc's plots

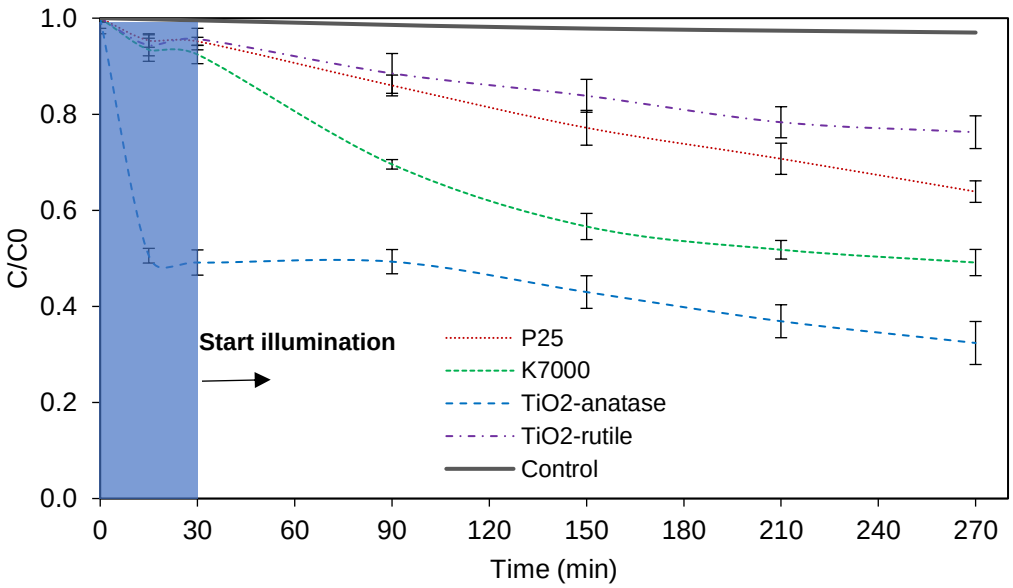

Figure 15.6 Photo-catalytic performance of the four T_iO_2 in the degradation of methylene blue under visible light irradiation (in solution phase)

Figure 15.6 shows the change in concentration of methylene blue in the aqueous solution as a function of time due to absorption in the first 30 min and photo-catalytic decomposition after the visible light source is on. As can be seen, the dye solution achieved adsorption equilibrium after 15 min under the dark condition. It was found the adsorption capability of P25, K7000, and T_iO_2-rutile is much lower than that of T_iO_2-anatase. The concentration of dye in solution dropped rapidly in the first 15 min and about 50% of dye was adsorbed on the surface of T_iO_2-anatase.

Figure 15.6 shows that the photocatalytic activity in the presence of T_iO_2-rutile was the lowest one although T_iO_2-rutile has the smallest bandgap and higher SSA than TiO2-anatase, as shown in Table 15.3. It is not surprising as the reaction was thermodynamically not permissible due to the band energy level of T_iO_2-rutile. According to literature, the conduction band of rutile is more positive than the reduction potential of electron acceptor (H+/H2) [216]. In consequence, such condition inhibits electron transfer process, which in turn increase electron hole recombination and diminish photocatalytic activity.

It is noteworthy that while T_iO_2-anatase has the lowest surface area according to the BET result (Table 15.3Table 15.3), it shows the highest dye adsorption capability (Figure 15.6). Previous studies demonstrated that surface charges of T_iO_2 may play an important role in the adsorption process [217–219]. The electrostatic interactions between the organic dye and T_iO_2 are the important factor controlling the interaction mechanism of contaminant/dye particles to T_iO_2 surfaces [217]. The surface charges of the four T_iO_2 was therefore measured using a zeta potential analyzer. As shown in Table 15.3, the TiO2-anatase was more electro-negative than the other three T_iO_2, supporting stronger adsorption capability with cationic methylene blue dye which is positively charged.

From Figure 15.6, it was observed that T_iO_2-anatase displayed the highest total decrease in the concentration of dye after 4 h visible light illumination. However, the decrease of dye concentration for T_iO_2-anatase mainly occurred during the adsorption process (51%, Table 15.3) and was very slow during visible light exposure (17%, Table 15.3). On the contrary, the total decrease in dye concentration for the other commercial products was highly controlled under visible light irradiation. Table 15.3 shows that K7000 (43%) generally outperformed other TiO2 materials used in this study for the degradation of dye in visible light.

Considering the bandgap of various commercial T_iO_2, it all lies in the UV region which should have no response in visible light. It was suggested that the degradation of MB dye in visible light was ascribed to the dye photosensitization mechanism [220–222]. In this procedure, the MB molecule could absorb the visible light to generate electron-hole pairs. The excited electrons are then transferred from a singlet/triplet state of MB (MB*) into the conduction band of T_iO_2 which further could react with oxygen, O2, to produce O_2- radicals (superoxide anion). The radicals generated could oxidize the aromatic rings of MB. The performance differences among commercial T_iO_2 was mainly caused by their particle size and pore structure, which define active site available for the photosensitization process. Due to high surface area and porosity, K7000 provide a more active site for reaction, resulting in a good photocatalytic performance.

Due to its high photocatalytic performance under visible light irradiation, K7000 was selected to be used in composite formulation to impart visible light photo-catalytic property into white ECC. Further characterization on K7000 was therefore conducted. The chemical state of elements in K7000 was analyzed using XPS analysis. Figure 15.7 shows the full XPS spectrum of T_iO_2 K7000 (Figure 15.7a) and the corresponding high resolution XPS spectra and their deconvolution near O 1s (Figure 15.7b), Ti 2p (Figure 15.7c), and C 1s (Figure 15.7d) regions. As can be seen, the main component in the O 1s spectrum is at 531.98 eV and 533.40 eV which are attributed to lattice oxygen and surface adsorbed OH group [223]. Next, Ti 2p dominates the spectrum with binding energies of 460.76 eV and 466.46 eV (Figure 15.7c). The binding energy at 460.76 eV (Ti 2p3/2) and the binding energy at 466.46 eV (Ti 2p1/2) arises from spin orbit-splitting, which are consistent with Ti4+ in T_iO_2 lattice [224]. Lastly, the deconvoluted C 1s spectrum shows three main peaks at the binding energies of 284.80 eV, 286.70 eV and 288.23 eV (Figure 15.7d). Generally, the binding energy of 284.80 eV could be either connected to a signal of adventitious elemental carbon contamination adsorbed from ambient or ascribed to a graphitic C-C bonds [220,225]. The binding energy of 286.70 eV and 288.23 eV demonstrated the presence of C-O and C=O bonds as in other works [215,226]. This tells that the component at those value is usually carbonate-like species in carbon-doped T_iO_2 samples [224]. Besides its high specific surface area which provides high number of active site on photocatalytic surface, previous study reported that carbon modified T_iO_2 like K7000 shows improved charge separation and electron transfer process leading to an improved performance under visible light/low light condition.

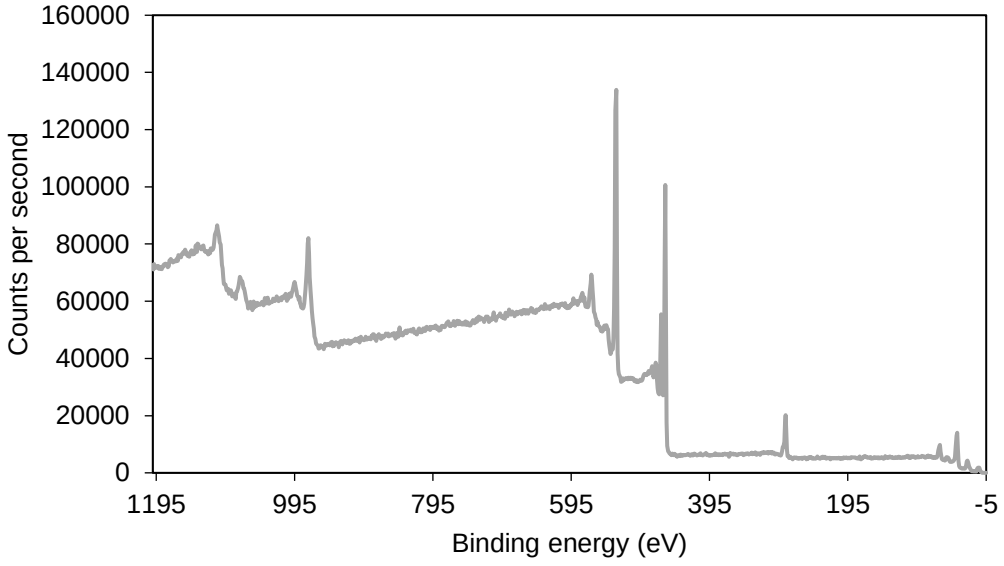

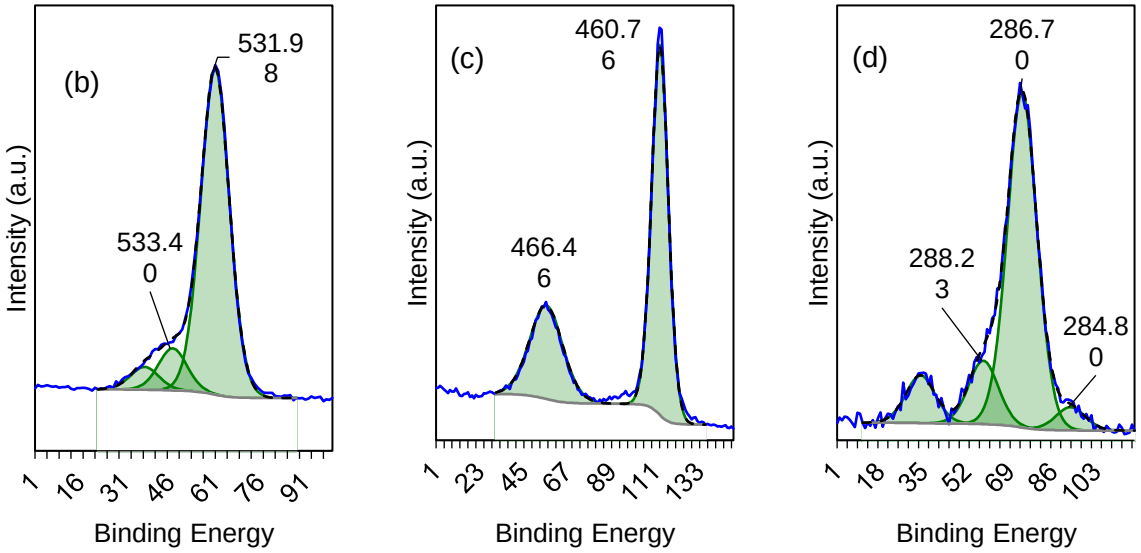

Figure 15.7 (a) The full XPS spectrum of K7000, and (b-d) high resolution XPS spectra and their deconvolution near (b) O 1s, (c) Ti 2p, and (d) C 1s

15.3.2. Effects of silica sand on mechanical properties

Table 15.4 summarizes the mechanical properties of the four white ECC mixes with different silica sand contents. As can be seen, the compressive strength increases while the tensile strength and tensile ductility of white ECC decrease with increasing silica sand dosage. This may be attributed to that the inclusion of hard silica sand increases the matrix toughness, and thus the chances for the formation of steady-state cracks and multiple cracking are reduced [160,161,163]. However, all mixes still possess moderate mechanical properties (i.e., compressive strength > 30 MPa, tensile strength > 3 MPa, and tensile strain capacity > 1%) suitable for pavement applications [44,200].

Table 15.4 Mechanical properties of ECC

Specimen	Compressive strength (MPa)	Tensile strength (MPa)	Tensile strain capacity (%)
S00-T0	38.06±0.06	5.04±0.75	3.71± .50
S10-T0	38.56±1.00	3.84±0.51	2.80±0.52
S20-T0	49.02±1.74	3.14±0.79	2.35±0.10
S30-T0	49.10±2.86	3.03±0.16	1.40±0.34
S20-T1	55.07±3.02	3.36±0.96	2.69±0.34
S20-T2	52.81±4.56	4.58±0.46	3.90±1.83
S20-T5	52.41±1.69	4.69±0.55	4.14±1.20

BPN of white ECC specimens are presented in Table 15.5. As can be seen, without the addition of silica sand, S00-T0 has a BPN of 54±6.6 lower than the required skid resistance of 55 for new roadways in accordance to the local standard set by the Land Transport Authority of Singapore [69]. This suggests conventional ECC cannot be used for road application [177]. A significant improvement of skid resistance was observed when silica sand is included in the ECC mix (BPN above 65). The S10-T0 possesses a BPN of 66 and S20-T0 possesses a BPN of 79, about 20% and 45% improvement, respectively, compared to the control. However, more silica sand inclusion (i.e., S30-T0) only lead to very mild improvement of the skid resistance of white ECC.

As shown in Table 15.5, the MTD of S00-T0 is very low with the surface texture of only 0.09±0.002 mm. Addition of 10% silica sand (S10-T0) remarkably increases the MTD to 0.22±0.04 mm. While the addition of 20% silica sand (S20-T0) further enhance the MTD to 0.37±0.04 mm, continuous increment of silica sand dosage only leads to moderate enhancement of MTD (S30-T0).

Table 15.5 Skid resistance performance of ECC-SS-T_iO_2

Specimen	Microtexture (BPN)	Macrotexture, MTD (mm)
S00-T0	54 ± 6.6	0.09 ± 0.002
S10-T0	66 ± 0.8	0.22 ± 0.04
S20-T0	79 ± 1.6	0.37 ± 0.04
S30-T0	83 ± 1.9	0.43 ± 0.04

15.3.3. Effects of TiO2 on mechanical properties

As shown in Table 66, addition of T_iO_2 leads to slight improvement of the compressive strength of white ECC from 49 MPa to 52-55 MPa. The maximum improvement was observed with 1% T_iO_2 addition, which is in line with previous studies [227–229], due to decreased crystalline $Ca(OH)_2$ content required for C-S-H gel formation and unsuitably dispersed nanoparticles in the cement matrix [229–231]. Furthermore, tensile strength and tensile ductility of white ECC increase with increasing T_iO_2 content. Addition of T_iO_2 nano-particles may densify the interface between fiber and matrix leading to enhanced interface friction bond. As a result, the fiber bridging strength as well as complimentary energy increase, and thus the tensile strength and tensile ductility of white ECC increase.

Photocatalytic activity of white ECC samples incorporating a different amount of T_iO_2 was evaluated by measuring the degradation of RhB after visible light irradiation as shown in Figure 15.8. After light exposure, the reflectance spectra exhibits a recovery after 2 h irradiation, and yet even a stronger recovery after 4 h irradiation of visible light for samples with T_iO_2 addition. Distinct reflectance spectra were observed in the UV region (< 400 nm) after addition of T_iO_2. The reflectance in UV region reduces with increasing T_iO_2 dosage. This is because K7000 has strong absorption of UV as shown in Figure 15.5. Furthermore, the reflectance spectra in the visible light range (400-700 nm) is slightly reduced for samples (w/o RhB) with T_iO_2 addition due to minor absorption of visible light of K7000 (Figure 15.5). When RhB was applied to the sample surface (w/ RhB), significant reflectance reduction was observed in the wavelength between 450 nm and 600 nm with the lowest peak at 555 nm which is corresponding to the absorption spectrum of the pink color of RhB solution. The application of RhB also affect the spectra in the UV region for the specimen with 0% T_iO_2 (i.e., ST20-T0), as shown in Figure 15.8 (a), due to the domination of RhB reflectance at UV region.

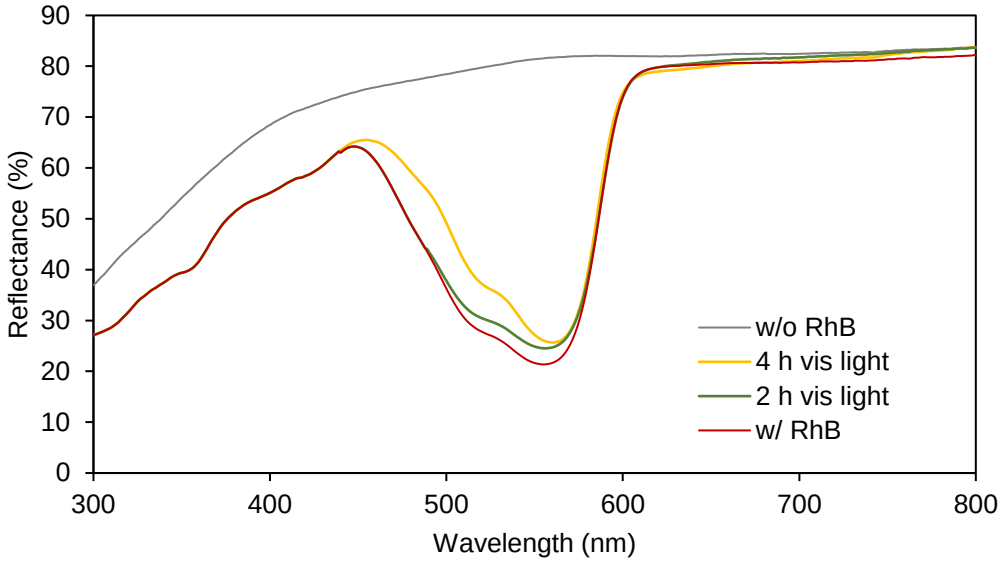
Reflectance (%)
Wavelength (nm)
w/o RhB
4 h vis light
2 h vis light
w/ RhB

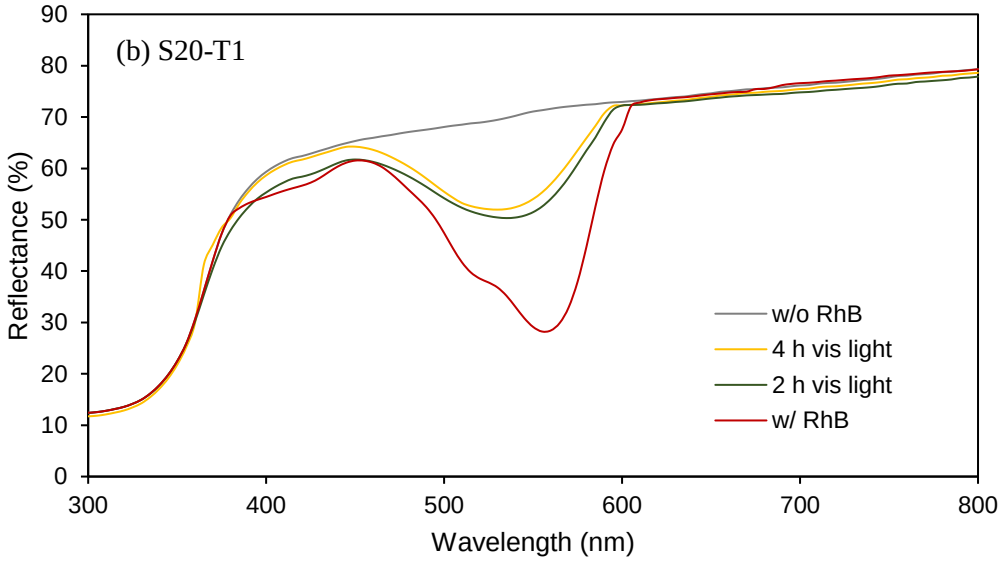
(b) S20-T1
Reflectance (%)
Wavelength (nm)
w/o RhB
4 h vis light
2 h vis light
w/ RhB

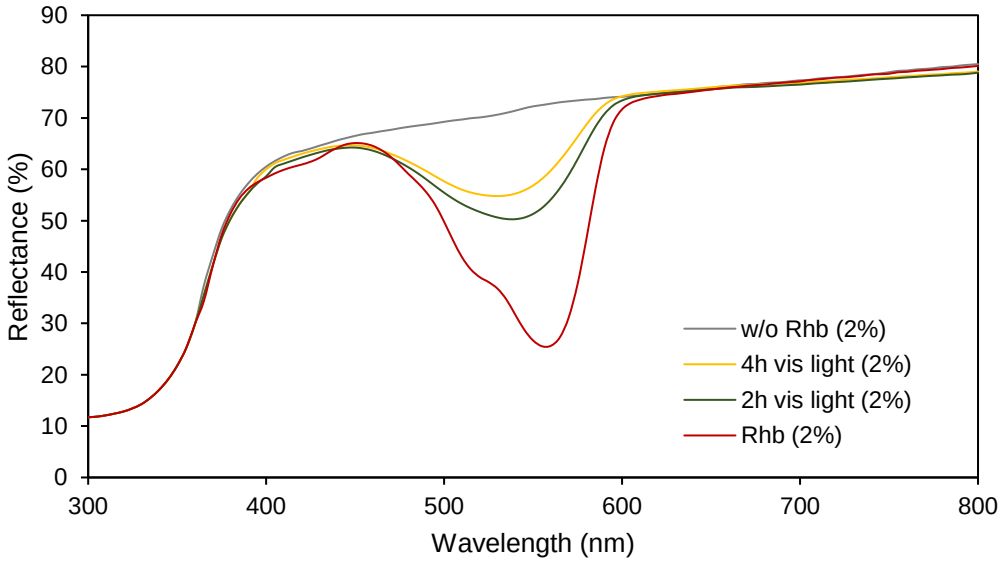
Reflectance (%)
Wavelength (nm)
w/o Rhb (2%)
4h vis light (2%)
2h vis light (2%)
Rhb (2%)

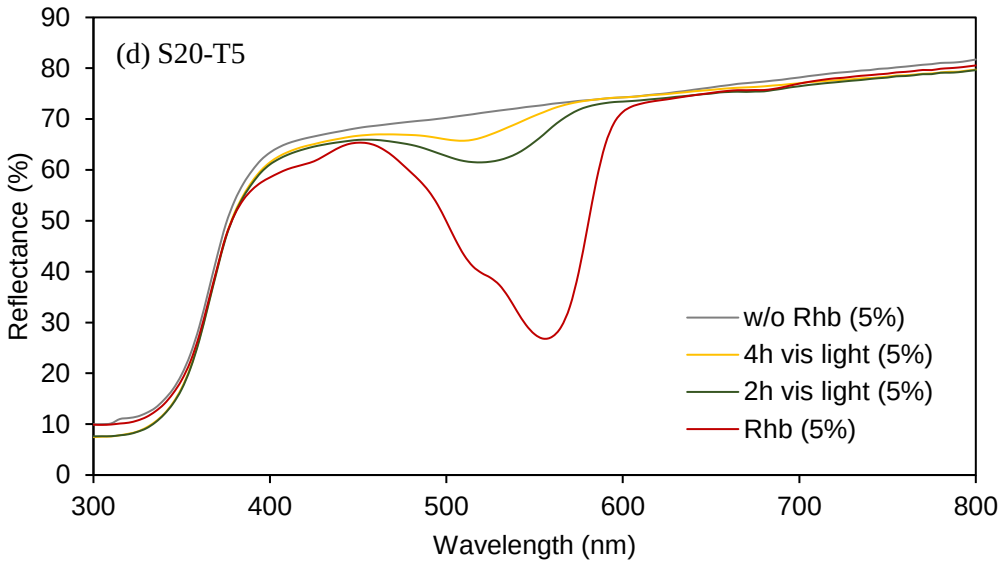

Figure 15.8 Photo-decomposition performance of (a) S20-T0, (b) S20-T1, (c) S20-T2, and (d) S20-T5 under visible light irradiation

Figure 15.9 shows the reflectance recovery of white ECC with different T_iO_2 content after visible light irradiation. The reflectance recovery was defined as the ratio of the total reflectance recovery after visible light irradiation exposure (i.e., area between the x h visible light curve and the w/ RhB curve) to the total reflectance reduction after applying RhB (i.e., area between the w/o RhB curve and the w/ RhB curve).

$$Solar\ reflectance\ recovery\ (\%) = \frac{Area\ between\ curve\ (x\ h\ vis)\ and\ curve\ \left(\frac{w}{RhB}\right)}{Area\ between\ curve\ (x\ h\ vis)\ and\ curve\ \left(\frac{w}{RhB}\right)} x100 \quad \text{(Eq. 42)}$$

As can be seen, reflectance recovery increases with increasing T_iO_2 dosage and visible light exposure duration. With 5% T_iO_2 addition, the reflectance recovery of white ECC can reach up to almost 89% after 4 h visible light irradiation.

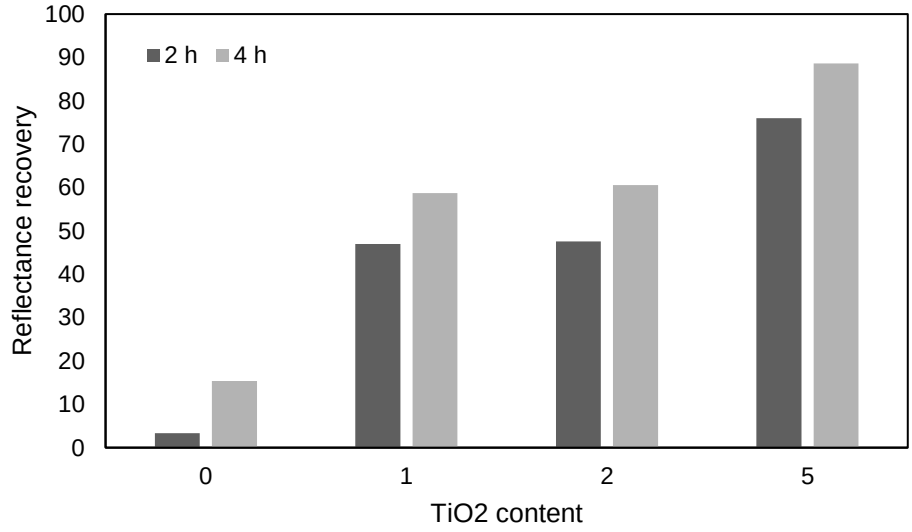

Figure 15.9 Reflectance recovery of ECC-SS-T_iO_2 based on visible light irradiation

15.3.4. Accelerated dirt-pick up resistance (DPUR) under visible light

Figure 15.10 presents the surface brightness (L*) of the white ECC samples before and after the accelerated DPUR test, where L* = 100 represents the brightest white and L* = 0 indicates the darkest black. As can be seen, the surface brightness decreases with increasing T_iO_2 dosage due to the minor absorption of visible light of K7000. The surface brightness of all white ECC samples were reduced after accelerated DPUR test. However, samples with higher T_iO_2 content showed less reduction of the surface brightness. With 5% T_iO_2 addition, the surface brightness reduction of S20-T5 is only about 8%. This means dirt is more difficult to stick to the surface on the resulting white ECC.

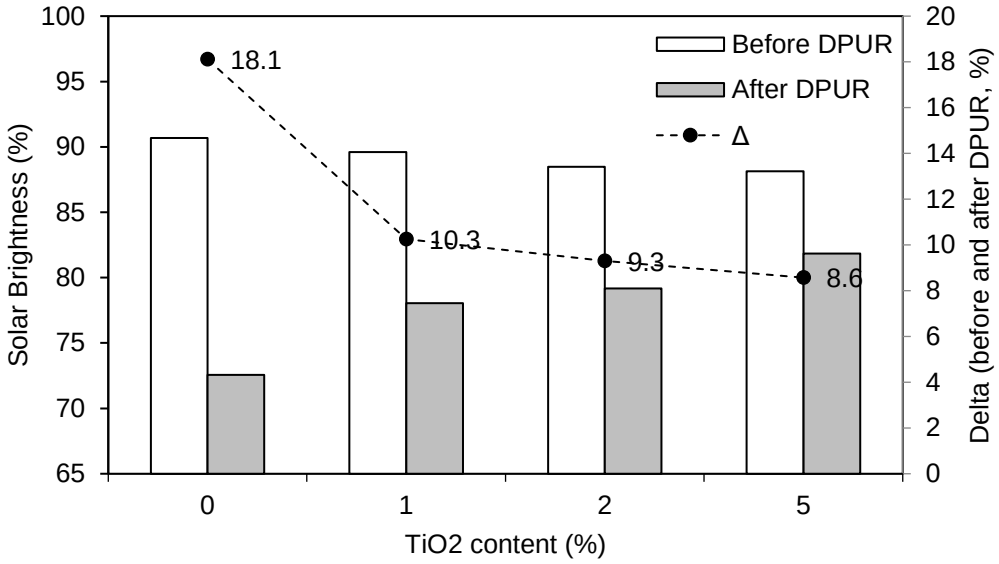

Figure 15.10 Accelerated DPUR under visible light

16. Conclusions and Recommendations

16.1. The Outlook

A novel comprehensive study of the functional performance of engineered cementitious composites (ECC) for pavement application with a case study: electrified roadway with dynamic wireless power transfer in Singapore has been conducted. The conventional materials may not be suitable for the electrified roadway with inductive charging as it is using a lot of steel-reinforcements, which potentially increasing losses in power transfer efficiency. Therefore, a new system has to be developed.

The ECC material has been carefully studied whether it can be used for prefabricated electrified roadway system, by using a method of a modified Performance Driven Design Approach (PDDA). The ECC can be modified to improve the functional performance without neglecting the structural performance. Laboratory and field tests have been conducted to study the skid resistance, surface water drainage, and noise. Further, a validated Finite Element and Fluid Dynamic models have been utilized to understand better about the related functional performance. A comprehensive multi-criteria decision analysis (MCDA) was developed to have a better understanding of the standards, the surface treatment methods, and the measurement method. More than 10.000 data have been collected worldwide and analyzed to identify the performance for each surface treatment. The MCDA gives a comprehensive overview on how the surface pavement is designed which then provides better understanding in investigating as well as designing the functional performance, especially in skid resistance, surface water drainage, and noise, of pavement made of ECC. The method has been illustrated in a simple flow chart, that can be seen in Appendix I.

As conventional ECC does not fulfil the safety requirements for roadway, a modified mixture design of ECC for roadway application is then developed by introducing corundum and silica sand material into ECC, namely ECC-Cor and ECC-SS. The study shown the skid resistance and surface water drainage performance of the modified ECC is significantly improved. Yet, it was not sufficient as the modified ECC was not providing sufficient surface drainage for the water outflow. Further surface treatment by introducing grooves successfully improve the water outflow. A strong correlation model between skid resistance and water outflow according to pavement geometry is proposed.

Noise performance cannot be neglected. After the safety factor, the comfort factor is the next stage that has to be considered. Many stakeholders are paying attention to the noise level, especially for traffic noise in the urban environment. The tire-pavement noise for pavement made of ECC was investigated. However, it was very clear from the beginning that ECC material is very dense and stiff, which makes ECC is not suitable for quieter pavements. But, with innovative texture, the noise can be decreased to the below of the standard limit.

It is very desirable to impart additional functions, i.e., self-cleaning and air purification, into concrete for pavement. Self-cleaning helps to maintain the brightness and reflectivity of the surface, while air purification improves the air quality in urban as well as in tunnels. The inclusion of TiO_2 in ECC-SS successfully engages photocatalytic function under the visible-light, facilitates the decomposition of Rhodamine B (RhB). The addition of TiO_2 increases self-cleaning performance. In summary, pavement made of ECC not only useful in structural, but also in functional performance, including the self-cleaning function.

Further, in this final chapter, key contributions, findings, as well as recommendation for further research according to the specific topic of functional performance on ECC material for pavement application are summarized.

16.2. The Study of MCDA

Key contributions and findings from the study include:

- The study of MCDA is carefully designed to understand better about the functional performance of pavement. It consists of many steps with two main key steps are: (1) scoring, and (2) weighting. The new scoring criteria is set up based on literature review regulated by agencies. The criteria are set from 1 to 5 (1=lowest performance, and 5=highest performance), and they are mainly based on the performance, required actions, and risk of accidents. The new weight proportion has been proposed for specific MCDA study on a functional performance for surface pavement which prioritized safety function. The criteria studied includes durability, cost, microtexture, macrotexture, surface drainage, tire-pavement noise, and pavement roughness.
- The second analysis is done by plotting multiple constraints scenario. This analysis allows comparison for many texturing methods. However, it is limited to two constraints. The plot is not determined to give a correlation between constraint (criterion), instead it gives a picture what are the performance of two constraints for each texturing method.
- More than about 10.000 data have been collected, and then they are analyzed for different texturing methods for asphalt and concrete pavements for seven different criteria (constraint): microtexture and friction, macrotexture, water outflow, pavement roughness, and tire-pavement noise, cost, and durability.
- According to data, best practice of texturing methods for skid resistance and macrotexture includes longitudinal diamond grooving, transverse diamond grooving, and turf drag. Additionally, exposed aggregate, longitudinal tining, and burlap drag can be used to improve skid resistance to the required safety standards.
- In terms of surface drainage, diamond grooving gives the best results. However, other texturing methods such as diamond grinding, tining, burlap drag, exposed aggregate resulting sufficient performance for water outflow.
- The optimum texturing methods for both low tire-pavement noise and skid resistance includes longitudinal tining, turf drag, broom drag, exposed aggregate, and followed by diamond grinding. The least solution for noise is transverse diamond grooving.

Recommendation for further research on MCDA are given:

- To include more standards/regulation/methods which are existing worldwide.
- To update the questionnaires on the scoring and weighting based on current policies. As policies might be changing from time to time. Alternatively, scoring and weighting can be opted to be changed by user. In this way, user can define their own MCDA based on their local standards/regulations.
- To develop more robust software tools/websites so many stakeholders can generate information based on data collected and analyzed.

16.3. The Study of Skid Resistance

Key contributions and findings from the study include:

- A normal ECC (ECC-Cor 0) has a British Pendulum Number (BPN) of 53±9.1 which is lower than the required skid resistance of 55 for new roadways in accordance with local standard set by the Land Transport Authority of Singapore. This suggests ECC without any modification (ECC-Cor 0) cannot be used for road application unless surface treatments are introduced.

- ECC mixed with corundum (i.e., ECC-Cor 50 to 100) with surface exposure after three days shows some improvement in skid resistance as most of the results are above 55 PN on average, except ECC-Cor 90. The moderate improvement may be attributed to delayed surface exposure process at day 3, where the matrix, a fiber-reinforced paste, was very hard to be removed and thus less corundum aggregates were exposed on the surface.

- A significant improvement of skid resistance of ECC-Cor with exposing process one day after casting was observed (BPN above 65). It can be observed that skid resistance (BPN) increases with increasing amount of corundum used in the ECC-Cor mix. The ECC-Cor 100 possesses a BPN of 75, about 40% improvement compared to ECC-Cor 0. This is because the surface exposure process was carried out at day 1 and the paste can be removed easily and evenly as evidenced by the reduced variation of the BPN results.

- High skid resistance is also observed for the ECC-Cor specimens with exposed method (BPN around 75, comparable to the ECC-Cor 100). Even with much less corundum was included in the ECC-Cor 0-S specimen (150 kg/m3) as compared to other ECC-Cor mixes (e.g., 225 and 450 kg/m3 for ECC-Cor 50 and 100 mixes, respectively). Since skid resistance is a surface property, ECC-Cor 0-S represents a potential approach to strategically use corundum to improve the surface property while keeping the superior mechanical performance of the original ECC. Ultimately, this approach may be applied for both cast-in-situ and precast construction.

- A significant improvement of skid resistance was observed when silica sand is included in the ECC mix (BPN above 65). The ECC-S10 possesses a BPN of 66 and S20 possesses a BPN of 79, about 20% and 45% improvement, respectively, compared to the control. However, more silica sand inclusion (i.e., S30-T0) only lead to very mild improvement of the skid resistance of white ECC.

- The Mean Texture Depth (MTD) of ECC-S00 is very low with the surface texture of only 0.09±0.002 mm. Addition of 10% silica sand (ECC-S10) remarkably increases the MTD to 0.22±0.04 mm. The addition of 20% silica sand (ECC-S20) further enhance the MTD to 0.37±0.04 mm, continuous increment of silica sand dosage only leads to moderate enhancement of MTD (ECC-S30).

- BPN for longitudinal grooves is considered remain the same, while BPN for transversal grooves are increases. MTD for ECC with grooves is also increased about three times compare to specimen without grooves.

- The grooved ECC mixed with aggregates method comes with its advantages including: (1) it is significantly increase the skid resistance, and (2) it is relatively easy procedure to cast ECC mixed with aggregates followed by grooving process. The grooves can be done by both precast or groove in situ methods.

- The results from casting in situ ECC in large scale does not satisfied the requirement for pavement application. Not only the skid resistance is considerably low, but also it results

in wrinkles. The wrinkles occurred due to the low workability of the ECC itself. The existence of fiber inside the mixture combined with low water cement ration causing difficulties when leveling works need to be done on the field. Therefore, material ECC is not recommended for pavement application, except there is an improvement on the mixture design to improve the workability for the material.

- More slabs of modified ECC were made with precast method with steel formworks. By using steel formworks, the deformation which was occurred on the first trial with wooden formwork seems do not appeared anymore. About 12 slabs were mixed and casted in different days in Tuas South Avenue area. Five full-size slabs and 6 half-size slabs were installed on busbay in Jurong Island. BPT and SPM tests were taken on site. As results, various results are observed due to differences during mixing, casting, and finishing work. However, all slabs with precast method result more than 55 BPN, with average of 68±6.5 BPN for slab 02 to slab 11. The average for macrotexture is 0.44±0.09 mm.

- Alternatively, the reverse precast method is designed to solve previous issues faced including deformation in early stage, as well as inconsistency in flat and smooth surface. The reverse precast method for modified ECC gives results in microtexture 68±2.45 BPN and macrotexture MTD 0.24±0.02 as average value. Further, this method improves the end-result of physical appearance as the surface is flatter and smoother compare to other previous methods.

- The trend shows BPN reduces while MTD remains unchanged with increasing load cycles. Even after 100,000 load cycles, the BPN is still above 65 BPN and the MTD maintains at 0.34 mm. It can be concluded the surface texture and skid resistance made of ECC-Cor can last until the end of the pavement life-time without any further intervention. This is mainly due to the hardness of corundum.

- The 3D FEM model on BPT for skid resistance was conducted to predict the BPN of ECC samples. Validation and calibration of the model were performed with consideration of key parameters of the BPT mechanism: the mass, the center of gravity of the model and the sliding distance of the rubber slider. The simulation results show a good correlation with laboratory measurements.

- The 3D FEM model was validated by comparing the BPN results from the FEM analysis with BPN results from laboratory tests. The sample used for validation is from sample with mixture design of ECC-Cor 80. Samples were prepared for both flat and grooved texture. From the results, it can be seen the different between FEM model and laboratory test is below 5%, considerably good model.

Recommendation for further research are given:

- The laboratory scale test on durability shows good trend on durability. A further study of the durability on skid resistance study based on field investigation can be performed every after 10 years to investigate the long-term performance.

- Further study on skid resistance based on different textures can be performed. The utilization of silicone-based method for the formwork can be easily applied to study different textures.

16.4. The Study of Surface Water Drainage

Key contributions and findings from the study include:

- The outflow times on normal ECC cannot be measured as the surface is very smooth that the rubber ring of the Outflow test (OFT) meter device is stick to the surface tightly. This condition makes water flowing out in very slow rate. The outflow times on ECC mixed with corundum is improved as the corundum provides a microtexture on the surface pavement which allowing the water to find a gap between the aggregates. The average outflow time result of ECC-Cor is 62.11±4.99 s. Similar result is observed in ECC-SS 01 with 65.06±3.51 s.

- The outflow times for the grooved ECC-Cor specimens are even shorter. The combination of the microtexture provided by the corundum and the macrotexture provided by the grooves makes the space between the rubber ring of the Outflow Meter device and the surface pavement specimens even bigger, which results in a lower value of outflow times. The outflow times of grooved ECC-Cor with a land area of 25.0 ± 0.5, 20.0 ± 0.5, 15.0 ± 0.5, and 7.5 ± 0.5 mm is 7.73 s, 7.30 s, 5.83 s and 3.38 s, respectively.

- The average Water film thickness (WFT) on ECC-Cor for water drained above the ECC-Cor surface pavement (grade 1%) with flow rate of 1.0, 3.1, 5.1, and 8.9 liter/minute, are 1.33, 1.91, 2.66, and 4.10 mm, respectively. There is not much different between the average WFT results derived from the equation and direct measurement (less than 10%). The average WFT on ECC-Cor for water drained above the ECC-Cor surface pavement (grade 5%) with flow rate of 1.0, 3.1, 5.1, and 8.9 liter/minute, are 1.03, 1.18, 1.93, and 2.78 mm, respectively. There is not much different between the average WFT results derived from the equation and direct measurement (less than 10%).

- The average WFT on grooved ECC-Cor for water drained above the ECC-Cor surface pavement (grade 1%) with flow rate of 1.0, 3.1, 5.1, and 8.9 liter/minute, are 0.09, 0.15, 0.22, and 0.35 mm, respectively. There is not much different between the average WFT results derived from the equation and direct measurement (less than 10%). The average WFT on grooved ECC-Cor for water drained above the ECC-Cor surface pavement (grade 5%) with flow rate of 1.0, 3.1, 5.1, and 8.9 liter/minute, are 1.03, 1.18, 1.93, and 2.78 mm, respectively. There is not much different between the average WFT results derived from the equation and direct measurement (less than 10%).

- The WFT will be significantly decreased when such a surface pavement equipped with grooves. As the water will fill the grooves immediately when it drained above the surface. Once, the grooved filled with water, the remaining of water will only then drained along the original surface of the pavement.

- The grooves can reduce the WFT up to 50% of its original thickness, depends on the dimension of the grooves, as well as the grade of the pavement.

- When the grade of the slab increased, the average WFT will be reduced. The higher the grade, will results more reduction of the WFT. With similar dimension of grooves, the WFT is reduced up to 30% between the flat and grooved ECC-Cor with 1% grade. While the WFT can reduced up to 50% between the flat and grooved ECC-Cor with 5% grade.

- From field investigation, it was found out that the outflow results of brushed ECC mixed with corundum improved when there is more corundum on the surface as they have been exposed (see after six hours and 21 hours). When the matrix is not fully hardened, more corundum aggregated have been removed away in the process. This phenomenon can be seen on the “after four hours exposed” part.
- The difference between time of processing does not affect water outflow results as all of them are below than 10 s. However, it should be noted that based on microtexture and macrotexture, good results are coming from brushing time in range between 6 to 12 hours.
- It should be mentioned that the results from field investigation is faster than results acquired in laboratory tests. Where outflow times are more approximately 60 s and less than 10 s for laboratory tests and field investigation results, respectively. This is occurred because the leveling process of ECC in full-scale application is considerably difficult, resulting rougher surface.
- Grooves on ECC-Cor specimens reduce the WFT on the surface. With the same total area (2 m x 0.5 m), the WFT on grooved ECC-Cor surface will be more than 50% decreased in comparison to ECC-Cor surface. The number is, however, might be varied on the dimension of the grooves (width, length, and thickness). In consequence, thinner WFT will cause a higher safety for motorists/vehicles as it creates smaller risks of hydroplaning effect between tire of vehicles and pavement in wet condition.
- The validated 3D Computational Fluid (CFX) model gives a strong correlation with a lab test and equation results. In comparison to lab tests, the 3D CFX model gives 1.1% and 5.6% differences for 1% and 5% grades, respectively. While in comparison to (Eq. 33, the 3D CFX model gives 3.5% and 5.6% differences for 1% and 5% grades, respectively. This means 3D CFX model can be used to study and to design a surface water drainage. Several parameters can be studied with this model, including the effect of macrotexture, effect of grade, and the effect of grooves to water film thickness.
- The roughness of the material, which is sand grain roughness in the CFX model, is negatively affecting the velocity of the water flow. The higher roughness of the material applied, the slower is the water flow in results.

Recommendation for further research are given:

- Numerical studies from different aspects can be done including the wet tire pavement interaction and hydroplaning model. Similarly, those numerical studies were done on different materials, tire, and scales.
- The OFT method can be used as one alternative for a quick assessment to evaluate the drainage performance based on texture properties in Singapore.

16.5. The Study of Correlation between Skid Resistance and Surface Water Drainage Performance

Key contributions and findings from the study include:

- Due to the absence of coarse aggregates in ECC mix design, the skid resistance and surface water drainage performance of ECC is a concern for pavement applications. Corundum as fine aggregates was incorporated into ECC mix to improve the microtextures and skid resistance of ECC. The tensile strain capacity generally reduces with increasing corundum content. However, the resulting ECC-Cor still possesses a tensile strain capacity around 1% and flexural strength of 10 MPa, which are satisfactory for most pavement applications.
- Addition of corundum significantly improves the microtexture of ECC, resulting high BPN more than 70. ECC-Cor shows good durability and the microtextures can last for more than 100,000 load cycles.
- ECC-Cor Spread method can be a good alternative to fulfil skid resistance requirements for pavement application. This method maintains the mechanical properties of normal ECC, while the brushed surface of corundum layer acts as a surface layer to provide the skid resistance.
- While the addition of corundum enhances the microtexture and skid resistance of ECC, improvement on macrotexture and surface water drainage is marginal and the risk of hydroplaning still exist. Further surface treatment with grooves successfully improves the functional performance, not only by minimizing the risk of hydroplaning (OFT < 4 s) but also by improving the skid resistance (BPN > 90).
- It was found that pavement geometries affect surface water drainage performance, particularly for surface with low MTD. The empirical model proposed in the current study is able to correlate the relation between water drainage (OFT) and MTD and pavement geometries.

Recommendation for further research are given:

- With the inclusion of synthetic fibers with high aspect ratios, practical use of ECC-Cor for full scale pavement applications should ensure few aspects. Properties of ECC-Cor produced in large scale processing should be maintained by selecting suitable raw materials, mix design, mixer, and mixing sequence and controlling fresh properties of paste to ensure uniform fiber dispersion.
- With high unit volume cost of ECC-Cor, it is advisable to use the material strategically. For example, instead of using ECC-Cor to build full depth pavement, the overlay approach greatly reduces the required volume of material.
- ECC-Cor pavement can be an economical solution from the life cycle cost perspective by reducing rehabilitation and maintenance frequency and extending service life. Further study is necessary for large scale processing of ECC-Cor and life cycle and life cycle cost assessments of ECC-Cor pavement.

16.6. The Study of Noise

Key contributions and findings from the study include:

- The evaluation of the Mean Profile Depth (MPD)-value (acc. to ISO 13473-1) and the shape factor of the profile; are giving a good indication whether the road surface is suitable to reduce the tire-road noises.
- The noise level coming from the pavement made of ECC can be up to 65 dB(A), which is quite safe as it is below of many standard values regulated by the authorities. However, from the perspective of skid resistance and surface water drainage performance, the ECC slab is not safely to be used for roadways.
- The noise level for ECC-Cor-Gro 1 increased up to 69.2 db(A) because of the lower shape factor (G) due to a rougher surface as results from the existence of corundum aggregate on the ECC surface. The shape factor at ECC-Cor is at 55% which is very low for dense surfaces.
- It can be seen from the analysis from four parameters namely vibration, air, cavity, and residual, that the biggest differences can be found in the vibrational noises, meaning that ECC-Cor has a rough surface that stimulates the tire to vibrate more.
- The modification of ECC-Cor by introducing grooves (ECC-Cor-Gro 1) has successfully reduced the sound level coming from the vibration. The sound level from the air parameter is decreased slightly, mainly in the frequency from 315 to 1250 Hz. The shape factor is then increased for ECC-Cor-Gro 1.
- The ECC-Cor with grooves can be a solution for the (electrified or normal) roadways with pavement made of ECC in Singapore condition, where the National Environment Agency (NEA) of Singapore regulates the noise limit for 67 dB to new roads and expressways.

Recommendation for further research are given:

- As has been discussed, three parameters are significantly affecting noise level for pavement namely stiffness, porosity, and texture. For further research, ECC can be modified to decrease the stiffness and or increase the porosity. However, the study needs to be comprehensive as changing those two parameters will affect the mechanical properties and durability performance.
- Absorption noise test can be done to see how the noise level is affected by the material itself. The test is more suitable for experimental test in relation to changing the density and the porosity of ECC material.
- Field test noise related on full scale pavement application made of ECC can be done to see direct results when there is a minimum length of pavement made of ECC applied on real roadways.

16.7. The Study of Self-Cleaning and Slip-Proof

Key contributions and findings from the study include:

- Different T_iO_2 nano-particles were tested first to evaluate their photocatalysis property under visible light irradiation. Among the four commercially available T_iO_2 nano-particles, KRONOClean K7000 possessed the best photocatalytic performance under visible light irradiation due to high surface area and porosity, providing more active sites for reaction.
- Experiments were carried out to study the effects of white silica sand content and T_iO_2 dosage on the mechanical properties, micro- and macrotexture for skid resistance related properties, self-cleaning performance, and dirt pick-up resistance of the resulting white ECC. Mechanical tests showed that the compressive strength and skid resistance increase while the tensile strength and tensile strain capacity of white ECC decrease with increasing silica sand content. Furthermore, compressive strength, tensile strength, tensile strain capacity, self-cleaning performance, and dirt pick-up resistance of white ECC increase with increasing T_iO_2 dosage.
- The inclusion of T_iO_2 in ECC-SS successfully engages photocatalytic function under the visible-light, facilitates the decomposition of RhB. The addition of T_iO_2 increases self-cleaning performance.
- X-ray photoelectron spectroscopy (XPS) analysis revealed that K7000 is a type of carbon modified T_iO_2 which might improve charge separation and electron transfer process, leading to improved performance under visible light/low light condition.
- KRONOClean K7000 was then selected for the development of the bright and slip-proof ECC with the inclusion of white silica sand. With 20% silica sand and 5% T_iO_2 inclusion, the resulting white ECC possess excellent mechanical properties (i.e., compressive strength > 50 MPa, tensile strength > 4.5 MPa, and tensile strain capacity > 4%) and high skid resistance (~ 80 BPN), and has high surface reflectivity with a brightness value of 90.
- The resulting white ECCs shows strong visible light activated photocatalysis property (i.e., 90% reflectance recovery after 4 h visible light irradiation, 8% surface brightness reduction after DPUR test).

Recommendation for further research are given:

- With the inclusion of synthetic fibers with high aspect ratios, practical use of ECC-SS- T_iO_2 for full scale pavement applications should ensure the properties produced in large scale processing. It should be maintained by selecting suitable raw materials, mix design, mixer, and mixing sequence and controlling fresh properties of paste to ensure uniform fiber dispersion.
- Further study is necessary for the durability of ECC-Cor / ECC-SS with T_iO_2. Not only the durability of the surface texture, but also the self-cleaning performance.
- Further study on life cycle cost assessments of ECC-Cor/ ECC-SS with T_iO_2 for pavement application.

References

[1] AASHTO. Design of pavement structures. Washington, D.C.: AASHTO; 1993.

[2] TUMCREATE. The Center for Electromobility in Megacities. [2017]; Available from: https://www.tum-create.edu.sg/about/center-electromobility-megacities.

[3] Land Transport Authority. Land Transport Master Plan 2013. Singapore; 2013.

[4] GovTech. Public Transport Utilisation - Average Daily Public Transport Ridership: Singapore Open Data Licence. [April 12, 2017]; Available from: http://www.mytransport.sg/content/mytransport/home/dataMall.html#Facts_&_Figures.

[5] Land Transport Authority. Singapore Land Transport Statistics in Brief 2013. Singapore; 2014.

[6] Department of Statistics Singapore. Singapore in Figures 2016. Singapore; 2017.

[7] NCSS. Singapore Emission Profile. [January 2018]; Available from: https://www.nccs.gov.sg/climate-change-and-singapore/national-circumstances/singapore's-emissions-profile.

[8] Siau Ming En. Singapore cut carbon intensity; Available from: https://www.todayonline.com/singapore/singapore-cut-carbon-intensity-30-cent.

[9] Land Transport Authority. Standard Details of Road Elements. Singapore: Land Transport Authority; 2015.

[10] Jung Y, Zollinger D, Tayabji S. Best Practices of Concrete Pavement Transition Design and Construction. Austin, Texas; 2007.

[11] D.Q Wu, Y. Zhang. The semi-rigid pavement with higher performances for roads and parking aprons. Engineering Challenges and Opportunities 29 (2011).

[12] Land Transport Authority. Code of Practice for Works on Public Streets. 6th ed. Singapore: Land Transport Authority; 2008.

[13] Hernando D, del Val MA. Guidelines for the design of semi-rigid long-life pavements; 2016.

[14] IPT Technology. Competitive, clean, and efficient public transport with IPT charge bus. Efringen-Kirchen; 2016.

[15] Highways Agency. Preparing the Strategic Road Network for electric vehicles (2014).

[16] The Economist. An infrastructure for charging electric vehicles takes shape; Available from: https://www.economist.com/business/2017/09/07/an-infrastructure-for-charging-electric-vehicles-takes-shape.

[17] Mark Harris. Electric cars may stall without a battery revolution; Available from: https://www.theguardian.com/sustainable-business/2017/jul/19/electric-cars-battery-revolution-tesla-volvo.

[18] Hutin M, Leblanc M. Transformer System for Electric Railways (527827).

[19] I. System Control Technology. Roadway Powered Electric Vehicle Project Track Construction And Testing Program Phase 3D(ISSN 10551425) (1994).

[20] A. Bresnock, M. Miller, E. Lechner, S. Shladover. Roadway electrification: regional impact assessment. Transportation Research Record 1416 (1993).

[21] Transport Research Laboratory. Feasibility study: Powering electric vehicles on England's major roads. Birmingham; 2015.

[22] eRoadArlanda. Roads of the future - electrified roads: Vehicles are recharged while driven; Available from: https://eroadarlanda.com/.

[23] A. Brecher, D. Arthur. Review and Evaluation of Wireless Power Transfer (WPT) for Electric Transit Applications.(FTA Report No. 0060) (2014).

[24] ICNIRP. ICNIRP Guidelines for limiting exposure to time-varying electric, magnetic, and electromagnetic fields (up to 300 GHz); 1998.

[25] Bombardier. Datasheet Primove E-Bus (2015).

[26] S.Y Choi, S.Y Jeong, B.W Gu, G.C Lim, C.T Rim. Ultraslim S-Type Power Supply Rails for Roadway-Powered Electric Vehicles. IEEE Trans. Power Electron. 30 (11) (2015) 6456–68.

[27] Implementing recharging inductive technology on heavy duty pavement bringing unlimited autonomy to electrical vehicles. 8th RILEM International Conference of Mechanisms of Cracking and Debonding in Pavements (2016).

[28] M. L. Nguyen, P. Hornych, J.-P. Karzreho, S. Perez. Accelerated full scale test on prefabricated concrete slab pavement for electrical supply by induction of urban transport sytems (2014).

[29] N. NguyenDinh. Precast Ultra-Thin Whitetopping (PUTW) in Singapore [Doctoral Thesis]. Munich: Technical University of Munich; 2017.

[30] D.DS Pereira, J.T Balbo, L. Khazanovich. Theoretical and field evaluation of interaction between ultra-thin whitetopping and existing asphalt pavement. International Journal of Pavement Engineering 7 (4) (2006) 251–60.

[31] Li Z, Vandenbossche JM. Redefining the Failure Mode for Thin and Ultra-thin Whitetopping with a 1.8- x 1.8-m (6- x 6-ft) Joint Spacing. Washington, D.C; 2012.

[32] Z. Li, J. M. Vandenbossche. Redefining the Failure Mode for Thin and Ultra-thin Whitetopping with a 1.8- x 1.8-m (6- x 6-ft) Joint Spacing (2013).

[33] J.A Eid. Theoretische und experimentelle Untersuchungen dünner Betondecken auf Asphalt (2012).

[34] G. Fischer, V.C. Li. Deformation Behavior of Fiber-Reinforced Polymer Reinforced Engineered Cementitious Composite (ECC) Flexural Members under Reversed Cyclic Loading Conditions. ACI Structural Journal 100 (1) (2003) 25–35.

[35] S. Qian, V. Li. Durable pavement with ECC (2008).

[36] V.C Li, T. Kanda. Engineered Cementitious Composites for Structural Applications. ASCE Journal of Materials in Civil Engineering 10 (2) (1998) 66–9.

[37] M.D Lepech, V.C Li. Water permeability of engineered cementitious composites. Cement and Concrete Composites 31 (10) (2009) 744–53.

[38] K. Rokugo. Applications of SHCC in Japan - tools and tips for promoting its use (2017).

[39] K. Rokugo, M. Kunieda, S. C. Lim. Patching repair with ECC on cracked concrete surface (2005).

[40] M. Kunieda, K. Rokugo. Recent Progress on HPFRCC in Japan Required Performance and Applications. Journal of Advanced Concrete Technology 4 (1) (2006) 19–33.

[41] J. Zhang, V.C Li. Monotonic and fatigue performance in bending of fiber-reinforced engineered cementitious composite in overlay system. Cement and Concrete Research 32 (3) (2002) 415–23.

[42] H. Zhang, G. Keoleian, M. Lepech. An integrated life cycle assessment and life cycle analysis model for pavement overlay systems (2008).

[43] Y.M. Lim, V.C Li. Durable repair of aged infrastructures using trapping mechanism of engineered cementitious composites. Cement and Concrete Composites. Cement and Concrete Composites 19 (4) (1997) 373–85.

[44] S. Mueller, V. Mechtcherine. Use of Strain-Hardening Cement-Based Composites in Real Scale Applications (2017).

[45] V.C Li, S. Wang, C. Wu. Tensile Strain-Hardening Behavior of Polyvinyl Alcohol Engineered Cementitious Composite (PVA-ECC). ACI Materials Journal(98-M52) (2001).

[46] Li VC. Concrete Construction Engineering Handbook: Engineered Cementitious Composites (ECC) - Material, Structural, and Durability Performance. Michigan: CRC Press; 2007.

[47] E.-H. Yang, E. Garcez, V.C Li. Development of pigmentable engineered cementitious composites for architectural elements through integrated structures and materials design. Mater Struct 45 (3) (2012) 425–32.

[48] M. Li, V.C Li. Rheology, fiber dispersion, and robust properties of Engineered Cementitious Composites. Mater Struct 46 (3) (2013) 405–20.

[49] E.-H. Yang, V.C Li. Tailoring engineered cementitious composites for impact resistance. Cement and Concrete Research 42 (8) (2012) 1066–71.

[50] S. Wang, V. C. Li. Polyvinyl Alcohol fiber reinforced ECC: Material design and perfomances (2006).

[51] V.C Li. On engineered cementitious composites (ECC) a review of the material and its applications. Advanced Concrete Technology. Japan Concrete Institute 1 (3) (2003).

[52] P. Sathishkumar, P. Sampathkumar, M. Karthik, C. Vignesh. Significance of Various Fibres on Engineered Cementitious Concrete. International Journal of Science, Engineering and Technology 4 (1) (2016).

[53] C. Redon, V.C Li, C. Wu, H. Hoshiro, T. Saito, A. Ogawa. Measuring and modifying interface properties of PVA fibers in ECC matrix. Journal of Materials in Civil Engineering (2001).

[54] S.H Said, H.A Razak. The effect of synthetic polyethylene fiber on the strain hardening behavior of engineered cementitious composite (ECC). Materials & Design 86 (2015) 447–57.

[55] S.FU Ahmed, Z. Ronnie, M. Abdullah, S.Z Abd Rahim, M.E Muhammad Suandi, M.N Mat Saad et al. Ductile behavior of polyethylene fibre reinforced geopolymer composite. MATEC Web Conf. 97 (1) (2017) 1047.

[56] V.C Li, C. Wu, S. Wang, A. Ogawa, T. Saito. Interface Tailoring for Strain-Hardening Polyvinyl Alcohol Engineered Cementitious Composite (PVA-ECC). 99 5 (2002) 463–72.

[57] A.M Grabiec. Influence of viscosity modifying agent on some rheological properties, segregation resistance and compressive strength of self-compacting concrete. Journal of Civil Engineering and Management 19 (1) (2013) 1–8.

[58] A. M. Neville. Properties of Concrete. Prentice Hall; 2012.

[59] E.-H. Yang, Y. Yang, V.C Li. Use of high volumes of fly ash to improve ECC mechanical properties and material greenness. ACI Materials Journal. 104-M68 (2007).

[60] E.-H. Yang, V.C Li, J. Qiu. Early Age Cracking in a SHCC Bridge Deck Link Slab. Seventh Congress on Forensic Engineering (2015).

[61] Tubey L, Hosking J. Synthetic aggregates of high resistance to polishing - Corundum Rich Aggregates. Crowthorne, Berkshire; 1972.

[62] Werner R, Peck M. Kreisverkehrsflächen in Beton: Erfahrungen in der Schweiz, Deutschland und Österreich. Swiss; 2010.

[63] Anderson KW, Russel M, Sheets J, Burkey D, Uhlmeyer JS, Weston J. Evaluation of Tyregrip® High-Friction Surfacing. Washington; 2012.

[64] Huhta R, Meyer D, Zelnak P. The aggregate handbook; 2001.

[65] J. Roa. Evaluation of IFI and high-friction surfaces [Master Thesis]. Blacksburg, Virgnia: Virginia Polytechnic Institute; 2008.

[66] Kuemmel DA, Jaeckel JR, Satanovsky A. Investigative Study of the Italgrip System – Noise Analysis. Milwaukee, Wisconsin; 2000.

[67] Mohamad M. The use of limestone aggregate in concrete. Malaysia; 2005.

[68] E.-H. Yang. Precast Bendable Concrete Paving Slab for Speedy Road Construction (2017).

[69] LTA Singapore. Code of Practice Traffic Control at Work Zone. Singapore: LTA Singapore; 2018.

[70] FHWA. Evaluation of Pavement Safety Performance. Washington, D.C; 2015.

[71] Data Government of Singapore. Causes of Road Accidents: Causes of Accidents by Severity of Injury Sustained; Available from: https://data.gov.sg/dataset/.

[72] Henry J. Evaluation of Pavement Friction Characteristics: A synthesis of highway practice. Washington, D.C; 2000.

[73] Corsello P. Evaluation of surface friction guidelines for Washington State Highways. Olympia, Washington; 1993.

[74] ASTM E274/E274M-11. Standard Test Method for Skid Resistance of Paved Surfaces Using a Full-Scale Tire. West Conshohocken, PA: ASTM International; 2011.

[75] Sandburg U, Ejsmont J. Tyre/Road Noise Reference Book. Kisa, Sweden: Informex; 2002.

[76] Permanent International Association of Road Congresses. Report of the Committee on Surface Characteristics (1987).

[77] Wallman C, Astrom H. Friction measurement methods and the correlation between road friction and traffic safety: A literature review. Sweden; 2001.

[78] Hall JW, Smith KL, Littleton PC. Texturing of Concrete Pavements (Appendixes). Washington, D.C; 2009.

[79] R. Davies, P. D. Cenek, R. J. Henderson. The effect of skid resistance and texture on crash risk (2005).

[80] Hall J, Smith K, Littleton P. Texturing of Concrete Pavements: NCHRP Report 634. Washington, D.C; 2009.

[81] Karim M, Chyc-Cies J, Schick D, Dechkoff C. Evaluation of a Skid Resistant Material at High Incident Intersection Locations. New Brunswick; 2012.

[82] Land Transport Authority. Materials and workmanship specification for civil and structural works(Land Transport Authority). Singapore: Land Transport Authority; 2010.

[83] ASTM E501. Standard Specification for Standard Rib Tire for Pavement Skid-Resistance Tests. West Conshohocken, PA: ASTM International; 2015.

[84] ASTM E524. Specification for Smooth Tire for Pavement Skid-Resistance Tests. West Conshohocken, PA: ASTM International.

[85] ASTM E670. Standard Test Method for Testing Side Force Friction on Paved Surfaces Using the Mu-Meter. West Conshohocken, PA: ASTM International; 2015.

[86] ASTM E1859-E1859M. Test Method for Friction Coefficient Measurements Between Tire and Pavement Using a Variable Slip Technique. West Conshohocken, PA: ASTM International.

[87] ASTM E445. Test Method for Stopping Distance on Paved Surfaces Using a Passenger Vehicle Equipped With Full-Scale Tires. West Conshohocken, PA: ASTM International.

[88] ASTM E2101. Standard Test Method for Measuring the Frictional Properties of Winter Contaminated Pavement Surfaces Using an Averaging-Type Spot Measuring Deceloremeter. West Conshohocken, PA: ASTM International; 2015.

[89] ASTM E1911. Standard Test Method for Measuring paved surface frictional properties using the Dynamic Friction Tester. West Conshohocken, PA; 2009.

[90] ASTM E303-93. ASTM Standard Test Method for Measuring Surface Frictional Properties Using the British Pendulum Tester. West Conshohocken, PA: ASTM International; 1993.

[91] ASTM E965 - 96. Standards test method for Measuring Pavement Macrotexture Depth Using a volumetric technique (reapproved 2006). West Conshohocken, PA: ASTM International; 2006.

[92] Guada I, Spinner D, Rezaei A, Harvey J. Evaluation of Grind and Groove (Next Generation Concrete Surface) Pilot Projects in California. California; 2012.

[93] G. Flintsch, I. Al-Qadi, R. Davis, K. McGhee. Effect of HMA Properties on Pavement Surface Characteristics (2002).

[94] T.F Fwa, Y.S Choo, Y. Liu. Effect of aggregate spacing on skid resistance of asphalt pavement. J. Transp. Eng. 129 (4) (2003) 420–6.

[95] Y.P.K. Lee, T.F. Fwa, Y.S. Choo. Skid Resistance Evaluation of Concrete Pavement Surfaces. Journal of the Eastern Asia Society for Transportation Studies 5 (2003).

[96] Land Transport Authority. Kranji Expressway (KJE) Projects. [August 2016]; Available from: http://www.lta.gov.sg/content/ltaweb/en/roads-and-motoring/projects/kranji-expressway-kje.html.

[97] Land Transport Authority. Using steel slag aggregate in construction. [August 2016]; Available from: https://www.lta.gov.sg/content/ltaweb/en/about-lta/lta-and-the-community/lta-and-the-environment/using-steel-slag-aggregate-in-construction.html.

[98] K. Lee. Analyzing laboratory skid resistance test using Finite Element Modeling [Doctoral Dissertation]. Singapore: National University of Singapore; 2004.

[99] I. Moore, N. Purushothaman, B. Heaton. Three-dimensional elastic finite element study of the skid resistance of grooved pavement. International Journal for numerical methods in engineering 26 (1988) 437–52.

[100] Y. Liu, T.F Fwa, Y.S Choo. Finite-Element Modeling of Skid Resistance Test. J. Transp. Eng. 129 (3) (2003) 316–21.

[101] Y.P.K. Lee, T.F. Fwa, Y.S. Choo. Effect of pavement surface texture on British Pendulum Test. Journal of the Eastern Asia Society for Transportation Studies 6 (2005) 1247–57.

[102] Nicklow, Boulous, Muleta. Comprehensive Urban Hydrologic Modeling Handbook for Engineers and Planners. United States: MWH Soft, Incorporated; 2006.

[103] AASHTO. Highway Drainage Guidelines: Chapter 9: Storm Drain Systems. Washington, D.C.: AASHTO; 2007.

[104] Gallaway BM, Ivey DL, Hayes G, Ledbetter WB, Olson RM, Woods DL et al. Pavement and Geometric Design Criteria for Minimizing Hydroplaning; 1979.

[105] Guven O, Melville JG. Pavement Cross Slope Design - a technical review. Auburn, Alabama; 1999.

[106] M. Gallaway B, E. Schiller R, G. Rose J. Effects of Rainfall Intensity, Pavement Cross Slope, Surface Texture, and Drainage Length on Pavement Water Depths. Texas; 1971.

[107] Mahboub KC, Liu Y, Allen DL. Evaluation and Analysis of Highway Pavement Drainage. Lexington, Kentucky; 2003.

[108] PUB Singapore. Managing Urban Runoff (Drainage Handbook). Singapore: PUB and IES; 2013.

[109] D. Hua, L. Y. Wen. Managing Stormwater in Urbanised Singapore for Flood Control (2011).

[110] Singapore Business Review. Singapore needs 5,600ha more land supply by 2030; Available from: https://sbr.com.sg/economy/news/singapore-needs-5600ha-more-land-supply-support-69m-population-2030.

[111] the Public Utilities Board of Singapore. Managing Urban Runoff. Singapore: PUB and IES; 2013.

[112] Texas DOT. Pavement Texturing Special Specification 7331. 6165th ed. Texas: Texas DOT; 2004.

[113] State of North Carolina DOT. Contract Proposal Division 03; 2012.

[114] Louisiana Department of Transportation. Special Provision State Project no 737-99-1102. Louisiana: Lousiana DOT; 2010.

[115] ASTM. Frictional Interaction of Tire and Pavement: ASTM Special Technical Publication 793. Ohio, USA; 1981.

[116] ASTM Standard E2380M-15 Test Method for Measuring Pavement Texture Drainage Using an Outflow Meter. West Conshohocken, PA: ASTM International; 2015.

[117] Gallaway B, Ivey D, Hayes G, Ledbetter W, Olson R, Woods D et al. Pavement and Geometric Design Criteria for Minimizing Hydroplaning; 1979.

[118] Caltrans. Rigid Pavement Preservation: Chapter 5: Diamond Grinding and Grooving. 2nd ed. California: Caltrans; 2007.

[119] T.N Mansour, B.J Putman. Influence of Aggregate Gradation on the Performance Properties of Porous Asphalt Mixtures. J. Mater. Civ. Eng. 25 (2) (2013) 281–8.

[120] A. Wolff. Simulation of pavement surface runoff using the depth-averaged shallow water equations [Doctoral Dissertation]. Stuttgart: University of Stuttgart; 2012.

[121] Y. Liu. Three dimensional finite element modeling of pavement subsurface drainage systems [Doctoral Dissertations]. Kentucky: University of Kentucky; 2005.

[122] M. Illgen, K. Harting, T.G. Schmitt, A. Welker. Runoff and Infiltration characteristics of permeable pavements – Review of an intensive monitoring program (2007).

[123] A. Alam, L. Haselbach, W.F. Cofer. Three-Dimensional Finite Element Modeling of pervious concrete pavement: vertical porosity distribution approach. International Journal of Research in Engineering and Technology 2 (12) (2013).

[124] D.F. Moore. A theory of Viscous Hydroplaning. International J. Mechanical Science. Volume 9 (1967) 797–810.

[125] A. Browne. Dynamic hydroplaning of pneumatic tires. Illinois, USA: North Western University; 1971.

[126] M. Zmindak, I. Grajciar. Simulation of the aquaplane problem. Computers and Structures 64 (1997) 1155–64.

[127] T. Okano, M. Koishi. A New Computational Procedure to Predict Transient Hydroplaning on a Tire. Tire Science and Technology 29 (1) (2001) 2–22.

[128] Andrén P, Jolkin A. Elastohydrodynamic aspects on the tyre-pavement contact at aquaplaning. Linkoping; 2003.

[129] Ong Ghim Ping Raymond. Hydroplaning and skid resistance analysis using numerical modeling [Ph.D Thesis]. Singapore: National University of Singapore; 2006.

[130] S.S Kumar, K. Anupam, T. Scarpas, C. Kasbergen. Study of Hydroplaning Risk on Rolling and Sliding Passenger Car. Procedia - Social and Behavioral Sciences 53 (2012) 1019–27.

[131] Goh Chin Lian. Noise pollution in Singapore: When buzz becomes noise; Available from: http://wildsingaporenews.blogspot.sg/2010/11/noise-pollution-in-singaporewhen-buzz.html#.WBMRYC196Uk.

[132] Gibbs D, Iwasaki R, Bernhard R, Bledsoe J, Carlson D, Corbisier C et al. Quiet Pavement Systems in Europe. Virginia; 2005.

[133] Rasmussen RO, Bernhard R, Sandberg U, Mun EP. The Little Book of Quieter Pavements. Austin, Texas: FHWA; 2007.

[134] Müller G, Moser M (eds.). Handbook of Engineering Acoustics. Berlin: Springer-Verlag; 2012.

[135] Donavan PR. Comparative measurements on tire pavemet noise in Europe and the USA. California; 2006.

[136] Van Keulen W, Li M, Ceylan H, Molenaar A, Van de Ven M. SIROTOL: Statistical model of tyre-road noise for thin layer surfacing.

[137] Indraneel Bhanap. An analysis of roadway noise at residential estates in close proximity to expressways in Singapore. Noise Health 2013 15 (64) (2013) 183–9.

[138] G. Jurrians, W. v. Keulen, W. Kramer. New guidelines for exposed aggregate surfaces in the Netherlands (2012).

[139] Jens Skarabis, Christoph Gehlen, Ulrike Stöckert, Tim Alte-Teigeler. Noise emission of concrete pavement surfaces produced by diamond grinding. Innovative Solutions – Benefiting Society (2014).

[140] Birnbaum R, Price D, Batiuk R, McCullough M, Smith R. Nitrogen Oxides: Impacts on Public Health and the Environment. Washington, D.C; 1997.

[141] A. Fujishima, X. Zhang. Titanium dioxide photocatalysis: Present situation and future approaches. Comptes Rendus Chimie 9 (5-6) (2006) 750–60.

[142] L. Cassar, C. Pepe, N. Pimpinelli, G. Tognon, G. Guerrini, R. Amadelli. White cement for architecture concrete, possessing the photocatalytic properties (2003).

[143] F. Vallee, L. Bonafous, L. Guillot, N. Pimpinelli. Innovative self-cleaning and de-polluting facade surfaces (2004).

[144] G. Bolte. Photocatalysis in cement-bonded materials. Cement International 3 (92) (2005).

[145] T. Yuranova, V. Sarria, W. Jardim, J. Rengifo, C. Pulgarin, G. Trabesinger et al. Photocatalytic discoloration of organic compounds on outdoor building cement panels modified by photoactive coatings. Journal of Photochemistry & Photobiology 188 (2) (2007) 334–41.

[146] Bonafous L, Cassar L, Cassat P, Colombet P, Guillot L. Photocatalytic granular mixture for mortar and concrete and its use(US 7,556,683 B2); 2009.

[147] A. Zhao, J. Yang, E.-H. Yang. Self-cleaning engineered cementitious composites. Cement and Concrete Composites 64 (2015) 74–83.

[148] E. Boonen, A. Beeldens. Recent Photocatalytic Applications for Air Purification in Belgium. Coatings 4 (3) (2014) 553–73.

[149] C.S Poon, E. Cheung. NO removal efficiency of photocatalytic paving blocks prepared with recycled materials. Construction and Building Materials 21 (8) (2007) 1746–53.

[150] M. Gallus, V. Akylas, F. Barmpas, A. Beeldens, E. Boonen, A. Boréave et al. Photocatalytic de-pollution in the Leopold II tunnel in Brussels: NOx abatement results. Building and Environment 84 (2015) 125–33.

[151] E. Boonen, A. Beeldens. Photocatalytic applications in Belgium, purifying the air through a double layered concrete pavement (2011).

[152] M.M. Hassan, H. Dylla, L.N. Mohammad, T. Rupnow. Methods for the Application of Titanium Dioxide Coatings to Concrete Pavement. International Journal of Pavement Research and Technology 5 (1) (2012) 12–20.

[153] Ashby MF. Materials Selection in Mechanical Design. Oxford: Butterworth-Heinemann; 1999.

[154] A. A. Bawono, E. Caliskan, B. Lechner, E.-H. Yang. Multi criteria analysis for the functional performance of surface pavement (2019).

[155] Hall J, Smith K, Titus-Glover L, Wambold J, Yager T, Rado Z. Guide for Pavement Friction. Washington, D.C; 2009.

[156] S.J Hong, S.-W. Park, S.W Lee. Tire-Pavement Noise Prediction using Asphalt Pavement Texture. KSCE J Civ Eng 22 (9) (2018) 3358–62.

[157] V.V. Saykin. Pavement macrotexture monitoring through sound generated by the tire-pavement interaction [Master of Science in Civil Engineering]. Boston Massachussets: Northeastern University; 2011.

[158] W. Paterson. International Rougness Index Relationship to other measures of roughness and riding quality. Transportation Research Record 1084 (1986).

[159] A. A. Bawono, B. Lechner, F. I. Alhaz. Asphalt Pavement Analysis with 3D FEM Model using Actual Tire Pavement Contact Stresses Measure with Pressure Mapping System Device (2018).

[160] M. Sahmaran, M. Lachemi, K.M. Hossain, R. Ranade, V. Li. Influence of Aggregate Type and Size on Ductility and Influence of aggregate type and size on ductility and mechanical properties of Engineered Cementitious Composites. ACI Materials Journal(106) (2009).

[161] N. Ueda, A. Kawamoto. Influence of Coarse Aggregate on the Mechanical Properties. Strain-Hardening Cement-Based Composites (2017).

[162] C09 Committee. Test Method for Flexural Strength of Concrete (Using Simple Beam with Third-Point Loading). West Conshohocken, PA: ASTM International; 2018. doi:10.1520/C0078_C0078M-18.

[163] J. Li, E.-H. Yang. Macroscopic and microstructural properties of engineered cementitious composites incorporating recycled concrete fines. Cement and Concrete Composites 78 (2017) 33–42.

[164] Z. Karaca. Reliability of BPT on macrotextured surfaces. International Journal of Innovation Sciences and Research 5 (1) (2016) 611–6.

[165] Z. Karaca. Reliability of BPT on macrotextured surfaces. International Journal of Innovation Sciences and Research 5 (1) (2016) 611–6.

[166] Hills DA, Nowell D. Mechanics of Elastic Contacts. Oxford: Butterworth-Heinemann; 1993.

[167] R. Seracino. FRP composites in civil engineering (2004).

[168] A. A. Bawono, N. NguyenDinh, B. Lechner, E.-H. Yang. Study of Finite Element Model on Skid Resistance for Pavement made of Engineered Cementitious Composite (2019).

[169] PUB Singapore. Managing Urban Runoff: Drainage Handbook. Singapore: PUB and IES; 2013.

[170] Current Results Publishing Ltd. Average Annual Precipitation by State. [October 2016]; Available from: https://www.currentresults.com/Weather/US/average-annual-state-precipitation.php.

[171] Road Design Drainage Technical Sub-committee. Guide to road design part 5a: Drainage - road surface, netoworks, basins, and subsurfaces. Sydney: Austroads; 2013.

[172] M.V Villar, P.L Martin, F.J Romero, V. Gutierrez-Rodrigo, J.M Barcala. Gas and water permeability of concrete. Geological Society, London, Special Publications 415 (1) (2015) 59–73.

[173] ANSYS. ANSYS CFX. ANSYS Workbench.

[174] Kays W, Crawford M (eds.). Convective heat and mass transfer. Singapore: McGraw-Hill; 1993.

[175] Schlichting H (ed.). Boundary-layer theory. New York: McGraw-Hill; 1955.

[176] S. Ge, M. Celikin, M. Isac, R.IL Guthrie. Mathematical Modeling and Microstructure Analysis of Al–Mg–Sc–Zr Alloy Strips Produced by Horizontal Single Belt Casting (HSBC). ISIJ Int. 54 (2) (2014) 294–303.

[177] A. A. Bawono, N. NguyenDinh, E.-H. Yang, B. Lechner. Evaluation of highway pavement skid resistance performance made of Engineered Cementitious Composite (ECC) (2017).

[178] M.E. Broz, R.F. Cook, D.L. Whitney. Microhardness, toughness, and modulus of Mohs scale minerals. American Mineralogist 91 (2006) 135–42.

[179] C09 Committee. Test Method for Flexural Strength of Concrete (Using Simple Beam with Third-Point Loading)(C78/78M). West Conshohocken, PA: ASTM International; 2018. doi:10.1520/C0078_C0078M-18.

[180] S. Qian, V.C Li. Simplified Inverse Method for Determining the Tensile Strain Capacity of Strain Hardening Cementitious Composites. Journal of Advanced Concrete Technology 5 (2) (2007) 235–46.

[181] N. NguyenDinh, E.-H. Yang, B. Lechner. Precast electrified roadway pavement systems using ECC (2014).

[182] S. Sarsam. Field evaluation of Asphalt Concrete Pavement surface texture and skid characteristics. 5th Eurasphalt & Eurobitume Congress (2012).

[183] ASTM. Standard test method for measuring pavement texture drainage using an Outflow Meter(E2380M-15). West Conshohocken, PA: ASTM International; 2015. doi:10.1520/E2380_E2380M-15.

[184] Müller-BBM. SPERoN - Rolling noise prediction model; Available from: https://www.muellerbbm.com/environment/traffic-environment/speron/.

[185] T. Beckenbauer, A. Kuijpers. Prediction of pass-by levels depending on road surface parameters by means of a hybrid model (2001).

[186] Ertsey-Bayer M, Bawono AA, Janaki T, Lechner B. Prediction sound level for pavement made of ECC. Munich; 2020.

[187] T. Beckenbauer, P. Klein, J. Hamet, W. Kropp. Tyre/road noise prediction: A comparison between the SPERoN and HyRoNE models - Part 1. The Journal of the Acoustical Society of America 123 (5) (2008) 3388.

[188] S. Alves, M. Maennel. Application of Speron to the development of low noise road surfaces (2016).

[189] J.-F. Hamet, P. Klein. Road texture and tire noise (2000).

[190] M. Haider, R. Wehr, M. Conter, M. Kriegisch, S. Gasparoni. Texture and noise characteristics of exposed aggregate concrete road surfaces. Innovative Solutions – Benefiting Society (2014).

[191] European Asphalt Pavement Association. Asphalt pavement in tunnels. Belgium; 2008.

[192] Jofré C, Romero J, Rueda R. Contribution of Concrete Pavements to the Safety of Tunnels in Case of Fire. Brussels; December 209.

[193] Knaze P. Concrete pavements in tunnels. Bratislava; 2005.

[194] Longley I. Criteria for In-Tunnel and Ambient Air Quality. New South Wales; 2014.

[195] The World Health Organization. Guidelines for Air Quality. Geneva: The WHO; 2000.

[196] Fotios S, Boyce P, Ellis C. The Effect of Pavement Material on Road Lighting Performance. Sheffield; 2005.

[197] Jackett MJ, Frith WJ. Measurement of the reflection properties of road surfaces to improve the safety and sustainability of road lighting. Wellington, N.Z.: NZ Transport Agency; 2009.

[198] F. Salata, I. Golasi, S. Bovenzi, E. Vollaro, F. Pagliaro, L. Cellucci et al. Energy Optimization of Road Tunnel Lighting Systems. Sustainability 7 (7) (2015) 9664–80.

[199] J. Vercammen, A. Audenaert. High performance lighting - On the road for energy efficiency in tunnels (2016).

[200] A.A. Bawono, B. Lechner, E.-H. Yang. Skid resistance and surface water drainage performance of engineered cementitious composites for pavement applications. Cement and Concrete Composites 104 (2019) 103387.

[201] A. Andaloro, E.S Mazzucchelli, A. Lucchini, M.P Pedeferri. Photocatalytic self-cleaning coatings for building facade maintenance. Performance analysis through a case-study application. FDE 4 (3-4) (2017) 115–29.

[202] I. Ahmad, C.-w. Kan. Visible-Light-Driven, Dye-Sensitized TiO2 Photo-Catalyst for Self-Cleaning Cotton Fabrics. Coatings 7 (11) (2017) 192.

[203] H. Witkowski, W. Jackiewicz-Rek, K. Chilmon, J. Jarosławski, A. Tryfon-Bojarska, A. Gąsiński. Air Purification Performance of Photocatalytic Concrete Paving Blocks after Seven Years of Service. Applied Sciences 9 (9) (2019) 1735.

[204] A. Fujishima, K. Honda. Electrochemical photolysis of water at a semiconductor electrode. Nature 238 (1972) 37–8.

[205] A. Awadalla, M.FM Zain, A.A Kadhum, Z. Abdalla. Improve Indoor Air Quality by Using Titanium Dioxide as Coating Photocatalyses under UV Irradiation. Research J. of Applied Sciences 6 (2) (2011) 99–103.

[206] E. Boonen, V. Akylas, F. Barmpas, A. Boréave, L. Bottalico, M. Cazaunau et al. Construction of a photocatalytic de-polluting field site in the Leopold II tunnel in Brussels. J Environ Manage 155 (2015) 136–44.

[207] A.L. Linsebigler, G. Lu, J.T. Yates. Photocatalysis on TiO2 Surfaces: Principles, Mechanisms, and Selected Results. Chem. Rev. 3 (3) (1995) 735–58.

[208] A. Fujishima, X. Zhang, D. Tryk, (None). TiO2 photocatalysis and related surface phenomena. Surface Science Reports 63 (12) (2008) 515–82.

[209] KRONOS. KRONOClean7000 degrades pollutants with visible light and with UV radiation; Available from: https://kronostio2.com/en/.

[210] A. Synnefa, T. Karlessi, N. Gaitani, M. Santamouris, D.N Assimakopoulos, C. Papakatsikas. Experimental testing of cool colored thin layer asphalt and estimation of

its potential to improve the urban microclimate. Building and Environment 46 (1) (2011) 38–44.

[211] Kurt E. Gustafson* and and Rebecca M. Dickhut. Particle/Gas Concentrations and Distributions of PAHs in the Atmosphere of Southern Chesapeake Bay. Environ. Sci. Technol. 31 (1) (1996) 140–7.

[212] B. Ruot, A. Plassais, F. Olive, L. Guillot, L. Bonafous. TiO2-containing cement pastes and mortars: Measurements of the photocatalytic efficiency using a rhodamine B-based colourimetric test. Solar Energy 83 (10) (2009) 1794–801.

[213] S.-S. Chang, B. Clair, J. Ruelle, J. Beauchêne, F. Di Renzo, F. Quignard et al. Mesoporosity as a new parameter for understanding tension stress generation in trees. J Exp Bot 60 (11) (2009) 3023–30.

[214] E. Jimenez-Relinque, I. Llorente, M. Castellote. TiO2 cement-based materials: Understanding optical properties and electronic band structure of complex matrices. Catalysis Today 287 (2017) 203–9.

[215] Y. Zhang, C. Pan. TiO2 graphene composite from thermal reaction of graphene oxide and its photocatalytic activity in visible light. Journal of Material Science 46 (8) (2011).

[216] O. Carp, C. Huisman, A. Reller. Photoinduced reactivity of titanium dioxide. Progress in Solid State Chemistry 32 (1-2) (2004) 33–177.

[217] M. Dai. The effect of zeta potential of activated cabon on the adsorption of dyes from aquesous solutin. Journal of colloid and interface science 164 (1994) 223–8.

[218] S. Karaca, A. Gurses, M. Açıkyıldız. Adsorption of Cationic Dye from Aqueous Solutions by Activated Carbon. Microporous and Mesoporous Materials 115 (3) (2008) 376–82.

[219] M.F Butman, N.L Ovchinnikov, N.S Karasev, N.E Kochkina, A.V Agafonov, A.V Vinogradov. Photocatalytic and adsorption properties of TiO2-pillared montmorillonite obtained by hydrothermally activated intercalation of titanium polyhydroxo complexes. Beilstein J Nanotechnol 9 (2018) 364–78.

[220] J. Liu, W. Zhu, S. Yu, X. Yan. Three dimensional carbogenic dots/TiO 2 nanoheterojunctions with enhanced visible light-driven photocatalytic activity. Carbon 79 (2014) 369–79.

[221] B. Cabir, M. Yurderi, N. Caner, M.S Agirtas, M. Zahmakiran, M. Kaya. Methylene blue photocatalytic degradation under visible light irradiation on copper phthalocyanine-sensitized TiO2 nanopowders. Materials Science and Engineering: B 224 (2017) 9–17.

[222] G. Mamba, X.Y Mbianda, A.K Mishra. Gadolinium nanoparticle-decorated multiwalled carbon nanotube/titania nanocomposites for degradation of methylene blue in water under simulated solar light. Environ Sci Pollut Res Int 21 (8) (2014) 5597–609.

[223] B. Bharti. Formation of oxygen vacancies and Ti3+ state in TiO2 thin film and enhanced optical properties by air plasma treatment. Scientific Reports 6 (2016).

[224] D.M Tobaldi, M.P Seabra, G. Otero-Irurueta, Y.R de Miguel, R.J Ball, M.K Singh et al. Quantitative XRD characterisation and gas-phase photocatalytic activity testing for visible-light (indoor applications) of KRONOClean 7000®. RSC Adv. 5 (124) (2015) 102911–8.

[225] C. Chen, W. Cai, M. Long, B. Zhou, Y. Wu, D. Wu et al. Synthesis of visible-light responsive graphene oxide/TiO(2) composites with p/n heterojunction. ACS Nano 4 (11) (2010) 6425–32.

[226] H. Zhang, X. Lv, Y. Li, Y. Wang, J. Li. P25-graphene composite as a high performance photocatalyst. ACS Nano 4 (1) (2010) 380–6.

[227] A.S. Kushwaha, R. Saxena, S. Pal. Effect of Titanium Dioxide on the compressive strength. Journal of Civil Engineering and Environmental Technology 2 (2015) 482–6.

[228] J. Sorathiya, S. Shah, S. Kacha. Effect on Addition of Nano Titanium Dioxide TiO2 on Compressive Strength of Cementitious Concrete (2017).

[229] J. Silvestre, N. Silvestre, J. de Brito. Review on concrete nanotechnology. European Journal of Environmental and Civil Engineering 20 (4) (2015) 455–85.

[230] A. Yousefi, A. Allahverdi, P. Hejazi. Effective dispersion of nano-TiO2 powder for enhancement of photocatalytic properties in cement mixes. Construction and Building Materials 41 (2013) 224–30.

[231] F. Pacheco-Torgal, S. Jalali. Nanotechnology: Advantages and drawbacks in the field of construction and building materials. Construction and Building Materials 25 (2) (2011) 582–90.

[232] S. Shladover. PATH at 20 - History and Major Milestones (2006).

[233] Suh NP (ed.). The on-line electric vehicle: Wireless electric ground transportation systems. Cham: Springer; op. 2017.

[234] Lechner B. Braking and Suspension (Road), Lecture Script. Munich; 2013.

[235] Road Research Laboratory Ministry of Transport. Instructions for using the portable skid resistance tester. Crowthorne, Berkshire: Road Research Laboratory; 1969.

[236] Department for Transport, Energy & Infrastructure. Road surface texture measurement recommended investigatory levels. Australia; 2016.

[237] Highways Agency. Surfacing Materials for New and Maintenance Construction: Pavement Design and Maintenance. 7th ed. United Kingdom; 2006.

[238] Highways Agency. Skid Resistance: Pavement design and maintenance. Design Manual Roads and Bridges. United Kingdom; 2004.

[239] Victorian Road Transport Agency. Measurement and Interpretation of Skid Resistance using SCRIM. 110th ed. Australia; 2015.

List of Figures

List of Tables

Appendices

Appendix A: DPT Components

Details of the components for RPEV system:

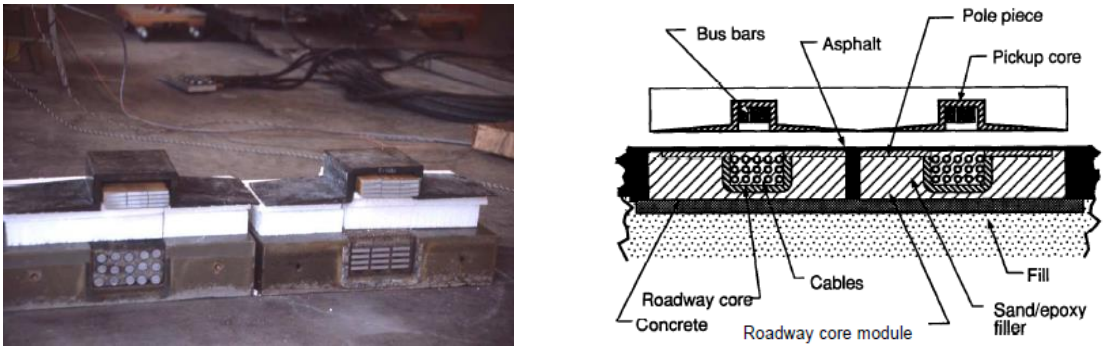

(a) (b)

Figure 0.1 Onboard Power Inductors for RPEV (a) real (b) illustration [232]

Table 0.1 RPEV system dimensions

System	Description	Units
Inductive coupling system	Airgap height	6 cm
	On board controller weight	395 kg
Pickup	Length	436 cm
	Width	100 cm
	Weight	545 kg
	Core length	15 cm
	Core width	50 cm
	Total pickup core weight	354 kg
Roadway inductor core modules	Width	51 cm
	Length	280 cm
	Thickness	11 cm
	Weight	409 kg
Roadway conductors	Aluminium cable	1.8 cm diameter
	Aluminium busbar	0.64 x 3.81 cm

Figure 0.2 Configuration of the proposed ultra slim S-type power supply modules including two magnetic poles. (a) Bird’s eye view for two unfolded modules. (b) Top view of a folded module.

An innovative power supply developed by OLEV:

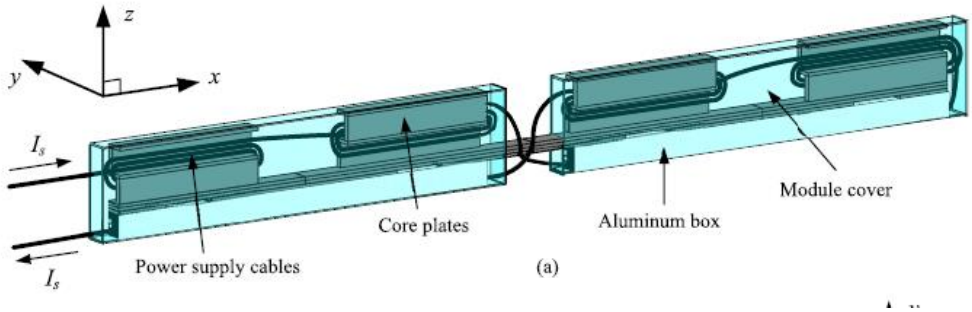

(a)

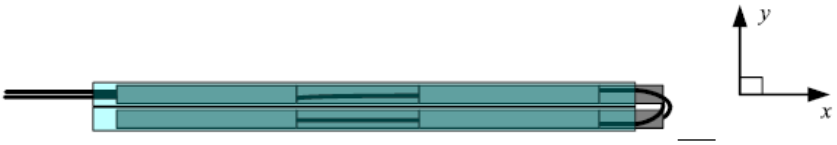

(b)

Table 0.2 OLEV development [26,233]

	1G (Bus)	2G (Bus)	3G (Bus)	4G (Bus)	I-type	S-type
Rail width	140 cm	80 cm	80 cm	80 cm	10 cm	4 cm
Air gap	17 cm	23 cm	23 cm	23 cm	20 cm	20 cm
Output power (pick up unit)	12 kW	15 kW	33.3 kW	20 kW	27 kW	22 kW
EMF	< 51 mG	< 50 mG	< 62.5 mG	< 62.5 mG	< 10 mG	< 10 mG
Efficiency	72%	81%	85%	85%	74%	71%

Appendix B: Design of PUTW

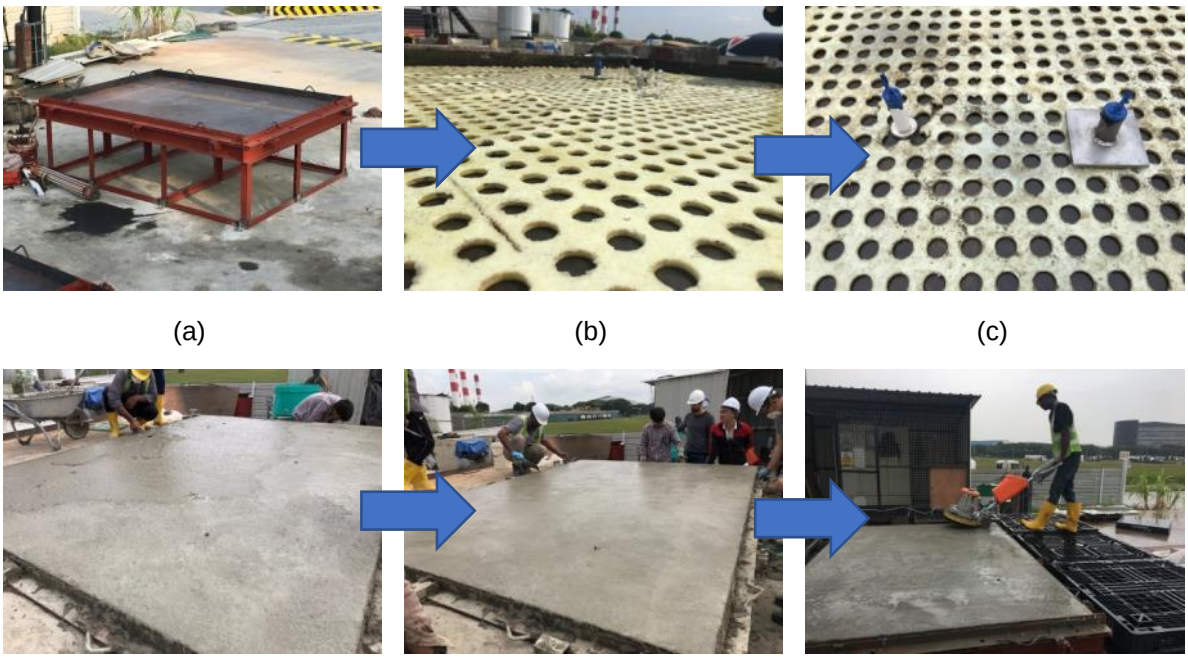

(a) (b) (c)

(d) (e) (f)

Figure 0.3 Steps of manufacture process (a) steel formwork. (b) rubber mat with convex. (c) grouting port and lifting/leveling device (d) casting the first ECC layer (60 mm). (e) casting the second modified ECC layer (10 mm). (f) brushing process of the surface layer

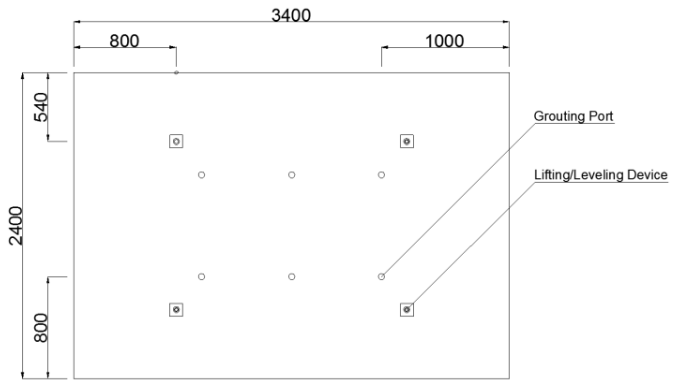

Figure 0.4 Dimension of PUTW slab and location of grouting port and lifting/leveling device

(a)

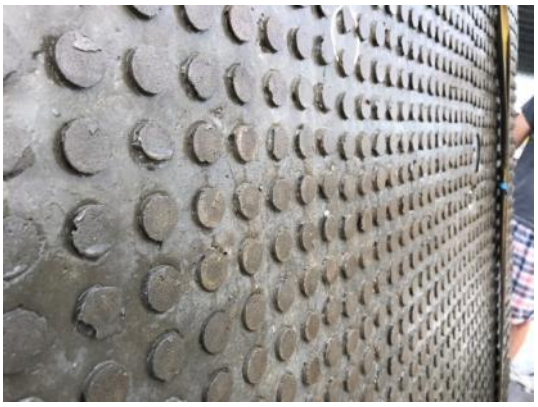

(b)

Figure 0.5 Keys of PUTW design. (a) grouting. (b) convex nodes

(a)

(b)

Figure 0.6 Lifting and leveling device. (a) lifting bolt. (b) levelling bolt.

Appendix C: ECC material

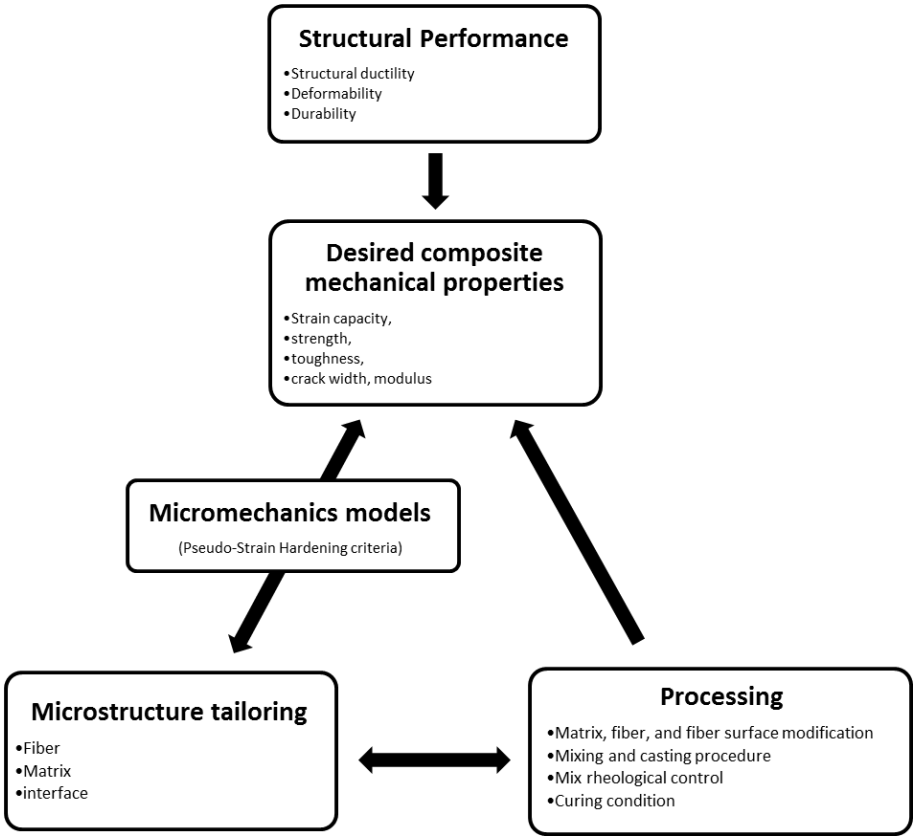

Figure 0.7 PDDA approach on (PVA) ECC design [45]

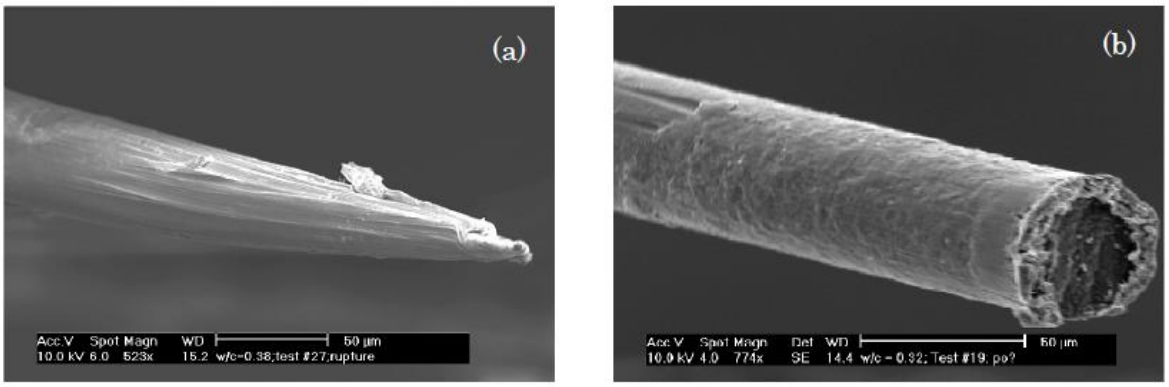

Figure 0.8 Effect of oiling agent on delamination of fiber (a) ruptured. (b) pulled out. [56]

Appendix D: Surface Texture Methods and Tests

Summary of test method for pavement surface texture

Table 0.3 Pavement surface texture test method [80]

Test method/ Associated standard	Description	Applicability
Sand Patch Method (SPM); ASTM E965, ISO 10844	This volumetric-based test method provides the mean depth of road surface macrotexture. The operator spreads a known volume of glass beads (ASTM D 1155) in a circle onto the surface and determines the diameter and subsequently mean texture depth (MTD).	• Simple and inexpensive • Localized method • Accuracy 2%
Outflow (OF) meter; ASTM WK 364	Volumetric test method that provides a measure of the escape time for water beneath a moving tire. The operator measures the rate of gravity-controlled outflow from a cylinder placed on a road surface.	• Simple methods and relatively inexpensive equipment. • Localized measurement. • Accuracy 0.01 sec
Circular Texture (CT) Meter; ASTM E 2157	Provides a mean profile depth of the road surface macrotexture. The equipment measures a 284 mm circular profile of the road surface at intervals of 0.87 mm.	• Measures same diameter as DFT. • Localized measurement • Texture measured in 2 directions. • Accuracy 0.03 mm
Texture Depth Gauge (TDG); ASTM T 261	Provides an average depth of PCC grooves or tines. The gauge is inserted into 10 grooves to measure their depths.	• Simple methods and inexpensive equipment. • Not a measure of defined texture
British Pendulum Tester (BPT); ASTM E303	Provides an indirect measure of relative microtexture. The testing device measures drag on a rubber footed pendulum swung across the road surface.	• Methodology is critical • Can be done in laboratory • Accuracy 1.2 BPN
Electro-optic (laser light sectioning, ultrasonic, stylus) method (EOM); ASTM E 1845 ISO 13473-1 ISO 13473-2 ISO 13473-3	Provides a profile of the road surface macrotexture. This equipment uses an optical distance measuring sensor to collect surface elevation data at intervals of 0.25 mm or less.	• Some equipment collects at high speeds. • Correlates well with MTD. • Continuous measurement possible. • One direction only • Accuracy 0.15 mm

Table 0.4 Summary of texturing methods

Application	Mix/Texture Type	Description
New AC or AC Overlay	Dense Fine-Graded HMA	Dense-graded HMA is a dense, continuously graded mixture of coarse and fine aggregates, mineral filler, and asphalt cement (5 to 6 percent). Dense-graded HMA can be modified with polymers or crumb rubber, and may include recycled materials. Nominal MAS range from 9.5 mm to 19.0 mm.
	Dense Coarse-Graded HMA	Coarse HMA mixes have gradations that pass below the MDL at the No. 8 sieve (2.36-mm) (WSDOT, 2005).
	Gap-Graded HMA or Stone Matrix Asphalt (SMA)	SMA is a gap-graded mixture of course aggregate (typically, 10 to 15 mm), filler, fibers and polymer-modified asphalt. Its primary advantage is resistance to deformation, but its relatively coarse surface yields good frictional characteristics.
	Open-Graded Friction Course (OGFC)	OGFC is an open-graded mixture of mostly coarse aggregate, mineral filler, and asphalt cement (3 to 6 percent). Open-graded HMA can be modified with polymers, fibers, and/or crumb rubber.
Friction Restoration of Existing AC Pavement	Chip Seal	Thin surface treatment containing single-sized, high-quality, angular aggregates (9.5 to 15 mm), spread over and rolled into a liquid asphalt or asphalt emulsion binder. Aggregates are sometimes pre-coated with asphalt emulsion prior to spreading. Completed surface is somewhat coarse, yielding good frictional characteristics.
	Slurry Seal	Slurry mixtures of fine aggregate, mineral filler, and asphalt emulsion. They are similar to micro-surfacing, without interlocking aggregates. Polymers are not always used in the emulsion. Their surface is typically gritty.
	Micro-Surfacing (polymer-modified slurry seal)	A slurry mixture containing high-quality crushed, dense-graded aggregate, mineral filler, and polymer-modified asphalt emulsion. It is placed over a tack coat and is capable of being spread in variable thickness layers for rut-filling, correction courses, and wearing course applications.
	HMA Overlay	See HMA surface mixes above.
	Ultra-Thin Polymer-Modified Asphalt (e.g., NovaChip)	Thin gap-graded asphalt surfaces placed using specialized equipment immediately over a thick polymer-modified asphalt emulsion membrane. Following slight compaction the surface provides a semi-porous texture.
	Epoxied Synthetic treatment (e.g., Italgrip)	A very thin surface treatment consisting of a two-part polymer resin placed on an existing pavement and covered with a man-made aggregate of re-worked steel slag (3 to 4 mm). The surface is designed to substantially improve the frictional characteristics of pavements.
Retexturing of Existing AC Pavement	Micro-Milling	Milling equipment, consisting of a self-propelled machine with carbide teeth mounted on a rotating drum, typically removes 19 to 32 mm from the asphalt surface. The spacing of cuts is approximately 5 mm versus 6 mm cut of conventional cold-milling machines. The resulting surface has a fine, smooth pattern that gives a smoother ride.

Application	Mix/Texture Type	Description
New PCC or PCC Overlay	Broom Drag (longitudinal or transverse)	A long-bristled broom is mechanically or manually dragged over the concrete surface in either the longitudinal or transverse direction. Texture properties are controlled by adjusting the broom angle, bristle properties (length, strength, density), and delay behind the paver. Uniform striations approximately 1.5 to 3.0 mm deep are produced by this method.
	Artificial Turf Drag (longitudinal)	An inverted section of artificial turf is dragged longitudinally over a concrete surface following placement. Texture properties are controlled by raising/lowering the support boom, adding weight to the turf, and delaying application to allow surface hardening. This method produces uniform 1.5 to 3.0 mm deep surface striations.
	Burlap Drag (longitudinal)	One or two layers of moistened coarse burlap sheeting are dragged over the concrete surface following placement. Texture properties are controlled by raising/lowering the support boom and adjusting the delay following concrete placement.
	Longitudinal Tine	A mechanical assembly drags a wire comb of tines (~127 mm long and 3 m wide) behind the paver (and usually following a burlap or turf drag). Texture properties are controlled by the tine angle, tine length, tine spacing, and delay for surface curing. Grooves from 3 to 6 mm deep and 3 mm wide are produced by this method, typically spaced at 19 mm.
	Transverse Tine	Accomplished using methods similar to longitudinal tining, however, the mechanical assembly drags the wire comb perpendicular to the paving direction. Variations include skewing the tines 9 to 14° from perpendicular and using random or uniform tine spacing from 12 to 38 mm. Ranges from 0.4 to 1.0 mm.
	Diamond Grinding (longitudinal)	A self-propelled grinding machine with a grinding head of gang-mounted diamond sawing blades removes 3 to 19 mm of cured concrete surface, leaving a corduroy type surface. Blades are typically 2 to 4 mm wide and spaced 4.5 to 6 mm apart, leaving 2 to 4 mm high ridges. This method is most commonly used to restore surface characteristics of existing pavements.
	Porous PCC	Gap-graded, small-diameter aggregate are combined with cement, polymers, and water to form a drainable surface layer (typically 200 mm thick). That surface layer is bonded to the underlying wet or dry dense concrete layer.
	Exposed Aggregate PCC	A set retarder is applied to the wet concrete surface and the surface is protected for curing. After 12 to 24 hours, the unset mortar is removed to a depth of 1 to 2 mm using a power broom.
Friction Restoration of Existing PCC Pavement	HMA Overlay	See HMA surface mixes above.
	TyreGrip	Tyregrip® is a resurfacing system that consists of a two-part epoxy resin top dressed with calcined bauxite aggregate. The aggregate is fractured 100 percent and is approximately No. 10 (2 mm) size material.

Application	Mix/Texture Type	Description
	Italgrip	
	White topping, Thin White Topping (TWT) and Ultra white topping (UTW)	According to (Rasmussen et al., 2004), white topping is a PCC layer constructed atop an existing HMA pavement structure. Conventional whitetopping—a concrete overlay of 200 mm or more, designed and constructed without consideration of a bond between the concrete and underlying HMA. TWT—an overlay of greater than 100 mm and less than 200 mm in thickness. UTW—with a thickness equal to or less than 100 mm (4 in.), this overlay requires a bond to the underlying HMA to perform well.
Retexturing of Existing PCC Pavement	Diamond Grinding (longitudinal)	See diamond grinding above.
	Longitudinal Diamond Grooving	A self-propelled grooving machine saws longitudinal groove in the road surface about 3 to 6 mm deep and spaced 13 to 38 mm apart. This method adds macrotexture for drainage but relies on the original surface for microtexture.
	Transverse Diamond Grooving	Completed in a manner similar to longitudinal diamond grooving, except the grooves are sawn transverse to the travel direction.
	Shot Abrading	An automated machine hurls recycled round steel abrasive material at the pavement surface, abrading the surface and/or removing the mortar and sand particles surrounding the coarse aggregate to a depth of up to 6 mm. Texture properties are controlled by adjusting the steel abrasive material velocity and approach angle and by modifying the forward equipment speed.

Appendix E: Standards for Skid Resistance on Different Countries

E.1. Requirement for new roads

To guarantee the safety for motorist, highway agencies are implementing standards for their new roads. In Singapore, the skid resistance standard is referring to the Code of Practice (COP) for Works on Public Streets [12] and Materials and Workmanship specification [82]. According to the COP, concrete surface paving on footpath shall be approved sprayed-on acrylic modified UV stable pigmented cementitious topping with minimum thickness of 1 mm, minimum cured compressive strength of 45 N/mm² and skid resistance not less than 50. Concrete Surface paving on carriageway shall be approved spray-on acrylic modified UV stable pigmented cementitious topping with minimum thickness of 1mm, minimum cured compressive strength of 60 N/mm² and skid resistance not less than 65. While according to the specification, the minimum limitation of skid resistance for asphaltic pavement is 55.

Table 0.5 Standard of skid resistance in Singapore

Category	Site definition	Skid resistance (BPN)
Surface Coating	Paving on carriageway	≥ 65
Concrete surface	Paving on footpath	≥ 50
Asphaltic	Open graded asphalt	≥ 55

In Germany, the skid resistance standard follows the German specification of ZTV Asphalt-StB 07 and ZTV Beton-StB 07. It stated that the friction coefficient for road pavements must never fall short the limits by 0.03 with SCRIM measurement [234].

Table 0.6 Standard of skid resistance in Germany

Speed of Measurement (km/h)	Limits μ_{SCRIM}	
	Acceptance value (new road)	Up to termination of guarantee
40	0.56	0.49
60	0.51	0.45
80	0.46	0.40

In Switzerland, the friction level for construction and surface restoration are defined by using Skiddometer BV-8 or the Stuttgarter Reibungsmesser. The friction levels, which are shown in Table 0.7 are defined based on the speed limit.

Table 0.7 Friction levels for construction in Switzerland

Speed limit (km/h)	Using Skiddometer BV-8	
	Speed	μ
≤ 60	40	0.48
> 60 and ≤ 100	60	0.39
> 100	80	0.32

TRRL used British Pendulum Number to determine its skid resistance [235]. They categorized three different categories of skid resistance based on different type of site.

Table 0.8 Standard of skid resistance by TRRL

Category	Type of site	Minimum BPN
A	Difficult sites such as: Roundabouts, Bends with radius less than 150 m on unrestricted roads, Gradients 1 in 20 or steeper of lengths greater than 100 m, Approaches to traffic lights on unrestricted roads	65
B	Motorways, trunk and class 1 roads and heavily trafficked roads in urban areas (carrying more than 2000 veh per day)	55
C	All other sites	45
Note: for Category A and B sites where the speed of traffic is high (in excess of 95 km/h) an additional requirement is a minimum texture depth of 0-65 mm.		

The skid resistance level is different throughout the states in USA. Some of the Departments of Transport (DOT) under its state by using Skid Number (SN) while the other use Friction Number (FN) or even Polished Stoned Value (PSV) to determine Investigatory Level related to Skid Resistance. Referring to the summary of friction guidelines under the Report of Evaluation of Surface Friction Guidelines for Washington State Highways (Corsello, 1993), different values and actions are determined by each DOT.

Table 0.9 Standard of skid resistance in different state in USA

State	Limit	Explanation
California	Office of traffic safety notified when SN40 is below 30	Varies
Idaho	Range in numbers	At 35, section is listed. At 30, section is recommendable
Illinois	Less than FN 40 = 35	FN ≤ 30: contributing to wet-pavement accidents 31 ≤ FN ≤ 35: pavement friction is the primary factor. FN ≥ 36: some condition other than pavement friction
Indiana	Minimum friction number (FN40) is 30	
Louisiana	SN equal to or over 35 for new construction Friction Rating 1 (all mixtures): PSV > 37. Friction Rating 2 (all mixtures): PSV = 35 to 37. Friction Rating 3 (all mixtures, except wearing courses with ADT > 7,000 vehicle/day): PSV = 30 to 34. Friction Rating 4 (all mixtures except wearing courses): PSV = 20 to 29.	
Michigan	ADT < 100 veh/day/lane: no AWI requirement. ADT ≥ 100 and < 500 veh/day/lane: AWI ≥ 220. ADT ≥ 500 veh/day/lane: AWI ≥ 260	Special attention is given to investigate surfaces with SN at 30 or below
Ohio	Below 30 – poor 30 to 40 – adequate, depending on traffic and geometry Over 40 – satisfactory	Some correction likely where SN = 30

State	Limit	Explanation
Tennessee	Above FN 35 : acceptable FN 30 to 35 : questionable FN below 30 : unsatisfactory	
Vermont	Monitor are if SN is 40 or below; inform proper personnel of problem when SN is below 30	
Virginia	Based on bald tire FN40 minimum of approximately 20	

Fewer standards are found for new road which measured the thresholds by the macrotexture of the surface pavement. [155] mentioned MTD should be achieved with-in a range of 0.80 to 1.50 mm for new pavement with longitudinal grooves. However, some agencies are implementing both micro- and macrotextures for their standards. Those are: United Kingdom, Australia, and Austria.

The Britain attempts to provide an MTD of 1.5 mm (0.06 in.) for new pavements [72]. A 16 to 10 mm coarse aggregate with a 1.5 mm texture depth is required to provide adequate skidding resistance. [236] recommends a texture depth of 0.40 mm should be achieved for freeways and other high-class facilities with free-flowing traffic conditions, and a texture depth of 0.60 is the minimum limit for highways and other major main roads. While in Austria, an 8 mm maximum sized aggregate was used to reduce the macrotexture in the texture range >10 mm, and achieve good noise reducing properties. An 8 to 4 mm sized aggregate with a 1.0 mm texture depth is recommended for lower speed roads (90 km/hr) where the risk of aquaplaning is less than for high speed roads [237]. Singapore only specifies a criterion for acceptance of open graded asphalt based on a texture depth of minimum 1.20 mm.

E.2. Requirements for investigatory and intervention levels

In pavement management system, the investigatory levels can be set which represent a limit, above which the skid resistance is considered to be satisfactory but at or below which the road is judged to require an investigation of the skid resistance requirements. Once roads have been identified requiring treatment to improve the skid resistance, signs warning is ideally erected. Then the intervention level is set as a threshold when a surface roadway needs to be improved.

The investigatory level of skid resistance which is set 50 km/h (SCRIM) for pavement is stated in Design Manual for Roads and Bridges for Skid Resistance stated by [238]. The investigatory level values in UK can be seen in Table 0.10.

.

Table 0.10 Standard of skid resistance by UK Highway Agency

Site category and definition		Site Investigatory Level					
		0.3	0.35	0.4	0.45	0.5	0.55
A	Motorway						
B	Dual carriageway non-event						
C	Single carriageway non-event						
Q	Approaches to and across minor and major junctions, approaches to roundabouts						
K	Approaches to pedestrian crossings and other high risk situations						
R	Roundabout						
G1	Gradient 5-10% longer than 50m						
G2	Gradient >10% longer than 50m						
S1	Bend radius <500m – dual carriageway						
S2	Bend radius <500m – single carriageway						

Notes:

Investigatory Levels are for the mean skidding resistance within the appropriate averaging length

Investigatory Levels for site categories A, B, and C are based on 100m averaging lengths (50m lengths for some Overseeing Organizations) or the length of the feature if it is shorter.

Investigatory Levels and averaging lengths for site categories Q, K, G and S are based on the 50m approach to the feature but this shall be extended when justified by local site characteristics.

Investigatory Levels for site category R are based on 10m lengths.

Residual lengths less than 50% of a complete averaging length may be attached to the penultimate full averaging length, providing the site category is the same.

As part of site investigation, individual values within each averaging length should be examined and the significance of any values which are substantially lower than the mean value assessed.

While in Victoria (Australia), the investigatory level for skid resistance is divided into six site category, and it is depends on the traffic [239].

Table 0.11 Standard of skid resistance in Victoria, Australia (VicRoads)

Site Category	Site Description	Investigatory Level (SFC 50)	
		Primary Roads and Secondary Roads >2.500 vehicles per lane per day	Secondary Roads <2.500 vehicles per lane per day
1	Traffic light-controlled intersections Pedestrian/school crossings Railway level crossings Roundabout approaches	0.55	0.50
2	Curves with radius ≤ 250m Gradients ≥5% and ≥50m long Freeway/highway on/off ramps	0.50	0.45
3	Intersections	0.45	0.40
4	Maneuver-free areas of undivided roads	0.40	0.35
5	Maneuver-free areas of divided roads	0.35	0.30
		Investigatory level (SFC20)	
6	Curves with radius ≤100m	0.60	0.55
7	Roundabouts	0.55	0.50

Intervention levels based on friction can be determined with different measurements. The values are different depends on the level of roadways. The minimum friction levels for intervention action are summarized in Table 0.12.

Table 0.12 Intervention levels for friction [72]

Road Category	Motorways	Primary	Secondary
Denmark	Speed < 80 km/h; μ = 0.4; Speed > 80 km/h; μ = 0.5		
Hungary	SCRIM > 0.50	SCRIM > 0.40	SCRIM > 0.33
Japan	Friction > 0.25		
The Netherlands	DWW > 38	DWW > 38	
New South Wales	SCRIM > 0.30 – 0.55		
New Zealand	SCRIM > 055 om event sites, 35 for no-event sites		
Quebec	SCRIM > 0.7	SCRIM > 0.7	SCRIM > 0.55
South Australia	BPN > 45	BPN > 45	BPN > 45
Switzerland	Same as for construction and rehabilitation		
United Kingdom	Same as investigatory levels		
USA: Arizona	34 (MuMeter)	34 (MuMeter)	34 (MuMeter)
USA: Idaho	SN40S > 30	SN40S > 30	SN40S > 30
USA: Illinois	SN40R > 30	SN40R > 30	SN40R > 30
USA: Kentucky	SN40R > 28	SN40R > 25	SN40R > 25
USA: New York	SN40R > 32	SN40R > 32	SN40R > 32
USA: South Carolina	SN40R > 41	SN40R > 37	SN40R > 37
USA: Texas	SN40R > 30	SN40R > 26	SN40R > 22

While in some countries, the intervention levels are also defined by the texture. The requirements are higher for motorways compare to primary roads. Intervention levels for texture can be seen in Table 0.13.

Table 0.13 Intervention levels for texture [72]

Road Category	Motorways	Primary	Secondary
Hungary	RMS < 0.22 mm	RMS < 0.14 mm	RMS < 0.10 mm
New Zealand	MTD < 0.90 mm	MTD < 0.90 mm	MTD < 0.90 mm
Quebec	MTD < 0.60 mm	MTD < 0.60 mm	MTD < 0.60 mm
South Australia	0.4 < MTD < 0.8 mm	0.2 < MTD < 0.4 mm	0.2 < MTD < 0.4 mm

Appendix F: Multi Criteria Analysis

F.1. Radar Chart Analysis

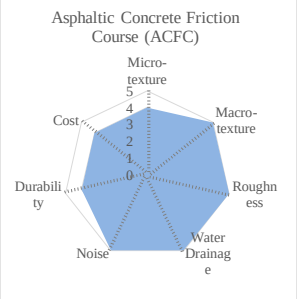

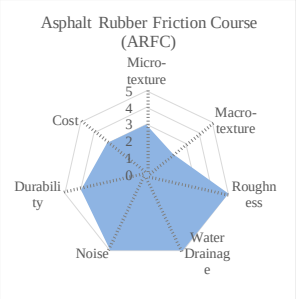

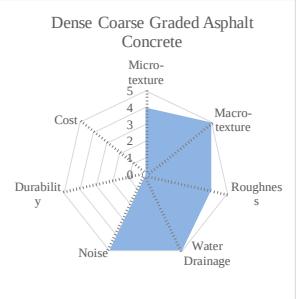

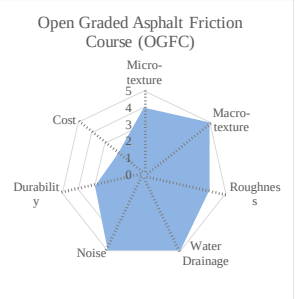

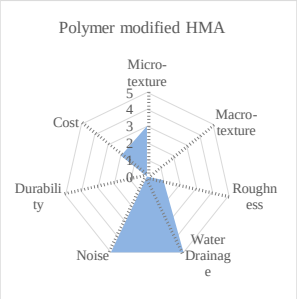

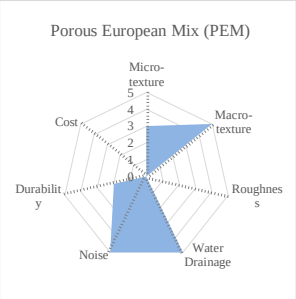

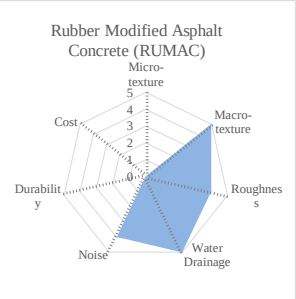

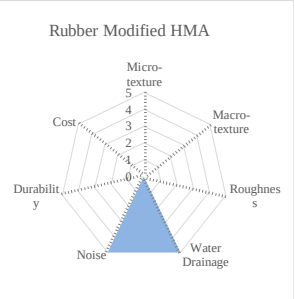

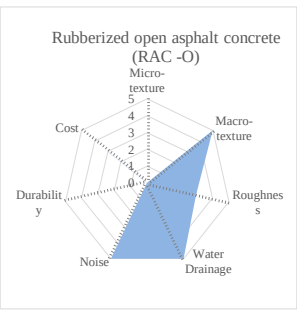

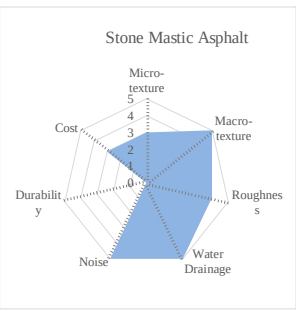

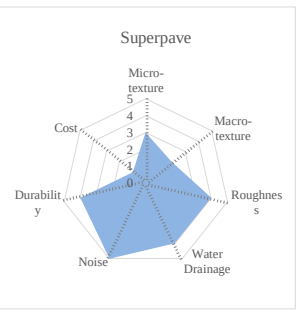

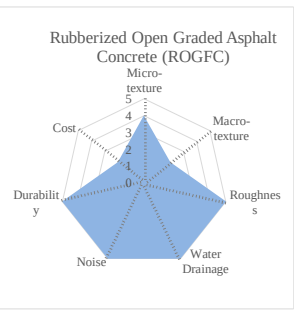

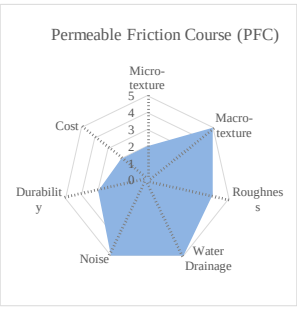

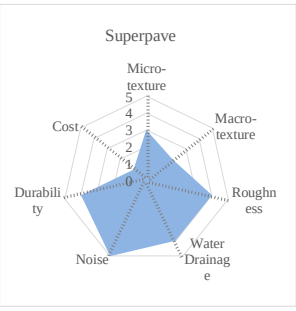

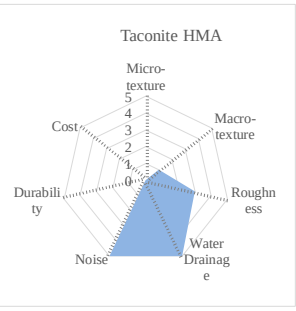

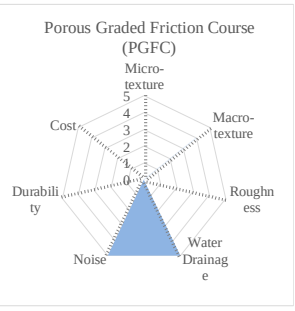

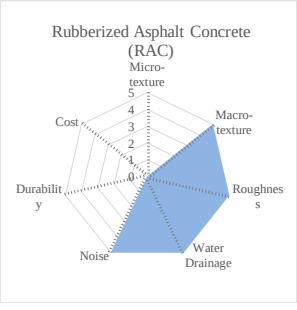

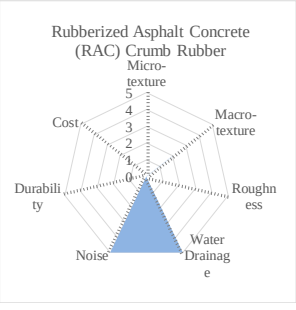

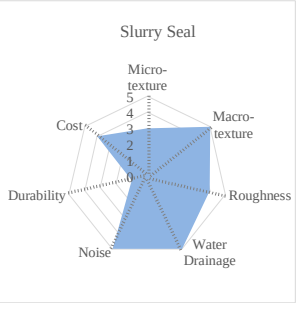

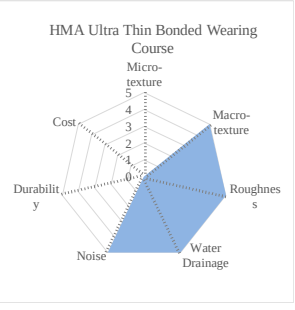

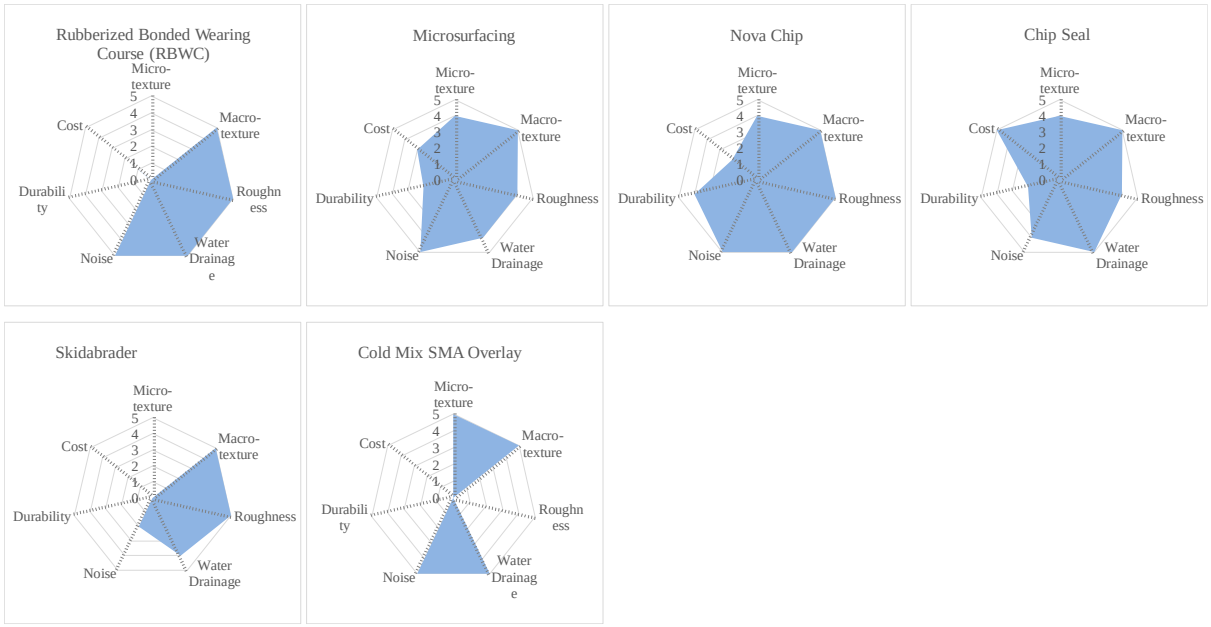

Figure 0.9 Functional performance on asphalt pavement texturing methods

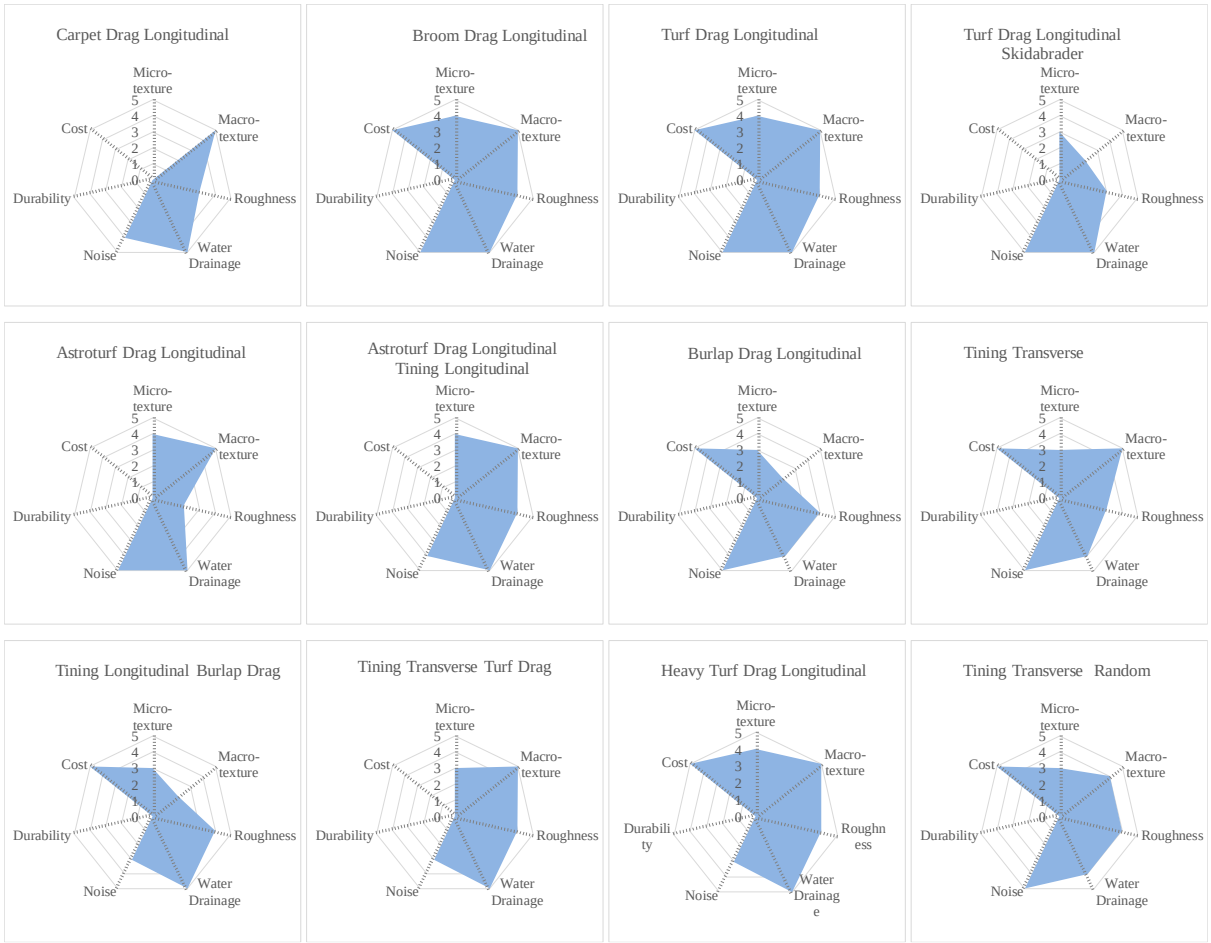

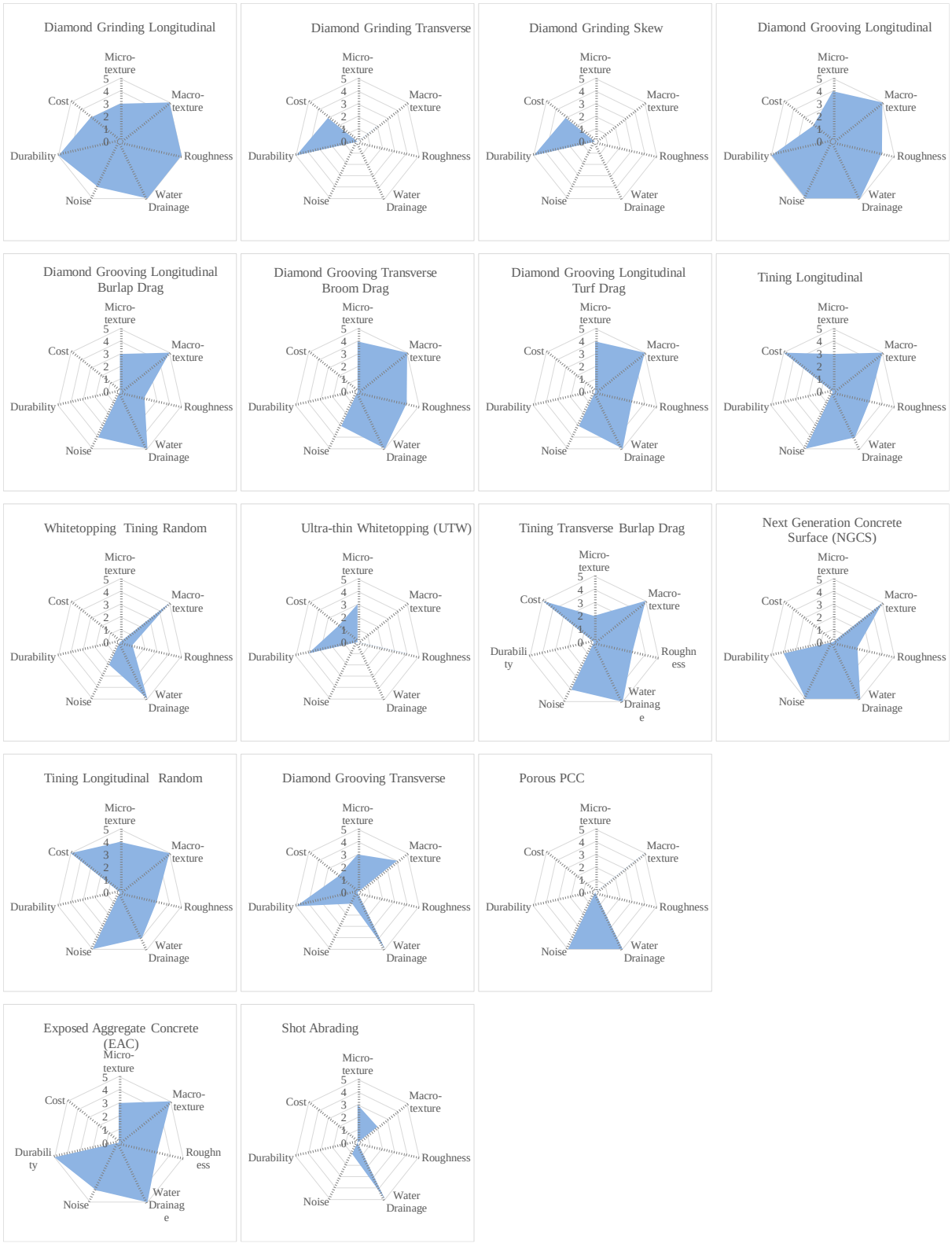

Figure 0.10 Functional performance based on concrete pavement texturing methods

F.2. Multiple two-constraints Analysis

Figure 0.11 gives the individual two-constraint analysis. The plot is illustrated with scatter chart, with each dot represent as the average value of one single texturing method. The value is completed with standard deviation in both direction (each for one constraint).

The first Figure 0.11a shows plot chart of microtexture against macrotexture for different texturing methods. There are various texturing methods available resulting good skid resistance (as an objective) as well as macrotexture for asphalt and concrete pavements. It is noted from the plot that diamond grooving is giving one of the most optimum design in terms of microtexture and macrotexture. The second-best optimum design is given by chip seal and longitudinal diamond grooving.

The second plot, Figure 0.11.b, gives an overview of texturing methods regarding to microtexture and surface water drainage constraints. Results gives best scenario is given by diamond grooving for concrete pavement and rubberized open graded asphalt concrete. In general, surface with water outflow less than 10 seconds resulting sufficient performance for surface drainage resulting lower risks of hydroplaning. As can be seen from the figure, most of texturing methods are able to achieve these criteria. Yet, on the other hand, it should be noted that fair performance (>55 BPN) of microtexture (skid resistance) is preferred to be fulfilled.

Figure 0.11.c shows texturing methods performance regarding to microtexture and tire-pavement noise. The first best options include heavy turf drag and longitudinal tining. The second-best options include diamond grooving, and rubberized open graded asphalt concrete.

Figure 0.11.d shows texturing methods performance regarding to microtexture and pavement roughness. The first best options include longitudinal heavy turf drag, diamond grooving, and Nova chip. The second-best options include longitudinal diamond grooving, rubberized open graded asphalt concrete, and asphaltic concrete friction course.

Figure 0.11.e shows texturing methods performance regarding to macrotexture and surface water drainage. The first best options include whitetopping with tining and shot abrading. The second best include longitudinal diamond grooving.

Figure 0.11.f shows texturing methods performance regarding to macrotexture and tire-pavement noise. The first best option includes open graded asphalt friction course. The second-best options include longitudinal diamond grooving, and longitudinal tining.

Figure 0.11.g shows texturing methods performance regarding to macrotexture and pavement roughness. The first best options include longitudinal turf drag, astroturf drag, and Nova chip. The second-best options include transverse tining, rubber modified asphalt course, and longitudinal diamond grooving.

Figure 0.11.h shows texturing methods performance regarding to surface water drainage and tire-pavement noise. The first best options include asphalt rubber friction course, longitudinal turf drag, and rubberized open graded asphalt concrete. The second-best options include Porous European Mix.

Figure 0.11.i shows texturing methods performance regarding to surface water drainage and pavement roughness. The first best options include rubberized bonded wearing course, rubberized open graded asphalt concrete, transverse tining, longitudinal tining. The second best include Porouse European Mix, and longitudinal turf drag.

Figure 0.11.j shows texturing methods performance regarding to tire-pavement noise and pavement roughness. The first best options include rubberized bonded wearing course,

asphalt rubber friction course. The second-best options include diamond grooving, Nova chip, rubberized open graded asphalt concrete polymer modified HMA. As expected, texturing methods for asphalt pavement able to generate less noise compare to those for concrete pavement generally.

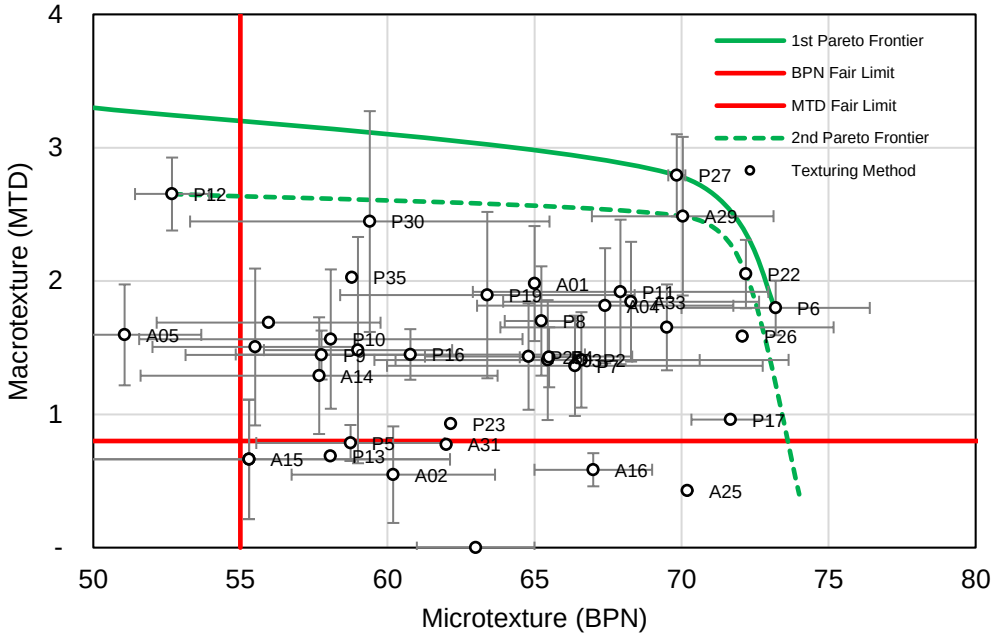

(a)

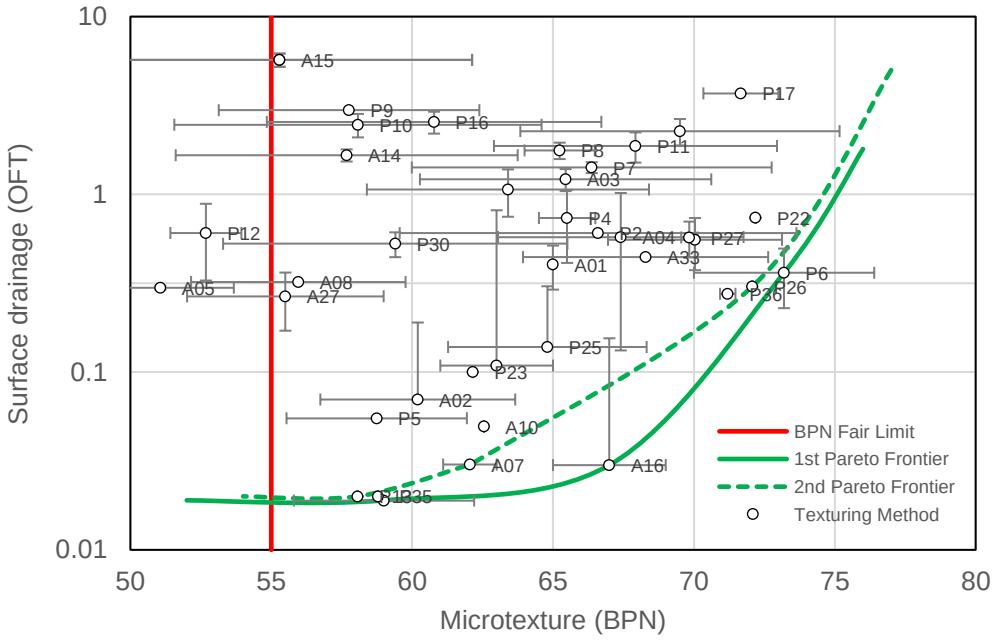

(b)

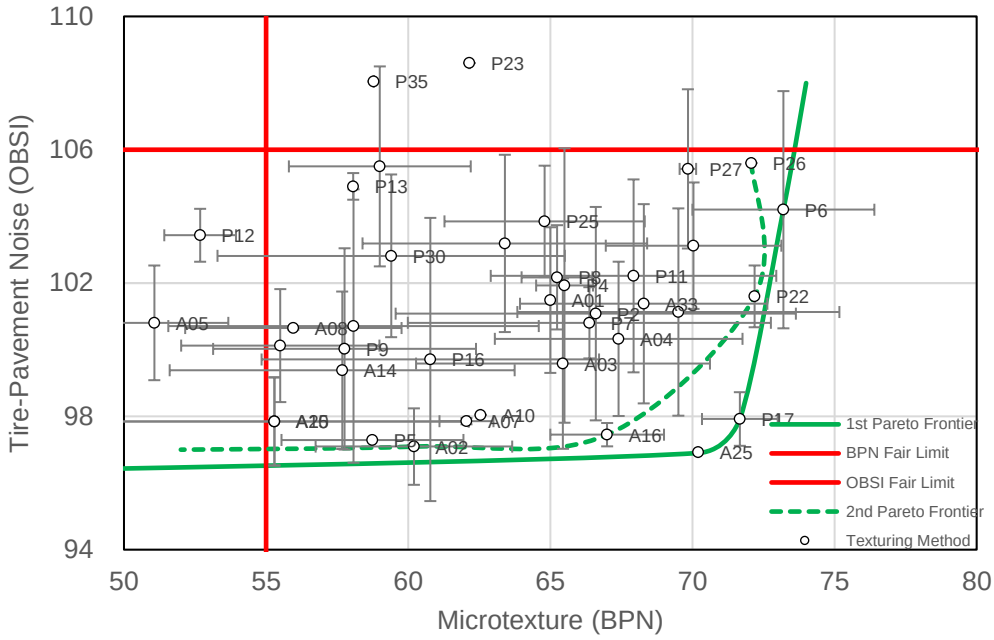
Tire-Pavement Noise (OBSI)
Microtexture (BPN)
110
106
102
98
94
50
55
60
65
70
75
80
1st Pareto Frontier
BPN Fair Limit
OBSI Fair Limit
2nd Pareto Frontier
Texturing Method

(c)

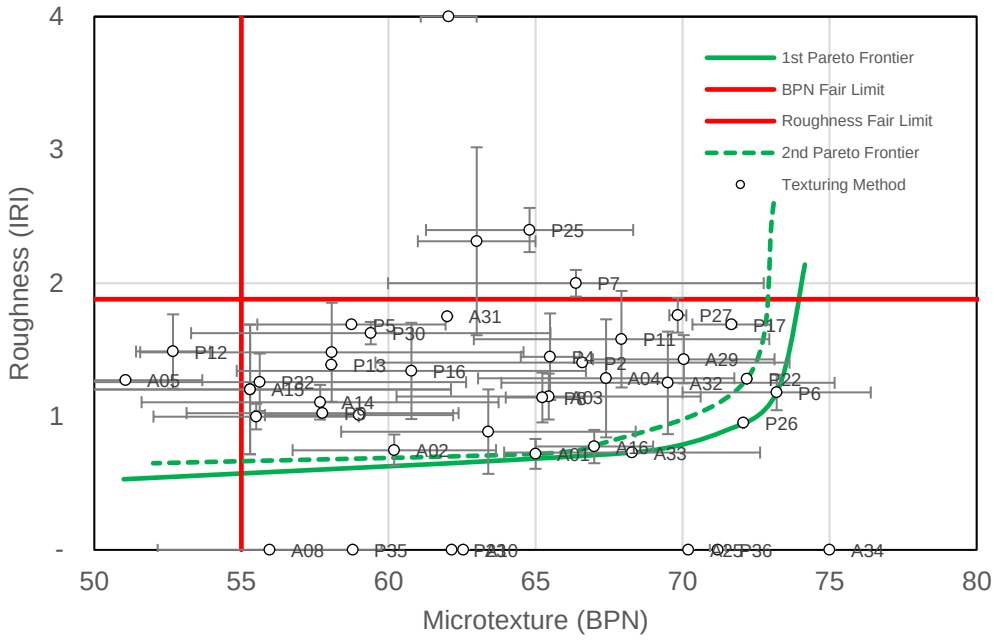
Roughness (IRI)
Microtexture (BPN)
4
3
2
1
-
50
55
60
65
70
75
80
1st Pareto Frontier
BPN Fair Limit
Roughness Fair Limit
2nd Pareto Frontier
Texturing Method

(d)

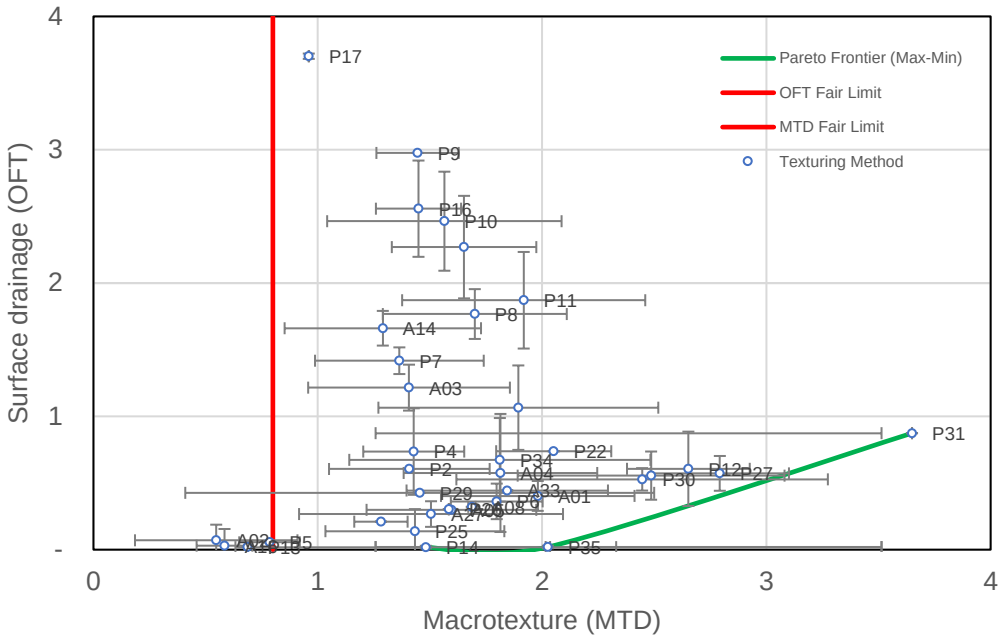
Surface drainage (OFT)
Macrotexture (MTD)
Pareto Frontier (Max-Min)
OFT Fair Limit
MTD Fair Limit
Texturing Method
P17
P31
P35
4
3
2
1
-
0
1
2
3
4

(e)

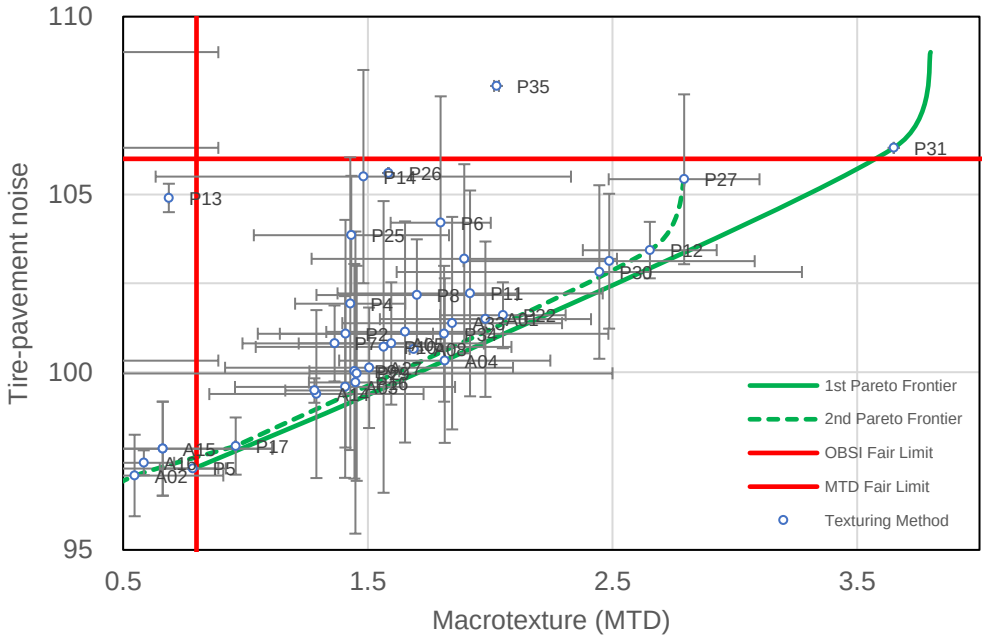
Tire-pavement noise
Macrotexture (MTD)
1st Pareto Frontier
2nd Pareto Frontier
OBSI Fair Limit
MTD Fair Limit
Texturing Method
P35
P31
P27
P13
P17
110
105
100
95
0.5
1.5
2.5
3.5

(f)

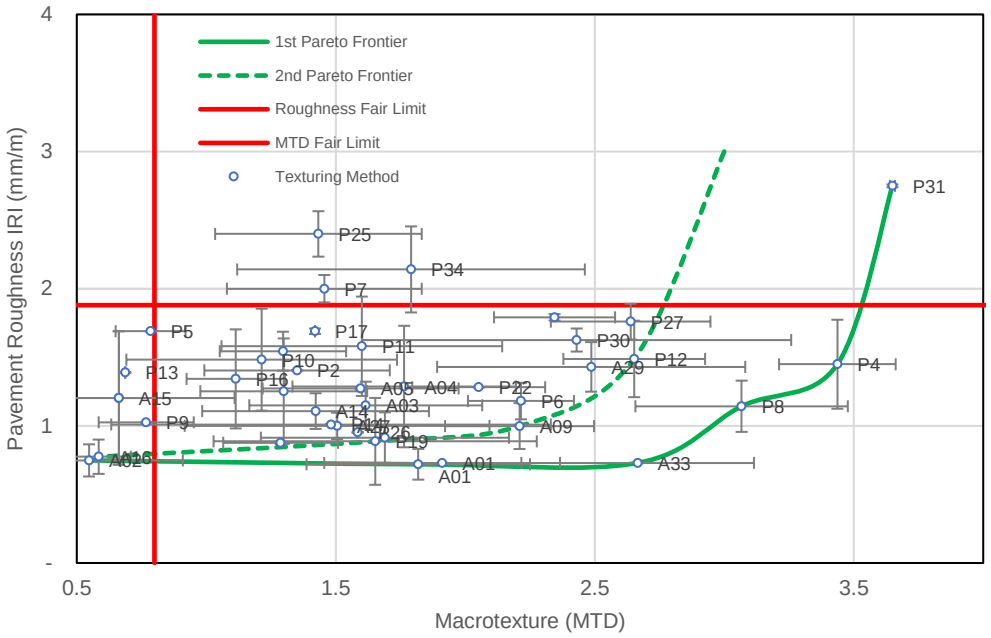
1st Pareto Frontier
2nd Pareto Frontier
Roughness Fair Limit
MTD Fair Limit
Texturing Method
Pavement Roughness IRI (mm/m)
Macrotexture (MTD)
4
3
2
1
-
0.5
1.5
2.5
3.5
P31
P25
P34
P7
P5
P17
P11
P30
P27
P10
P2
P12
P4
P13
P16
A15
A05
A04
P22
P6
P8
A03
A09
P9
A01
A33

(g)

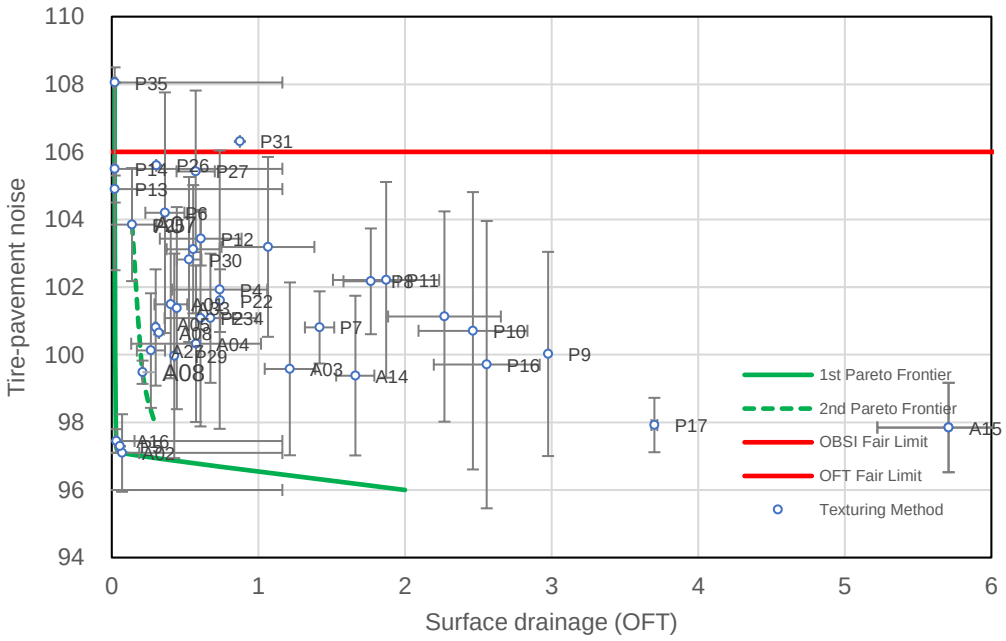
1st Pareto Frontier
2nd Pareto Frontier
OBSI Fair Limit
OFT Fair Limit
Texturing Method
Tire-pavement noise
Surface drainage (OFT)
110
108
106
104
102
100
98
96
94
0
1
2
3
4
5
6
P35
P31
P14
P26
P27
P13
P12
P30
P4
P22
P7
P10
P9
P16
A08
A03
A14
P17
A15

(h)

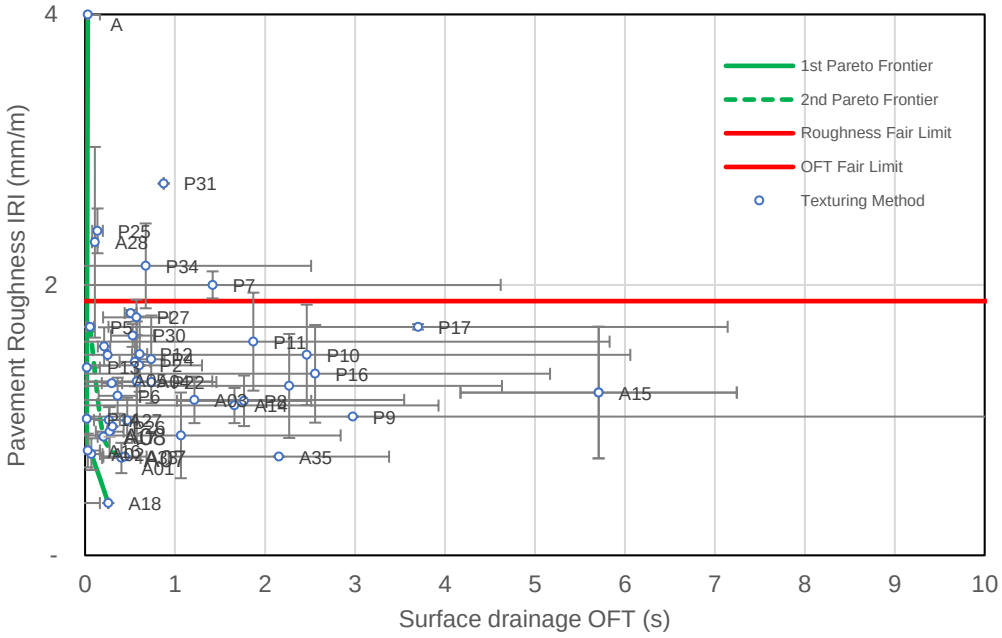

(i)

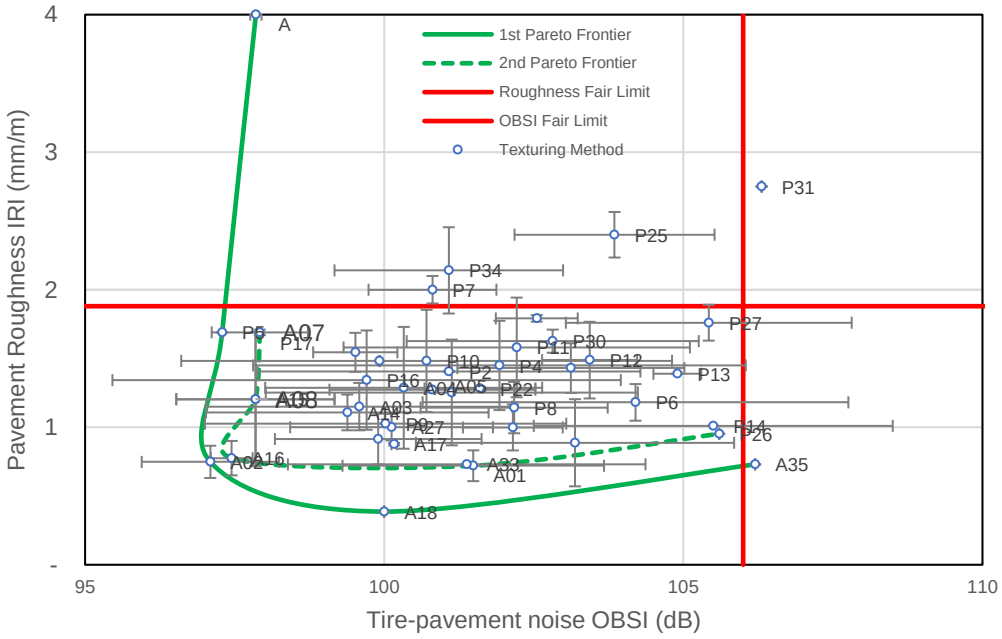

(j)

Figure 0.11 Two-constraints analysis of functional performance for pavement (a) microtexture and macrotexture, (b) microtexture and surface water drainage, (c) microtexture and tire-pavement noise, (d) microtexture and pavement roughness, (e) macrotexture and surface water drainage, (f) macrotexture and tire-pavement noise, (g) macrotexture and pavement roughness, (h) surface water drainage and tire-pavement noise, (i) surface water drainage and pavement roughness, and (j) tire-pavement noise and pavement roughness

F.3. Code and Name of Texturing Methods

Table 0.14 Code and name of texturing method for asphalt pavement

Name of Texturing Method	Name Code	Application Code	
Asphaltic Concrete Friction Course (ACFC)	A01	ACNO	
Asphalt Rubber Friction Course (ARFC)	A02	ACNO	
Dense Coarse Graded Asphalt Concrete	A03	ACNO	ACRF
Open Graded Asphalt Friction Course (OGFC)	A04	ACNO	ACRF
Permeable Friction Course (PFC)	A05	ACNO	
Porous Graded Friction Course (PGFC)	A06	ACNO	
Polymer modified HMA	A07	ACNO	ACRF
Porous European Mix (PEM)	A08	ACNO	
Rubber Modified Asphalt Concrete (RUMAC)	A09	ACNO	
Rubber Modified HMA	A10	ACNO	ACRF
Rubberized Asphalt Concrete (RAC)	A11	ACNO	
Rubberized Asphalt Concrete (RAC) Crumb Rubber	A12	ACNO	
Rubberized open asphalt concrete (RAC -O)	A13	ACNO	
Stone Mastic Asphalt	A14	ACNO	
Superpave	A15	ACNO	
Rubberized Open Graded Asphalt Concrete (ROGFC)	A16	ACNO	
HMA Ultra Thin Bonded Wearing Course	A17	ACNO	ACRF
Rubberized Bonded Wearing Course (RBWC)	A18	ACNO	
Semi Rigid	A19	ACNO	ACRF
Taconite HMA	A21	ACNO	ACRF
Bonded Wearing Course (BWC)	A22	ACNO	
ASPEN Sealer	A23	ACRF	
Cold Mix SMA Overlay	A24	ACRF	
Carbonyte sealer	A25	ACRF	
Micromilling	A26	ACRF	
Slurry Seal	A27	ACRF	
Polymer modified Slurry Seal	A28	ACRF	
Chip Seal	A29	ACRF	
Ital Grip	A30	ACRF	
Fog Seal	A31	ACRF	
Microsurfacing	A32	ACRF	
Nova Chip	A33	ACRF	
Cargill SafeLane*	A34	ACRF	
Skidabrader	A35	ACRF	ACRF

Table 0.15 Code and name of texturing method for concrete pavement

Name of Texturing Method	Code	Application	
Carpet Drag Longitudinal	P1	PCCNO	
Broom Drag Longitudinal	P2	PCCNO	
Broom Drag Longitudinal Diamond Grooving	P3	PCCNO	
Turf Drag Longitudinal	P4	PCCNO	
Turf Drag Longitudinal Skidabrader	P5	PCCNO	
Heavy Turf Drag Longitudinal	P6	PCCNO	
Astroturf Drag Longitudinal	P7	PCCNO	
Astroturf Drag Longitudinal Tining Longitudinal	P8	PCCNO	
Burlap Drag Longitudinal	P9	PCCNO	
Tining Transverse	P10	PCCNO	
Tining Longitudinal	P11	PCCNO	
Tining Transverse Burlap Drag	P12	PCCNO	
Tining Longitudinal Burlap Drag	P13	PCCNO	
Tining Transverse Turf Drag	P14	PCCNO	
Tining Longitudinal Turf Drag	P15	PCCNO	
Tining Transverse Random	P16	PCCNO	
Tining Longitudinal Random	P17	PCCNO	
Tining Skew	P18	PCCNO	
Diamond Grinding Longitudinal	P19	PCCNO	PCCRF
Diamond Grinding Transverse	P20	PCCNO	PCCRF
Diamond Grinding Skew	P21	PCCNO	PCCRF
Diamond Grooving Longitudinal	P22	PCCNO	PCCRF
Diamond Grooving Transverse	P23	PCCNO	PCCRF
Diamond Grooving Skew	P24	PCCNO	PCCRF
Diamond Grooving Longitudinal Burlap Drag	P25	PCCNO	PCCRF
Diamond Grooving Transverse Broom Drag	P26	PCCNO	PCCRF
Diamond Grooving Longitudinal Turf Drag	P27	PCCNO	PCCRF
Diamond Grooving Transverse Turf Drag	P28	PCCNO	PCCRF
Porous PCC	P29	PCCNO	
Exposed Aggregate Concrete (EAC)	P30	PCCNO	
Whitetopping Tining Random	P31	PCCNO	PCCRF
Ultra-thin Whitetopping (UTW)	P32	PCCNO	PCCRF
Thin Whitetopping (TTW)	P33	PCCNO	PCCRF
Next Generation Concrete Surface (NGCS)	P34	PCCNO	
Shot Abrading	P35	PCCRF	

Name of Texturing Method	Code	Application	
VDOT Modified EP-5	P36	PCCRF	
Smooth troweled	P37	PCCRF	

Appendix G: Tekscan Results for contact stresses on slabs

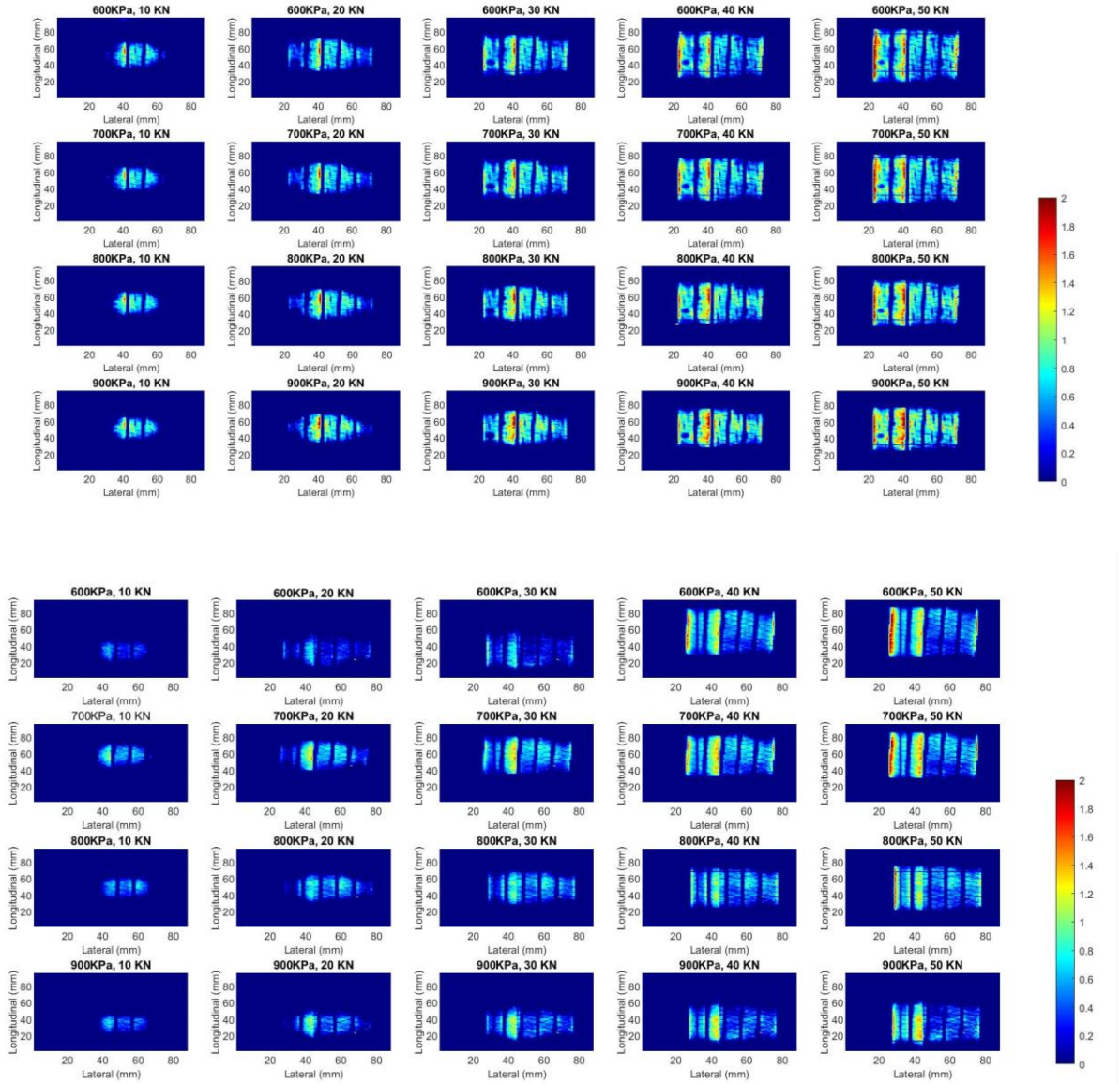

Figure 0.12 Tekscan I-Scan results for (top) ECC-Cor and (bottom) ECC-Cor Gro 1

Appendix H: 3D CFX Surface Water Drainage Model

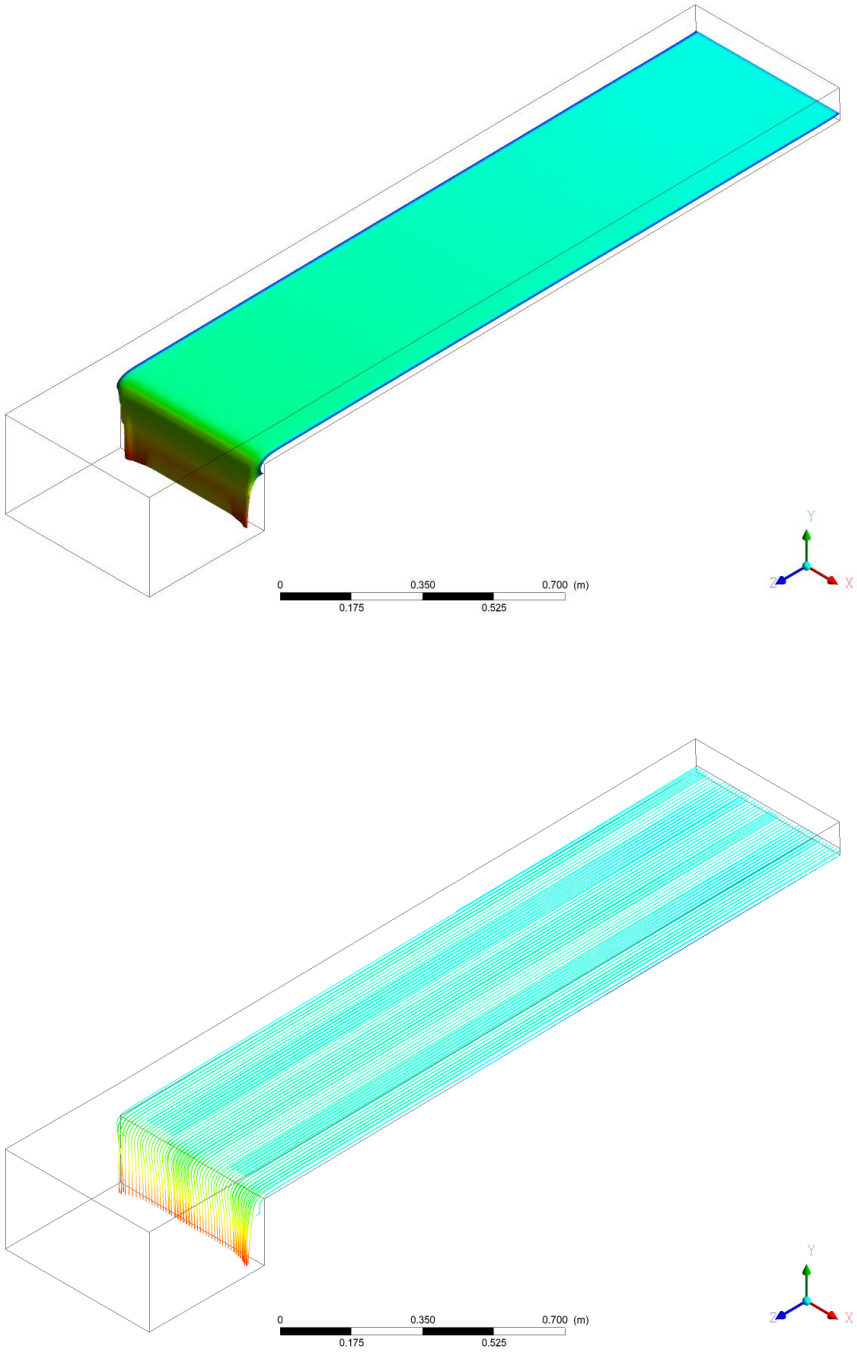

Figure 0.13 CFX results of WFT on ECC-Cor with (a) isosurface, (b) isoclip

Appendix I: Flow Chart

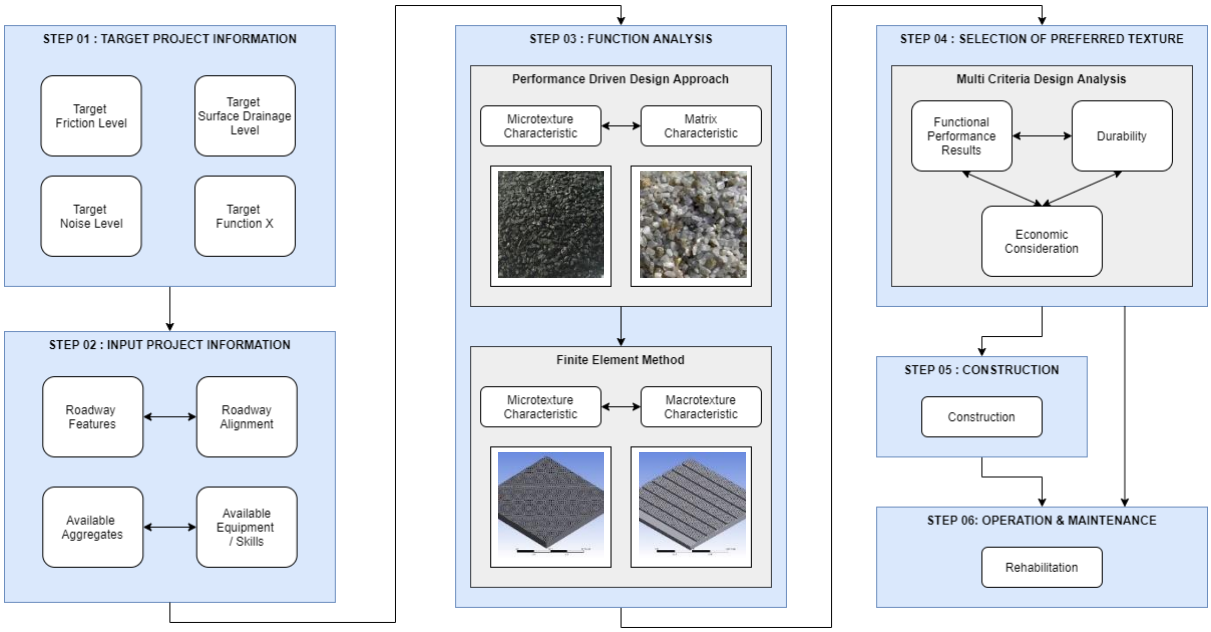

Figure 0.14 Flow chart for comprehensive analysis